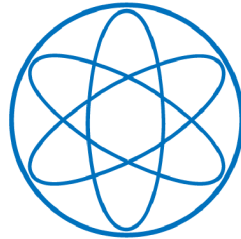


PHYSIK - DEPARTMENT

-

LEHRSTUHL FÜR EXPERIMENTALPHYSIK
UND ASTROTEILCHENPHYSIK



Experimental Determination of the
Antineutrino Spectrum of the Fission
Products of ^{238}U

DISSERTATION

VON

NILS-HOLGER HAAG



TECHNISCHE UNIVERSITÄT MÜNCHEN

TECHNISCHE UNIVERSITÄT MÜNCHEN
Physik-Department
Lehrstuhl für Experimentalphysik und Astroteilchenphysik
Univ.-Prof. Dr. Stefan Schönert

Experimental Determination of the Antineutrino Spectrum of the Fission Products of ^{238}U

Nils-Holger Haag

Vollständiger Abdruck der von der Fakultät für Physik der Technischen Universität München zur Erlangung des akademischen Grades eines

Doktors der Naturwissenschaften (Dr. rer. nat.)

genehmigten Dissertation.

Vorsitzender: Univ.-Prof. Dr. N. Kaiser

Prüfer der Dissertation:

1. Univ.-Prof. Dr. L. Oberauer
2. Priv.-Doz. Dr. H. Kroha

Die Dissertation wurde am 13.08.2013 bei der Technischen Universität München eingereicht und durch die Fakultät für Physik am 09.10.2013 angenommen.

Abstract

Nuclear reactors are intense emitters of electron antineutrinos and thus ideal sources for experiments studying various aspects of neutrino physics, like the determination of the angles present in the neutrino mixing matrix and the search for sterile neutrinos. A key to accurately perform experiments detecting reactor antineutrinos is the knowledge of the total antineutrino spectrum emitted by a reactor core. This $\bar{\nu}_e$ -spectrum consists of several thousand branch-level spectra produced in the beta decays of the fission daughters of the four main fuel isotopes ^{235}U , ^{238}U , ^{239}Pu , and ^{241}Pu . One approach to predict the total antineutrino spectrum is based on the experimental determination of the $\bar{\nu}$ -spectrum emitted after fission for each fuel isotope separately. The four individual antineutrino spectra are weighted by the fission rate of the particular isotope in the nuclear reactor and add up to the total antineutrino spectrum. The measurement of the individual $\bar{\nu}$ -spectra is accomplished by the measurement of the total beta spectrum emitted after the fission of the particular isotope and a subsequent conversion of this β -spectrum into an antineutrino spectrum. In the late 1980's, the β - and $\bar{\nu}$ -spectra of three of the main fuel isotopes (^{235}U , ^{239}Pu , and ^{241}Pu) have been determined by irradiation of the isotopes with thermal neutrons in the BILL experiment at the ILL in Grenoble. However, ^{238}U - contributing $\sim 10\%$ to the total antineutrino flux of a reactor core - is fissionable with fast neutrons only ($E_n \gtrsim 1\text{ MeV}$), and up to now only theoretical predictions of the antineutrino spectrum of ^{238}U exist.

The present work is dedicated to the experimental determination of the antineutrino spectrum of the fission products of ^{238}U . For this purpose, an experiment is set up at the neutron source Heinz Maier-Leibnitz (FRM II) in Garching. A fast-neutron beam induces fissions in a natural uranium foil and the beta spectrum emitted is detected by a gamma-suppressing electron telescope. The target is irradiated for about 53 hours, but data from the first 11 h is neglected in the analysis to minimise off-equilibrium effects. The detector consists of two parts: a spectroscopic module, made of a plastic scintillator coupled to a photomultiplier, and a multi-wire chamber (MWC) in front of it. The two modules are operated in coincidence. Due to the low density of the counting gas of the MWC, the majority of gamma radiation emitted by the target foil passes the MWC undetected, leading to a suppression of gamma background by more than 99.5%. The energy resolution of this setup is determined to be $8\% \cdot \frac{1}{\sqrt{E[\text{MeV}]}}$ (FWHM).

Additionally to the beta spectrum emitted after fission of ^{238}U by fast neutrons, the β -spectrum after thermal neutron irradiation of ^{235}U is measured at the same experimental site with an identical uranium foil. The comparison of the results from this ^{235}U measurement with the already known ^{235}U spectrum determined by the BILL experiment allows to cross check the energy-dependent response function of the setup and minimises its impact on the data.

Furthermore, the comparison allows to extract a normalisation function to perform an absolute calibration of the ^{235}U spectrum without the knowledge of the neutron flux, the beam profile and, consequently, the number of fissions in the uranium foil. Subsequently, the normalisation function is applied to the measured ^{238}U spectrum, terminating many possible sources of systematic errors. The absolute calibration of the final ^{238}U beta spectrum is performed by the determination of the relative amount of fissions in the uranium foils in the thermal and the fast neutron beam by germanium γ -spectroscopy of the irradiated targets.

Finally, the beta spectrum obtained is converted into an antineutrino spectrum. This is done by shifting the beta spectrum by ~ 0.5 MeV to account for the differences of the beta and antineutrino spectra due to the mass and the electric charge of the electron. The remaining corrections to be applied after this shift are of the order of 5 %.

As final result, the antineutrino spectrum of the fission products of ^{238}U is provided in 250 keV bins in a range from 2.875 - 7.625 MeV with an energy-dependent error of 3.5 % at 3 MeV, 7.6 % at 6 MeV and $\gtrsim 14$ % at energies $\gtrsim 7$ MeV (68 % confidence level). In addition to that, there is a nearly energy-independent error of ~ 3.3 % due to the absolute normalisation.

The antineutrino spectrum measured reveals an underestimation of the flux obtained by theoretical predictions in the energy regime $\lesssim 4$ MeV of the order of 10 % and an overestimation above $\gtrsim 4$ MeV of 5 - 10 %. This may lead to small changes in the global fit values of current reactor antineutrino experiments.

The average antineutrino cross section per fission determined for the energy range of 2.875 MeV - 7.625 MeV is $(8.51 \pm 0.37) \cdot 10^{-43} \frac{\text{cm}^2}{\text{fission}}$ (68 % C.L.). This value is nearly identical to the ones from theoretical predictions, validating that the reactor antineutrino anomaly currently discussed is not caused by faulty predictions of the ^{238}U antineutrino spectrum.

Zusammenfassung

Kernreaktoren sind hoch-intensive Quellen für Elektron-Antineutrinos. Es existieren zahlreiche Experimente, die mit Hilfe von Reaktorantineutrinos verschiedene Aspekte der Neutrino-Physik behandeln, wie zum Beispiel die Bestimmung der Neutrino-Mischungswinkel oder die Suche nach sterilen Neutrinos. Grundlegend für die Analyse dieser Reaktorantineutrino-Experimente ist das Wissen um das gesamte von einem Reaktor emittierte $\bar{\nu}$ -Spektrum. Die Antineutrinoemission eines üblichen Druckwasserreaktors wird hauptsächlich durch die vier Brennisotope ^{235}U , ^{238}U , ^{239}Pu und ^{241}Pu erzeugt. Das gesamte Antineutrinospektrum ist die Summe mehrerer tausend einzelner Spektren, die in den Betazerfällen der durch Spaltungen der Brennisotope erzeugten Tochterisotope emittiert werden.

Eine Möglichkeit, das gesamte emittierte Antineutrinospektrum vorherzusagen, beruht darauf, das $\bar{\nu}$ -Spektrum nach der Spaltung für jedes der vier Brennisotope getrennt zu messen. Die so erhaltenen vier Spektren werden anschließend mit der Spaltrate des jeweiligen Isotops im Reaktor gewichtet und zu dem Gesamt- $\bar{\nu}$ -Spektrum zusammengesetzt. Die experimentelle Bestimmung der individuellen Antineutrinospektren erfolgt durch die Messung der Betaspektren, die nach der Spaltung emittiert werden. Diese werden dann in die zugehörigen Antineutrinospektren konvertiert. In den 1980er Jahren wurden die Antineutrinospektren von ^{235}U , ^{239}Pu und ^{241}Pu durch Bestrahlung mit thermischen Neutronen im BILL-Experiment am ILL in Grenoble auf die vorgestellte Art und Weise bestimmt. ^{238}U , welches einen Anteil von etwa 10% zum gesamten Neutrinofluss eines Reaktors beiträgt, ist jedoch nur mit schnellen Neutronen einer Energie von $E_n \gtrsim 1 \text{ MeV}$ spaltbar, weswegen bis heute nur theoretische Vorhersagen für das Antineutrinospektrum der Spaltprodukte von ^{238}U existieren.

Die vorliegende Arbeit befasst sich mit der experimentellen Bestimmung dieses Antineutrinospektrums der Spaltprodukte von ^{238}U . Hierfür wurde ein Experiment an der Forschungs-Neutronenquelle Heinz Maier-Leibnitz (FRM II) in Garching durchgeführt. Ein Strahl schneller Neutronen wurde genutzt, um Spaltungen in einer Folie aus natürlichem Uran zu induzieren. Das Betaspektrum, emittiert in einem Zeitraum von 42 Stunden - beginnend 11 Stunden nach Anfang der Bestrahlung - wurde mit einer Gammastrahlung unterdrückenden Elektronen-Teleskop aufgezeichnet. Dieser Detektor besteht im Kern aus zwei Teilen: Einem Spektroskopiemodul - bestehend aus einem Plastikszintillator, der an einen Photomultiplier angekoppelt ist - und einer Vieldrahtkammer. Diese beiden Module wurden in Koinzidenz geschaltet. Durch die geringe Dichte des Zählgas der Vieldrahtkammer passiert der Großteil der Gammaquanten die Kammer undetektiert, was bei der erwähnten Schaltung zu einer Unterdrückung des Gammauntergrundes von mehr als 99,5% führt. Die Energieauflösung des gesamten Systems ist $8\% \cdot \frac{1}{\sqrt{E[\text{MeV}]}}$ (Halbwertsbreite).

Zusätzlich zum Betaspektrum der Spaltprodukte von ^{238}U im schnellen Neutronenstrahl wurde mit einer identischen Uranfolie das β -Spektrum der Spaltprodukte von ^{235}U in einem thermischen Strahl gemessen. Durch den Vergleich dieses gemessenen Spektrums mit dem schon durch die BILL-Messungen bekannten ^{235}U -Spektrums konnte die energieabhängige Response-Funktion des Systems überprüft und ihr Einfluss auf die Daten minimiert werden. Zudem konnte aus dem Vergleich eine Normalisierungsfunktion extrahiert werden, die die absolute Kalibration des ^{235}U -Spektrums ohne Kenntnis des Neutronenflusses, des Strahlprofils und damit auch der Anzahl der Spaltungen im Urantarget ermöglichte. Die erhaltene Normalisierungsfunktion wurde auf die gemessenen ^{238}U -Daten angewandt, was das sonst mögliche Auftreten einiger systematischer Fehler verhinderte. Die Absolutkalibration des β -Spektrums der Spaltprodukte von ^{238}U wurde daraufhin durch eine Gammaspektroskopie der beiden im thermischen und schnellen Neutronenstrahl aktivierten Folien mit einem hochauflösenden Ge-Halbleiterdetektor durchgeführt, wodurch die relativen Spaltraten in den Folien während der Bestrahlung bestimmt werden konnten. Schließlich wurde das erhaltene Betaspektrum in das zugehörige Antineutrinospektrum konvertiert. Dies wurde durch eine Verschiebung des Elektronspektrums um 0,5 MeV erreicht, was die Einflüsse der Masse des Elektrons und dessen elektrischer Ladung auf das Spektrum korrigierte. Die verbliebenen Korrekturen, die danach durchgeführt wurden, waren im Bereich von nur etwa 5 %.

Das abschließende Ergebnis dieser Arbeit ist das in 250 keV breite Bins unterteilte Antineutrinospektrum der Spaltprodukte von ^{238}U in einem Energiebereich von 2,875 bis 7,625 MeV. Der kombinierte (statistische und systematische) Fehler beläuft sich auf 3,5 % bei 3 MeV, 7,6 % bei 6 MeV und $\gtrsim 14$ % bei Energien $\gtrsim 7$ MeV (68 % Signifikanz-Intervall). Hinzu kommt ein nahezu energieunabhängiger Fehler der absoluten Kalibration von 3,3 %. Das gemessene Antineutrinospektrum zeigt, dass die bisherigen theoretischen Vorhersagen das Spektrum im Energiebereich unterhalb von 4 MeV in der Größenordnung von 10 % unterschätzen und im Energiebereich über 4 MeV im Bereich von 5-10 % überschätzen. Die nun auf die bisherigen Reaktorspektren anzuwendende spektrale Korrektur wird vermutlich zu kleinen Änderungen in den globalen Fits der aktuellen Reaktorantineutrino-Experimente führen.

Der in diesem Experiment bestimmte gemittelte Antineutrino-Wechselwirkungsquerschnitt pro Spaltung von $(8,51 \pm 0,37) \cdot 10^{-43} \frac{\text{cm}^2}{\text{Spaltung}}$ (68 % C.L.) im Bereich von 2,875-7,625 MeV ist nahezu identisch mit demjenigen, der durch die Berechnungen vorhergesagt wurde. Somit wird ausgeschlossen, dass die momentan diskutierte Reaktorantineutrino-Anomalie durch eine fehlerhafte Vorhersage des Antineutrinospektrums der Spaltprodukte von ^{238}U erklärt werden kann.

Contents

1	Neutrino physics with nuclear reactors	1
1.1	Actual tasks of reactor antineutrino experiments	3
1.1.1	The reactor antineutrino anomaly	3
1.1.2	Determination of neutrino parameters	5
1.1.3	Neutrinos for non-proliferation of nuclear weapons	7
1.1.4	Reactor antineutrinos as background	8
1.2	Antineutrino production in nuclear reactors	9
1.3	Status of predictions for the reactor $\bar{\nu}_e$ -spectrum	10
1.3.1	Method 1: The summation approach	11
1.3.2	Method 2: Conversion of fission β -spectra	12
1.4	The concept of measurement	13
2	The experimental setup	15
2.1	The neutron source	15
2.1.1	The neutron beam at SR10	16
2.2	Conceptual overview of the setup	21
2.3	The spectroscopic module	23
2.4	The multi-wire chamber	25
2.5	Further mechanical components	28
2.6	Targets and Sources	30
2.7	Electronics and data acquisition	32
2.8	Simulation of the setup	36
3	Data analysis I: Calibration and detector performance	39
3.1	Data format	39
3.1.1	Cut on events in the multi-wire chamber	40
3.2	Response function	42
3.3	Energy calibration	49
3.3.1	The calibration with the ^{207}Bi source	50
3.3.2	Calibration with indium and chlorine foils	50
3.3.3	The final calibration	56
3.4	Stability over time	58
3.4.1	Stability tests in the laboratory	58

3.4.2	In-situ stability tests at the reactor site	59
3.5	Remarks on radioactive equilibrium	64
4	Data analysis II: The analysis chain	67
4.1	Accidental coincidences and β -decay-correlated background	68
4.2	Subtraction of beam-correlated background	72
4.2.1	The fast neutron beam	73
4.2.2	Notes on the experimental threshold	81
4.2.3	The thermal neutron beam	83
4.3	Subtraction of events due to fission of ^{235}U	89
4.3.1	The background-free beta spectrum of ^{238}U	93
4.4	The normalisation: Comparison to the BILL spectrum	94
4.5	Absolute calibration of the β -spectrum	97
4.5.1	The determination of the fission rates	97
4.5.2	γ -lines chosen for spectroscopy	100
4.5.3	Results of the germanium γ -spectroscopy	100
5	The final ^{238}U β- and $\bar{\nu}$- spectrum	103
5.1	Error budget	103
5.1.1	Impact of the inaccuracy of the energy calibration	106
5.2	The measured beta spectrum: Comparison to calculations	108
5.3	Conversion into the antineutrino spectrum	112
5.4	Discussion of the results	119
5.4.1	The $\bar{\nu}$ -spectrum: Comparison of experiment and prediction	119
5.4.2	Impact of the results on reactor $\bar{\nu}$ experiments	122
6	Summary and Conclusions	127
A	Neutron scattering	133
B	Exponential smoothing	137
B.1	The method of exponential smoothing	137
B.2	Test of the re-binning method on the final data	139
C	Tests of the electronics	143
C.1	Test of linearity	143
C.2	Test of the automatic dead-time correction	144
D	Tables	149
D.1	The main measurements	149
D.2	Fission yields	150
	List of Figures	151

List of Tables	153
Bibliography	155

Chapter 1

Neutrino physics with nuclear reactors

In the last decades, physics with neutrinos has evolved into one of the leading fields in particle and astroparticle physics. The existence of antineutrinos was proven experimentally in the early 1950's when Cowan and Reines were able to detect $\bar{\nu}_e$ emitted by a reactor core [Cow53]. Today, 80 years after the postulation of the neutrino by Pauli [Sch97], multiple international collaborations dedicated to neutrino physics are established.

Neutrino detectors, like the former Homestake [Dav68] and GALLEX [Ans95] experiments, both based on radiochemical detection, Borexino [Pal13], using liquid scintillator techniques, or SNO [Tol12], a heavy-water detector, were or are analysing mainly solar neutrinos. It is one of the most prominent achievements of these solar ν experiments to have resolved the issue of neutrino oscillations [Akh11]. In the high-energy regime, these efforts were accompanied by measurements of atmospheric neutrinos, for example by the IceCUBE collaboration [Aar13] and the Super-Kamiokande experiment [Hos06], both relying on the water Cherenkov detection technique (as solid-state detector or liquid-water detector, respectively). Furthermore, accelerator-based neutrino experiments like MINOS [Ada11] or LSND [Agu01] work with high-energy muon-flavoured beams at long baselines of several hundred kilometers, investigating the appearance of other flavours and additionally testing the CP - violating phase present in the neutrino mixing matrix [Fog12].

Apart from the three neutrino sources mentioned (the sun, cosmic ray production in the atmosphere and accelerators), there exist various other production mechanisms ranging from small artificial sources like in the KATRIN experiment [Wol10] to cosmological objects like supernovae or active galactic nuclei. But in the framework of this work, the focus will lie on another man-made, earthbound neutrino source: nuclear reactors¹. Since the first days of experimental neutrino physics, nuclear reactors have played a crucial role in our understanding of neutrinos and their interactions. Many short baseline

¹A brief summary of the production of antineutrinos in reactors is given in sec. (1.2).

experiments² helped to narrow down the parameter space of neutrino oscillations. These experiments were set up too close to the reactor core to observe any three-neutrino oscillation effect, but verified the theoretical predictions of the average cross section per fission (as will be defined later in equation 1.1). Palo Verde [Law98] and Chooz [App03] were the first experiments with a baseline of ~ 1 km, which turned out to be the ideal distance for the search for ϑ_{13} , and set limits for $\sin^2(2\vartheta_{13})$ about a factor of two higher than what only recently could be verified to be the true value. Three modern reactor $\bar{\nu}_e$ disappearance experiments, Double Chooz, RENO and Daya Bay (see sec. 1.1.2), published the observation of oscillations due to ϑ_{13} in 2012. The verification of the relatively large values of all three mixing angles now opens the gate for the search for CP-violation in the leptonic sector [Fog12]. Furthermore, a collaboration is currently being formed to design the JUNO experiment³ [Li13]. This is intended to be a reactor antineutrino experiment with a baseline of ~ 60 km. At this baseline, the oscillation due to the mass-squared difference Δm_{21}^2 is maximal. The small frequency shift induced by the interference of the oscillations due to Δm_{31}^2 and Δm_{32}^2 may enable a measurement of the mass hierarchy [Li13].

The present thesis is intended to contribute to the field of reactor $\bar{\nu}$ physics by improving the precision of the predictions of the total antineutrino spectrum emitted by a reactor core. To fully understand the importance of accurate predictions of this reactor spectrum, the next sections will cover the actual tasks of reactor $\bar{\nu}$ experiments (sec. 1.1) and will discuss the production and prediction of reactor antineutrino spectra (sec. 1.2).

²For a description of the history of reactor neutrino physics see, e.g., [Bem02] and references therein.

³This name was chosen only very recently by the collaboration. Up to now, this experiment has been known as *Daya Bay 2*.

1.1 Actual tasks of reactor antineutrino experiments

Today's reactor antineutrino experiments are concerned with several tasks. These are the explanation of the reactor antineutrino anomaly (sec. 1.1.1), the determination of neutrino parameters (sec. 1.1.2), and the concept study to use antineutrino detectors for non-proliferation of nuclear weapons (sec. 1.1.3). Additionally, reactor antineutrinos are a background for the search for geoneutrinos and the diffuse supernova neutrino background (sec. 1.1.4).

1.1.1 The reactor antineutrino anomaly

As mentioned before, various antineutrino experiments were performed in the vicinity of nuclear reactors testing the theoretical calculations of the cross section of the inverse beta decay. At the time of these experiments, the predictions and measurements of the detected antineutrino event rate in the detectors matched within the experimental errors. However, in 2011 new calculations⁴ of the predicted antineutrino spectrum from the reactor core tended towards a higher antineutrino flux emitted [Mue11, Men11]. Consequently, the former experiments are now interpreted to see too few antineutrinos (see figure 1.1). Also data from actual experiments like Double Chooz is started to be analysed in the context of the reactor anomaly [Zha13] by using the value for ϑ_{13} from the other two actual experiments Daya Bay and RENO and fixing it in the analysis of the Double Chooz data.

At the moment, it is discussed in the literature [Men13, Zha13], how to correctly interpret and correlate the data of the former experiments. This has a direct influence on the magnitude and the significance of the discrepancy seen. [Men13] prefers a global fit leading to a ratio of predicted to measured antineutrino event rate of 0.943 ± 0.023 , i. e. a deviation from unity at 98.6% confidence level, whereas [Zha13] quote the ratio to be 0.959 ± 0.009 (experimental uncertainty) ± 0.027 (systematic flux uncertainty), thus deviating from unity only by 1.4σ .⁵

It has to be clarified whether this discrepancy between the measurements and the calculations from the predictions are due to systematic errors of the reactor input parameters (e. g. the thermal power), some kind of correlated uncertainty in all measurements, faulty predictions of the antineutrino spectrum emitted from the reactor or due to new physics. One of the possibilities actually discussed is the existence of one or more sterile neutrinos, not taking part in weak interaction [Men11]. The electron antineutrinos could couple to this neutrino type and oscillate into this sterile particle. To fit the experimental data, sterile neutrinos with a mass of the order of eV are preferred at the moment [Men11].

⁴These calculations include predictions of the antineutrino spectra by the *summation method* explained in sec. (1.3.1) as well as re-evaluations of the conversion method applied to the measured beta spectra of previous experiments [Sch85], see sec. (1.3.2).

⁵A new publication by the authors of [Men11, Men13] updating the global fit is planned to be published [LhuPC].

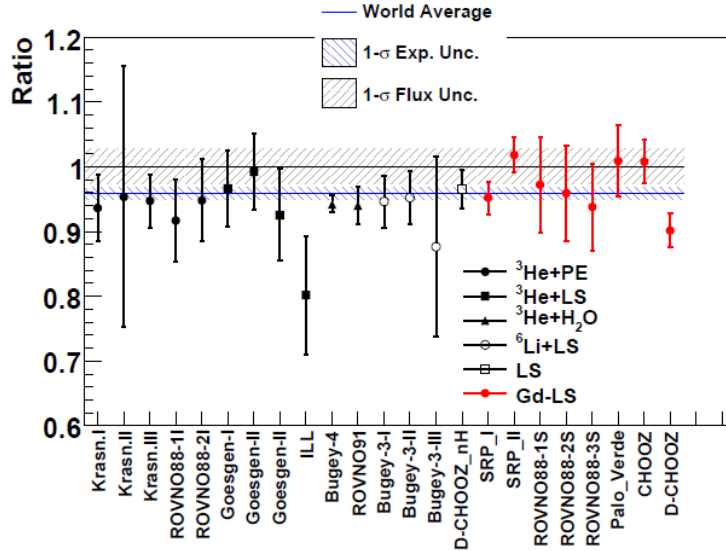


Figure 1.1: *Illustration of the reactor anomaly. Shown is the ratio of the experimentally obtained rate for various experiments performed to the predicted antineutrino rate in the detector. The black horizontal line indicates the expected ratio of 1 together with the 1σ uncertainty (2.7%) as shaded band. In blue, the global experimental average is shown together with its 1σ uncertainty as blue shaded area. One can see a deviation from unity, illustrating the reactor antineutrino anomaly. The exact value of the global average depends on the correlations between the experiments one includes and is currently being discussed in literature. Plot reprinted with permission from [Zha13].*

Several experimental methods are currently discussed to search for the existence of sterile neutrinos, like short-baseline oscillation experiments either with a strong neutrino source (e.g. in Borexino [Ian12]) or at a nuclear reactor.⁶ All the predictions of antineutrino event rates in the former measurements rely on the prediction of the mean antineutrino cross section per fission σ_f^{pred} [Men13]:

$$\sigma_f^{pred} = \int_0^\infty S_{tot}(E) \cdot \sigma_{IBD}(E) dE \quad (1.1)$$

with S_{tot} being the total antineutrino spectrum emitted by the particular reactor core, σ_{IBD} being the theoretical cross section for the inverse beta decay, and E the antineutrino energy. It is important for the investigation of the reactor anomaly to determine the antineutrino spectra of the fuel isotopes contributing to the power of a reactor and, hence, to further narrow down the possible sources of the anomaly. Uncertainties of the antineutrino spectra also effect the predicted event rates and, consequently, the significance of the reactor anomaly.

⁶There exist also other ways to test the sterile neutrino hypothesis, for example cosmology can contribute to this issue [Arc13, Mir13], but this shall not be topic of the present thesis.

1.1.2 Determination of neutrino parameters

The most recent milestone of reactor antineutrino physics was the determination of the value of the mixing angle ϑ_{13} in the neutrino mixing matrix. Three experiments, Double Chooz [Abe12b], RENO [Ahn12] and Daya Bay [An13] have been designed to measure the disappearance of electron antineutrinos from a reactor. As first experiment, Double Chooz published the indication of the non-vanishing value for ϑ_{13} , which was the only angle in the neutrino mixing matrix at this time with only an upper limit known [Abe12a]. RENO and Daya Bay were able to measure ϑ_{13} only shortly thereafter with high statistical significance. The current value $\sin^2(2\vartheta_{13}) = 0.095 \pm 0.010$ [Ber13] has already reached the 10 % accuracy regime.

The experiments mentioned rely on a relative measurement between two detectors, a near one, measuring the total spectrum and flux emitted from the reactor without being affected by three-neutrino oscillations, and a far one looking at the rate and shape changes due to the oscillation. At the time being, Double Chooz is running with the far detector only, nevertheless, it is the only experiment performing not only a rate but also a shape analysis. To accurately interpret the far detector data, it is necessary to substitute the near detector by predictions for the antineutrino flux and spectrum. This prediction is anchored on the Bugey 4 experiment [Dec94], in which the total cross section per fission for an antineutrino to interact in the detector is measured. The spectral shape of the reactor antineutrino flux is gained from the predictions described in sec. (1.3), but the average cross section per fission σ_f (and thus the total rate) is normalized to the Bugey 4 rate measurement and the cross section σ_f^{Bugey} determined therein [Abe12b]:

$$\sigma_f^R = \sigma_f^{Bugey} + \sum_k (\alpha_k^R - \alpha_k^{Bugey}) \sigma_{f,k}^{pred} \quad (1.2)$$

R stands for each reactor of Double Chooz, $k \in \{^{235}\text{U}, ^{238}\text{U}, ^{239}\text{Pu}, ^{241}\text{Pu}\}$ ⁷, α_k being the fission rate of isotope k, and $\sigma_{f,k}^{pred}$ being the predicted mean antineutrino cross section per fission as defined in eq. (1.1). The second term is a correction for the different fuel compositions in the Bugey 4 and the Chooz reactor cores. This treatment reduces uncertainties in the total reactor antineutrino event rate at the far site to 1.8 % [Abe12b] and cancels effects of hypothetical short-baseline oscillations into sterile neutrinos.

More than for the rate-only analysis, where uncertainties in the spectral shape are largely absorbed in this normalisation to the Bugey 4 experiment, a shape analysis fully depends on the knowledge of the spectral shape of the antineutrino spectrum emitted. Without the near detector running, there is no way to cross-check the non-oscillated $\bar{\nu}_e$ -spectrum and the accuracy of the predictions limits the final result.

But even experiments with near detectors online suffer from the lack of knowledge of the reactor antineutrino spectrum. This becomes clear by a look at the rate seen in a detector

⁷These are the four main fuel isotopes contributing to the antineutrino emission of a reactor - see sec. (1.2).

i (for each energy bin separately):⁸

$$N_i = \sum_j N_{\{ij, no\ osc.\}} \cdot P_{\bar{\nu}_e \rightarrow \bar{\nu}_e}(\vartheta_{13}, \Delta m_{31}^2, L_{i,j}) \quad (1.3)$$

$$N_{\{ij, no\ osc.\}} = S_{\bar{\nu},j} \cdot \sigma \cdot \epsilon \cdot R(L_{i,j}) \quad (1.4)$$

With:

- N_i : Event rate seen in detector i;
- $N_{\{ij, no\ osc.\}}$: Event rate due to the antineutrinos emitted by reactor j, as it would be seen in the detector i without neutrino oscillation. This is, in fact, the product of the number $S_{\bar{\nu},j}$ of antineutrinos emitted by reactor j in the energy bin considered, the cross section σ for the detection reaction of an antineutrino of this energy, the detector efficiency ϵ and the function $R_{i,j}$ describing the $\frac{1}{L_{i,j}^2}$ - normalization due to the distance $L_{i,j}$ between detector i and reactor j;
- $P_{\bar{\nu}_e \rightarrow \bar{\nu}_e}$: Survival probability of a $\bar{\nu}_e$ emitted by reactor assembly j at the detector i;
- ϑ_{13} and Δm_{31}^2 are the mixing angle and the mass-squared difference in the neutrino oscillation matrix, respectively.

This equation is valid for each detector (Double Chooz will finally have two detectors monitoring two reactor cores, Daya Bay is running with six detectors at the moment in the vicinity of six reactor cores). Thus the rate seen in an energy bin in the detector is simply the rate one would see without oscillations, modified by the survival probability. If one assumes that all efficiencies, distances and Δm^2 are known, one has one global parameter ϑ_{13} and one rate $N_{\{ij, no\ osc.\}}$ for each reactor left as free parameters. Consequently, with J being the total number of reactor cores and I being the number of detectors, there are J + 1 free parameters and I equations to solve. To be able to resolve this system analytically, one needs more detectors than reactors, which is not the case for any experiment performed at the moment. This shows the need for further input or approximations.

For simplicity considering two reactors and two detectors, the number of unknown parameters is three: the mixing angle and the two non-oscillated spectra emitted by the two cores. These parameters are embedded in a system of two linear equations, one for each detector.

One approach is to assume that the two reactors are identical and emit the same spectrum, reducing the number of free parameters and enabling an analytical solution. However, even if the reactors in an experiment are of the same type, they are operated with shifted fuel cycles. This leads to different fuel compositions, to different fission rates of the fuel isotopes and, finally, different antineutrino spectra produced.

⁸This is intended to be an analytical description to check for the feasibility to, in principle, determine ϑ with ideal detectors without background. Thus, usual experimental restrictions as, e. g., limited statistics are not taken into account. For a discussion of the effects of systematic errors in multiple-reactor experiments, see [Sug06].

	^{235}U	^{239}Pu
E_f [MeV]	201.7	210.0
\bar{E} [MeV]	2.94	2.84
$N_{\bar{\nu}}(\text{IBD})$	1.92	1.45
$\bar{\sigma}$ [cm^2]	$3.2 \cdot 10^{-43}$	$2.8 \cdot 10^{-43}$

Table 1.1: *Characteristics of antineutrinos emitted in thermal fission of the two main fuel isotopes ^{235}U and ^{239}Pu . E_f is the energy released per fission, \bar{E} is the average $\bar{\nu}_e$ energy, $N_{\bar{\nu}}(\text{IBD})$ is the number of antineutrinos emitted above 1.8 MeV - the threshold of the inverse beta decay - and $\bar{\sigma}$ is the average interaction cross section for the inverse beta decay. Data taken from [Fal07].*

One could also use the predicted reactor spectra as input for the analysis. In this case, one eliminates even two of the three free parameters, making it possible to also determine Δm_{31}^2 by treating it as a free parameter.

In addition, there is a publication planned by the Double Chooz collaboration [DCPre], describing a reactor rate modulation analysis (RRM). This RRM is a rate-only analysis describing the observed $\bar{\nu}_e$ rate by a sum of the background rate and the oscillated predicted reactor spectrum. The RRM allows to determine ϑ_{13} and the background rate without the use of any background model. This is possible as DC was and is able to take data in different modes: two reactors on; one reactor on and one reactor off; two reactors off. However, the analysis relies on accurate predictions of the expected rate seen in the detector, which is directly connected to the $\bar{\nu}$ -spectrum emitted from the reactor cores.⁹

1.1.3 Neutrinos for non-proliferation of nuclear weapons

As the antineutrino spectra of the main fuel constituents are not the same, the total spectrum emitted by a reactor depends on the composition of its core. Table (1.1) illustrates differences in the antineutrino emission in the fission of ^{235}U and ^{239}Pu . In the fission process of uranium, on average $\sim 30\%$ more antineutrinos are emitted and these have slightly higher energies and a higher averaged cross section, whereas the energy released per fission differs by only $\sim 5\%$. Consequently, even when running at the same thermal power, the antineutrino rate detected and the spectrum can significantly differ depending on the core composition.

Antineutrino detectors may monitor fuel assemblies non-intrusively from outside of the reactor containment and independently from input given by the reactor staff. Core-level changes in the fuel composition can be seen in real-time by the detector, being a valu-

⁹Another issue reactor neutrino experiments are concerned with is the search for the magnetic moment of the neutrino. For this purpose, experiments like GEMMA at the Kalinin Nuclear Power Plant [Bed13] or measurements at the Kuo-Sheng Nuclear Power Station [Den10] are set up at a short baseline to measure the cross section of $\bar{\nu} - e^-$ scattering. For further information see the publications mentioned.

able tool in the non-proliferation of fissionable isotopes. The International Atomic Energy Agency (IAEA) is therefore interested in the study of portable, remotely controlled and cheap detectors [Fur10].

Prototype detectors like the Rovno neutrino spectrometer [Kli94] and many reactor experiments close to the core, as mentioned before, have already proven the practicability of neutrino detectors near a reactor core. Current experiments like Nucifer [Por10] and PANDA [Kur12] show that the design approaches a level to be mobile and industrially producible.

1.1.4 Reactor antineutrinos as background

Besides the applications mentioned, reactor antineutrinos can be background for other experiments. In particular, experiments like Borexino [Bel13], KamLAND [Gan11] or the future LENA detector [Wur12] are able to measure so-called geoneutrinos. These geoneutrinos are electron antineutrinos emitted by ^{40}K and in the decay chains of ^{232}Th and ^{238}U present in the earth's mantle and crust¹⁰. By studying these geoneutrinos, various earth models can be tested, e. g., conclusions about the abundance of these isotopes and the radiogenic heat production inside the earth can be drawn.

Alike reactor antineutrinos, geoneutrinos are produced in beta decays of neutron-rich nuclei. Hence, they have similar energies and reactor antineutrinos are a significant source of background for the measurement of geoneutrinos. For example, the LENA detector currently in the design phase¹¹ expects to see ~ 500 reactor antineutrino events in the detector per year in the energy window up to ~ 3.2 MeV [MoePC], which is the maximum energy of geoneutrinos [Ara05]. This compares to ~ 1000 geoneutrino events [MoePC], thus, signal and background are of the same order of magnitude. Spectral fits of the reactor antineutrino background can be anchored on the energy regime above the geoneutrino spectrum, but for an accurate subtraction the reactor spectra have to be known precisely. For further information on the production, characteristics and range of application of geoneutrinos, see for example [Sra12].

In addition to the investigation of geoneutrinos, neutrino experiments might be able to detect electron antineutrinos from the diffuse supernova neutrino background (DSNB) [Bea10]. These antineutrinos, mainly produced in the cooling phase of the supernova, are expected to account for only 80-160 events per 10 years (depending on the supernova energy spectrum used) in the LENA detector in an energy interval of 1.8-30 MeV. Approximately 50 to 100 events per 10 years are expected at energies above ~ 9.5 MeV, an energy regime in which reactor antineutrinos account for ~ 5 events per 10 years [MoePC]. These estimations emphasize the importance to fully understand the background contribution due to reactor antineutrinos in the DSNB analysis.

¹⁰The beta decay of ^{40}K has an endpoint of 1.3 MeV [Fir96a], hence, antineutrinos from this isotope are not detectable via inverse beta decay. This interaction has a threshold of 1.8 MeV [Str03].

¹¹LENA is planned to be a neutrino detector based on 50 kt liquid scintillator [Wur12]. Its preferred location is situated in Finland, where the background of reactor antineutrinos is relatively low.

In summary, all experiments detecting reactor antineutrinos benefit from the exact knowledge of the spectrum emitted by the fuel assembly. The present work supports these efforts by an experimental determination of the antineutrino spectrum of the fission products of ^{238}U . To realize the necessity to precisely know this contribution to the total antineutrino spectrum, the next section (1.2) briefly explains the production and the current predictions of the total antineutrino spectrum emitted by a reactor.

1.2 Antineutrino production in nuclear reactors

In a standard pressurized water reactor, the dominant contribution to the power production - and thus also to the neutrino generation - is caused by the fissioning of the four main fuel isotopes¹², ^{235}U , ^{238}U , ^{239}Pu , and ^{241}Pu [Eme82], see also figure (1.2). Each fission process most often produces two neutron-rich daughter nuclei, which on average undergo three β -decays until a stable isotope is reached [Bem02]. Hence, for one fissioned nucleus, six electron antineutrinos are generated with a spectrum to be determined. Approximately 200 MeV of total energy are released in a fission process¹³ and on average ~ 10 MeV are distributed amongst the six neutrinos [Kop03]. About 60% of the energy emitted in form of antineutrinos is carried by antineutrinos with energies ≥ 2 MeV [Kop03]. This is of particular interest for experiments relying on the inverse beta decay detection technique, like Double Chooz or Daya Bay, as the threshold for this reaction is 1.8 MeV [Str03].

The mass distribution of isotopes produced in a fission process can be seen in fig. (1.2). The distribution shows two peaks separated by a valley with a depth depending on the kinetic energy of the fissioning neutron: the higher the neutron energy the more homogeneous the distribution. The figure illustrates that one has to include a huge variety of neutron rich and partly exotic nuclei if one tries to predict the antineutrino spectrum emitted by a reactor core. Section (1.3) covers the actual status of these predictions.

¹²The next-to-leading contribution is due to ^{240}Pu and is about two orders of magnitude lower than the one from ^{241}Pu [Bem02], which has the lowest input of the four main fuel isotopes. Antineutrinos from fission of ^{240}Pu and further less contributory are not used in the calculations of the reactor $\bar{\nu}_e$ -spectrum.

¹³The total energy release E_{tot} depends on the isotope fissioned, but the differences are rather small. See also table (1.1).

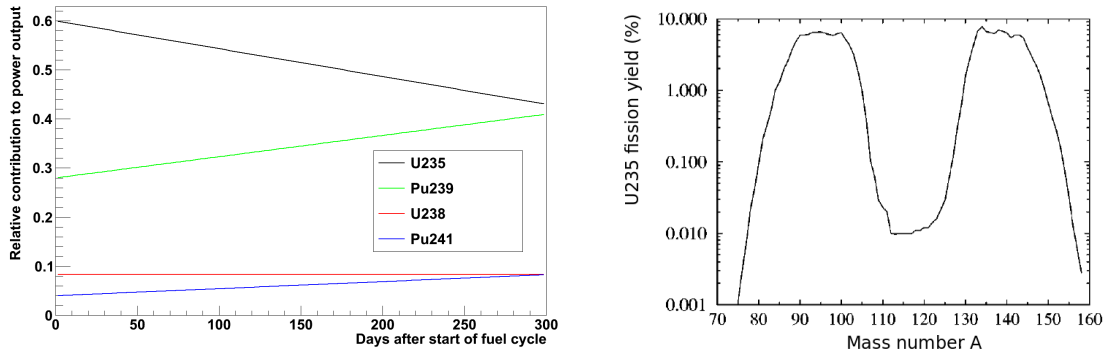


Figure 1.2: *Left: Schematic drawing of the fuel evolution of a typical pressurized water reactor. The plot shows the fraction each of the four main fuel isotopes contributes to the total thermal power depending on the time after refueling. ^{235}U is the dominant isotope; the contribution from ^{238}U is at a constant level of $\sim 10\%$. Data extracted from [Bem02] and [FalPC]. Right: Yields for the production of a fission isotope with mass A by fissioning of ^{235}U with thermal neutrons. The integral of the distribution is normalized to 200 %, as on average two fission fragments are produced. Plot reprinted with submission from [Bem02].*

1.3 Status of predictions for the reactor $\bar{\nu}_e$ - spectrum

Considering radioactive equilibrium, the total $\bar{\nu}_e$ spectrum emitted by a nuclear reactor $S_{tot}(E)$ in a certain time interval can be parameterized by¹⁴

$$S_{tot}(E) = \sum_i \alpha_k S_k(E) \quad (1.5)$$

with $k \in \{^{235}\text{U}, ^{238}\text{U}, ^{239}\text{Pu}, ^{241}\text{Pu}\}$. α_k denotes the number of fissions of isotope k per unit time and $S_k(E)$ is the antineutrino spectrum emitted after the fission of this isotope, including the beta decays of all fission daughters.

The determination of the fission rates α for each element is accomplished with the help of reactor evolution codes like MURE [MUR12] or DRAGON [Mar94], which calculate the fuel isotope composition of a reactor assembly at different times. As the present thesis is concerned with the spectra of the fission products of the fuel isotopes, no further discussion of these codes will be presented. The reader may find more information on the current precision of these predictions in [Jon12].

There are basically two different techniques to predict the four β spectra $S_k(E)$: The *summation method*¹⁵ and the method of converting measured fission β -spectra. The following sections will treat these two complementary methods.

¹⁴The parameterization is chosen to be the same as in [Mue11].

¹⁵This is the same technique as discussed in [Mue11]. Therein, the method is called *ab initio* method, but the authors of this paper are currently discussing to use the name *summation method*.

1.3.1 Method 1: The summation approach

The $\bar{\nu}$ -spectrum from the fission products of a given fuel isotope k is the sum of all individual antineutrino spectra emitted in the decays of the fission daughters f . Knowing the fission yields, one can compute the average number of atoms of each of these daughter isotopes produced in a fission process and of the number of subsequent instable isotopes. The total β -spectrum $S_k(E)$ of each of the main fuel isotopes can then be written as:

$$S_k(E) = \sum_f A_{f,k} S_f(E) \quad (1.6)$$

with the activity $A_{f,k}$ of the isotope f (determined by reactor evolution codes as mentioned above) and the beta spectrum $S_f(E)$ emitted by isotope f . To be finally able to predict the total electron spectrum of the fission products of a fuel isotope, $S_k(E)$, these beta spectra $S_f(E)$ have to be known. This is achieved either by direct measurement or by prediction. A lot of effort has been put into the measurements of the individual beta spectra $S_f(E)$. However, the highest-energetic part of the electron and antineutrino spectrum is dominantly fed by short-lived isotopes. Not all of these partly exotic nuclei are well known and the beta-spectra of them are not yet fully determined experimentally. Although already more than 800 nuclei and ~ 10.000 branches are included in the calculations, the authors of [Mue11] quote the error on the predictions due to this missing contribution to be of the order of 10% at 2 MeV, rising to 20% at 7 MeV.

But also the spectra already determined experimentally have to be taken with care. Part of the beta spectra used in the tables of isotopes are deduced from the gamma spectra measured with high resolution but low efficiency spectrometers. This experimental approach can lead to faulty predictions of the branching ratios and the endpoint distribution of an isotope. This is called the *pandemonium effect* [Har77]. The impact of this effect is visualized in the discussion of the final antineutrino spectrum obtained in the present thesis, when comparing the results to predictions that have partly be corrected for this effect (see sec. 5.4). For the isotopes not experimentally investigated so far, one has to analytically predict the beta spectra emitted in the decay. This method is depending on the knowledge of many parameters, e.g., present in the Fermi function, the electroweak magnetism correction, the radiation correction and the shape factors.

Finally, the β -spectrum obtained by this summation (eq. 1.6) has to be converted into an antineutrino spectrum. It is possible to finally deduce the antineutrino spectrum with nearly the same precision as the electron spectra, as one converts the spectra on the branch-level. The uncertainties of this conversion are discussed in detail in [Hub11] and shall not be explained herein. The calculations can be tuned and verified by the total β -spectrum of already measured isotopes as, e.g., ^{235}U , which shows an energy dependent difference between measurement [Sch85] and prediction of up to 10 percent.

Further information on the *summation approach* as well as the prediction of the $\bar{\nu}_e$ -spectrum of the fission products of ^{238}U can be found in [Mue11].

1.3.2 Method 2: Conversion of fission β -spectra

Instead of ascribing the total $\bar{\nu}_e$ -spectrum of a fissionable isotope to its constituent spectra of the single fission daughters, one can directly measure the total β -spectrum $S_k(E)$ and deduce the antineutrino spectrum from this. This means to irradiate the fuel isotope to be investigated with neutrons to induce fission and to measure the beta spectrum emitted. This technique has the big advantage not to depend on the knowledge of the fission yields, the life times of the daughter nuclei, the individual beta branching ratios, and all further nuclear parameters to treat the single β -decays.

In the past, experiments installed in the vicinity of reactor cores irradiated targets from the three fuel isotopes ^{235}U , ^{239}Pu , and ^{241}Pu with thermal neutrons to measure the beta spectrum emitted [Car59, Tso71, Sch85, Sch81, Hah89]. Carter et al. [Car59] came up with the first experiment in 1959, determining the electron spectrum emitted by an ^{235}U foil irradiated by thermal neutrons from the Omega West Reactor in Los Alamos. A plastic scintillator was used to determine the electron spectrum emitted from the target foil and an argon transmission counter served as coincident detector suppressing gamma radiation. They had to assume rather large errors due to uncertainties, e.g., in the absolute calibration and the detector response function, but more than 20 years later, more precise measurements with a magnetic spectrometer BILL at the ILL in Grenoble [Sch85] in the 1980's showed that the results obtained by Carter were already very accurate. This BILL experiment is up to now used as reference measurement for the beta spectra of the fission products of ^{235}U , ^{239}Pu , and ^{241}Pu .¹⁶

However, fission of the even-even nucleus ^{238}U is only possible with neutrons with energies above ~ 1 MeV, and the collaborations mentioned were not able to address the spectrum of this fourth contribution. Until now, the antineutrino emission due to fission of ^{238}U relies on calculations using the *summation method* (sec. 1.3.1) and it is inevitable to cross check these predictions by a measurement. The present thesis is concerned with the measurement of this missing contribution of ^{238}U to the total reactor antineutrino output.

The main difficulty of the determination of the antineutrino spectrum via the measurement of the corresponding total β -spectrum is to accurately convert the electron spectrum obtained into an antineutrino spectrum. As one does not use any input of the branch-level beta decays, there is no possibility to analytically perform such a conversion¹⁷. However, there exist two empirical methods to perform the conversion.

The first method uses a set of virtual branch-level beta-spectra to fit the measured electron spectrum. These spectra are then converted individually into antineutrino spectra, which are summed to build the total $\bar{\nu}_e$ -spectrum. The second technique, which is the one in use in the present thesis, uses the fact that the total antineutrino spectrum and the total beta spectrum are very similar in shape. The main differences are introduced by the charge and the mass of the electron. Shifting the measured β -spectrum by ~ 0.5 MeV

¹⁶Antineutrino spectra of these three fuel isotopes can be found in [Hub11].

¹⁷There does, in fact, exist an analytical solution to extract the beta end-point distribution from the experimental data [Car59], but this involves the third derivative of the measured spectrum. A direct application to real measured spectra is not feasible when high accuracy is required.

largely compensates the differences and one obtains the antineutrino spectrum with good accuracy. Later, in section (5.3), the two methods will be discussed in more detail.

1.4 The concept of measurement

The present work is concerned with the determination of the $\bar{\nu}_e$ -spectrum emitted subsequently to the fission of ^{238}U nuclei¹⁸. An experiment is performed to measure the β -spectrum emitted by a natural uranium foil irradiated with neutrons from a reactor core. Subsequently, this electron spectrum is converted into an antineutrino spectrum. For this purpose - similar to the setup of Carter et al. [Car59] - a coincidence is set up between a spectroscopic module, consisting of a plastic scintillator and a photomultiplier, and a detector to reject background from gamma radiation, in this case a multi-wire chamber. As neutron source, the research reactor FRM II in Garching near Munich is chosen. The detector, the experimental site, and the neutron beams used are described in chapter (2).

There exists an experimental site at FRM II with the possibility to switch between a thermal and a fast neutron beam without any need to change the detector setup. This allows to record the pure ^{235}U spectrum by irradiating a second, identical uranium foil with thermal neutrons in addition to the ^{238}U spectrum obtained by irradiation of fast neutrons¹⁹. It is of valuable advantage that the spectrum of the fission products of ^{235}U has already been measured by the BILL collaboration with high precision [Sch85]. By a comparison of the beta spectrum of ^{235}U obtained to the BILL data set, the systematic errors of the present experiment are reduced to a minimum. With this procedure, described in detail in sec. (4.4), the absolute calibration of the beta spectrum of ^{238}U reduces to the determination of the relative numbers of fissions in the two foils in the different neutron beams. This is achieved by gamma spectroscopy on the irradiated targets with a Ge-semiconductor detector, see sec. (4.5).²⁰ While Carter et al. suffered from uncertainties concerning the absolute calibration of the setup and the detector response function, the uranium experiment described in the present thesis is able to minimise all impact of these quantities by the normalisation to the BILL spectra mentioned.

The general performance of this setup, including the response function, the energy calibration and the stability of the system, is given in chapter (3), followed by the analysis of the background and the final extraction of the beta spectrum in chapter (4). This chapter also describes the analysis chain processed to identify and subtract different background

¹⁸Throughout this thesis, it will sometimes be spoken of the beta spectrum of uranium. This exclusively means the total beta spectrum of all products from fission of uranium and not the beta decay of the uranium nucleus.

¹⁹Of course, in the fast neutron beam also ^{235}U fissions occur. The data is corrected for this contribution - see sec. (4.3).

²⁰The presented method to measure the ^{235}U and ^{238}U beta spectra with the same setup and to perform a normalization via gamma spectroscopy was already proposed in [Hah89].

spectra and includes the normalisation to the BILL spectrum and the absolute calibration with the help of gamma spectroscopy.

Subsequently, in chapter (5) the final beta spectrum is presented and the conversion into the antineutrino spectrum is discussed. Unless explicitly described otherwise, all uncertainties are quoted on 1σ confidence level assuming a Gaussian distribution (68% C.L.).

Chapter 2

The experimental setup

The next paragraphs describe the hardware used to measure the β -spectra of different targets and sources. This experimental setup has mainly been developed in the course of the author's Diploma thesis [Haa08]. Therein, the selection process of the parts is explained and the feasibility of the measurement is proven. Therefore, this chapter will only be concerned with an overview of the experimental setup including improvements of the prototype, but will skip some technicalities. The next section (2.1) gives a summary of the neutron source. Section (2.2) describes the whole detector setup. Thereafter, the single components are described in more detail.

2.1 The neutron source

The neutrons for this experiment are delivered by the neutron source Heinz Maier-Leibnitz (FRM II) in Garching near Munich, a scientific reactor of 20 MW thermal power [Gae02, Goe00, Has01, Roe10]. In the center of a moderator tank filled with D_2O a single compact fuel rod containing about 8 kg of highly enriched uranium (93% ^{235}U) is placed. Several secondary neutron sources and neutron guide tubes around the core in the moderator provide experiments with neutrons of different energies.

The secondary neutron source most interesting for this work is the *converter facility* at the beam tube *SR10*. The heart of this converter is built up by two fuel plates consisting of in total 500 g of ^{235}U in the form of an uranium silicide U_3Si_2 . The plates are positioned in the moderator tank and, hence, inside a dense thermal neutron cloud. The uranium is fissioned by the neutrons producing a thermal power of ≈ 80 kW. The fission process isotropically emits *fast neutrons* corresponding to a spectrum peaking at energies of 1-2 MeV (see fig. 2.4 and the following section for more details). Neutrons by chance flying in the direction of the beam tube SR10 are then used at the experimental site.

An additional advantage of this beam place is the possibility to also provide thermal neutrons by removing the converter plates from their working position. This is possible without changing anything in the experimental setup. In this mode, the beam line directly looks at the moderator tank and is thus fed by thermal neutrons. The next section will

give more detailed information on the experimental site and the spectrum of the neutron beam.

2.1.1 The neutron beam at SR10

The experimental site

SR10 is in use for different applications. The first of two rooms (see fig. 2.1) is primarily used for medical application like cancer therapy with fast neutrons. The neutron flux at this position²¹ can reach up to 10^8 to $10^9 \frac{\text{neutrons}}{\text{cm}^2\text{s}}$. Behind a dividing wall with a window for the beam feed through, a beam place for neutron tomography is situated. Here, the uranium experiment performed in this work was installed. The thermal neutron flux (without converter plate) can reach up to some $10^8 \frac{\text{neutrons}}{\text{cm}^2\text{s}}$, but was lowered by filters in the beam line. The fast neutron flux is in the range of $10^6 \frac{\text{neutrons}}{\text{cm}^2\text{s}}$. The exact neutron flux is not of interest for the data analysis, because γ -spectroscopy is performed on the irradiated target foils to directly determine the number of fissions - see sec. (4.5).

The spectra at the experimental site

To get rid of thermal neutrons in the fast beam, the neutrons pass a boron-plastic filter inserted directly after some beam shutters. In both beams the thermal and the fast one, the neutrons propagate through a set of lead filters to remove the gamma content of the beam. By changing the thickness of the lead absorbers, also the neutron flux, and with it the count rate in the experiment, can be regulated. The neutron beam is further collimated by a multi-leaf collimator that can be adjusted in width and height. The leafs of the collimator are each made from iron, polyethylene, and lead with a total thickness of 50 cm [WagPC]. Further information on the filters and collimators can be found in [Bre07]. Directly after the multi-leaf collimator, an approximately 3.5 m long, evacuated steel tube housing further collimators guides the neutrons to the target foils (fig. 2.2). This extension is attached to the main cross piece as shown in figs. (2.6) and (2.13) and shares the vacuum with the target chamber²².

In the thermal neutron beam, several boron-apertures assure a collimation of the neutrons and for the fast neutron measurements, inside the beam tube two iron blocks with a lent of 25 cm and a rectangular hole of $30 \times 20 \text{ mm}^2$ (width x height) and $25 \times 15 \text{ mm}^2$, respectively, shape the neutron beam. The entrance and exit windows of the iron blocks are covered with ^6LiF tiles of in total 4 mm thickness to remove a possible content of thermal neutrons from the beam. The last collimator has a distance of about 15 cm to the foils. The end-cap of the experiment is also partly covered with ^6LiF to reduce an activation of the aluminium exit window. A sketch of all collimators and filters arranged in the neutron beam is given in figure (2.3).

²¹The value is approximately the same for thermal neutrons in the mode without converter plate and fast neutrons with converter. Depending on the application, the neutron flux and beam area can be modified in a wide range due to several changeable filters and the adjustable multi-leaf collimator. The values for the neutron fluxes are given by [Bre07, BrePC].

²²A description of the experimental setup is given in sec. (2.2) ff. .

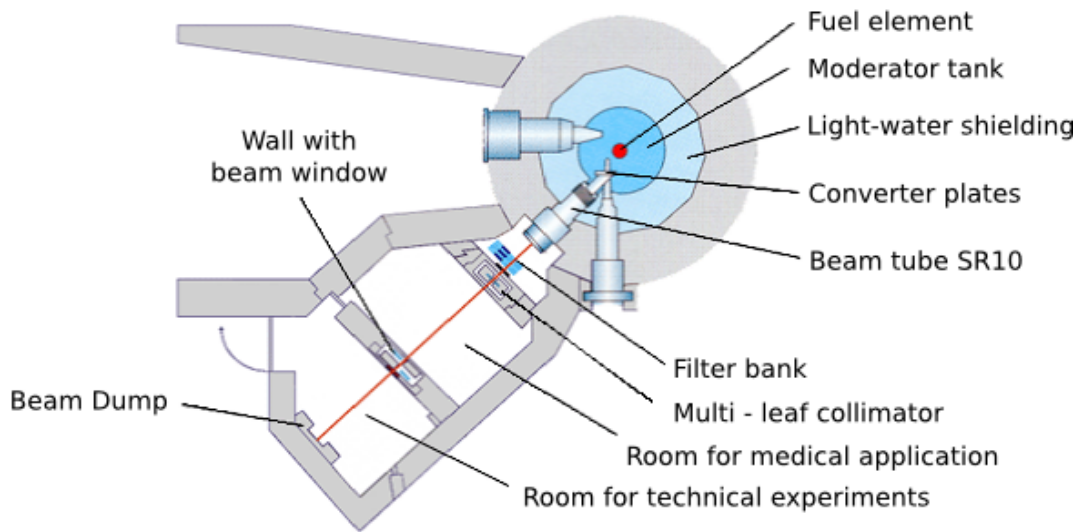


Figure 2.1: *Sketch of the experimental site. One can identify the reactor core (red dot) surrounded by the moderator (D_2O) and a light-water shielding. In this simplified illustration, most of the other beam tubes and secondary sources are not shown. The converter is positioned in the thermal neutron cloud of the moderator and is looked at by beam tube SR10. The neutrons pass several filters and collimators before entering the experimental rooms - see also fig. (2.3). The first room is dedicated to medical applications and the second room behind a dividing wall is used for neutron tomography and technical experiments. In this rear room, approximately 9.5 m away from the converter plates, the uranium experiment was established. Picture taken from [Gae02]; copyright by FRM II / TUM.*

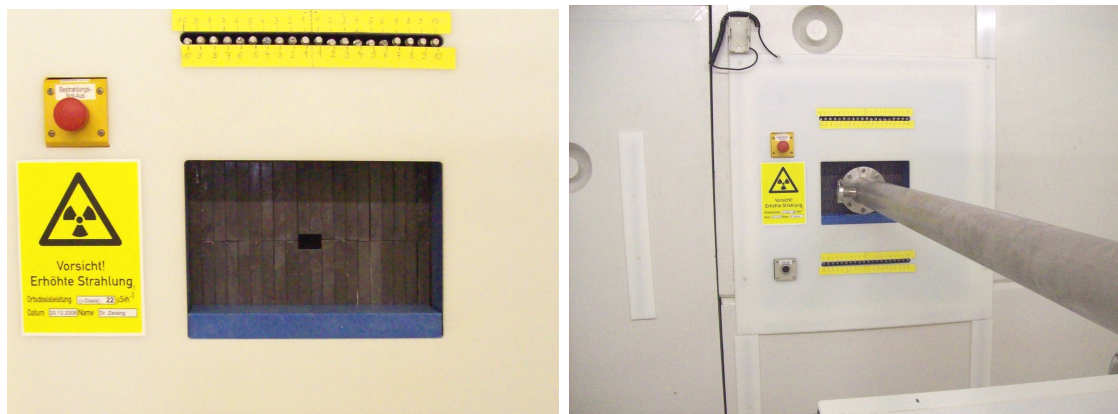


Figure 2.2: *Left: The multi-leaf collimator consists of 20 pairs of sheets that can individually be opened or closed to shape the neutron beam. It is shown in the configuration used in the experiment shaping the beam to an area of $3 \times 2 \text{ cm}^2$. Right: In front of the multi-leaf collimator, an evacuated beam tube housing further collimators and filters is positioned.*

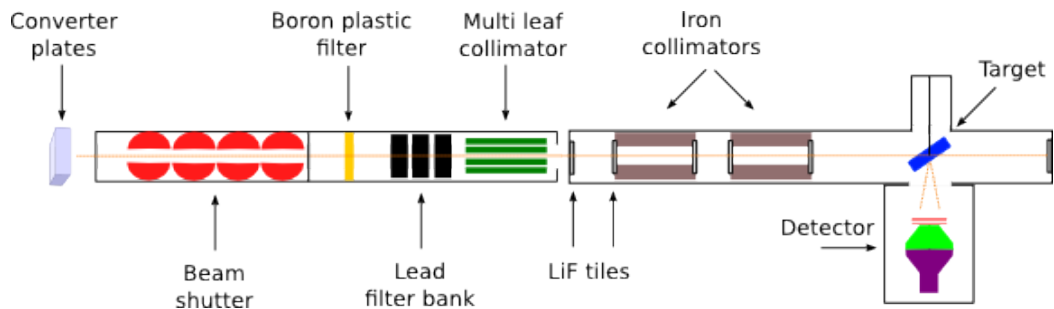


Figure 2.3: Sketch of the filters and collimators in SR10 and the experiment in the fast beam measurement. The neutrons are produced in the converter plates to the left and enter the beam tube SR10. They pass the open beam shutters and a boron plastic filter removing the thermal neutron content. This filter is removed in the thermal beam measurement. A lead filter bank follows, consisting of several lead blocks with different thickness that can arbitrarily and remotely be placed in the beam. With these filters, γ -radiation is attenuated and the neutron beam intensity can be regulated. A multi-leaf collimator shapes the beam to the final geometry. In the experiment, the neutrons enter the expansion tube that houses further filters and collimators. In case of the fast beam, ${}^6\text{LiF}$ tiles are placed in the beam to further reduce possible background of thermal neutrons. Thick iron collimators define the beam width and height before the neutrons finally reach the target position. With exception of the tile at the exit of the beam tube to the very right, no LiF filters and iron collimators are in use during the thermal beam measurement. Instead, 2 mm thin boron and LiF collimators shape the thermal neutron beam.

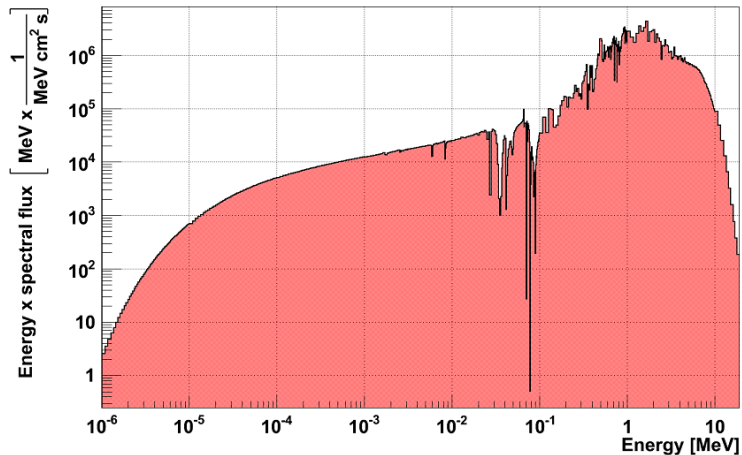


Figure 2.4: *The spectral flux of the fast neutron beam as calculated by the author of [Bre07] for the filter configuration in the uranium experiment on a double-logarithmic scale. The flux is multiplied by the energy to illustrate the weight of the respective energy regimes. Thermal neutrons (at 25 meV, not shown) are efficiently suppressed by the lithium and boron filters.*

The neutron spectrum obtained in this exact configuration including the used 10.5 cm of lead in the filter bank, the aluminium entry flange of the beam tube, and the lithium tiles, was calculated by the author of [Bre07]. This spectrum can be found in fig. (2.4). The thermal content in the beam is suppressed to a negligible amount and also the epithermal part of the fission spectrum from the converter facility has only minor influence. This is important as the experiment uses natural uranium foils and even the small content of 0.7% of ^{235}U would contribute the dominant amount of fissions in the target. It will be shown in sec. (4.3) that due to the suppression of low-energy neutrons, the total fission rate in the fast neutron beam due to ^{235}U is only about 3.5 percent of all fissions²³.

At the target position, both the fast neutron flux in the fast beam and the thermal neutron flux in the thermal beam are of the order of $10^6 \frac{\text{neutrons}}{\text{cm}^2 \text{s}}$ [BrePC]. It is a great advantage of the experimental method performed herein that the exact knowledge of the neutron fluxes is not required as γ -spectroscopy on the irradiated targets is used to determine the relative numbers of fissions in both beams very accurately²⁴. Thus, the absolute

²³A cross-check was performed to prove that there are no thermal neutrons left at the target position in the fast neutron beam measurements. As will be shown in section (3.3), the β -spectrum emitted by an indium target irradiated by thermal neutrons was used for calibration purposes. With about 200 barn, ^{115}In has a high cross section for thermal-neutron capture, whereas the cross section at 2 MeV neutron energy is about 3 orders of magnitude lower [END12]. No signal of the ^{116}In beta decay could be found in the fast neutron beam, indicating that the thermal-neutron content in the fast beam was highly suppressed.

²⁴Section (4.5) on page 97 ff. treats the absolute normalisation of the ^{238}U spectrum with the help of γ -spectroscopy. In the context of this section, it will turn out that the fission rate in the thermal beam

calibration of the ^{238}U spectrum can be achieved precisely without any knowledge of the absolute neutron beam intensity²⁵.

Gammas in the beam The neutron beam still has a huge content of photons that may scatter off the target foils and lead to background in the detectors. These gammas are mainly produced promptly in the neutron capture on the materials of the beam tube and the filters, in beta decays of activated isotopes or in fission itself. For the fast beam, the author of [Bre07] provided spectral calculations of the γ -spectrum as present in the uranium measurement. This spectrum is illustrated in fig. (2.5). Although several lead filters are present in the beam, the total intensity of the gamma flux is only slightly lower than the neutron flux [JunPC]. As the flux is not known precisely, this is a fit parameter in the background model described in section (4.2.1).

The gamma background in the thermal neutron beam is significantly smaller than in the fast beam, as the converter plates are driven to a rest position and the SR10 looks directly onto the moderator. Hence, the gamma content from the fission in the uranium plates is missing. Because of the high fission cross section of ^{235}U for thermal neutrons (≈ 583 barn [Fir96b]), it was furthermore possible to increase the lead filter thickness in the thermal neutron measurements, in this way shielding an additional amount of gammas. Calculations of the gamma spectrum in beam tube SR10 were provided by [RoePC], affirming a nearly negligible flux. Section (4.2.3) shows that in the measurement of the β -spectrum of uranium with the thermal neutron beam the background induced by gammas is very small.

was about 44 times higher than in the fast beam.

²⁵Nevertheless, it had to be cross checked that the neutron flux was stable in time. A relative change of the neutron beam intensity during the measurements, e.g. due to the fuel burn-up of the reactor, would have to be included in the analysis and the absolute calibration. However, it could be deduced from measurements of the neutron density in the moderator that the neutron beam intensity did not change [MeiPC].

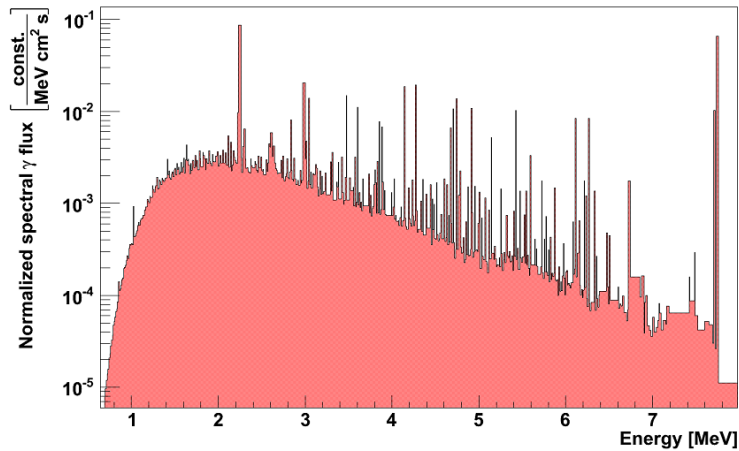


Figure 2.5: *The spectral flux of the gamma content in the fast neutron beam as calculated and provided by [BrePC] for the conditions in the uranium experiment. Above ≈ 7.7 MeV, which is the neutron capture gamma line of aluminium, the intensity is negligible. The intensity of the gamma spectrum is not accurately known, but information on the spectral shape is sufficient for the analysis of the background - see sec. (4.2.1).*

2.2 Conceptual overview of the setup

The center piece of the setup is a γ -suppressing electron telescope²⁶ consisting of a plastic scintillator (PS), a photomultiplier (PM) and a multi-wire chamber (MWC) as shown in figures (2.6) and (2.7). The plastic scintillator converts the kinetic energy deposited by ionising particles into scintillation light, which is then detected by the photomultiplier. This module is explained in sec. (2.3). The multi-wire chamber (sec. 2.4) is located directly in front of this module and enables a coincidence measurement: Any ionising particle may leave a signal in the plastic scintillator, but due to the low density of the counting gas, only charged particles leave a track in the multi-wire chamber. Thus, by setting up a coincidence between PM and MWC, events due to gamma radiation can be suppressed efficiently.

This telescope looks towards the target position where different foils and sources (sec. 2.6) can be positioned and irradiated with thermal or fast neutrons (see sec. 2.1.1). The main targets are thin foils from natural uranium, positioned 10 cm above the detector module. The target location is also used for measurements with dummy targets consisting of Pb or Ni and with calibration sources (In and Cl). The foils are, consecutively, irradiated by the neutron beam, whose line of flight is perpendicular to the active direction of the telescope.

²⁶As mentioned in chapter (1.3.2), already in 1959 Carter et al. [Car59] measured the spectrum of the fission products of ^{235}U with a similar method and proved that such an experiment has an accuracy sufficient to determine the fission spectra. Various other groups, as for example [Tso69, Gro92], measured or at least studied very similar experimental setups.

A calibration device allows to place a ^{207}Bi source directly beneath the target position. A quick-coupling enables the insertion and removal of this calibration source without opening the experimental setup. Thus, it is possible to perform a calibration under exactly the same conditions as for the measurements before and after the ^{207}Bi -calibration run. Between ^{207}Bi -calibration and a measurement, the vacuum is not broken and the PM does not have to be turned off due to the inevitable exposure of light during a target exchange.

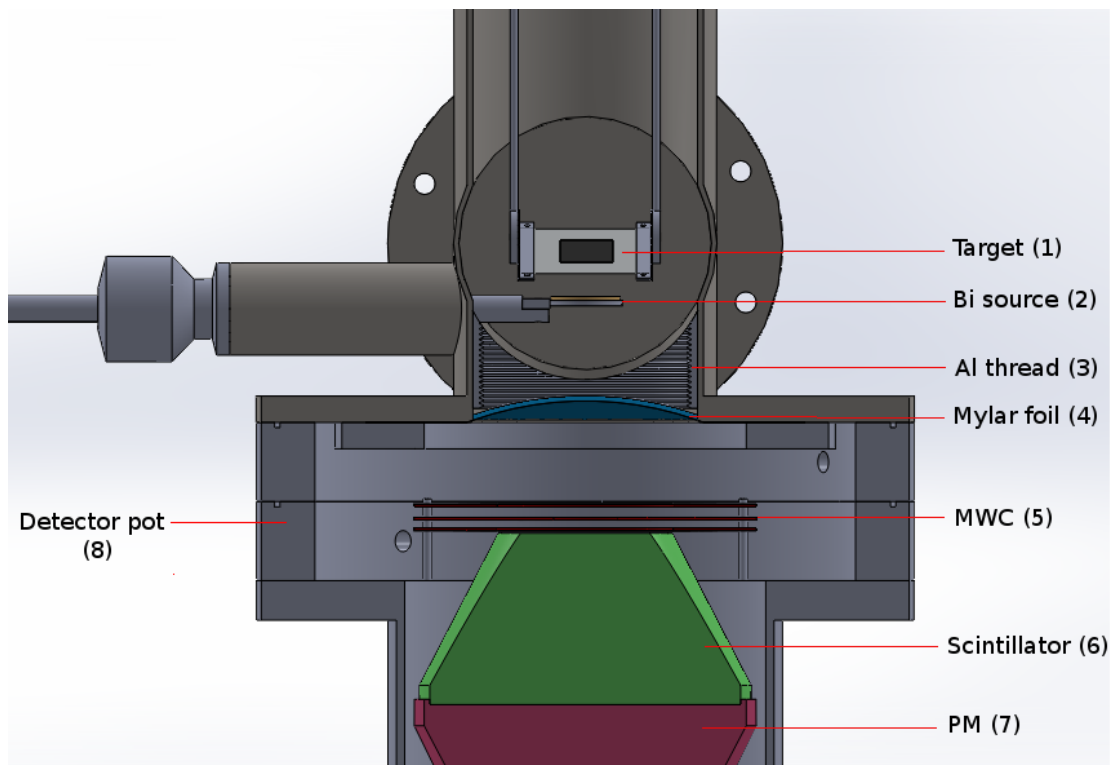


Figure 2.6: Schematic view of the experimental setup. The line of sight corresponds to the direction of flight of the neutrons. For a better look onto the target region, the collimators in the line of sight are omitted. The neutrons hit the target (1), which is consisting of a material in the center (either U, Pb or Ni; depicted in black) between nickel foils (light grey). During neutron irradiation of the targets, the ^{207}Bi source (2) is hidden in the source containment to its left - the position shown here is only in use without neutron beam. Electrons from the target or the source have to pass a $36\ \mu\text{m}$ thick Mylar foil (4) to enter the gas filled detector pot (8). To prevent electrons that would hit the neck of the cross piece to be scattered into the direction of the detector, an aluminium thread (3) is installed beneath the target location. The detector module consists of a multi-wire chamber (5), a plastic scintillator (6), and a photomultiplier (7). All parts are explained in more detail in the following sections.

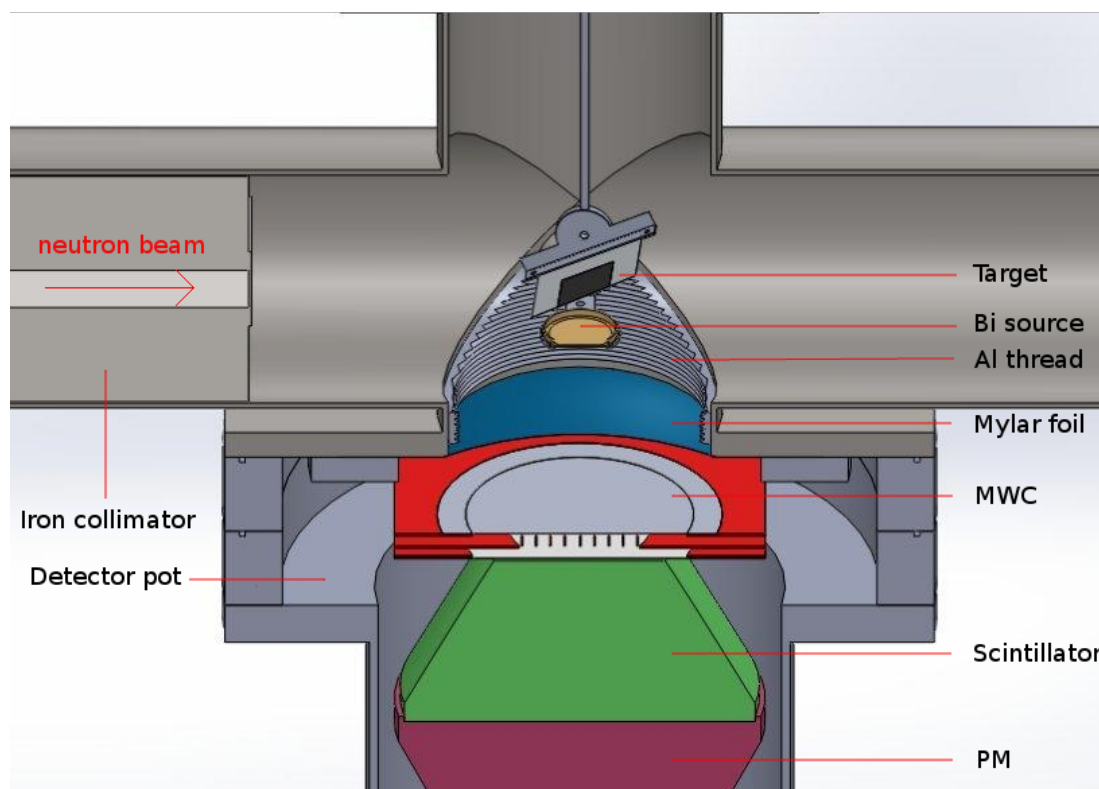


Figure 2.7: *Tilted view of the setup. The various parts of the experiment are labelled in fig. (2.6). To the left of the target, one can see the iron collimator in use in the fast beam.*

2.3 The spectroscopic module

As mentioned, the kinetic energy of the incoming electrons is determined with a module consisting of plastic scintillator and a photomultiplier²⁷. The scintillator (fig. 2.8) has the shape of a truncated cone. The opening angle is optimised such that electrons coming from any position in the target foils and entering the scintillator at the top can deposit their whole kinetic energy. Electrons not entering through the top plane generally are discarded as they do not hit the active area of the MWC, explained in the following section (2.4). Of course, the charged particles' trajectory in the scintillator is not a straight path, but this geometry minimises the amount of electrons leaving the scintillator at the sides. In fact, the ratio of the number of electrons being scattered out of the scintillator at the sides to the number of those being backscattered is negligible²⁸. In addition, the geometry favours the reflection of scintillation light towards the photomultiplier, improving the energy resolution due to better photon statistics.

²⁷The working principle of scintillators and photomultipliers as well as the underlying theory will not be explained here. See, e.g., [Bir64], [Ham07], and [Leo94] for further information.

²⁸See section (3.2) for a calculation of the impact of electrons being backscattered off the scintillator.



Figure 2.8: *The plastic scintillator used. On the left, the original plastic scintillator is seen, in the middle the scintillator is thinly covered with reflective paint. The geometry of a truncated cone (right, values in [mm]) assures that electrons from the target entering the scintillator on the top deposit their whole energy and do not leave the detector at the sides.*

The organic scintillator is of the type *BC-404* from *Saint-Gobain Crystals*²⁹ and based on polyvinyl toluene. Further technical details concerning the properties of the plastic scintillator can be found in [Sai08a] and the selection process is described in [Haa08]. The scintillator is covered with a thin layer of *BC-620*, a titanium dioxide based reflective paint from the same company. The peak wavelength of the emitted scintillation light is at 408 nm, where the paint has a diffuse reflectivity between 90 and 95 %. The bottom plane of the plastic scintillator is not painted, as there the photomultiplier is positioned and the photons are supposed to leave the scintillator. Finally, black tape is wrapped around the side mantle of the cone to minimise the nuisance from potentially occurring light leaks.

The photomultiplier is of the type *XP3540* from *photonis*³⁰, a 10-stage tube with a Bi-alkali photo-cathode [Pho06], equipped with the voltage divider *VD202K/01*. The maximum sensitivity is at 420 nm, close to the emission wavelength of the organic scintillator. Its 5" entrance window of borosilicate glass has the same geometrical dimensions as the scintillator, enabling an accurately fitting coupling. The PM is surrounded by a Mu-metal shield (*MS175* from photonis) to neglect the impact of magnetic fields on the performance of the photomultiplier. Together with the scintillator, it forms the spectroscopic module shown in figure (2.9).

The performance of the spectroscopic module concerning the energy resolution and the linearity of the energy calibration will be addressed in sections (3.2) and (3.3).

²⁹GC Technology Messgeräte Vertriebs GmbH, Freidling 12, 84172 Buch am Erlbach.

³⁰Photonis SAS, Avenue Roger Roncier, 19106 Brive cedex, France.



Figure 2.9: *The spectroscopic module consists of the plastic scintillator, partly covered by reflective paint and wrapped in black tape, and the photomultiplier, shielded from magnetic fields by the Mu-metal mantle.*

2.4 The multi-wire chamber

To accurately measure the β -spectrum emitted by the uranium foil, it is of paramount importance to reject events in the plastic scintillator occurring from uncharged particles. Most of all, this means to veto all energy depositions caused by gamma radiation. These gammas are produced in various processes: Neutrons captured on the material surrounding the detector either emit spontaneous gamma radiation or lead to beta decays possibly including gamma cascades. In addition, fission itself produces gammas in the uranium target or the converter plate of the reactor. Thus, gammas are present in the neutron beam - see sec. (2.1.1).

To distinguish these events mentioned from those of electrons, one has to introduce a second detector to set up a coincidence. This detector is chosen to be a multi-wire chamber³¹ (MWC) positioned directly in front of the entrance plane of the scintillator. The advantages of an MWC are obvious: Due to the small density of the counting gas, the cross section for gamma interactions is minimal and by far most of the uncharged particles pass the detector unseen. Furthermore, the energy deposition and angular distraction of the incoming electrons is small, which is important to minimise the distortion of the original spectrum of the electrons emitted in the β -decays of the fission products.

During the development of the MWC, simulations with the *Garfield* program [Gar05] were performed to determine the optimal parameters of the wire chamber. This included studies of the geometric dimensions, the wire arrangement, and the choice of the counting gas. This is explained in detail in [Haa08] and only the key features are shown in the following.

³¹The basic working principle of a wire chamber will not be described herein. See [Sau77] for details.

The MWC is built of three circuit boards. The main board has a hole in the middle with 25 gold-coated tungsten wires spanned over it, creating a circular active area with a diameter of 5 cm (fig. 2.10). The wires have a diameter of $10\ \mu\text{m}$ and are alternately supplied with 660 V and 2460 V. The lower voltage defines so-called *potential wires*, shaping the electric field in such a way that the secondary electrons are directly focussed onto the *sense wires* without creating traps and flat areas in the field configuration (see fig. 2.11). To create a homogeneous field, the two other boards serve as grounded cathode planes. To achieve this, an aluminised Mylar foil with a thickness of $6\ \mu\text{m}$ is spanned over a hole of 8 cm diameter in each board. The boards are positioned in 5 mm distance to the active plane to each side.

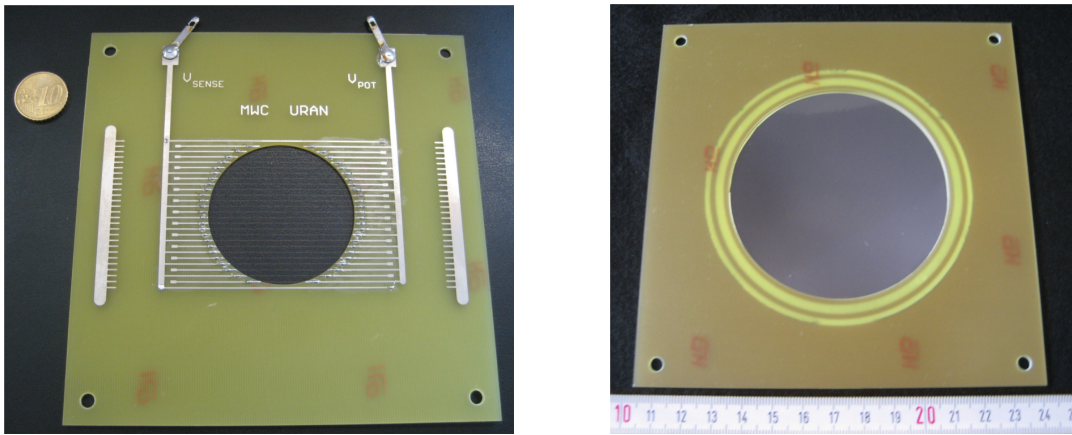


Figure 2.10: *The two different planes of the multi-wire chamber. Left: The hole in the middle of the main board contains 25 wires and defines the active area of the MWC. One can identify two different connections, V_{sense} and V_{pot} , supplying 2460 V and 660 V alternately to the sense- and potential wires, respectively. The upper- and lower-most conductive paths are not crossing the active area and create defined boundary conditions for the electric field. The pads to the very left and right have no further use and were only implemented to support the tensioning of the wires during manufacturing. Right: One of the two secondary planes that act as cathodes. The rings shining through are filled with glue to fix an aluminised Mylar foil on the board. The side shown is directed towards the inner, active board.*

The geometric arrangement of the wires and conductive tracks has a rectangular form, even though the active area is circular. This assures an electric field configuration mostly independent of the position of the track of the passing primary electron. Electrons that do not pass the active inner circle do not leave a recognisable signal in the chamber, as secondary electrons produced outside of the active area are collected by the conductive paths without avalanche. To assure defined boundary conditions at the edges of the wire chamber, a conductive path was implemented next to each of the outermost wires, shielding the inner area from electrons from outside by collecting these electrons without avalanche. Fig. (2.11) illustrates the field configuration inside the chamber by showing the drift

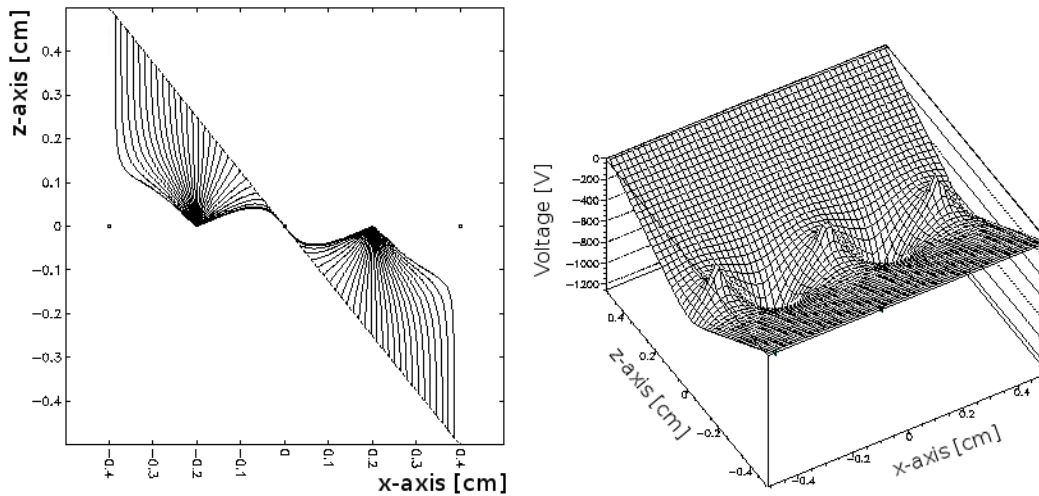


Figure 2.11: A *Garfield* simulation [Gar05] of the multi-wire chamber. *Left:* A schematic view from the side of the multi-wire chamber with a line of sight parallel to the wires. The five dots at $z = 0$ represent wires of the MWC. The left-most, the one in the middle and the one on the very right are potential wires at 660 V, the other two are sense wires at 2460 V. One can see the drift paths of 60 secondary electrons manually placed and mimicking the track of a charged particle passing the MWC. Even electrons created in close vicinity to the potential wires are redirected towards the sense wires. *Right:* The potential inside the active area of the multi-wire chamber. At $z = -0.5$ and $z = 0.5$ the grounded secondary boards are positioned, defining a potential of 0 V. The three peaks represent potential wires, whereas the two valleys indicate the position of two sense wires.

tracks of secondary electrons and the electromagnetic potential with the final geometry and voltages implemented, simulated with the *Garfield* program [Gar05].

The counting gas of the MWC was chosen to be tetrafluoromethane³² (CF_4). With electron drift velocities of $10 \frac{\text{cm}}{\mu\text{s}}$ and ion-mobilities of about $1 \frac{\text{cm}^2}{\text{Vs}}$, it is amongst the fast counting gases [Chr79, Yam92]. In addition, the relatively low Z of the material assures a small cross section to gamma interactions, which is an advantage compared to Argon or Xenon mixtures. It is non-toxic and not flammable, the latter being an important prerequisite for the use near the reactor core. For a further discussion of the properties of counting gases and the selection of CF_4 see [Haa08, Sha98, Sau77]. The pulse-height spectrum of the MWC³³ and the gamma discrimination³⁴ are extensively explained in [Haa08].

³² CF_4 5.0 (R 14) of the company *Linde Gas* (Linde AG, Geschäftsbereich Linde Gas Deutschland, Seitnerstr. 70, 82049 Pullach).

³³A spectrum of the MWC can be seen in fig. (3.1) on page 41 in the present thesis.

³⁴The gamma suppression is defined by measuring a gamma source in coincidence and without coincidence. The suppression factor represents the reduction in the number of events recorded in coincidence relative to the measurement without coincidence. The gamma suppression is determined in [Haa08] to be better than 99.4%.



Figure 2.12: *The spectroscopic module (see also fig. 2.9) is inserted into the detector steel pot and the MWC is positioned 1 mm above the plastic scintillator. One can recognise the three boards of the MWC with a total height of the chamber of 10 mm. This combined module is then mounted to the cross piece as indicated in figs. (2.6), (2.7) and (2.13).*

The mounting of the combined detector module consisting of plastic scintillator and multi-wire chamber is illustrated in figure (2.12).

2.5 Further mechanical components

A ~ 3.5 m long evacuated steel tube extends the neutron beam line SR10 (see sec. 2.1) to the experiment. This beam tube contains several collimators explained in section (2.1.1). The neutron beam then enters the main part of the experiment, consisting of a cross piece from steel as is shown in fig. (2.13).

From the top of the cross piece, the target foil can be inserted, held by a target mounting device shown in fig. (2.14). The foils are clamped at an angle of 20 degrees with respect to the neutron beam. Directly beneath the target, a ^{207}Bi calibration source can be positioned. As indicated in fig. (2.6), a quick-coupling device is used to move the source either to an inactive position or to the calibration location below the target. This movement can be done without any manipulation to other systems of the setup. This ensures the exactly same conditions for the calibration compared to the measurements taken before and afterwards. This is a main improvement compared to the prototype setup described in [Haa08].



Figure 2.13: *A side view on the experimental setup. The neutron beam enters the setup on the left and propagates horizontally through the cross piece. A target holder is inserted from the top, positioning the foils in the neutron beam. The multi-wire chamber is situated between the two yellow gas in- and outlet valves, 9 cm beneath the neutron beam. The lower part houses the scintillator and the photomultiplier, which looks towards the target position.*

In the neck of the cross piece below the target and source position, an aluminium screw thread is located. This minimises the amount of electrons being scattered off the walls prior to being detected in the scintillator. Due to the thread, most of the electrons hitting the wall are absorbed. After passing the neck, the electrons propagate through an aluminised Mylar foil $36\ \mu\text{m}$ thin. This foil separates the evacuated beam line and the target chamber from the detector pot filled with the MWC counting gas. The aluminium layer on the foil serves as electrical grounding and prevents the foil from being charged. This foil only accounts for approximately 8 keV of energy deposition and thus does not have a major impact on the kinetic energy of the β particles. However, the foil is included in the simulation of the response function described later (see sec. 3.2).

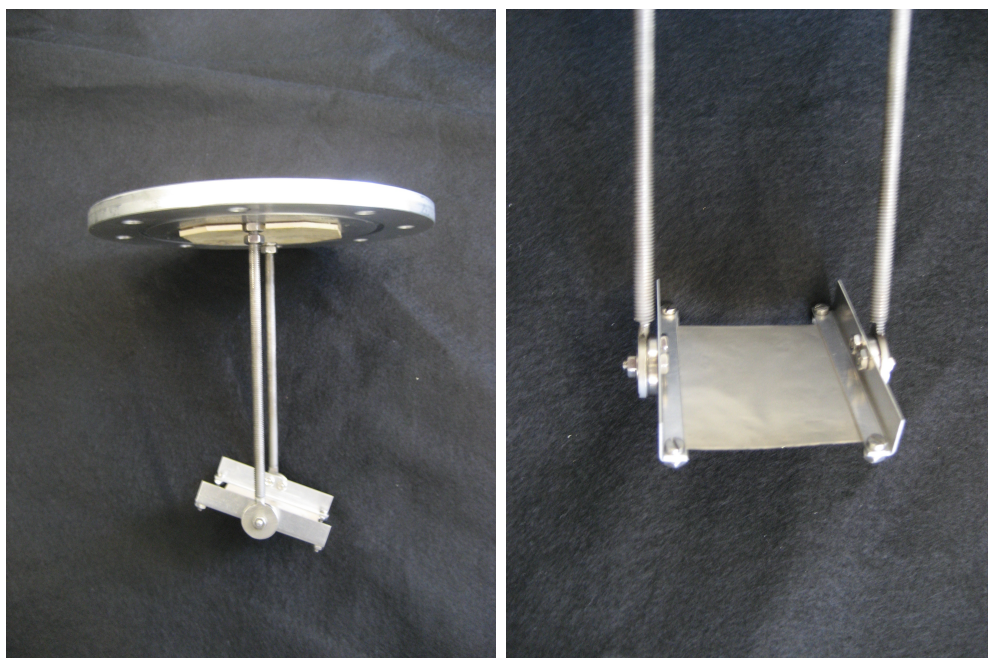


Figure 2.14: *Left: The target mounting device for positioning the foils in the neutron beam, seen from the side. Right: The $60\ \mu\text{m}$ thick and $5 \times 5\ \text{cm}^2$ Pb dummy target foil is shown clamped to the holder. The line of sight is roughly the direction of the neutron beam. The internal structure of the target foils is described in section (2.6).*

2.6 Targets and Sources

For calibration purposes and accurate background subtraction, the setup is capable of housing different types of targets and sources. Besides the ^{207}Bi calibration source, these are all built as thin foils to be clamped to the target holder. All target foils consist of $25 \times 25\ \text{mm}^2$ foils of the individual core material wrapped between two $10\ \mu\text{m}$ thick nickel foils of $48 \times 48\ \text{mm}^2$ size. This containment was introduced to prevent radioactive daughters from fission of uranium to leave the target and possibly accumulate at the Mylar foil between target and detector. The nickel wrapping is used as well for the dummy targets to match the neutron scattering cross sections across the targets.

U: Two identical, metallic foils from natural uranium (99.3% of ^{238}U and 0.7% of ^{235}U) are the main targets for the spectral measurements of the β -decays of the fission products of uranium. Each foil is $25\ \mu\text{m}$ thick, with an area density of $47.6\ \frac{\text{mg}}{\text{cm}^2}$. As already mentioned, the targets are covered by nickel foils.

Pb: A dummy target consisting of lead foils of $40\ \mu\text{m}$ thickness is used for measurements of the background. Lead has a similar cross section for photon interactions as uranium and can be used to simulate the background spectrum at the uranium target to good approximation. The thickness is chosen in such a way that the area density, and thus

the energy deposition of electrons in the target, is equal to the one of the uranium foil (see sec. (3.2) for validation). In first order, the only difference between the spectra taken with the lead and the uranium target is due to fission of uranium.

Ni: A nickel foil of $50\ \mu\text{m}$ thickness (in addition to the $20\ \mu\text{m}$ from the encapsulation) is used to measure the background with a material with highly different proton number ($Z_{Ni} = 28$). The area density was matched to the one of the uranium target, however, the cross sections for neutron scattering, β - and γ -interactions are highly different. This allows to verify the result of a simulation of the background (see sec. 4.2.1).

Apart from these foils used to measure either the beta spectrum of the fission products or to determine the background in these data sets, several sources are used for energy calibration³⁵:

- ²⁰⁷Bi : A ²⁰⁷Bi source provides a calibration point at $\approx 1\ \text{MeV}$. This is due to the fact, that the $1063.6\ \text{keV}$ γ line has a relatively high probability for internal conversion [Led78]: In approximately 10 percent of all emissions, the gamma exhibits photo-effect at the K - shell of the atomic electron cloud, leading to a mono-energetic electron emission at $1047.6\ \text{keV}$. Together with the electron peak at $973.1\ \text{keV}$, which stems from conversion of the $1063.6\ \text{keV}$ gammas at the L - shell with a relative occurrence of about 2.6 %, this forms a double - peak structure, which can be used for calibration purposes. Analogously to the peaks at $1\ \text{MeV}$, internal conversion of the γ line with $569.9\ \text{keV}$ leads to a similar structure at lower energies.
- ³⁸Cl: A target built from PVDC foils (Polyvinylidene chloride - $[C_2H_2Cl_2]_n$), also encapsulated between two nickel foils, is activated in a neutron beam at the ANTARES [Gru05] beam site at the FRM II. The produced ³⁸Cl decays under emission of a β - spectrum with an endpoint of $4916.8\ \text{keV}$ and a half-life of $37.18\ \text{min}$.
- ¹¹⁶In: Natural indium foils of $75\ \mu\text{m}$ thickness between nickel foils. In a thermal neutron beam, ¹¹⁶In is produced, emitting a beta spectrum with an endpoint of $3274\ \text{keV}$ and a half-life of $14\ \text{s}$. This target was also used to prove that there is no significant amount of thermal neutrons left in the fast beam.

³⁵See sec. (3.3) for a description of the calibration.

2.7 Electronics and data acquisition

A sketch of the electronics is given in fig. (2.15). Herein, one can follow the paths of the signals from the detectors to the data acquisition module. This electronic chain has a branch for the energy signal of each detector separately and a merging branch for the fast validation of a possible coincidence in time between the signals from both detectors.

The following list briefly describes the function of the devices used, while tab. (2.1) focuses on the models of the devices.

HV: The photomultiplier is operated with 0.5 kV and the multi-wire chamber is supplied with two different voltages. The sense wires used for amplification of the secondary electrons are supplied with of +2460 V and the field wires are supplied with +660 V. The HV modules provides an off/on toggle switch allowing to restore exactly the same voltage before and after the change of the target foils for which the HV has to be turned off.

Energy branch:

PA: The signals of both detectors are pre-amplified before passing the ~ 10 m long cables between the beam place and the electronics hut. The charge of the detector output pulse is converted into a voltage pulse proportional to the input charge.

MA: The main-amplifiers shape the signal (Gaussian) and further enhance the pulse. The shaping time is $2 \mu\text{s}$ for the PM signal and $0.5 \mu\text{s}$ for the MWC signal.

LGS: The linear gate and stretcher create a rectangular-shaped pulse with a height identical to the maximum height of the input pulse. The length of this pulse is set to approximately $2 \mu\text{s}$. These modules additionally allow to shift the signals by several microseconds to adjust for the different response times of the PM and the MWC.

Coincidence branch:

Disc: The discriminators digitize the signals and allow to delay the signals to correct for the different timing inherent to the MWC and the photomultiplier.

GG: For the measurements of the accidental background, a gate generator was used in the coincidence branch to be able to shift the timing pulses of PM or MWC. This allows to delay the signal by several microseconds and perform off-window measurements.

Coinc: The coincidence module triggers a gate-output signal to be sent to the ADC if the digital timing input signals from the PM and the MWC overlap.

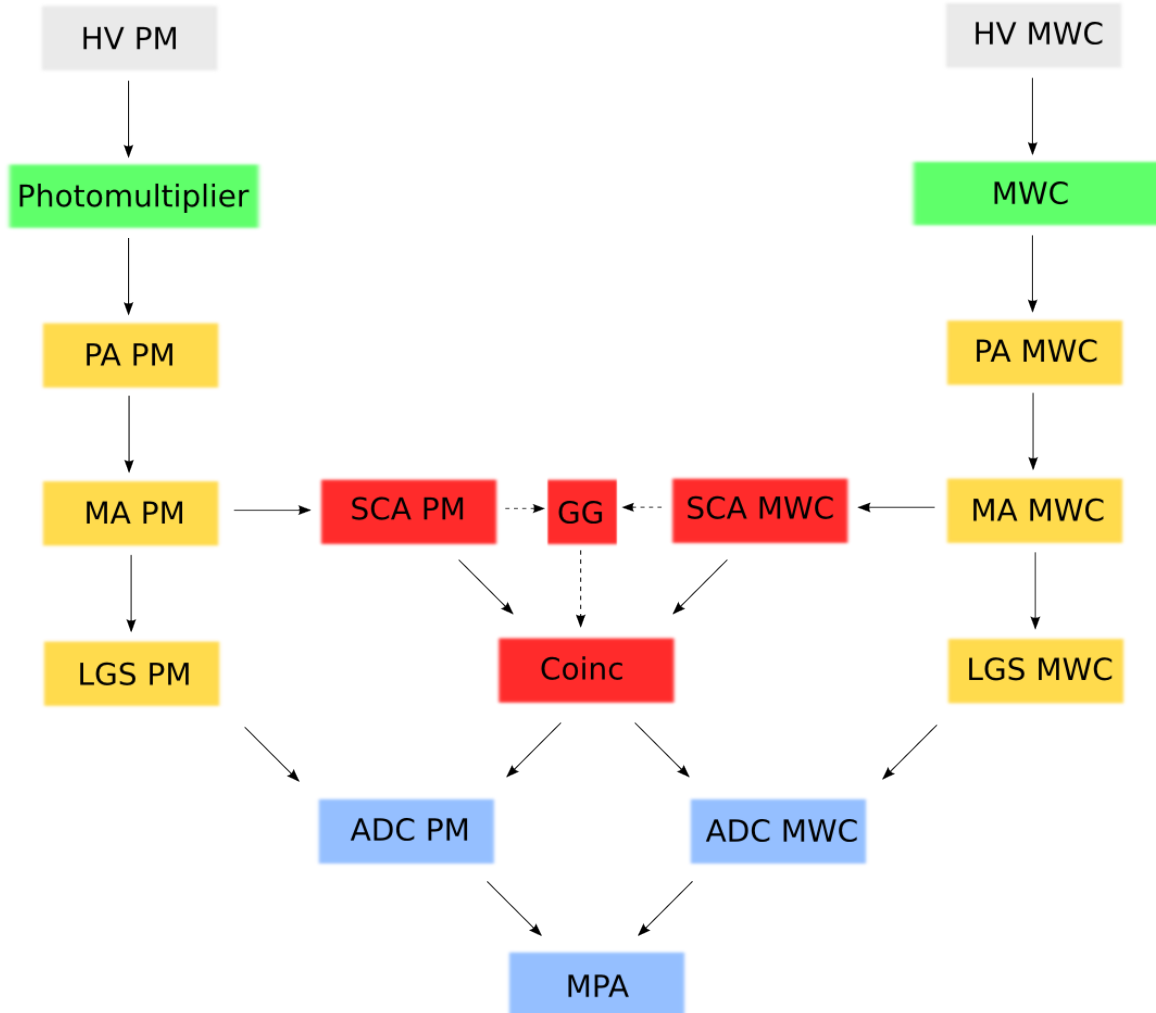


Figure 2.15: Scheme of the electronics used for data acquisition. For both detectors, the PM and the MWC, the signal handling is generally the same: The detectors are supplied with high voltage (HV) and the signals are preamplified (PA) and fed to the main amplifiers (MA). The signal is then split into an energy branch (yellow), passing the pulse to a linear gate stretcher (LGS), and a coincidence branch (red), in which the signal is digitized and assigned to a coincidence module (Coinc). The Gate generator (GG) allows to shift the timing signals of PM or MWC, e.g., to perform off-window measurements of the accidental background. The ADCs collect the energy signal and the gate information. If the gate condition is met (the ADC can be operated in coincidence and anti-coincidence mode) the data is handed over to the multi-parameter system (MPA). A description of the modules is given in the text.

Data acquisition:

ADC: The analog to digital converters are 100 MHz Wilkinson type ADCs set to a range of 8192 channels. They collect the rectangular pulses from the linear gate stretchers and convert their height into a digital signal that is handed over to the MPA-3 unit depending on the signal status at the gate input. This gate input is addressed by the coincidence device. The ADCs can be operated in *coincidence mode* or in *anti-coincidence mode*.

MPA: The multi-parameter system MPA-3 is a data acquisition module to collect data from several ADCs and send them to a PC. The data can be saved in *list mode* containing timing flags and the ADC data. This allows to introduce software cuts on time and assign each PM signal to its specific MWC coincidence signal.

The gates and windows in the modules are set to create a coincidence window of $2.5 \mu\text{s}$ within which the signals from photomultiplier and MWC have to fall to be considered as coincident. It is evident from the discussion in sec. (4.1) that this window is small enough not to introduce any significant background by accidental coincidences. The electronics was intensively checked for linearity and time stability prior to the measurement campaign, as discussed in appendix C.

<i>Device</i>	<i>Label</i>	<i>Type</i>	<i>Data sheet</i>
High voltage PM	HV PM	Canberra HV 3102D	[DataA]
Preamplifier PM	PA PM	Ortec model 113	[DataB]
Main-amplifier PM	MA PM	Ortec model 575 A	[DataC]
Linear Gate and Stretcher PM	LGS PM	Ortec model 542	[DataD]
Analog to Digital Converter PM	ADC PM	Canberra ADC 8701	[DataE]
Single Channel Analyser PM	SCA PM	Ortec 551 Timing SCA	[DataJ]
Gate Generator	GG	THM GG 1300	n/a
High voltage MWC	HV MWC	Canberra HV 3106D	[DataF]
Preamplifier MWC	PA MWC	Canberra Preamplifier 2006	[DataG]
Main-amplifier MWC	MA MWC	Ortec Spectroscopy Amplifier 672	[DataH]
Linear Gate and Stretcher MWC	LGS MWC	Ortec Linear Gate and Stretcher 542	[DataD]
Analog to Digital Converter MWC	ADC MWC	Canberra ADC 8701	[DataE]
Single Channel Analyser MWC	SCA MWC	Ortec 551 Timing SCA	[DataJ]
Multichannel Analyser System	MPA	FAST ComTecModel MPA-3	[DataK]

Table 2.1: The types of the electronic devices used in the experiment. The links to the data sheets can be found in the bibliography. The device with no data sheet available is marked with n/a. This module was manufactured by the Physics Department of Technische Hochschule München which is now Technische Universität München, James Franck Straße 1, 85748 Garching, Germany.

2.8 Simulation of the setup

Performing measurements on both uranium isotopes (^{235}U and ^{238}U) and performing a comparison to the BILL measurements minimises the systematic errors, e.g. due to the unknown neutron beam parameters as described in the former section. The normalisation of the spectra and a compensation of the response function is achieved by this competitive technique. Nevertheless, there is some background that cannot be handled this way. Electrons are created in interactions of gamma quanta coming with the neutron beam or in the neutron activation and subsequent decay of aluminium. The spectra of those backgrounds vary with the target inserted, as gammas and electrons have different interaction cross sections for the different materials. The electrons produced this way cannot be tagged and therefore cannot be separated from the fission spectra, creating background to be considered. Measurements with dummy targets - nickel and lead - were performed to give an estimation of the spectrum and the order of magnitude of these effects. These isotopes are not fissioned, thus the only background stems from scattering of incoming electrons and from Compton-, photo-effect and the pair production inside the targets. Because of the complex interaction and geometry of the setup, an analytical, calculative extrapolation to uranium can not be accomplished with sufficient accuracy.

A GEANT4-based Monte Carlo simulation³⁶ [Ago03] was written to simulate this background and to affirm the correct interpretation of the measured spectra:

- With the help of the mono-energetic electron lines of the ^{207}Bi source, one can study the response function of the detector system. This response has also been simulated to further explain the features of the response function - see sec. (3.2). Although the response function cancels out in the final spectrum due to the comparison of the spectra taken herein to the BILL spectrum, the simulation is a valuable tool to study backscattering processes and to understand the shape of the detector response function.
- It is tested in sec. (4.1) with the help of the simulation, that the gamma radiation being emitted in the beta decays simultaneously with the electrons has no influence on the final spectrum.
- The γ content in the fast neutron beam produces electrons either directly at the target foils or at the last lithium filter in front of the target. In first order and due to the similar atomic numbers of uranium and lead ($Z(\text{U}) = 92$ and $Z(\text{Pb}) = 82$), the background present in the measurement at the lead dummy can be considered to be similar to the one at the uranium target. To make an analysis more precise, GEANT4 is used to simulate the background for Pb, Ni and U. Due to the good agreement between simulation and data for the dummy targets Pb and Ni, the simulation is used to predict the background caused by gammas at the uranium target. This procedure is explained in detail in sec. (4.2.1).

³⁶The version used is GEANT4 9.3, released September 17th, 2010 (patch-02).

- Similar to the background due to gammas, a small content of electrons not produced by gammas but by neutron capture on aluminium is simulated. As will also be shown in sec. (4.2.1), electrons from the ^{28}Al decay build up a target-dependent contribution to the background below about 2.75 MeV. The simulation is used to predict the scaling factor and to translate the background measured at the lead target to the one present at the uranium target.

The working principle of GEANT4 will not be explained here - see [Ago03, GEA13] for further information. The material implemented in the simulation does not include all of the components of the beam line. For the purposes mentioned above, it is sufficient to restrict to the modules and materials in direct vicinity of target and detector:

- The lithium filter in front of the targets is included.
- All targets and the holder are implemented identically to the real pendants, including their placement between the Ni foils.
- The plastic scintillator is implemented with a geometry identical to reality.
- The thin cathode foils and all circuit boards of the multi-wire chamber are implemented. The 25 thin anode wires are not included and the electric field inside the MWC is assumed not to have an influence on the energy of the electrons.
- The CF_4 inside the detector chamber is adjusted to atmospheric pressure and fills the whole volume between the scintillator and the $36\ \mu\text{m}$ Mylar foil, that separates the detector from the target volume. The distortion of this foil due to the 1 bar pressure difference between these two chambers is also taken into account.
- The neck of the cross piece is assumed to be the only part contributing to spectral distortions due to scattering of the electrons. Electrons scattering at other parts of the beam tube do not have any line of sight to the detector and are assumed to be absorbed.

The inner hole of the MWC is defined as a sensitive area. Electrons passing through the effective area of the MWC are flagged to mark these events as coincidence candidates. In addition, for every started event the energy deposition in the scintillator is recorded. If there is an energy deposition in the plastics, the state of the MWC flag is checked and the signal is saved as coincident or as non-coincident event.

Chapter 3

Data analysis I: Calibration and detector performance

The analysis of the experimental data is divided into two parts: Chapter (3) is dedicated to the calibration and the detector performance, while the second part of the analysis in ch. (4) focuses on the analysis chain executed to extract the β -spectrum from the fission daughters of uranium.

In this chapter (3), the data format will be briefly in sec. (3.1), followed by the determination and explanation of the detector response function in sec. (3.2). The energy calibration of the setup can be found in sec. (3.3). The stability of the setup during the measurements is presented in sec. (3.4). The chapter concludes with a discussion of the impact of off-equilibrium effects on the final data.

3.1 Data format

During a beam-time of 15 days, a data set of 169 files was recorded³⁷ - consisting of calibration runs, background measurements and the uranium data. Most spectra are recorded *in* coincidence between multi-wire chamber and scintillator using the hardware coincidence, and some in *anti*-coincidence and *without* coincidence.

As mentioned in the previous chapter, the MPA-3 hardware is the interface between the two ADCs and the PC. It allows to simultaneously save the spectra in different ways, from which two were chosen for the experiment.

Single spectra: The photomultiplier- and multi-wire chamber spectra are saved independently as single spectra. Therefore, there is no way to assign a specific PM event to a MWC event. These files are used in the measurements without coincidence and in anti-coincidence.

³⁷A list of the most important measurements with their irradiation time is given in table (D.1) in appendix (D.1).

List mode: In addition to the single spectra, a *list file* was written by default for every measurement. This file contains the spectra as a stream of timing signals and ADC-data. Every second a time flag is written, allowing to cut on time in the offline analysis. The data includes information, whether a single or both ADCs contain data, making it possible to extract a 2D coincidence matrix, assigning the PM and MWC data event-wise. The analysis of all coincidence measurements is based on these list files.

The list mode provides a handle to check for time dependencies in the energy calibration and detection efficiency. This analysis is performed in sec. (3.4) and shows no deviation from the expected stable behaviour. Furthermore, the evolution of the uranium spectra in time can be analysed to determine the influence of off-equilibrium effects in the measurement (sec. 3.5). The analysis of the spectra is done with the ROOT package, a C++ based framework developed at CERN, version 5.28 [Bru97].

3.1.1 Cut on events in the multi-wire chamber

Some calibration and test runs in between the physics runs required to lower the hardware threshold of the MWC. With this cross check it was assured that there is no noise with pulse heights close to the threshold, which would lead to unanticipated high dead-time in the system. No effect on the MWC spectrum was expected when changing the targets and the neutron beam, and in fact no influence on the spectral shape and the low energetic noise could be found. However, the change of the analog trigger threshold required to cut on the height of the MWC signal offline, to fit every spectrum to the same MWC conditions. As mentioned, the data acquisition for the coincident measurements records the spectra in *list mode*. This allows to link every MWC signal to a coincident PM signal and furthermore to introduce a common MWC threshold for every measurement in the offline analysis. Figure (3.1) shows an example of a 2D plot called *coincidence matrix* and indicates the common MWC threshold chosen.

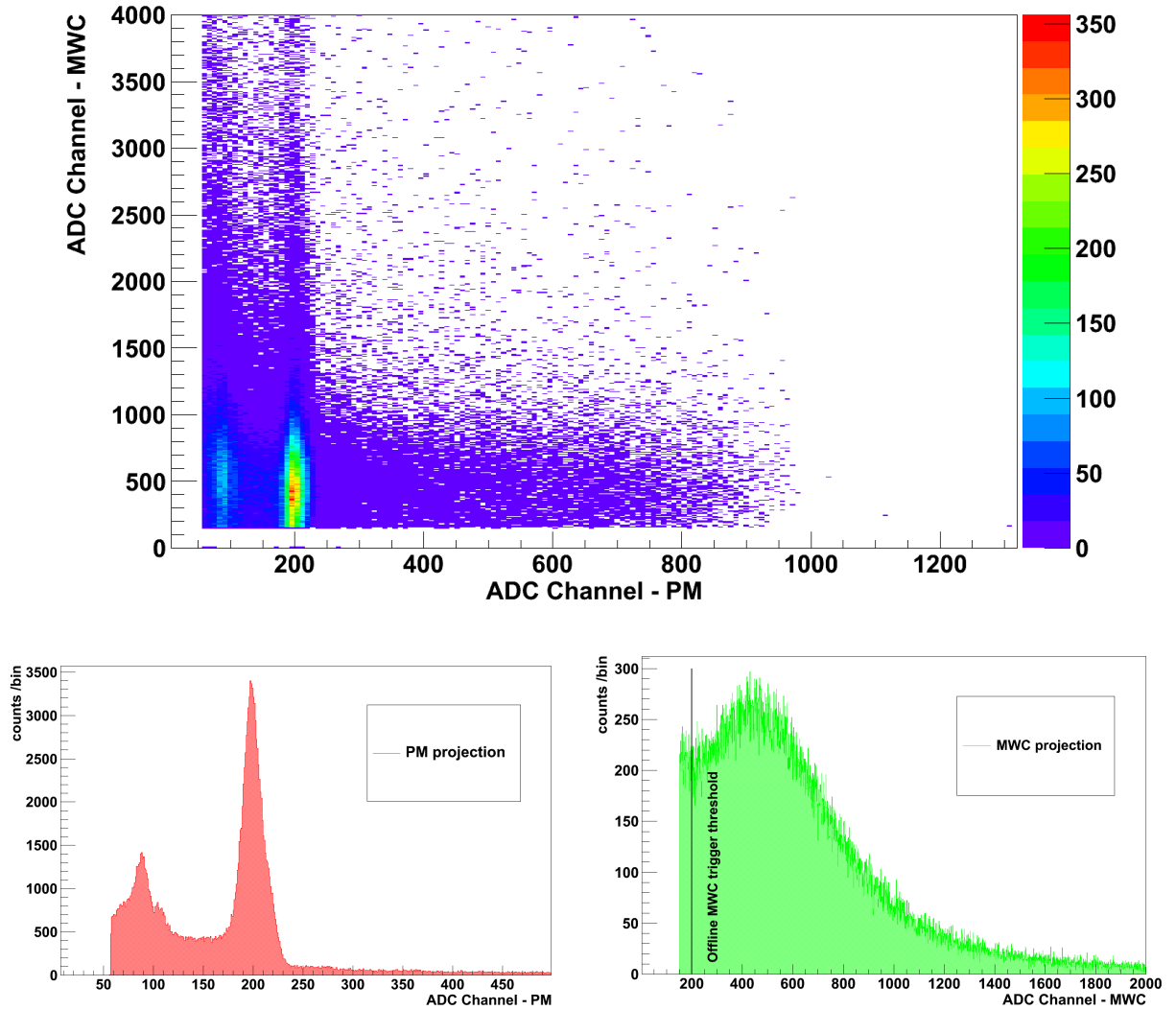


Figure 3.1: *Top*: An exemplary coincidence matrix of a measurement with the ^{207}Bi source. The matrix allows to connect the MWC and PM signals event-wise. *Bottom*: The zoomed-in projections on the PM axis (left) and the MWC axis (right). The two peak structures in the PM spectrum are due to mono-energetic electrons from internal conversion in the Bi decay; see also sec. (3.3). In the Landau-like MWC spectrum, the trigger threshold used in the offline analysis is indicated.

3.2 Response function

In the course of the thesis, the *response function* of the detector is defined to be the spectrum one observes, when exposing the detector to mono-energetic electrons. This response function obviously depends on the energy of the incoming electrons, as the cross sections for physical processes vary with kinetic energy. Hence, the term *response function* also represents the full set of response spectra, obtained at all different energies. The aim in determining the response function of the experiment is to be able to predict the outcome of a given input spectrum, by convolving this spectrum bin-wise with the response function. The result of this work has to be comparable to calculations and other measurements, e.g., the BILL spectrum [Sch85] that serves as normalisation to the herein presented data. But after subtraction of the background sources, the electron spectrum is still a convolution of the *true* spectrum arriving at the scintillator and the response function of the detector system. In general, only the knowledge of the response function allows to later compare the obtained fission spectra with the theoretical predictions or other measurements: Either the prediction has to be convolved with the obtained response and the result of this has to be compared with the measurement performed herein, or the spectrum taken herein has to be de-convolved of the response function, a task that is generally not unambiguous. However, section (4.4) addresses the impact of the response function on the final spectrum and comes to the conclusion that the normalisation of the measurement to the BILL spectrum minimises the influence of the response function on the final ^{238}U spectrum. Nevertheless, the response function is an important tool to understand the behaviour of the detector. There are several processes contributing to the shape of the response function:³⁸

- Backscattering of the electrons and bremsstrahlung are the two dominant processes that cause the loss of visible energy.
- The energy deposition in the material between the source/target and the detector leads to a shape distortion similar to a Landau distribution.
- Electrons from the target position, emitted not directly towards the detector module, may scatter (several times) off the housing material before being detected in the MWC and PM.
- The photon statistics leads to the observation of a Gaussian broadening. This comprises both the production process of scintillation light in the plastic scintillator and the light collection efficiency of the combined system scintillator - photomultiplier.

Calculating these energy dependent effects analytically by including the whole complex experimental geometry is not possible. Therefore, a dedicated *Geant4* -based Monte-Carlo simulation was set up to estimate all the involved processes and finally determine the

³⁸Of course the electronics is also a part of the detector and may affect the spectra due to energy dependent inefficiencies or non-linear behaviour. Those effects are not included in the following analysis of the response function, but will be taken into account of by an overall normalisation function, as it is described in section (4.4) during the normalisation of the spectra and the comparison with the BILL measurements.

response function of the detector. This simulation is also in use for some other applications during the analysis and is described in sec. (2.8).

The basic task in understanding the behaviour of the detector is to achieve the response function for different incoming electron energies. For this purpose, several simulations with mono-energetic sets of electrons were performed. The investigated kinetic energies of the electrons ranged from 1 MeV to 10 MeV in 50 keV steps³⁹. The electrons were homogeneously distributed over the target foil and started in a random direction. The program returned the energy deposited in the scintillator and a flag was set, in case a charged particle moved through the active area of the MWC. This allowed to generate hypothetical measurements with or without coincidence for every target foil and source. Figure (3.2) shows the outcome of the simulation and, therefore, represents the set of response functions in coincidence mode. The simulation does not include the Gaussian broadening due to the photon statistics, because of which a Gaussian is manually convolved to each of the output spectra discussed. The FWHM is set to 8 % at 1 MeV as it is determined by fitting the simulation of the Bi source to the measurement (see fig. 3.5 on p. 48) and evolves as $\frac{1}{\sqrt{E[\text{MeV}]}}$.

The following paragraphs are concerned with an discussion of the processes relevant for the response function.

1) Energy losses in the material between target and detector

The target foil itself, the three Mylar foils, the MWC gas and the reflective paint on the plastic scintillator serve as material the electrons can scatter off, depositing energy. Different angles of emission in the targets lead to a varying thickness of the absorber and therefore to the overlapping of many Landau distributions. This causes an effective and broadened Landau-like spectrum shifted from the initial energy of the electron by an average energy deposition.

Figure (3.3) shows the mean energy deposition of electrons started from the target position as it is returned by the simulation. The targets used were consecutively included in the simulation, giving a handle to study the influence of the target foils themselves.

One can clearly distinguish between the influence of the invariable contribution (gas, Mylar foils and paint) that occurs without a target foil, and the individual shifts of the targets, which adds to this. Apart from the very low energetic regime, where the electrons cannot be considered to be minimal ionising any more, the mean value is nearly constant⁴⁰. Thus, the average deposition⁴¹ in the invariant material is about 40 keV and consequently less than 2 % of the kinetic energy of the electrons measured in the detector. The contribution of the different target foils is in the same order of magnitude, varying from around additional

³⁹The energy threshold of the final β -spectrum measured in the present thesis is 2.25 MeV. See sec. (4.2.2) for a description.

⁴⁰The small rise due to the relativistic effects in the Bethe-Bloch formula can safely be neglected.

⁴¹Herein, the *average energy deposition* is defined as the difference between the energy of the emitted electrons and the peak of the Landau like distribution, thus slightly differing from the usual definition of a *mean* absorption.

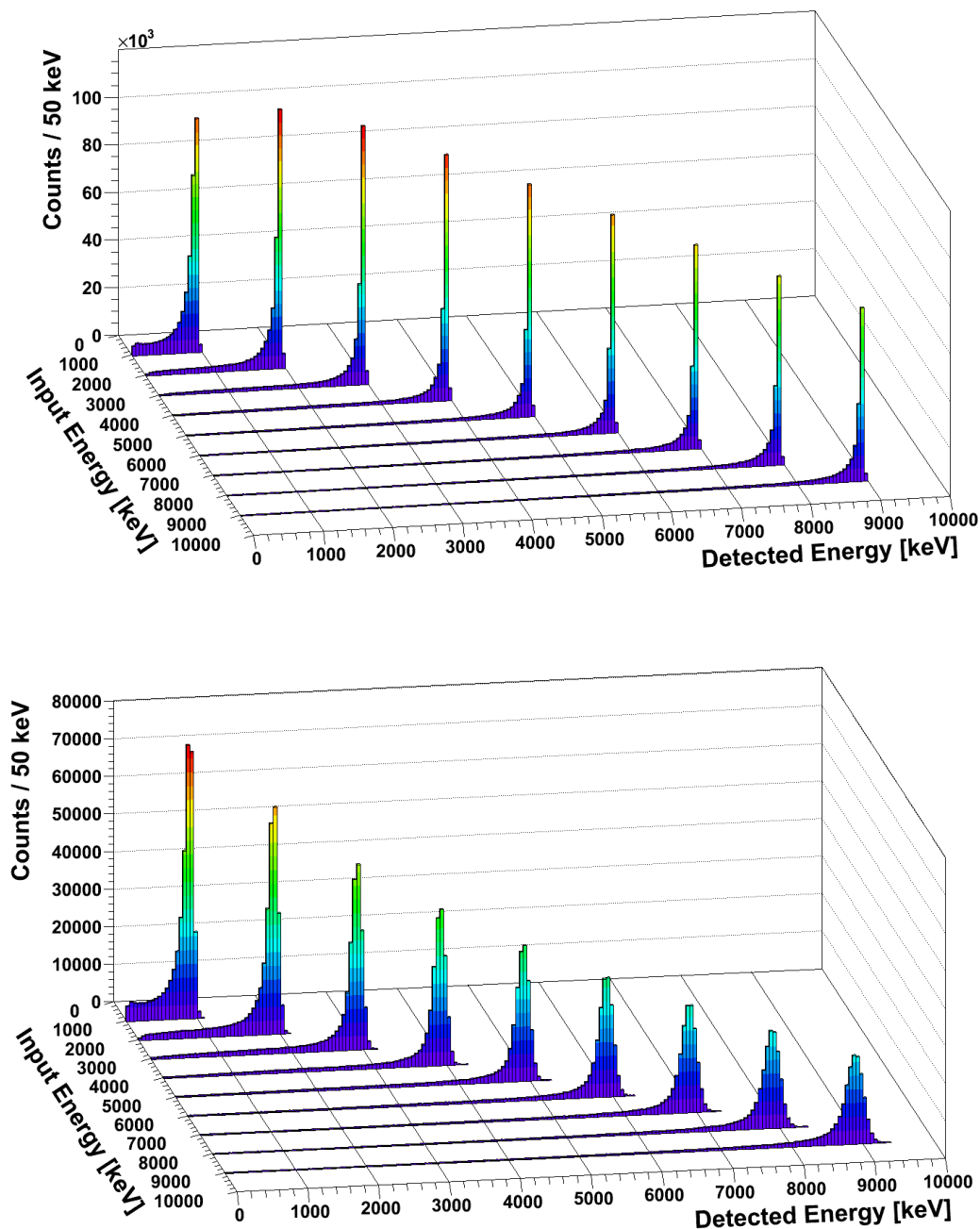


Figure 3.2: *Simulation of the response function for the uranium target. Mono-energetic electrons are started homogeneously distributed over the uranium foil and in random directions. The spectra show the detected energy in coincidence mode. The upper panel shows the outcome including the full geometry but does not take into account the photon statistics of the plastic scintillator. In the lower plot a Gaussian response with a FWHM of 8% at 1 MeV is additionally convolved to the spectrum, representing the statistics of light production and collection.*

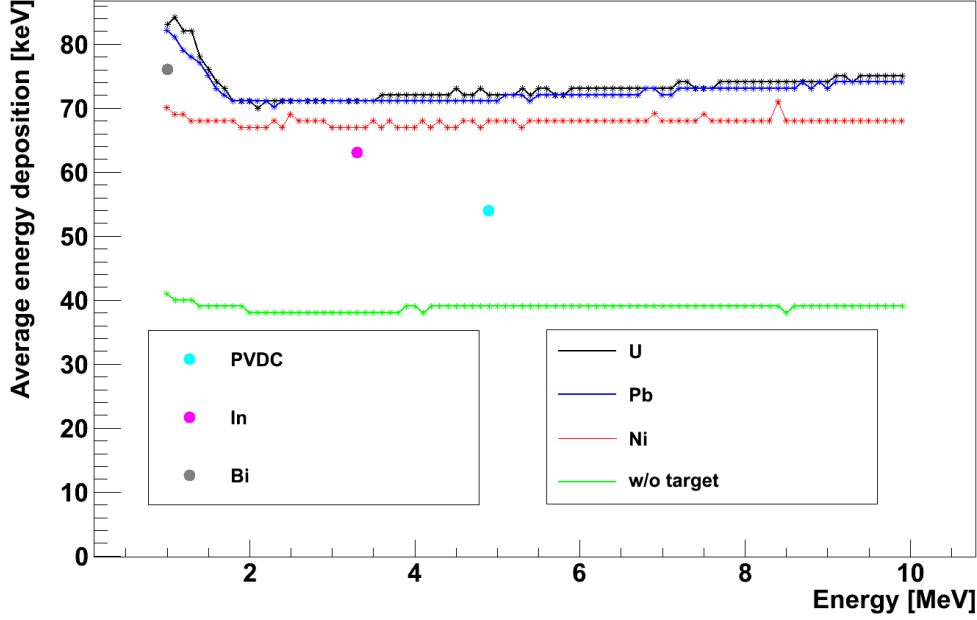


Figure 3.3: *The average energy deposition of electrons emitted from the target position as given by the simulation as a function of the initial kinetic energy of the e^- . Without target (green), only the gas, the Mylar foils and the reflective paint on the plastic scintillator contribute and lead to an absorption of about 40 keV, which is energy independent above the experimental threshold of about 2.25 MeV. The three targets Ni (red), Pb (blue) and U (black) lead to additional absorption in the order of 30 keV. For the sources used for calibration, only the deposition at the relevant energy is given.*

15 keV for the Cl foil to around 33 keV for the U and Pb foils. The difference in absorption in the targets has been considered in the energy calibration, but only effects the outcome at a sub-percent level.

As the electrons are emitted into 4π , a lot are scattered off the steel and aluminium housing and part of them may be scattered onto the detector. The aluminium thread placed in the neck between target and scintillator (see ch. 2) helps to greatly reduce this amount of scattering events. Of course, some of them remain and contribute to the low energetic pedestal of the response function.

2) Energy losses in the scintillator

Electrons arriving at the scintillator do not always deposit their full energy in the detector. The main sources of energy loss are bremsstrahlung and backscattering of electrons out of the detector.

With a thickness of 6.5 cm, the scintillator has a limited capability to detect photons. In fact, the plastic scintillator - consisting of hydrogen and carbon with a density of $1.0 \frac{g}{cm^3}$ - was chosen due to its low cross section for photon interactions. Thus, the bremsstrahlung emitted by the electrons in the scintillator can partly leave the detector module unseen. To investigate the energy dependence and the magnitude of these effects, the simulation mentioned above was programmed to track electrons entering the plastic scintillator. The results are summarized in fig. (3.4). The plot gives the ratio of electrons that deposit their full energy in the plastic scintillator as function of the kinetic energy they carry when entering the scintillator. The simulation shows that about 10 percent of the electrons are leaving the detector again - regardless of their input energy. The scintillator had the shape of a thick truncated cone to prevent any electrons from leaving at the sides or even at the bottom. It could be approved by simulation that the by far dominating part of electrons being scattered out of the scintillator leave it at the front side, categorizing this as backscattering.⁴²

Additionally, one can see that with rising energy more electrons start to loose their energy to another channel than scintillation light. While at smaller energies 80-90 % of the electrons deposit their whole energy in form of scintillation light, this fraction drastically shrinks to around 50 % at 10 MeV. This can be directly explained by repeating the simulation without the process of bremsstrahlung being activated⁴³. Then, the contributions of electrons that are scattered out of the scintillator and the ones that are fully absorbed add up to 1, showing that no other process significantly adds to the energy loss. Only when activating bremsstrahlung, there are a lot of events with missing energy. The energy dependence can directly be connected to the characteristics of the bremsstrahlung process, which has a higher cross section and yields a harder X-ray spectrum at higher energies of the charged particle [Leo94].

3) Photon statistics and the quality of the simulation

The plastic scintillator has a light yield of 10,000 photons/MeV with the maximum of emission at a wavelength of 408 nm [Sai01]. The photomultiplier has a borosilicate glass window with a transmission for perpendicular arriving photons of around 95 % for the given scintillation light and the quantum efficiency of the Bi-alkali photo-cathode is about 25 % [Ele03]. Further contributions to the light loss are due to the light collection in the scintillator, which is directly connected to its shape, the reflectivity of the paint and the

⁴²Tabata et al. [Tab71] give an empirical formula of the albedo for incoming electrons depending on Z. For further information and discussion of the angular and spectral distribution of backscattering processes see e. g. [Kal82]. In addition, [Tso69] describes the detector response of a plastic scintillator with measurements of a ²⁰⁷Bi source in a similar manner as in this work.

⁴³Geant4 offers the possibility to disable particular physics processes.

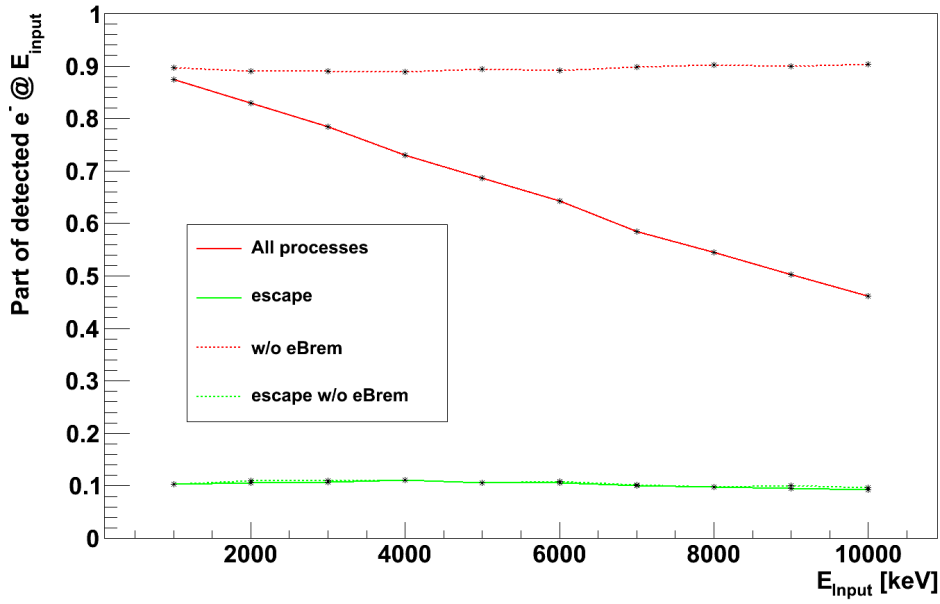


Figure 3.4: The ratio of electrons depositing their full kinetic energy in the plastic scintillator as a function of the kinetic energy E_{Input} they have when entering the plastic scintillator. The continuous red line shows the ratio as it is simulated with all physical processes being active. The dashed red line shows the ratio when switching off the process of bremsstrahlung in the Geant4 simulation, resulting in a constant value over the whole range. This proves that the main influence of energy loss is due to electrons emitting X-rays, which leave the scintillator undetected. In addition, the part of electrons escaping the scintillator is depicted in green, representing the albedo of the scintillator. This contribution is the same for each energy and does not change when switching bremsstrahlung on or off.

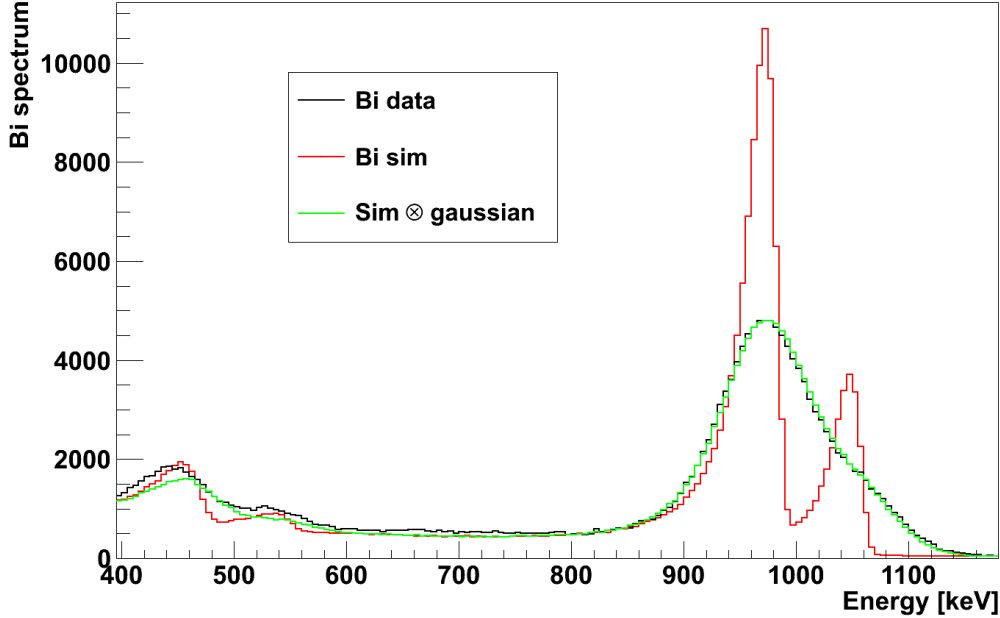


Figure 3.5: The ^{207}Bi spectrum as measured (black) and simulated (green). The simulation results in a spectrum not yet broadened by the photon statistics. A Gaussian with a FWHM of 8 % at 1 MeV has to be included in order that the simulation fits the data. This curve is shown in red as the full modelled simulation. See the text for further interpretation of the differences in the lower energy regime.

optical coupling to the PM. This last contribution is hard to estimate, but may lower the detected amount of photons in the order of a factor 2. If one combines all these estimates, this results in a statistical uncertainty of a few percent.

This can be directly observed in the calibration data of the ^{207}Bi -source⁴⁴. A comparison of a measured spectrum of the Bi source and a simulation, including the full term scheme of the ^{207}Bi decay and considering internal conversion in the Bi atoms, is given in fig. (3.5):

The simulated spectrum of ^{207}Bi as well as the results of the measurement is shown. In the simulation, one can see the two double-peak structures of the ^{207}Bi decay produced by the emission of gammas (570 keV and 1064 keV), which are converted into electrons. This conversion may happen at the K- or at the L-shell of the atom, leading to different kinetic energies of the outgoing electron⁴⁵. The simulation was convolved with a Gaussian and fitted to the data with the standard deviation being the free fit parameter. This yields a full width at half maximum of:

$$FWHM = 0.08 \cdot \frac{1}{\sqrt{E[\text{MeV}]}} \quad (3.1)$$

⁴⁴The energy calibration will be described in more detail in sec. (3.3).

⁴⁵For a detailed description of the spectrum, see also section (2.6) on the sources and targets.

At the lower energy peaks, the simulation and the data differ slightly in energy. This difference is based on the fact that the experiment was optimized to energies above 2 MeV. The linear gate stretcher used has a non-linearity close to its threshold, which was set to a voltage equivalent to approximately 350 keV. This disturbs the measurement in this low-energy region. It could be affirmed in other tests that the influence of this behaviour reaches about 200-250 keV above its threshold but has no effect on the spectrum above. In addition, the simulated response slightly underestimates the height of the plateau situated at the low energetic wing of the 1 MeV peaks and reaches down to lower energies. The deviation is small, but shows that some of the simplifications that were necessary to include the detector geometry in the Monte Carlo code may have an influence on the spectrum. Material not included in the simulation or geometrical inaccuracies of the detector construction file may have a noticeable influence. In particular, the aluminium thread in the neck of the cross piece, which is inserted to prevent electrons scattered at the walls to reach the detector, had to be simplified. Nevertheless, the simulation is highly able to reproduce the measured data.

The analysis of the effects mentioned above shows a good understanding of the underlying processes responsible for the loss of energy of electrons. Later, in section (4.4), a direct test of the simulation and the response function is performed when comparing the β -spectrum of the fission products of ^{235}U as measured by the BILL collaboration [Sch81, Sch85] with the spectrum measured in the course of the present thesis. It will turn out that the response function determined can describe reality to a very good extend.

3.3 Energy calibration

The energy calibration of the detector is based on three different points:⁴⁶

- At 973.1 keV and 1047.6 keV the two neighbouring mono-energetic lines from the conversion electrons of the ^{207}Bi source are used.
- A neutron activated In foil emits a beta spectrum of ^{116}In with an endpoint at 3274.0 keV.
- A neutron activated Cl foil emits a beta spectrum with an endpoint at 4916.8 keV from ^{38}Cl .

The final beta spectrum (see sec. 5) will be presented up to 7 MeV, with the errors being smaller than 10 percent up to about 6 MeV. Hence, the three data points cover nearly all of the final spectrum and there is no need to extrapolate the calibration far beyond the calibration points.

⁴⁶Values taken from [Fir96a, Fir96b]. The sources and foils are described in more detail in section (2.6).

3.3.1 The calibration with the ^{207}Bi source

The spectrum of the Bi source was taken multiple times spread over the whole beam-time. In the previous section (3.2) was shown that a mono-energetic peak is eventually detected as a Landau-like spectrum. Because of the Gaussian broadening due to photon statistics in the scintillator - photomultiplier system, at the peak position this spectrum is very similar to a Gaussian. Additionally, this peak is shifted by a few tens of keV due to energy depositions in the sources, foils and the material between them and the detector (see previous section 3.2). Therefore, two Gaussian functions were fitted to the peak structure at ~ 1 MeV, leaving all parameters (their position, peak height and width) as free parameters to the fit (see fig. 3.6). To simulate the low energetic pedestal, a Fermi function was additionally included as baseline⁴⁷. The height of the pedestal was determined by fitting a horizontal to the plateau left of the peaks and then was fixed. The other parameters of the Fermi function were left free, but had negligible influence on the outcome of the fit.

The fitted position of the 973 keV main peak is taken for calibration. The simulation of the response function showed that the energy deposition in the material in front of to the detector leads to a small shift of the observed energy, which is nearly the same for all targets and sources. The corrections applied are less than $\sim 0.5\%$ of the electron energy. As will be shown in section (3.4), the position of the peak was stable over the whole beam-time with only minor deviations. As no time-dependent shift of the peak can be seen, the weighted average of all the measurements is used to determine the value used for the final calibration. The errors of the single measurements are extracted from the fit of the Gaussian functions. This results in a position of the 973 keV peak at channel number 196.93 ± 0.45 .

3.3.2 Calibration with indium and chlorine foils

The use of ^{207}Bi as mono-energetic electron source helped to pin one point at lower energies in the calibration. Unfortunately, there are no isotopes that combine a moderate lifetime with a considerable probability of emitting mono-energetic electrons at energies of several MeV. Thus, another technique has been chosen to provide high-energetic calibration points. For this purpose, In and Cl foils were activated in a neutron beam and subsequently measured in the setup. The isotopes ^{38}Cl and ^{116}In then undergo beta decays with a high-energetic endpoint (5 MeV and 3 MeV, respectively) which then can be used for further calibration.

⁴⁷This technique is adapted from [Tso69], where a similar setup and also an analysis of a ^{207}Bi source is described for the detection of β -spectra from fission. See also the references quoted therein.

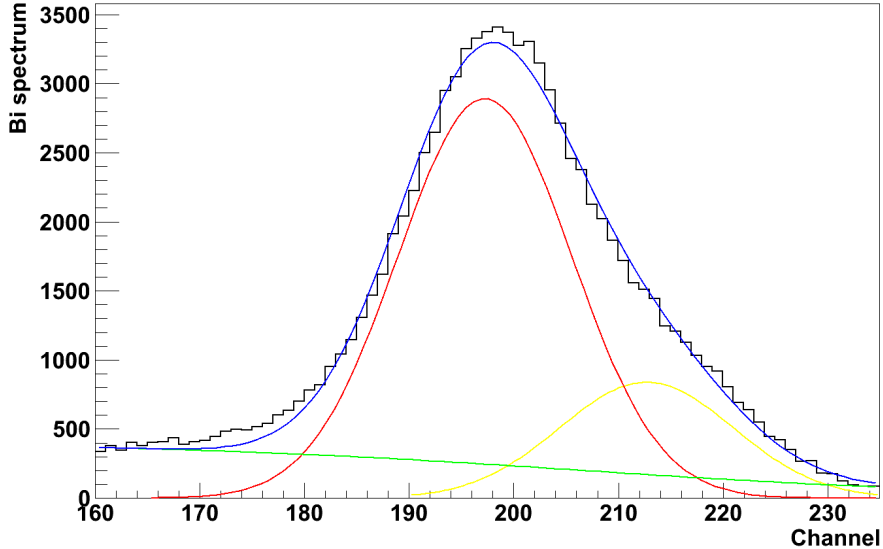


Figure 3.6: An exemplary calibration measurement on the Bi source. The two peak structure is fitted with two Gaussian functions, approximating the response function of the detector. A Fermi function is additionally included in the fit to simulate the plateau at the lower energy flank of the peaks. The parameters of this Fermi function do not affect the position of the peak in the fit by more than half of a bin. The position of the red main peak at 973.1 keV is used for calibration.

Due to the low neutron capture cross section of ^{37}Cl of 0.43 barn [Fir96a], the activation of the **chlorine foil** had to be done at a beam site with a higher intensity of the neutron beam than accessible at the SR 10. The target was inserted into the neutron beam at the ANTARES site⁴⁸ and irradiated for about one hour. Thereafter, it was inserted into the ^{238}U -experiment and the spectrum was recorded. With a half-life of ^{38}Cl of 37 minutes, the loss in intensity from this source during the approximately 10 minutes needed to set up the experiment with the new target was sufficiently small. This source could be activated and measured during both the thermal and the fast neutron beam period of the experiment and hence could be used to evaluate that no shift in the energy calibration has occurred. The β -spectrum of ^{38}Cl was used to get a calibration point at 4916.8 keV.

Natural **Indium** mainly consists of ^{115}In which can partly be converted to ^{116}In in a thermal neutron beam. This isotope has a half-life of only 14s and emits, amongst others, a β -spectrum with an endpoint of 3274 keV. Due to the short lifetime and the high thermal neutron capture cross section of more than 280 barn [Fir96a], the Indium foil was

⁴⁸The Advanced Neutron Tomography And Radiography Experimental System ANTARES is a neutron imaging facility operating with a cold ($E \approx 200 \mu\text{eV}$) neutron beam in the experimental hall of the FRM II. For additional information, see [Gru05].

activated in the experiment itself. This had the advantage that the setup did not have to be manipulated to insert the foil between the irradiation and the measurement of the spectrum. On the other hand, the fast neutron cross section is about 3 orders of magnitude smaller [END12], because of which one could only use this foil in the thermal beam and there was no way to repeat the calibration - as could be done with the Cl foil using the ANTARES beam - during the fast beam measurements. Nevertheless, it could be checked that the measurements with ^{38}Cl and with the ^{207}Bi source showed no drift during the beam-time, proving a stable detector.

The indium foil was also used to prove that no thermal neutron contribution was present in the fast beam. The neutron capture cross section for fast neutrons is negligible compared to the one for thermal neutrons, and thus one has a great handle to check for residual thermal neutrons in the fast beam. No sign of a beta spectrum could be found after irradiating the In foil in the fast beam - see also the discussion of the neutron spectra in sec. (2.1.1).

Following the procedure from [Fan52], the endpoints of the beta spectra were determined with the help of the Kurie-method. This technique linearises the spectrum near the endpoint and allows to determine the endpoint via a straight-line fit. The procedure requires a rough pre-calibration. For this purpose, the conversion line of ^{207}Bi at 1679.5 keV (fig. 3.7) is used additionally to the 973 keV line to perform a two-point energy calibration. The 1679.5 keV peak is very low in intensity and is, because of the bad statistics, not included in the final fit of the energy calibration explained below.

With this pre-calibration, one can calculate the Kurie spectrum:

$$\sqrt{\frac{N(\eta)}{\eta^2 \cdot F(\eta, Z) \cdot C(E)}} \sim (\epsilon_0 - \epsilon), \quad (3.2)$$

with:

- $N(\eta)$: Recorded spectrum, $F(\eta, Z)$: Fermi function, $C(E)$: Unique shape correction;
- $\eta = \frac{p}{m_e c}$, $\epsilon = \frac{E}{m_e c^2}$, $\epsilon_0 = \frac{E_0}{m_e c^2}$;
- p , E : Momentum and total energy of the electron, E_0 : Endpoint of the β -decay;
- m_e : Electron mass, c : Speed of light, Z : Proton number.

Equation (3.2) is linear in ϵ and intersects the x-axis at the endpoint of the β -spectrum. The Fermi function includes the effects of Coulomb attraction of the residual nucleus on the energy distribution of the emitted electrons. Tables of this energy-dependent function are given in [Fan52]. The decay of Cl is forbidden in first order and a unique shape correction function $C(E)$ has to be taken into account. Following the results of [Kli68], where the decay of ^{38}Cl is investigated with a focus on the description of this unique shape, and defining W as the total electron energy in units of its rest mass, a correction function $C(W)$ is applied to the data prior to the fit.

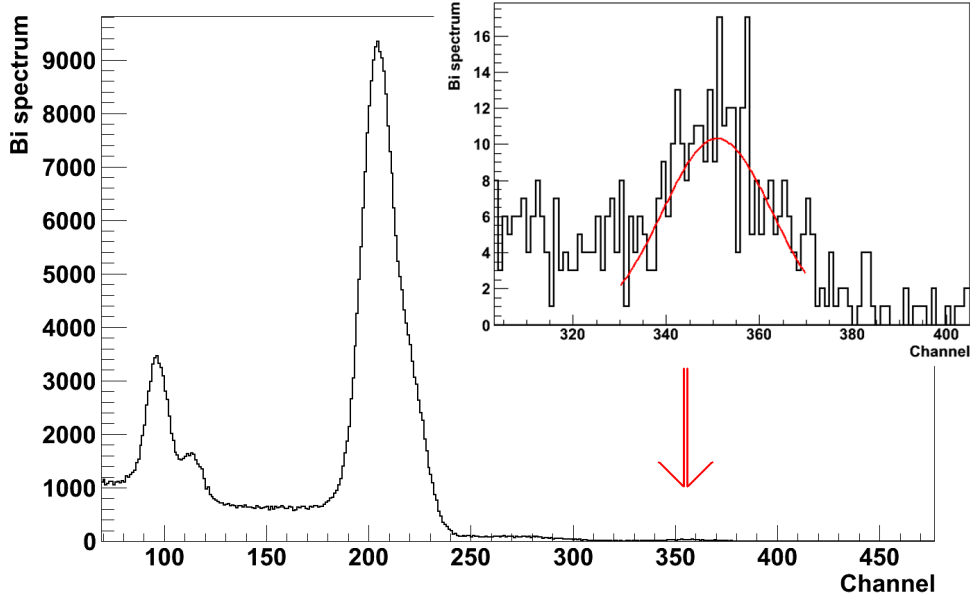


Figure 3.7: For the purpose of an energy pre-calibration necessary for the Kurie analysis of the Cl and In spectra, the 1679.5 keV line of the ^{207}Bi source was used. The plot shows the spectrum of the bismuth source and the position of the peak is indicated. The insert depicts a zoom into the electron line and the best fit of a Gaussian to the spectrum (red line). This peak, together with the 973 keV peak, was used for a first energy calibration.

The correction $C(W)$ applied is:

$$C(W) = (1 - 0.005 \cdot W) [(W^2 - 1) + (W_0 - W)^2]$$

This changes the outcome of the fit by $\sim 0.5\%$. For indium, such a correction is not necessary as the decay is allowed.

The linearisation described is only valid for ideal detectors with perfect energy resolution. In the experiment, the true spectrum is broadened by the detector response function, which leads to a non-linear tail around the endpoint. To closer investigate this aspect, a program written and described by the author of [Tho10] was used to generate a histogram following the analytical form of the indium beta spectrum. This spectrum is then convolved with the detector response and the Kurie plot is drawn. One can now compare the results of a straight-line fit to the broadened spectrum with the true endpoint. This is shown in figure (3.8).

One can directly see that the linear fit to the broadened calculated spectrum (mimicking the real data) leads to an overestimation of the position of the endpoint energy. As a consequence, the fit has to be restricted to an energy range a few 100 keV below the endpoint. When neglecting the last 400 keV of the spectrum for the fit, the endpoints

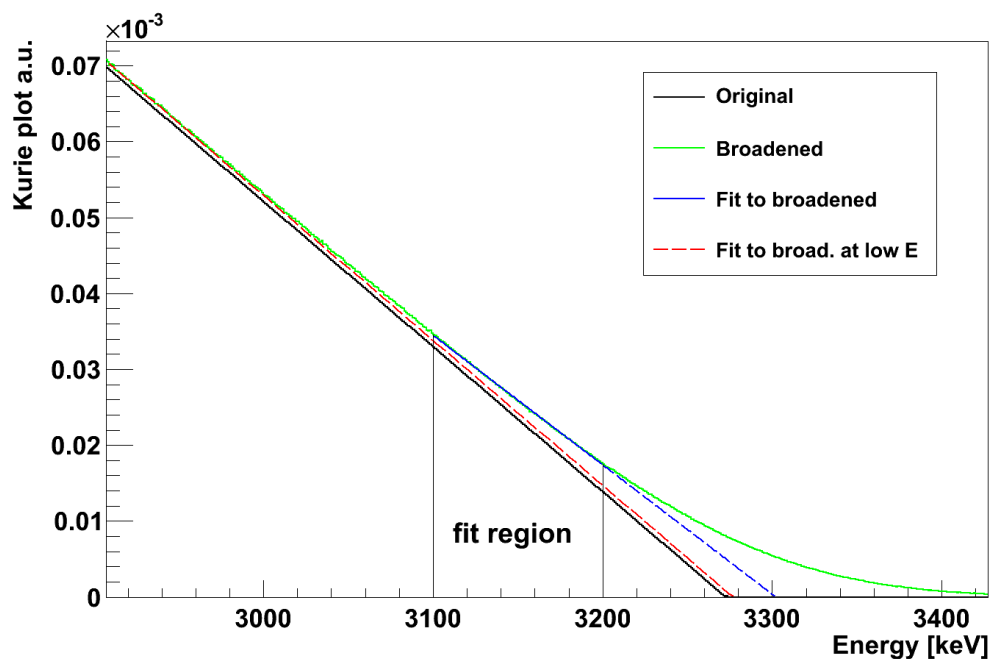


Figure 3.8: *Kurie plots of an analytical indium spectrum (black) and the identical one but broadened by the detector response (green). Although the Kurie plot of the original spectrum is perfectly linear, the broadening spoils the linearity of the Kurie plot and thus leads to an inaccurate endpoint determination when applying the fit near the endpoint (fit in blue restricted to the fit region, extrapolation as dashed line). Fitting to energies $< (E_0 - 400 \text{ keV})$ minimises the impact of the broadening on the endpoint determination: The dashed red line illustrates the outcome of a fit to the broadened spectrum, fitted to an energy region from 2500 - 2900 keV, where the Gaussian broadening of the spectrum has minimal impact. The endpoint determined by this fit to lower energies is very close to the true one.*

Measurement	Energy [keV]	Fitted endpoint (channel)
Indium before th	3274	678 ± 4.0
Indium after th	3274	671.4 ± 3.7
Cl before th	4917	1022.1 ± 3.2
Cl after th	4917	1003.4 ± 2.1
Cl before fast	4917	1015.3 ± 2.2
Cl after fast	4917	1015.5 ± 2.2

Table 3.1: *The results of the fits to the Kurie plots of chlorine and indium. The names of the measurements indicate their chronological order in comparison to the uranium measurements in the thermal (th) and fast neutron beam. The quoted errors represent the statistical errors of the straight-line fit.*

determined by the fits with and without artificial broadening result in nearly the same endpoint, only varying by 3%. Thus, in the In and Cl Kurie-calibration the straight line fits are applied to the 100 bins that approximately correspond to a range of 400-900 keV below the endpoint.

The end point obtained is used to generate an energy calibration and the procedure is repeated to tune the results. This method converges after the first repetition.

This energy calibration obtained for In is used as input for the Kurie plot of Cl which was handled the same way with a minor correction due to the unique shape as discussed above.

The results of the Kurie plots are summarised in table (3.1). The calibration runs were performed directly before and after each uranium measurements, as tagged in the table. As mentioned, the ^{116}In calibration could only be performed for the thermal beam measurements.

The determined endpoints of the ^{116}In do not differ significantly from their mean 674.2 ± 2.7 and also the Cl data of the fast beam indicates a very stable calibration. In the thermal measurement of the chlorine foils, however, a small deviation exceeding the statistical errors can be seen. This effect is not big and the values differ from the weighted mean (1012.6 ± 1.4) by less than a percent. Nevertheless, the error of the energy calibration may not stem only from the statistical uncertainties of the fits to the endpoints. It may be an artefact of the opening of the setup when the target foil is inserted and the PM was exposed to light (with the voltage turned off). Hence, the error on the mean value for the Cl endpoint is chosen to be the standard deviation of the four values leading to an endpoint of 1012.6 ± 6.9 , the error still being smaller than 1 percent.

In general, no significant variation of the calibration measurements over time can be seen, indicating a stable setup, including detector and electronics.

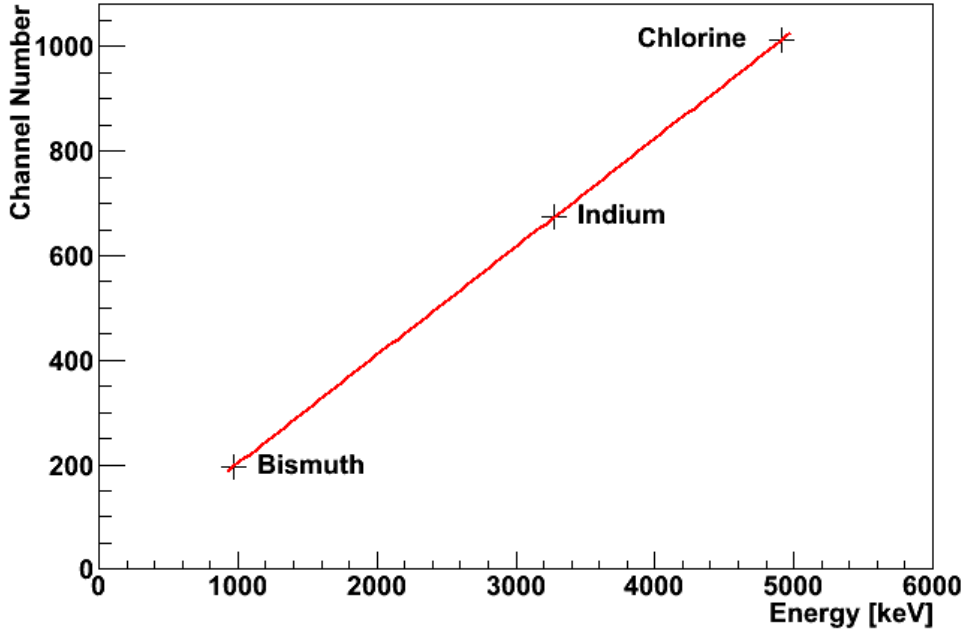


Figure 3.9: *The linear fit for the final energy calibration. The markers (+) are only to guide the eye where the anchor points of the three sources are positioned and are not correlated to the size of the error. No error bars are plotted as they would be too small to be recognised - see text for the exact values.*

3.3.3 The final calibration

The three anchor points discussed are utilised to achieve an energy calibration. This is performed as a straight-line fit to the three data points with no non-linear terms being taken into account. In the fit, the energy of the calibration points is considered to be precisely known. With CN being the channel number and E being the reconstructed energy, the linear fit yields:

$$CN = 0.207 (\pm 0.001) \cdot E [keV] - 4.46 (\pm 1.34) \quad (3.3)$$

with a correlation between slope and intercept of -0.94 and a covariance of -0.0016. This translates into an energy calibration of:

$$E[keV] = (4.83 \pm 0.03) \cdot CN + (21.52 \pm 3.21) \quad (3.4)$$

The fit was performed assuming a linear relation of energy and channel number. With three data points it is possible to check for deviations from linearity by having a look on the difference between the true energy of the calibration source and the one reconstructed by the final calibration and plotted in fig. (3.9). If there were quadratic and higher-order terms to be included, the three points would show an enhanced deviation from the

Isotope	True energy [keV]	Calibrated energy [keV]
Bi 207	973.1	972.6 ± 10.7
Indium 116	3274.0	3277.9 ± 17.2
Cl 38	4916.8	4909.5 ± 20.8

Table 3.2: *The energies of the sources used for calibration and the energies that are reconstructed by the final calibration. The final linear fit is able to reconstruct the energy of the sources better than a percent, indicating that non-linear terms are not necessary in the procedure.*

constructed straight line. Table (3.2) depicts the true energies of the calibration sources and indicates that the linear fit is able to match each of the anchor points to a very good extend. This affirms the procedure, not to include quadratic or higher-order terms in the calibration.

To check the impact of the inaccuracy on the final result, the whole analysis chain as described in sec. (4) was processed three times: once for the given calibration and once for a calibration corresponding to the upper and lower 1σ boundary, respectively. The result of this procedure is given in sec. (5.1.1) and the conclusion is reached that the inaccuracy induced by the energy calibration is only a minor contribution to the total imprecision of the final spectrum.

3.4 Stability over time

The experiment was performed over the period of approximately three weeks and it is of major importance that the system is stable during this time. This includes the energy calibration as well as the overall efficiency of the setup. To check this, tests were performed prior to and during the measurement campaign.

3.4.1 Stability tests in the laboratory

Before moving to the reactor site, the experiment was set up in the laboratory. The ^{207}Bi source was inserted and data was taken for two weeks without manipulating the setup. In addition, a pulser was adjusted to a 70 Hz signal rate with a pulse height corresponding to around 7 MeV and fed into the Linear Gate Stretcher. The data was saved every day and the different runs could be compared, checking for several issues:

- The position of the pulser peak did not change in energy and appears in exactly the same bin for every period, indicating stable electronics.
- The position of the Bi peak also showed no shift. Figure (3.10) shows the variation of the ^{207}Bi peak at 973 keV during the campaign at the reactor and the same analysis was performed for the off-site measurements. Similarly to the in-situ measurement, the position of the peak in the laboratory test was statistically distributed around the mean value with a standard deviation of less than a quarter of a bin, indicating that also the PM and the main-amplifier did not drift in time.
- The rate of the pulser was perfectly stable at 70 Hz and the rate of the Bi peak (around 100 Hz) had a standard deviation of 0.8 ‰, showing that also the efficiency of the system was stable.
- As there were some temperature changes during the week of the tests, the response of the system to laboratory temperature variations on the 5 K scale could be checked to be negligible. In addition, temperature variations of the electronics did not affect the output.

The only manipulation to the system during the tests was the regular change of the MWC gas before every new 24 h-run. Therefore, the stability of the system includes that the technique to change the gas was able to restore the same conditions, i.e. the pressure and the cleanliness of the CF_4 , and thus this manipulation had no influence on the data. In another measurement with the Bi source, the gas was checked for degradation over time by comparing data sets taken with fresh gas with data taken with gas that has been in use for one, two and three days. Again, no effect in the rate of the Bi peak could be seen.

During the data taking at the reactor, the setup had to be opened several times to change the targets and sources and this manipulation required the voltage of the PM to

be switched off. These two manipulations may affect the performance of the setup and introduce slight changes in the response. This was checked by opening and closing the setup several times and taking data with the Bi source. As in the other tests, no influence on the position and the rate of the spectral features could be identified. Thus, it can be stated that the digital voltage controller is able to restore the same photomultiplier voltage all the time and the opening and closing of the target flange does not spoil the measurements.

Tests to determine the influence of high rates on the dead-time of the system will be described in the next section, as with the beam-time data one can study the effect of varying count rates with the help of the prominent muon peak.

3.4.2 In-situ stability tests at the reactor site

The tests in the laboratory showed an excellent stability of the whole setup. Nevertheless, it is necessary to check for the stability during the three weeks of data taking at the beam site. For this purpose, the stability of the position of the Bi peak was monitored and the rate and dead-time could be screened by a peak originating from muons. Additionally, this muon peak confirmed the stability of the energy calibration.

To ensure that the energy calibration stayed stable over the whole period of time, a total of 22 measurements of the ^{207}Bi source were performed. These measurements were spread over the whole campaign, taken always before and after a background or uranium measurement. As the source is placed in an extension of the cross piece of the detector housing⁴⁹ and can be put into a position below the actual target without any need to change the gas or this target, the calibration data can be taken under the same conditions as the corresponding background or uranium measurement. The position of the 973 keV peak of the ^{207}Bi source shows no shift over the whole beam-time. The fitted position of the peak statistically spreads by less than 5%, indicating a stable detector behaviour.

As discussed in the previous section, the measurement with the chlorine calibration foil is also used to test the stability over time, confirming that no drift appeared. The stability of the energy calibration over time can additionally be tested by screening the position of the *muon peak*. As the scintillator has a thickness of 6.5 cm, cosmic muons traversing the detector deposit around 13 MeV in the plastic scintillator and trigger the multi-wire chamber. The energy deposition in the plastic scintillator is higher than the endpoints of the beta spectra of the fission products of uranium and thus the peak is free of background. In addition, it is present in every single measurement with the same rate and consequently offers an opportunity to cross-check the energy calibration at the high end of the spectrum and provides an in-situ handle to correct for the detector dead-time. This possibility is a great feature to ensure the correct absolute calibration of the obtained data sets.

⁴⁹See fig. (2.6) and chapter (2) for a description of the setup.

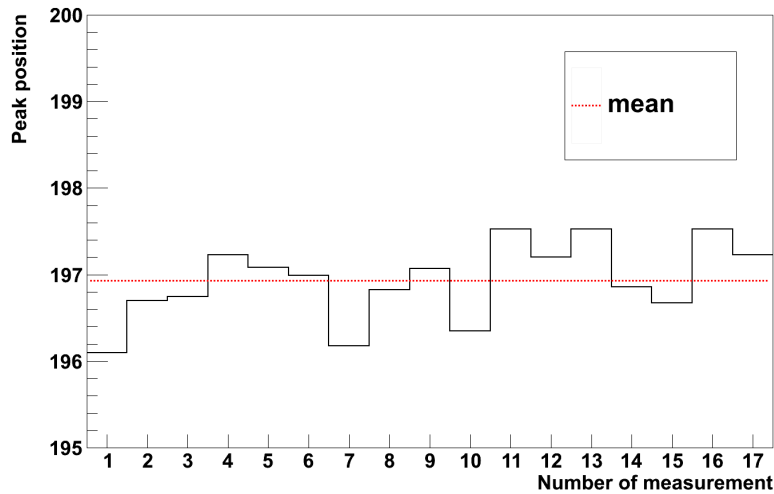


Figure 3.10: The position of the 973 keV peak of the ^{207}Bi source. Out of the 22 measurements taken, 17 were used to produce this plot. The others were recorded directly after a long irradiation, suffering from high background due to the activated surrounding. The fitted position of the peak is stable over the depicted range, which covers the whole beam-time beginning at the first day with measurement number one and ending with measurement number 17, which represents the last Bi measurement taken at the final day of the beam-time.

For this purpose, the main measurements at the reactor site are checked for the behaviour of the μ -peak, as they are in chronological order:

- The background measurement of the experimental hall without beam, taken directly before the thermal beam was turned on⁵⁰,
- the thermal measurements without target (WOT), with Pb and with U foils,
- the fast measurements without target, with lead and with uranium foils,
- the background measurement of the experimental hall without beam, taken a day after the fast beam was finally turned off.

The data just mentioned is plotted in fig. (3.11) in the relevant energy range, beginning at 8.5 MeV. The muon peak is widely broadened, as the particles can have a variety of incoming angles and therefore different track lengths in the plastic scintillator. The peak can be fitted by a Gaussian although it is not expected to have exactly Gaussian shape. This fit is not used for any energy calibration nor for the dead-time analysis, but it can act as rough cross check for both.

⁵⁰The measurements of the background without beam are labelled as *thermal* and *fast* although the beam was off. This helps to assign these measurements in time, as more than a week passed between these two blank measurements.

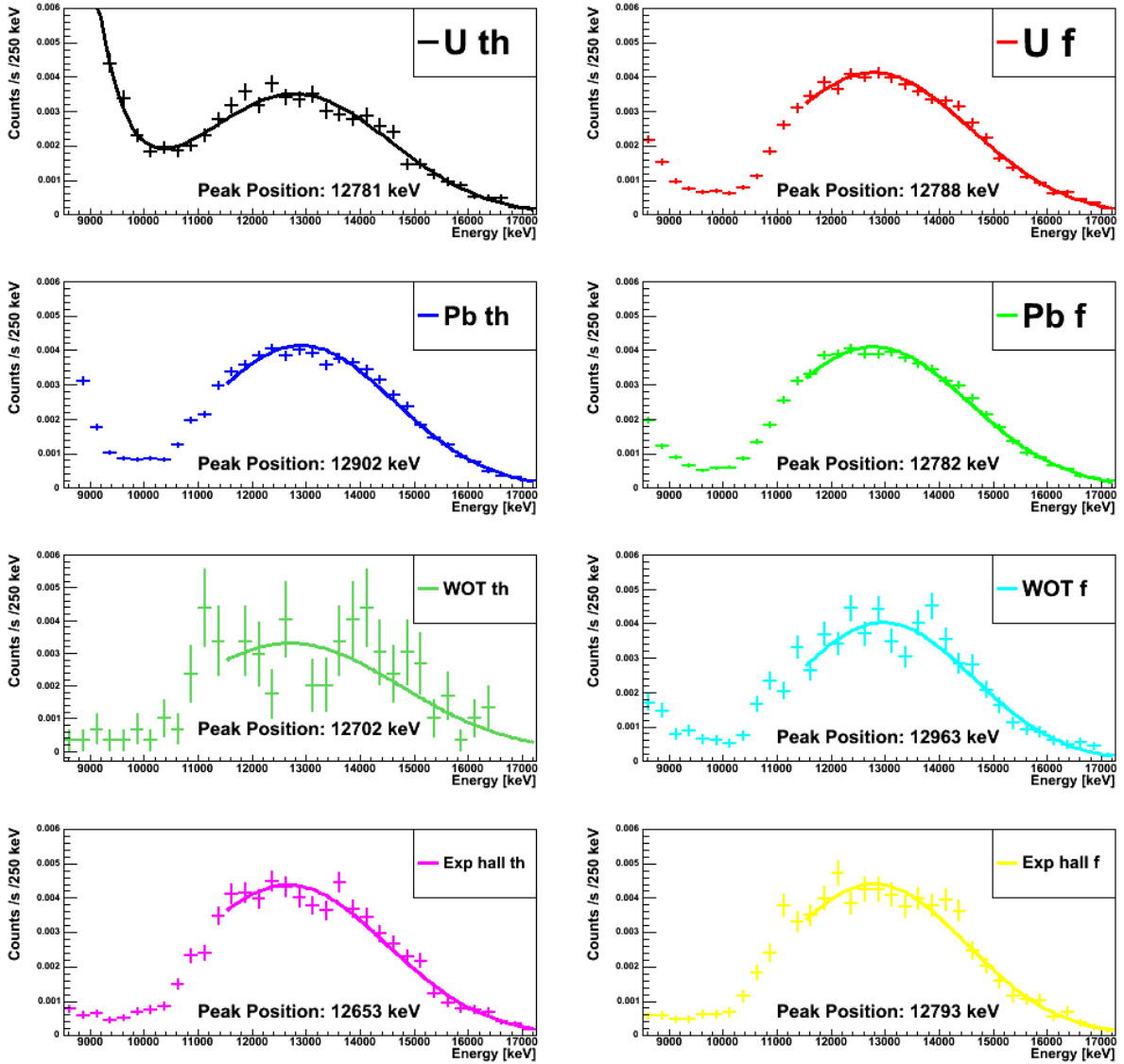


Figure 3.11: *The muon peaks of the main measurements. These provide a handle to cross-check the stability of the energy calibration and are used as an in-situ measure of the dead-time. "th" denotes the thermal measurement, whereas "f" is used for the data sets recorded with the fast neutron beam. Furthermore, "WOT" stands for the measurement without target and in the measurements labelled "Exp hall" the beam was offline, only measuring the background in the experimental hall (Although the beam was offline in the Exp hall-measurements, they are labelled as "th" and "f" to indicate their chronological order, see text).*

Left of the peak originating from muons, one sees the falling tail of the background and fission spectra. A Gaussian is fitted to the μ -peak in the marked range to estimate the peak position. In case of Uth an exponential contribution is added to account for the higher event rate at lower energies. See the text for a more detailed interpretation and analysis.

As one can see, at the low energy edge the background and fission events do not reach up to the muon peak. To be sure that there is no remaining influence on the spectra, all peaks are fitted from 11.5 MeV on, as indicated by the drawn curve. Only for the thermal neutron beam uranium measurement, in which the event rate is approximately one order of magnitude higher than for the fast beam uranium measurement, an additional exponential was taken into account in the fit⁵¹. The position of the peak is given in the figure, indicating that for all measurements performed in the beam-time the muon peak is not shifting in energy. There is only a minor statistical fluctuation in the order of one to two percent due to the fit. As the peaks are not expected to be Gaussian, the description via the ‘*peak position*’ of the Gaussian is quite inaccurate. Thus it is not used for energy calibration, but the stability of its position in energy nicely proves the stability of detector performance. The integral of the fitted Gaussian from ~ 9 MeV to ~ 18 MeV can serve as an estimate for the total muon rate in the experiment. Even although the Gaussian does not exactly reproduces the spectral shape of the peak, the integral results in the correct order of magnitude and affirms the explanation of this peak to be caused by muons. For example, the integration yields a muon rate of 0.056 Hz for the fast uranium measurement, which is equivalent to about $37 \frac{\text{Hz}}{\text{m}^2}$. This value is consistent with the expected muon flux at the reactor site⁵².

The peak additionally serves as a measure for the dead-time of the experiment. As no significant changes in the muon flux are expected over the beam-time⁵³, the area of the peaks have to be identical for every measurement. This gives an *in-situ* possibility to compare the dead-time of the single measurements without the need to rely on the ADC determination of the live time⁵⁴, and automatically corrects for all effects changing the efficiency of the system between and even during the measurements.

The integral of the spectrum from 11.5 MeV to 18.0 MeV is calculated for every measurement. This is not done by integration of the fit function, but by directly summing up the bin contents. By a comparison to the fast uranium measurement, one can normalise all spectra to the same live time. Table (3.3) compares the determined rates of the mentioned measurements to the rate obtained with the uranium target in the fast neutron beam. One can see that all data taken with the neutron beam online show, within the error bars, the same muon rate. The only exception is the thermal beam measurement, which shows

⁵¹In fact, the parameters of the Gaussian part of the fit to the *Uth* data do not change when neglecting the exponential and restricting the fit to the same range as for the others.

⁵²The total muon flux at the underground laboratory of the TUM in Garching was determined by [Bur12] to be $77 \frac{\text{Hz}}{\text{m}^2}$ inside and $200 \frac{\text{Hz}}{\text{m}^2}$ outside of the lab. This laboratory has a shielding of about 10 mwe and is located directly next to FRMII. The shielding at the experimental site inside the reactor building is not exactly known and also the efficiency and dead-time of the setup is not taken into account so far, but the correct order of magnitude confirms the interpretation of the peak to be originating from cosmic muons.

⁵³Several groups and collaborations in neutrino physics are concerned with the muon flux, as muons are responsible for many background contributions. Thus, the change of the muon intensity with time and weather conditions has been thoroughly investigated [Bel12]. No sun flares or severe weather conditions were present during the beam-time and especially at the date of the thermal uranium measurement.

⁵⁴In fact, the ADC does not quote its own live time correctly. This effect has been corrected for and is discussed in appendix (C).

Measurement	$R_\mu / R_{\mu,Uf}$
U th	0.855 ± 0.019
Pb th	1.007 ± 0.014
Pb f	0.985 ± 0.013
WOT th	1.006 ± 0.078
WOT f	0.975 ± 0.026
Exp hall th	1.051 ± 0.022
Exp hall f	1.041 ± 0.025

Table 3.3: *The total area of the muon peak integrated from 11.5 MeV to 18 MeV and normalised to the peak area in the fast uranium measurement. Abbreviations are the same as in fig. (3.11). The data is already normalised to the lifetime determined by the ADCs including the corrections described in appendix (C). The two data sets recorded without beam have a very low overall count rate and hence have the lowest detector dead-time. This results in a slightly higher efficiency seen as an enhanced muon peak. Except for the thermal uranium measurement, all recordings with neutron beam show the same rate within the error bars. The event rate with uranium target in the thermal beam is about a factor of ten higher than in the other data sets and therefore leads to a dead-time for which one must correct.*

only $85.5 \pm 2\%$ of this flux. This is a direct consequence of the high count rate in this measurement that exceeds that of the fast uranium measurement above threshold by a factor of 10, leading to enhanced dead-time. This measurement therefore has to be corrected by the normalisation factor determined. As this has an immediate influence on the absolute normalisation of the final ^{238}U spectrum, chapter (C) in the appendix is dedicated to cross-checks of the electronics, proving their linearity also at high count rates.

3.5 Remarks on radioactive equilibrium

As nuclei with different lifetimes reach radioactive equilibrium at different times, the total spectrum of the fission products is expected to evolve during the irradiation. Hence, the influence of the limited beam-time on the data has to be investigated. For this purpose, one can use the list mode, as described in sec. (3.1), to split the recorded data into user-defined time bins. This allows to follow the evolution of the spectrum through time and hence to investigate the time dependence of the different energy regimes.

In fig. (3.12) the bin-wise ratios of the spectra of the thermal uranium measurement at different times are given. No background subtraction is done yet, but in the lower energy range the signal to background ratio is around 10, as discussed later in sec. (4.2), and thus it does not smooth the ratio much. This low energy regime is affected by off-equilibrium effects the most, as the long-lived nuclei contribute mainly to lower beta energies.

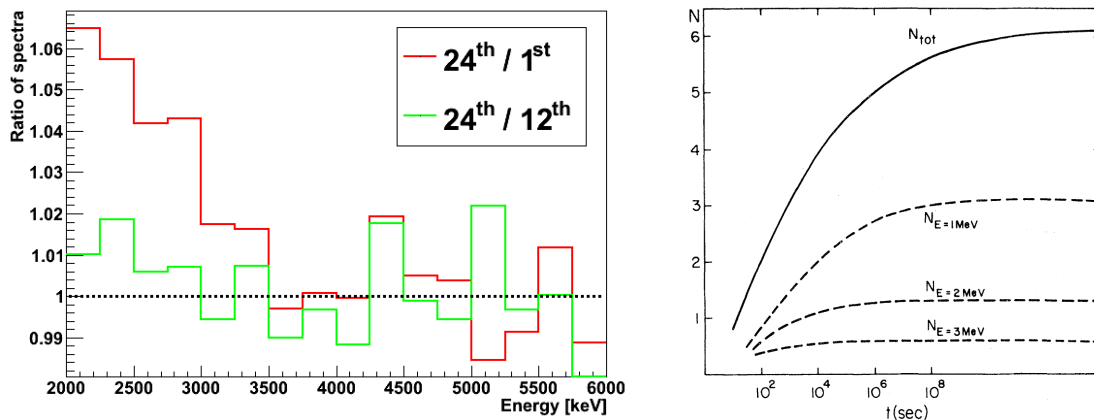


Figure 3.12: *Left:* The thermal uranium measurement is divided into two-hour long data sets. The plot compares the spectrum of the first two hours (marked as 1st), the spectrum from hours 12 & 13 (12th) and the end of the measurement from hours 24 & 25 after irradiation started. At the low energy side - equivalent to longer lifetimes of the decaying isotopes - the spectrum rises with time, indicating that the long-lived nuclei are not in radioactive equilibrium in the first hours. After 12 hours, this effect vanishes; in the experiment only data after this time is used for the analysis.

Right: Exposure time-dependence of the number of electrons per fission at different energies as calculated in [Vog81] for ^{235}U . Plot reprinted with permission from [Vog81]. One recognises that for energies above 2 MeV and irradiation times of more than $\sim 10^5$ s the spectrum does not change any more.

3.5. REMARKS ON RADIOACTIVE EQUILIBRIUM

Energy [MeV]	2.00	2.25	2.50	2.75	3.00
$\frac{N_{\beta;450 d} - N_{\beta;12 h}}{N_{\beta;450 d}}$ [%]	1.7	1.6	0.9	0.4	0

Table 3.4: *The relative difference of the fission beta spectrum of ^{238}U after 12 hours and 450 days of irradiation time for different energies. One can see, for energies between 2 and 3 MeV the effect of off-equilibrium is smaller than 2 percent. Data taken from calculations of [Mue11].*

The plot depicts the evolution of the spectrum with rising irradiation time of the uranium target in the thermal beam by binning the data set in bins of two hours length and comparing the spectrum at different periods. One can roughly split the spectrum in two energy regimes that nicely show the behaviour of the spectrum in time. The data set of the end of the irradiation shows an enhancement at the low energy part which is directly connected to the fact that early during irradiation the long-lived isotopes are not in radioactive equilibrium and hence their contribution is still growing. Contrariwise, at the high energy part of the spectrum the ratio equals 1, indicating that even after two hours the spectrum above 3.5 MeV has fully developed.

One can additionally see in the plot that after 12 hours⁵⁵ the full spectrum equals the one after 24 hours within statistical errors. Only at the very low energy bins a small variation of about one percent seems to be present, but no correction was inserted in the data analysis.

This behaviour is also discussed in [Vog81] and [Mue11]. In the first paper, the calculation of the fission spectrum of ^{235}U is discussed and the influence of off-equilibrium effects is shortly mentioned. It is stated therein that for time scales between 10^4 - 10^5 seconds the spectrum above 2-3 MeV reaches equilibrium. This paper provides a plot which helps to estimate the evolution at different energies (see fig. 3.12) which is in good agreement with the analysis presented above. The authors of [Mue11] also calculate fission spectra and give the spectrum of ^{238}U for 12 hours of irradiation time and for 450 days - being equivalent to radioactive equilibrium on any energy scale relevant for neutrino physics. Herein the difference between the spectra at these two time bins is predicted to be smaller than 2 percent for 2 MeV. The values obtained by their group are presented in table (3.4).

Concluding the discussion on the radioactive equilibrium, the effect of the evolution of the spectrum is significant in the first hours. Discarding the first half day of data taking is enough to minimise any dependence on time. After ~ 11 h, only the region close to the experimental threshold of 2.25 MeV is changing with ongoing irradiation, but this effect is of the order of about 1 percent. Consequently, using only data recorded after 11 h of irradiation, the spectrum presented in the present thesis can be taken as good approximation to the spectrum in radioactive equilibrium.

⁵⁵In this experiment, the data from the first approximately 11 h was not used for data analysis.

Chapter 4

Data analysis II: The analysis chain

In the previous sections, the energy calibration, the performance and the stability of the detector have been discussed. In the following, the focus will be on the data taken during the weeks of beam-time and will explain the operations to extract the background-free and normalised β -spectrum of the fission products of ^{238}U from the data. The analysis chain is illustrated in figure (4.1) and a brief summary is given in the list below.

- The *accidental background* is described and subtracted in the course of section (4.1). In addition, the term *β -decay-correlated background* is introduced, but it will be shown that this event class does not have an effect on the spectrum.
- The main background handling to extract the beta spectrum of the fission products from the raw data is given in sec. (4.2). Herein, background stemming from gammas and electrons present in the neutron beam and effects of scattered neutrons that induce background are described. The subtraction of this *beam-correlated background* automatically includes beam-independent events such as induced by cosmic muons.
- At this moment, the background-free spectra of the fission products of natural uranium in the thermal and the fast neutron beam are obtained. The spectrum from the thermal neutron irradiation is the spectrum from ^{235}U whereas the data recorded with the fast beam has to be cleaned from the contribution of ^{235}U to get a pure ^{238}U sample (sec. 4.3). The wave \sim in figure (4.1) is a mark that the spectra are still to be normalised, see next point.
- A comparison of the ^{235}U spectrum measured in the thermal beam with a ^{235}U spectrum recorded at high precision at the ILL [Sch81, Sch85] provides, on the one hand, an absolute normalisation of the ^{235}U spectrum and, on the other hand, corrects for possibly existing energy-dependent efficiency variations (sec. 4.4). A normalisation function can be extracted from this comparison that corrects for effects not accounted for in the response function. Furthermore, it converts the experiment-unique scale of $\frac{\text{betas}}{\text{s}\cdot\text{bin}}$ into the universal scale of $\frac{\text{betas}}{\text{fission}\cdot\text{MeV}}$. This procedure also minimises systematic errors, as no knowledge of the beam intensity, the beam profile, the neutron fission

cross sections, and - as a combination of the former points - the fission rates in the uranium foils is required. The normalisation function determined is then applied to the ^{238}U spectrum.

- Afterwards, an absolute normalisation of the ^{238}U spectrum is performed. As the ^{235}U spectrum is already normalised to the BILL spectrum, this reduces to a determination of the relative amount of fissions of ^{238}U in the fast beam and ^{235}U in the thermal beam. This is done by γ -spectroscopy on the irradiated targets. It is discussed in sec. (4.5).
- Finally, the β -spectrum is converted into the antineutrino spectrum (sec. 5.3), resulting in the antineutrino spectrum of the fission product of ^{238}U .

4.1 Accidental coincidences and β - decay - correlated background

Events in the multi-wire chamber and the photomultiplier are considered to be coincident if the time difference between the two triggers is less than $2.5\ \mu\text{s}$. Two physically independent events - one in the MWC and one in the scintillator - may by chance fulfil this coincidence condition. For example, an electron from an ^{28}Al decay⁵⁶ triggers the MWC without hitting the scintillator⁵⁷ and some random particle from (n,X) reactions, radioactive decays or from the scattered beam deposits its energy in the scintillator. In the course of this thesis, these events are referred to as *accidentals*. The term implies that there is no physically coincident event occurring at the same time.

The rate of the accidentals can be determined by shifting the coincidence window by a few tens of microseconds, directly measuring the rate and spectral shape of this kind of background. However, while the rate can be determined precisely even after a short time of data taking, an accurate spectral shape information is only obtained after a long measuring time. One can benefit from the fact that the spectral shape of the accidentals is the same as the spectrum of a measurement in anti-coincidence, which has a much higher count rate as there is no timing window limiting the effective lifetime of the measurement. Thus, the anti-coincidence measurement can be scaled using the count rate of the off-window data set to get the accidental spectrum.

In the data set with the highest rate, namely the irradiation of the uranium target in the thermal beam, the rate of accidentals was measured to be 2 Hz being around 0.6 % of the total coincident count rate. As the rates in all other measurements are about a factor of 10 lower, the contribution of the accidentals to these is even smaller. Nevertheless, every spectrum was corrected for accidentals.

⁵⁶The isotope ^{28}Al is produced by neutron capture on the Al parts of the detector surrounding.

⁵⁷Events with the electron triggering both detectors are treated within sec. (4.2).

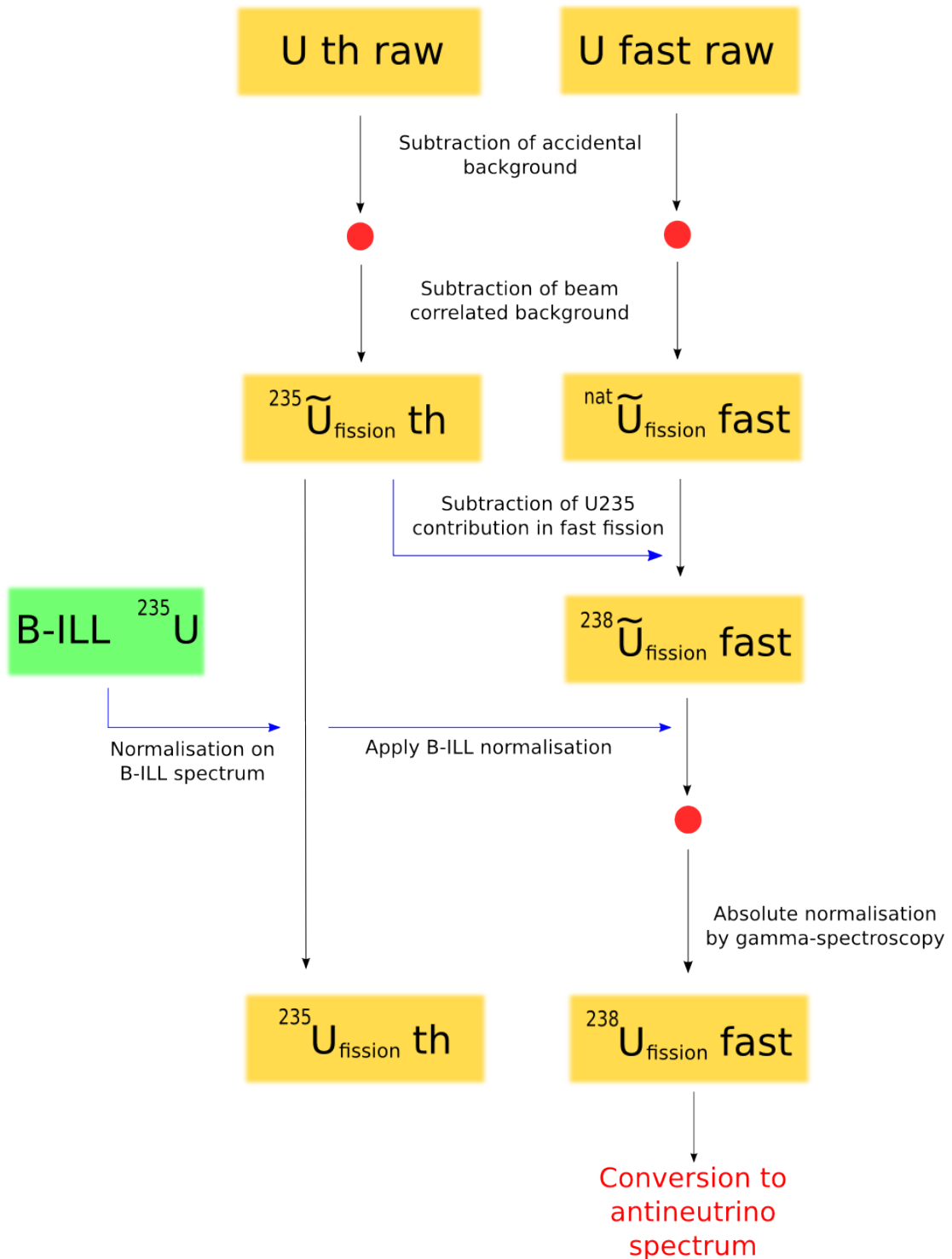


Figure 4.1: The analysis chain, illustrating the operations performed to extract the $\bar{\nu}_e$ -spectrum of the fission products of ^{238}U from the raw data. For a detailed description, see the list in the text.

Secondly, there is a contribution to the background caused by so-called β -decay-correlated background. This means, an electron from the beta decay in the target foils triggers the MWC and the PM channel⁵⁸, but the energy deposition in the scintillator is the sum of the signal of this electron and the energy deposition of a simultaneously incoming gamma emitted by the daughter nucleus. The impact of these decay-correlated events can not be measured by shifting the coincidence window, but has to be estimated. Under the assumption that there is no angular correlation between the electron and the gamma from the same beta decay⁵⁹, one can estimate the order of magnitude of this background. In the estimation it is assumed that a beta decay is directly followed by two gammas, which can be considered to be emitted at the same time as the electron. Because the emission of these gammas occurs on a time-scale in the picoseconds regime and the photomultiplier has a time spread of the order of nanoseconds, this is a valid approximation. In [Mai58], measurements of the gamma radiation associated with fission of ^{235}U are presented. As an approximation of this work, the gamma spectra given are smoothed to a single exponential of the type $e^{-\lambda E}$ with $\lambda = 1$ and E being the energy of the γ . To check for the consequence of possible systematic uncertainties in this rough spectral estimation, the following analysis is also performed with $\lambda = 2$ and with $\lambda = 0.5$, the latter highly overestimating the high energetic parts of the gamma spectrum. A simulation⁶⁰ randomly picks an electron following the spectral distribution from the uranium fission, which in this case was taken from calculations [Mue11]. This electron is emitted together with two gammas, which are also chosen randomly from the exponential distribution. For this estimation, the same gamma spectrum is taken for both the ^{235}U and the ^{238}U spectrum. The detection efficiency including the solid angle of the detector seen from the target foil and the probability to interact inside the scintillator is about 3 percent at gamma energies of 100 keV and less than 1.5 percent at energies above 1 MeV. Fig. (4.2) shows the influence of these decay-correlated events on the ^{238}U beta spectrum.

One can see a slight distortion of the input spectrum in the energy regime between 2 and 7 MeV with a similar behaviour for ^{235}U and ^{238}U . However, one has to remember that this distortion of the spectrum is not fully transported to the final ^{238}U spectrum. As mentioned before, the final spectrum of ^{238}U will be achieved by applying a normalisation function to the measured data, which is obtained by a normalisation of the measured ^{235}U to the BILL data (see sec. 4.4). The influence of these correlated background events is largely absorbed in the normalisation factor for ^{235}U . To check for the distortion in the final predicted ^{238}U spectrum, only the difference of the background to the beta spectra of ^{235}U and ^{238}U is of importance.

⁵⁸Due to the geometry of MWC and scintillator every electron coming from the target and triggering the MWC also hits the scintillator and deposits at least part of its kinetic energy. Simulations show that the contribution of electrons from the target passing the MWC but not depositing energy in the scintillator is below the 10^{-3} regime.

⁵⁹In fact, for allowed beta decays one does not expect any angular correlation [Fal50].

⁶⁰The simulation is the same as the one in use for the determination of the response function (sec. 3.2) and is described in sec. (2.8).

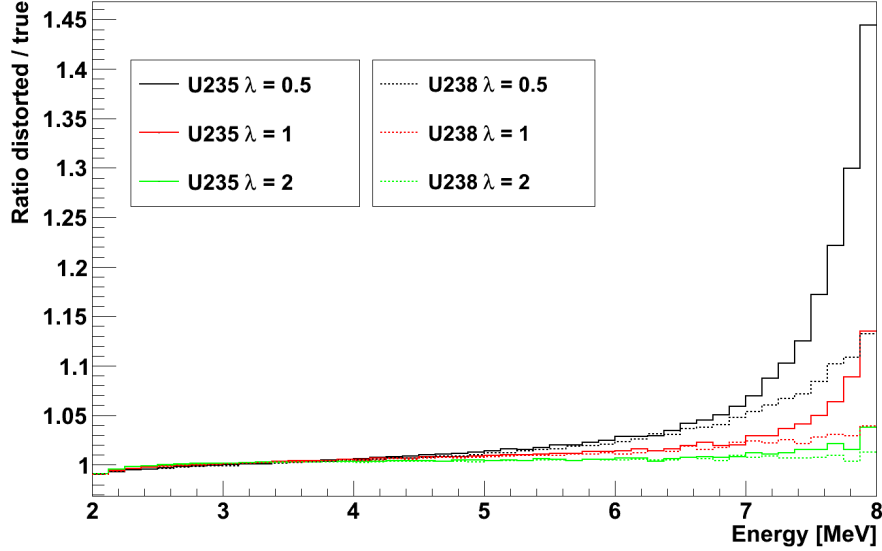


Figure 4.2: *Ratio between the distorted and the original uranium beta spectra. The distortion is caused by gammas from the beta decays of the fission products detected in the scintillator coincidentally to the electron. Up to ≈ 7 MeV the influence of this distortion is small and is nearly the same for ^{235}U and ^{238}U . λ denotes the constant in the exponential description of the input gamma spectrum. See also fig. (4.3).*

Thus, one has to investigate the change in the final spectrum after normalisation to ^{235}U . Fig. (4.3) shows the effective impact of these β -decay-correlated background by plotting the ratio of the final spectrum when simulating without correcting for correlated background divided by the true spectrum. Even for the worst case scenario with an over-estimated gamma intensity at high energies ($\lambda = 0.5$), the ratio is 1 over the whole energy range given in the final result (up to ~ 7 MeV).

Concluding the analysis of the decay-correlated background, one can state that there is no significant effect on the final prediction of the ^{238}U spectrum up to ≈ 7 MeV. Above this value, the estimation performed here is not accurate enough and especially the input gamma spectrum has to be investigated more thoroughly⁶¹. The final beta spectrum gained in this work will be shown to have an statistical error exceeding 20 percent at these high energies and thus will have an upper limit of 7 MeV. Hence, in this measurement the additional energy deposition due to gammas from the beta decays does not play any role.

Consequently, neither the influence of the accidental background nor the decay-correlated gammas disturb the measurement of the uranium β -decay.

⁶¹Furthermore, the method does not take into account the beta endpoint distribution of the fission daughters; in the simulation every gamma energy is allowed to add to any electron energy.

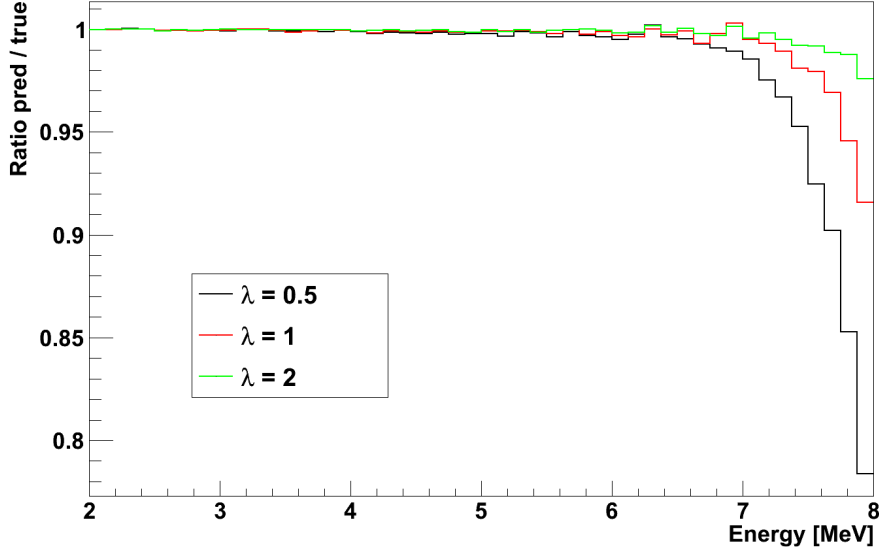


Figure 4.3: Ratio between the ^{238}U beta spectrum, which would finally be obtained when not correcting for the estimated effect due to decay-correlated gammas, and the true ^{238}U beta spectrum. As true input spectrum the calculations [Mue11] are used. Up to $\approx 7\text{ MeV}$ there is only a negligible systematic error due to this effect.

4.2 Subtraction of beam-correlated background

In contradiction to the events discussed above, background correlated to the neutron beam dominates the detected beta spectra. The following section is dedicated to the analysis and subtraction of events that are identified to be induced by particles from the neutron beam scattered or captured in the vicinity of the detector and mimicking beta decay events.

As described in section (2.1), the beam line at the experimental site reaches to the border of the moderator tank of the reactor. Considering the fast beam, the converter plate made from uranium is introduced into the thermal neutron gas near the boundary of the inner reactor pool (filled with D_2O). The beam line directly looks at this converter plate resulting in a mixture of thermal neutrons from the moderator, fission neutrons from the converter plate⁶², gamma radiation both from the moderator and from fission in the converter and to a smaller extend also of electrons, mainly coming from γ reactions on the filters and collimators. As shown in sec. (2.1.1), the thermal neutrons from the moderator could efficiently be suppressed in the beam, leaving only background contributions due to fast neutrons, gammas and electrons:

⁶²Of course, the thermal neutrons also stem from fission, namely from the core, but the nomenclature chosen herein refers to *fission neutrons* only for neutrons from the converter plate.

- *Neutrons* may not only lead to fission in the uranium foil but may be scattered off the targets and collimators and be captured in the surrounding of the detector - including the plastic scintillator itself - leading to beta decays of unstable radioisotopes. The electrons from these beta decays may be recognised as a coincidence in both the MWC and the plastic scintillator. In addition, (n,γ) reactions lead to high energetic photons that produce electrons over the whole energy range.
- *Gammas* scatter off the entrance window of the beam line, the filters, the collimators, the housing or the target foils and may be converted into electrons that cannot be distinguished from those of the beta decays of the fission fragments. This event class can further be subdivided by a target-dependent and a target-independent part, which will contribute to the so-called diffuse background defined below.
- *Electrons* in the beam may be generated by the gammas mentioned. An additional influence due to electrons, however, is expected to stem from decays of ^{28}Al in the vicinity of the detector. With an endpoint of 2.86 MeV [Fir96a], this beta spectrum reaches up to the energy regime interesting for reactor antineutrino experiments.

The beta decays of the fission products of the fast fission of ^{238}U have to be separated from these backgrounds. As the intensity and the spectral shape of the background varies between the measurement with fast and thermal neutron beam, the analysis has to be done separately for both cases.

4.2.1 The fast neutron beam

Measurements were performed *without any target* (WOT), with the *lead dummy target* (Pb), the *nickel dummy target* (Ni) and the *uranium foil* (U). The spectra can be seen in figure (4.4) without coincidence between MWC and scintillator and in fig. (4.5) in coincidence. For nickel only data in coincidence was recorded.

The measurements without coincidence are of minor importance for the analysis of the uranium beta decay data, but are shown for completeness to qualitatively illustrate the power of background suppression of the coincidence between scintillator and MWC. In these measurements without coincidence, two peak-like structures can be seen that do not show up in the coincidence data, as only an energy deposition in the scintillator is seen. The first one is due to neutron captures on hydrogen atoms in the plastic scintillator: Neutrons that are scattered out of the beam may be captured on hydrogen atoms building deuterium and emitting 2.2 MeV of gamma radiation inside the detector material itself. Because of this, a Compton spectrum with an edge at ~ 2 MeV occurs (See also sec. 4.2.2 for a discussion of these events). At ~ 7 MeV, there is a slight excess with a faster decrease at energies above. The entrance window of the beam line is made from Al as well as most of the support structures around the detector. Neutron captures on ^{27}Al emit prompt gamma radiation up to 7.7 MeV, which interacts via Compton scattering inside the scintillator. Above these energies, the contribution from this channel is not present.

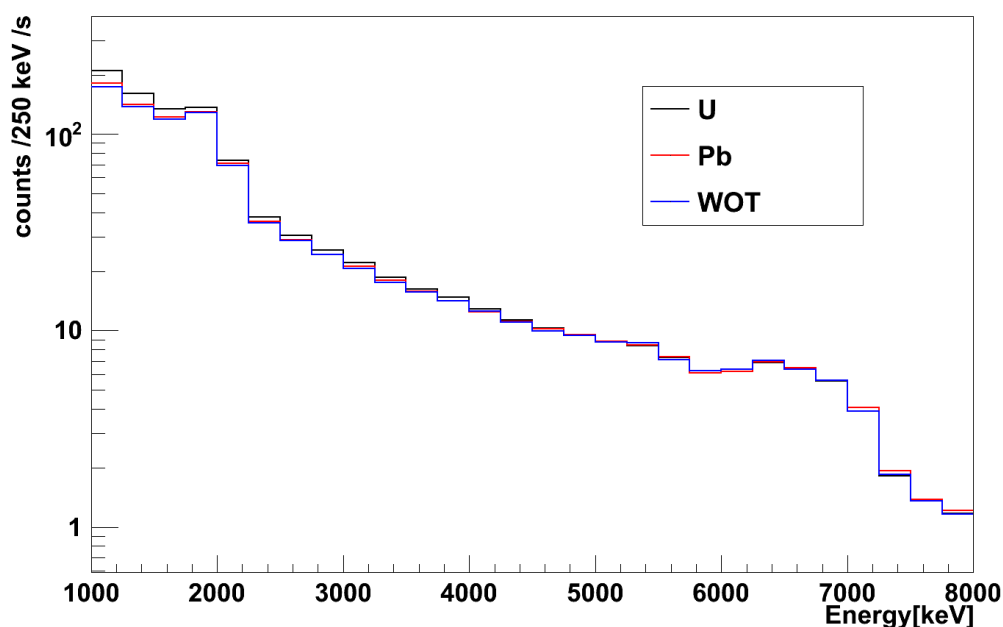


Figure 4.4: Spectra measured in the fast beam without coincidence with different targets: U (black), Pb (red), and without target (WOT, blue), on a logarithmic scale. For reasons of clarity and as no further analysis is performed on the no-coincidence data, no statistical errors are given. The two spectral features at ≈ 2 MeV and slightly above 7 MeV are due to Compton-edges of the gamma radiation emitted in the neutron capture by hydrogen in the scintillator and by aluminium in and around the whole setup, respectively.

4.2. SUBTRACTION OF BEAM-CORRELATED BACKGROUND

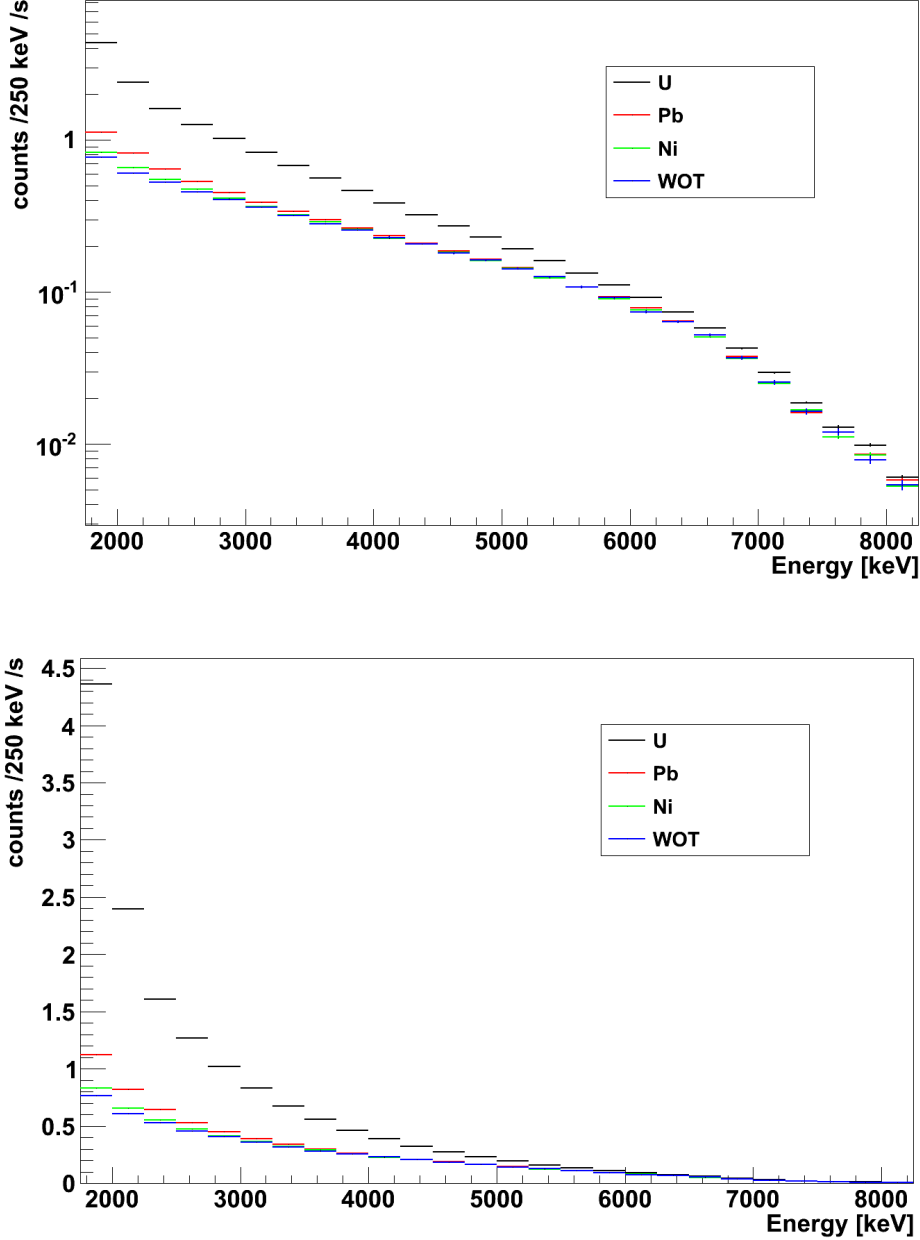


Figure 4.5: Spectra measured in the fast beam in coincidence on logarithmic scale (top) and on linear scale (bottom): U (black), Pb (red), Ni (green), and without target (blue). At energies above ≈ 4 MeV the contribution of the latter three, which are used to determine the background in the U measurement, is independent of the target. Only the statistical errors are given, which are small due to the long measurement time and the high rate; the bars in x-range mark the bin width of 250 keV. There are no remarkable spectral features in the data, especially the Compton-edges of neutron-induced gamma radiation vanished. For further interpretation of the spectra, see the text.

In the further analysis the focus lies on the data taken in coincidence:

The spectrum arising with neutron beam but without any target will in the following be referred to as *diffuse* background. This comprises every coincident event class that is independent of the target, including electrons, neutrons or gammas that are scattered (off the beam line, the collimators, the target holder or any other material around and in the setup) and converted into electrons, which eventually cross the multi-wire chamber and the scintillator. Additionally, this contains background present with the beam offline, such as natural radioactivity in the detector vicinity and events due to cosmic muons. The comparison to the dummy measurements shows that above ~ 4.5 MeV the target foils have no influence on the spectrum - except for the fission of uranium. The difference between the Pb dummy and the data without target is less than one percent, only statistically varying from zero. This reduces the further background handling in the fast beam to the low energy regime, which is a major advantage, as no systematic errors arise from the target-dependence at higher energies. As the beam-time for the diffuse events was about 8 hours long, the statistical errors are small⁶³. The diffuse background is subtracted from every measurement. The remaining spectra recorded with the Pb and Ni targets are referred to as *residual* background.

Below ~ 4 MeV, these residual spectra show differences between the nickel and the lead dummy data. Understanding the spectral shape and the ratio of the rates between these two dummies allows to draw conclusions on the background to be subtracted from the uranium measurement.

The event rate at the Pb target is slightly higher than at the Ni target, giving a hint that the main contribution to this background is due to gamma radiation scattered at the target and converted into electrons - either by photo effect, Compton scattering or pair production - and not induced by neutrons scattered and captured⁶⁴. In addition, gammas can be converted into electrons at the LiF filter in front of the target foil. The scattering of these electrons is also target-dependent.

To check for the assumption that this background is induced by gammas, a simulation has been set up starting a beam of gammas onto the three different target foils. The procedure is as follows: *If the simulation with only gammas implemented can describe the spectral shape of the background for lead and nickel after subtraction of the diffuse background, and if furthermore the correct bin-wise ratio between the spectrum at the Ni and the Pb targets is obtained, then the assumption of gammas being the dominant contribution to the background is confirmed. Additionally, the simulation is trusted to correctly calculate the background due to gamma radiation for the uranium target.*

The general setup and the main parameters of the simulation are described in section

⁶³The relative statistical error of the measurement without target is less than 2.5 percent at 7 MeV. Due to longer measuring time, for uranium this error is 1% at this energy.

⁶⁴Nickel has a higher cross section for neutron scattering than lead. In the thermal neutron beam, the background seen with the nickel target will turn out to be higher than the one in the lead and uranium data. Appendix (A) gives a calculation of the neutron scattering cross sections of the different targets.

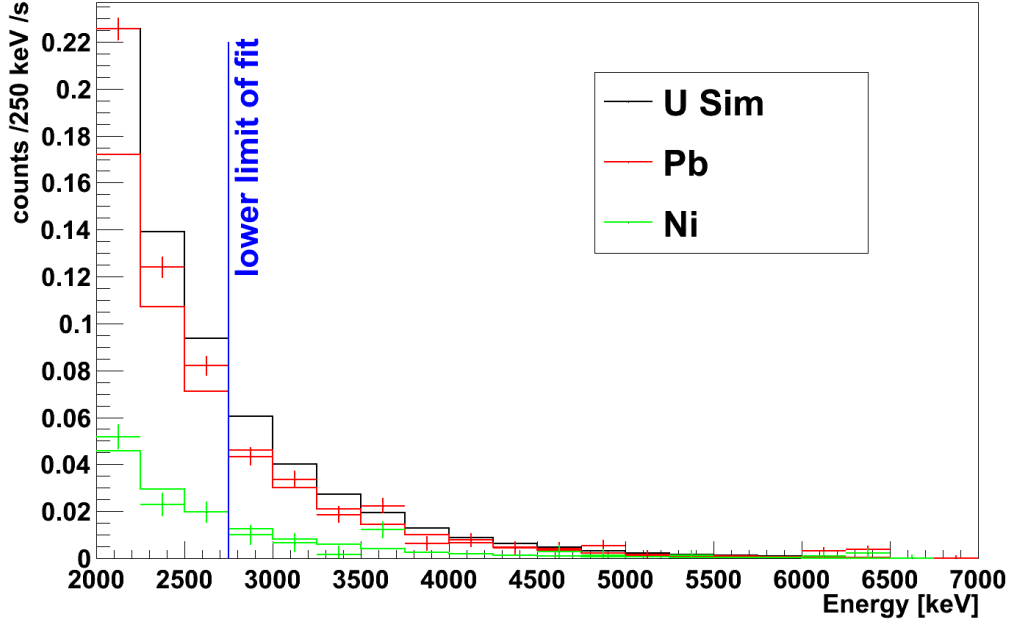


Figure 4.6: *The residual spectra (data points, the bars in x-direction illustrates the bin width, the bars in y-direction show the statistical uncertainties) with the nickel (green) and the lead (red) target after subtracting the diffuse background. The predictions from the simulation for the three different targets are plotted as lines. The only free parameter is the absolute normalisation of the simulation, which is the same for all targets. The simulation returns a correct ratio of background at the two different dummy targets, confirming the model of gammas being the dominating background. The fit to the data is only applied to the energy regime above the blue line, as below this the electrons from the beta decays of ^{28}Al are expected to add to the spectrum.*

(2.8). The spectrum used for the simulated gammas is the same as the one present in the real neutron beam as measured and calculated in [Bre07] for the same neutron filter setup at SR10 - see sec. (2.1). As there is no knowledge of the angle of beam spread, the beam is implemented to be parallel, which is a good approximation due to the variety of collimators and the length of the beam pipe.

10^8 gammas are started one by one towards the foils and for each event a trigger flag (whether or not a charged particle crosses the MWC) and the energy deposition in the scintillator is saved.

Fig. (4.6) shows the simulated data⁶⁵ in comparison to the residual background on the two dummy targets Pb and Ni. The only free parameter remaining in this model is

⁶⁵Every simulated data is always convolved with a Gaussian detector response with $\text{FWHM} = 8\% \cdot \frac{1}{\sqrt{E[\text{MeV}]}}$ to account for photon statistics in the detector module of the scintillator and the photomultiplier, see sec. (3.2).

the normalisation of the simulation. This constant normalisation factor was determined via a χ^2 analysis⁶⁶ fitting the simulation to the measured data in the energy range from 2.75 MeV to 4.5 MeV. Below 2.75 MeV, the electrons in the beam and from aluminium decays come into play (which are not considered in the simulation), and above 4.5 MeV no more significant information can be obtained due to the nearly zero background rate.

The fit to the data was done independently for the Ni and the Pb data taking the weighted average as final normalisation factor. Because of the significantly lower statistics at the Nickel target, this mean value is dominated by the lead measurement. Figure (4.7) shows the fitted χ^2 . One can find that the normalisation constants vary slightly but are consistent within the errors indicated. These errors of the best fit values are represented by the intersection of the $\frac{\chi^2}{NDF}$ parabola with the corresponding horizontal line at $y = \frac{\chi^2}{NDF} + 1$. The two values for the reduced $\chi^2_{\nu} = \frac{\chi^2}{NDF}$ are 1.28 for the Ni and 1.48 for the Pb residual. The data plotted in fig. (4.6) is normalised with the same factor, thus showing a remarkable agreement of both measurements. Hence, the simulated model correctly takes into account the different atomic structure of the targets over the whole mass range from nickel ($Z = 28$) to lead ($Z = 82$). It is therefore believed that also for uranium ($Z = 92$) the simulation supplies the correct background spectrum due to scattering and conversion of gammas from the beam. This background is subtracted from the uranium data.

The error on the normalisation factor, i.e. the error given by the χ^2 fit, is calculated to be $\approx 6\%$. As the residual background at the lead target is less than 10% of the residual uranium data⁶⁷, only a small error of less than a percent remains in the final U data. This error was taken into account being uncorrelated to the statistical errors included so far and therefore processed by quadratic error propagation.

Admittedly, this method is only applicable down to energies of about 2.75 MeV and the data in the energy regime below has to be handled in a more sophisticated way. As one can see in figure (4.6), below this energy, the simulated model cannot describe the data any more. Compared to the simulation, there is an excess of events in the lower energy bins in the data set of lead and thus there is another target-dependent source of background. Two classes of background sources may be responsible for this effect.

1) There is the possibility that neutrons are scattered off the targets into the vicinity of the scintillator module. As ^{27}Al is present in parts of the detector support structure, neutrons can be captured, resulting in the unstable isotope ^{28}Al . This would lead to additional electrons, indistinguishable from the ones from fission.

As one can see from fig. (4.6), the intensity of the additional background is not the same for the lead and the nickel dummy target. An estimation of the relative scattering rates

⁶⁶The χ^2 analysis follows the description in [Bev03] and [PDG04] for an 8-bin fit and one free fit parameter, leading to a Number of Degrees of Freedom (NDF) of 7.

⁶⁷Analogously to the Ni and Pb measurements, the term *residual uranium* data denotes the remaining events, when subtracting the diffuse background from the uranium data set. For Pb and Ni this includes mainly the background due to scattered gammas, whereas for uranium the electrons from the beta decays of the fission products survive this cut, too.

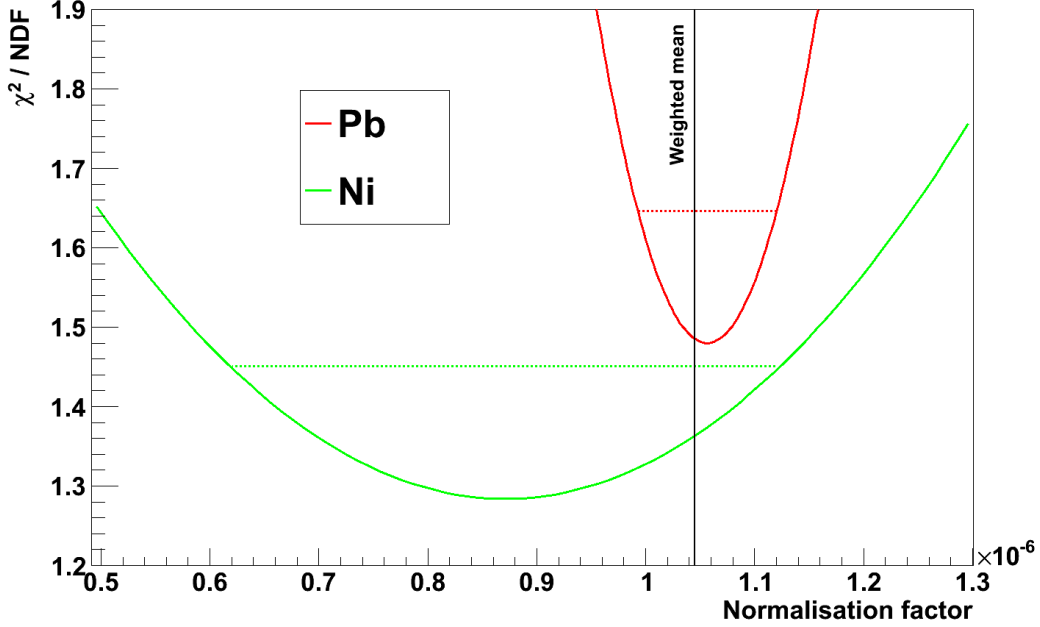


Figure 4.7: *The result of the χ^2 fit to the residual background at the lead (red) and nickel (green) targets in the fast beam. The parameter fitted is the absolute normalisation factor with which the simulation has to be scaled to match the data. Within the error bars, which are indicated by the intersection of the dotted lines with the parabolas, the two fits to the individual data sets return the same result, leading to the conclusion that the simulation models the background correctly. The weighted mean of the determined normalisation factors is used to calculate the gamma-induced background in the uranium measurement. See the text for more detailed interpretation.*

of neutrons for the different targets (performed in appendix A) yields that the number of neutrons being scattered off the lead target is only about three quarter of the one for the nickel target. As no sign of enhancement in the nickel spectrum can be seen and, on the contrary, there is a clear additional background in the lead data, the interpretation of neutron scattering being the dominant source of background can be ruled out.

2) Secondly, it is possible electrons are scattered off the target. These are mainly created in the capture of aluminium in the end-cap of the beam tube, which has a direct line-of-sight to the target-foil position. The lead target - due to its higher atomic number - has a higher scattering cross section for electrons than the nickel target, qualitatively explaining the observed effect of an increased background at the lead dummy foil. However, these electron events cannot be tagged or vetoed. Therefore, electrons appear in the beam and there is no spectral or integral information on these events, constricting a detailed analysis.

The simulation is set up to analyse these events due to scattered electrons, creating betas at the end-cap and starting them towards the target foils. The aim of this simulation is to estimate the relative amount of electrons being scattered off the different target foils and being detected in the scintillator above the threshold of 2.25 MeV (this limit will be explained in sec. 4.2.2). The spectral shape of the background present with the uranium target is then determined by the measurement of the lead dummy target and only the scaling factor is achieved by simulation.

The electrons are started with an energy distribution following the ^{28}Al beta spectrum. Thus, the region of interest does only include energies deposited in the detector between 2.25 MeV and 2.75 MeV, which corresponds to two bins in the spectrum, and these two bins are handled with the same scaling factor. The starting points of the electrons are homogeneously distributed over the part of the end-cap that is not covered by lithium tiles, as there is no knowledge of the spread of the beam and the last collimator is placed by roughly half a meter in front of the end-cap. It was tested and confirmed by changing this distribution of starting points and the direction of the starting vectors that these input parameters affect the outcome of the simulation by less than five percent. Analysing the simulation shows that the amount of detected electrons highly depends on the target foil implemented. The ratio of electrons scattered at the target and measured in the scintillator with an energy above 2 MeV is $\text{U/Pb/Ni} = 10.3 / 4.3 / 1$, meaning that about four times more electrons are scattered on the Pb target in comparison to the Ni target. The measured data cannot confirm the outcome of the simulation, as the statistics at the Ni target is too low and the electron background is compatible with zero. To implement the electron background into the uranium data, it is assumed that the simulation quotes the correct ratio of electron events in the detector. Hence, the electron background at the Pb target, which is the difference between the measured residuum and the gamma simulation, and its error are enhanced by a factor of $10.3 / 4.3 = 2.4$ and subtracted from the uranium measurement.

The contribution of these electrons is small (*sim* 1%) compared to the total uranium intensity including fission, and thus this correction enlarges the total error in the lower energy regime of the final uranium spectrum by 1-2 percent only (see fig. 4.8).

Concluding the background analysis at the fast beam, one can divide the measured data into three energy regimes:

- a) Above 4.5 MeV, the background can be considered to be target independent.
 - b) Between 2.75 - 4.5 MeV, gamma radiation from the beam adds to the background and generates a target-dependent event rate in the order of 10% of the uranium signal.
 - c) Below 2.75 MeV, electrons lead to another target-dependent contribution of the order of 1% of the uranium signal.
- The lack of knowledge of the spectral shape and the intensity of the background below 2.25 MeV limits this experiment to energies above this threshold, as explained in sec. (4.2.2).

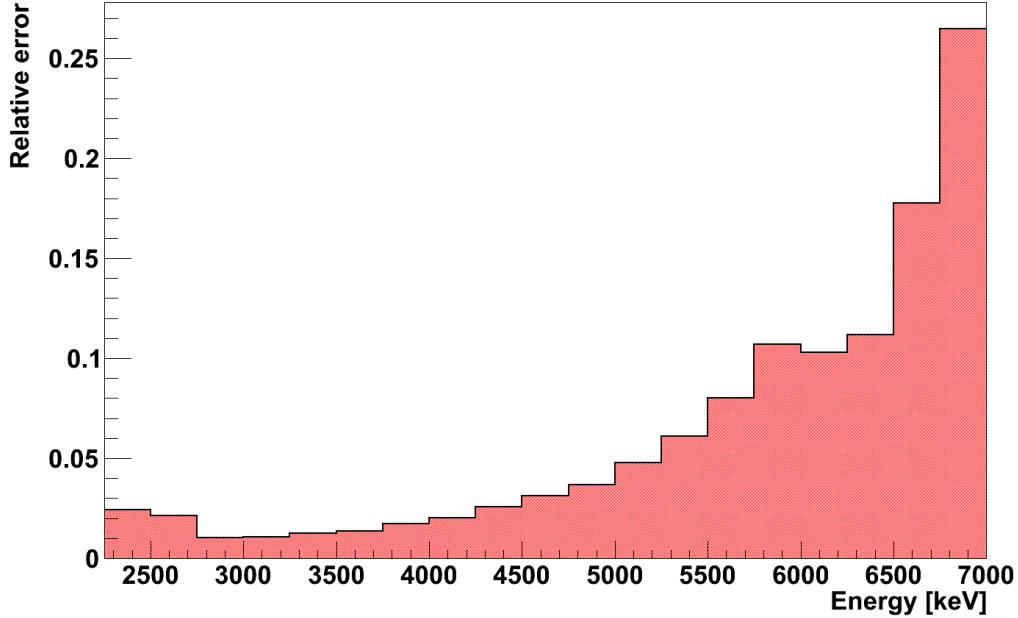


Figure 4.8: *The relative error of the fast neutron irradiated uranium data after subtracting the background induced by gammas from the beam and electrons from the decay of ^{28}Al . The first bins up to energies of 2750 keV are dominated by the uncertainty concerning contributions due to electrons. Above this energy, the error is mainly due to statistics.*

Figure (4.8) shows the relative error of the uranium β -spectrum after subtracting the discussed background. In the energy regime most interesting for neutrino oscillation experiments at reactors, the relative error is below 5 percent. From 2.25 to 6 MeV the error does not exceed 10 percent. As the resulting uranium spectrum is calculated by subtracting the diffuse background, which is significantly more intense than the uranium spectrum at higher energies, the rising relative error limits the measurement to approximately 7 MeV. A further study of the final errors of the measurement will be given later in sec. (5.1).

4.2.2 Notes on the experimental threshold

Neutrons present as diffuse gas around the detector and neutrons from the beam that are scattered off the targets can be captured on the hydrogen atoms of the plastic scintillator, producing deuterium under the emission of a 2.2 MeV gamma. In the data taken without coincidence, one can clearly see the Compton peak of the diffuse and scattered neutrons - see fig. (4.4) - indicating a very high contribution to the total spectrum. Due to the high gamma suppression of the coincidence between scintillator and multi-wire chamber, this peak vanishes in the coincidence data (fig. 4.5). Nevertheless, there is a low but finite probability for the gammas produced inside the detector material to deposit most

of their energy in the plastic scintillator and also trigger the MWC. This may be due to multi-Compton scattering with one electron leaving the scintillator or the gamma itself is finally scattered out of the detector with low energy, making it more probable to interact with the counting gas. Remember, the gamma suppression for the coincidence is given for gammas entering the detector from the target position and not for gammas produced directly in the detector. The suppression factor for these events may vary from the quoted value of $\geq 99.5\%$.

The impact of the diffuse neutrons is fully contained in the background measurement without target foil and in the neutron beam - as will be discussed in the next section and in appendix (A) - there is a way to approximate the number of neutrons scattered off the targets and scale the background spectrum by using the dummy measurements. But on one hand, it turns out that this approximation is only correct on the 10 percent scale, and on the other hand, there is another target-dependent source of neutrons, which is present only in the uranium data and thus cannot be deduced from dummy measurements. Fast fission of an uranium nuclei results in an emission of about 2.8 prompt neutrons^{68,69} [Kop03]. The number of beta decays per fission process is approximately 6 and thus one gets a neutron to electron ratio of $n/e \approx 0.47$. The prompt neutrons and the electrons from the decays can be considered to be uncorrelated in time. In [Sch81], the total beta spectrum of the fission products of ^{235}U are measured. One can extract from the published spectrum that the intensity of electrons with energies between 1.875 MeV and 2.125 MeV is about 8.5 % of the measured spectrum (which has a lower limit of 0.875 MeV). If one assumes this ratio to be approximately in the same order of magnitude for ^{238}U one can conclude that the ratio R of neutrons entering the scintillator to the number of betas entering the detector with an energy around 2 MeV is about $0.4/0.085 = 5.5$. If one takes into account also the spectrum below 0.875 MeV, which is not measured by the experiment quoted, this ratio will even be enhanced⁷⁰. Thus, one has more than five times the number of neutrons hitting the scintillator⁷¹ than electrons in the energy bin around 2 MeV. To determine the impact of these neutrons, one needs to know the probability of a neutron to be thermalized and captured in the scintillator and the probability of the emitted 2.2 MeV gamma to trigger a coincidence with nearly the full energy. It is not possible to accurately predict these parameters and even then, one would be forced to fully rely on simulations concerning the

⁶⁸The value varies for the different isotopes and also depends on the energy of the fission-inducing neutron, but for this estimation the exact value is not of importance. In addition, there is also a contribution to the neutron content due to delayed neutrons with energies of 2 MeV on average, produced by several fission daughters. This amount is in the order of 1 % and can safely be neglected for this rough estimation.

⁶⁹There is also an emission of on average 7 prompt gammas with a total energy of about 8 MeV, but due to the good gamma suppression of the setup and their mostly relatively low energies they do not have to be included in the analysis [Eme82].

⁷⁰The spectrum above the experimental threshold in [Sch81] follows an exponential. If one assumes the spectrum to follow this function for one more bin and adds only this bin to the calculation, this leads to an increase of the ratio R from 5.5 to 6.7.

⁷¹Herein, one assumes an isotropic emission of the prompt neutrons. This is correct only for energies of the fission-inducing neutrons from the beam of less than about 0.5 MeV. Above this, anisotropies occur in the angular distribution [Eme82].

spectrum of this background without the chance to cross check with data. In other cases, e.g. the neutron background spectrum in the thermal beam data (sec. 4.2.3) or the gamma background in the fast beam (sec. 4.2.1), the analytical predictions and simulations can be tested with the data from the dummy measurements, but this would not be the case here. In addition, the intensity background is not the same for the thermal and the fast beam measurement, because of the anisotropic prompt neutron emission in the fast fission, the different prompt neutron energies and the different production yields for prompt neutrons in the two beams. It is not possible to justifiably quote errors on the background below the deuterium gamma line and thus the experimental threshold is set to 2.25 MeV.⁷²

4.2.3 The thermal neutron beam

The background in the measurements with thermal neutron beam is different from the background with fast neutron beam. Figure (4.9) shows the coincident spectra recorded with the thermal beam. As the beam converter plate is removed, the sources of background reduce to gammas from the reactor core and to electrons and gammas from neutron captures. Thus, the signal to background ratio has improved and reaches 1 not before approximately 6.5 MeV (in the fast beam, this was the case at around 3.5 MeV).

In addition, also the relative contribution of the background sources to the spectra have changed. While with converter plate the diffuse background is dominant in the whole energy range, it is approximately an order of magnitude smaller than the background seen with the dummy targets in the thermal neutron beam. Furthermore, the nickel target measurement has a high coincident event rate in the detector that even exceeds the total event rate in the uranium data (including fissions) at high energies. This is a direct consequence of the thermal neutron scattering cross section of the different targets. The following paragraphs discuss the sources and the spectra of the background in more detail.

The sources of background can be split into four different classes:

- *Diffuse background*, which is defined (analogously to the fast beam) by being present without any target. This is a sub-dominant part in the thermal data set.
- *Neutron scattering* on the targets leads to the main contribution in the thermal spectra. These neutrons activate the material in the detector surrounding, leading to prompt gamma radiation and to electrons and photons from decays of the produced unstable isotopes.
- Events due to *gammas* scattered off the targets and converted into electrons play a minor role, as the gamma intensity is low.
- *Electrons* existent in the beam scattered towards the detector contribute to the lower energy regime. This contribution is assumed to be of the same order of magnitude as the gamma background.

⁷²Consequently, it is not necessary to estimate background due to neutron capture on ²³⁵U and ²³⁸U. The subsequent beta decays have Q-values significantly below the threshold [Fir96b] and the possibly occurring alpha decays do not cause background, as α particles cannot reach the scintillator.

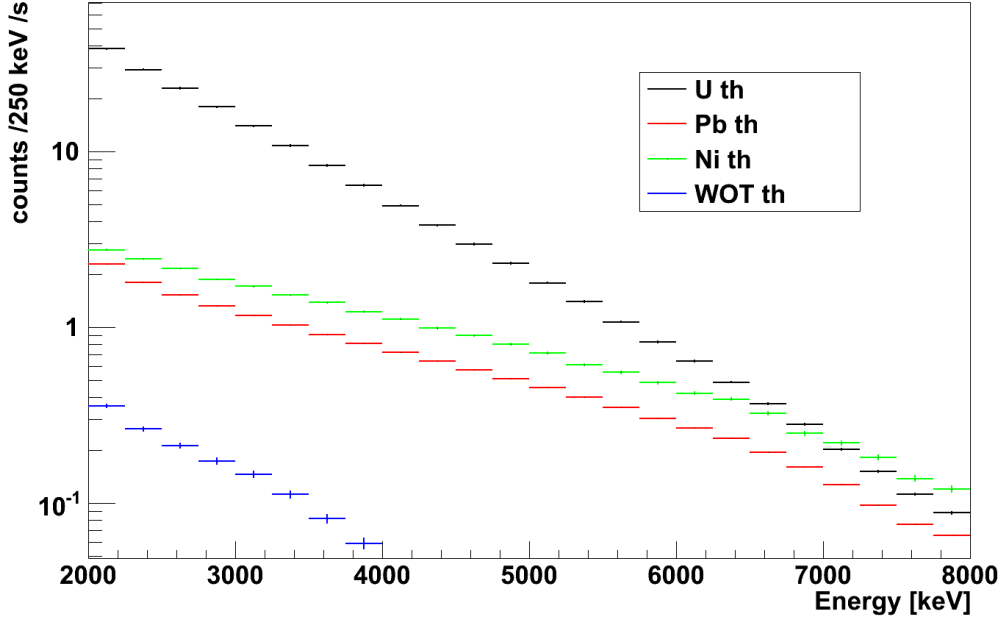


Figure 4.9: *The measured coincident spectra of uranium (black), lead (red), nickel (green) and without target (WOT, blue) in the thermal beam. The diffuse background is very small - in contrast to the fast-beam measurement. The main source of background comes from neutrons scattering off the target and the subsequent activation of the detector surrounding. Hence, the Ni dummy data shows a higher intensity compared to lead and even exceeds the spectrum of U (which includes betas from the fission daughters) at energies above ~ 7 MeV.*

At first, the diffuse background is subtracted from all spectra, as it is assumed not to change between the different measurements. Its contribution to the 3-3.5 MeV bin is about 10 percent of the intensity recorded with the lead target and decreases to only a few percent at higher energies.

The dominant part of the background can be discussed by comparing the two dummy data sets. In the planning phase of the experiment, the lead target was chosen because of its similar atomic mass compared to uranium. Thus, the background due to neutron scattering at the uranium target is expected to be more similar to the lead measurement than to the Ni measurement. Nevertheless, the Ni data helps to understand and to confirm the model used to deduce the background at the uranium foil.

The spectra in fig. (4.9) show that the difference in the background at the different targets reaches up to high energies. The mechanism responsible for this is the difference in the total scattering cross section for neutrons for the particular targets. Neutrons from the beam are scattered into the adjacency of the detector and are captured on various materials. The subsequent emission of high-energetic gammas from (n,γ) reactions and the conversion into high-energetic electrons lead to background in the detector. As this process is the

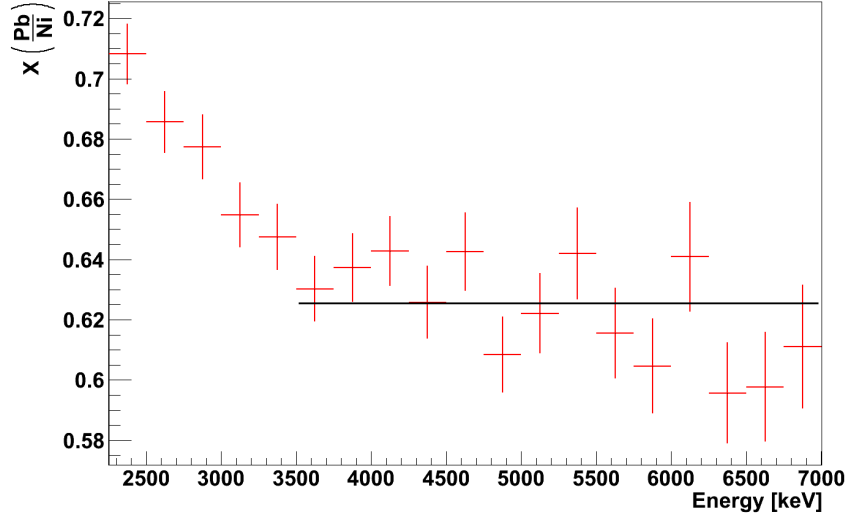


Figure 4.10: The ratio of the spectra taken with the lead and the nickel target. Above ~ 3.5 MeV the ratio is constant, showing that the spectra are the same in shape and only varying in intensity. This supports the model that the thermal neutron scattering is the main background contributing in these measurements. To lower energies the ratio increases, indicating that there are still also gammas and electrons in the beam. The error bars are purely statistical. The black line is a fit to the data performed from 3.5 to 7.0 MeV.

same for every target, the spectral shape is the same in the different measurements, whereas the intensity is coupled to the neutron scattering cross section of the individual target foils.

From the total scattering cross section of the particular foils, one can calculate the ratio of scattered neutrons at the Ni, Pb and U targets⁷³. The ratio X of scattered neutrons at the Pb and the Ni target is calculated to be $X(\frac{Pb}{Ni}) = 0.57 \pm 0.06$, whereas the number of scattered neutrons on the uranium target is comparable to that at the Pb target, resulting in a value of $X(\frac{U}{Pb}) = 0.96 \pm 0.01$. The theoretical value of $X(\frac{Pb}{Ni})$ can directly be checked by the measurements.

Figure (4.10) shows the ratio of the residual lead data to the residual nickel events. At energies above ~ 3.5 MeV the model that the background is mainly due to thermal neutrons is validated by a constant ratio. A fit to the data above 3.5 MeV concludes a ratio of $X(\frac{Pb}{Ni}) = 0.626$ being close to the theoretical prediction. The measured value can also be obtained by changing single parameters in the calculation of the ratio X. For example, a slight increase in the neutron beam width would directly increase the predicted calculation to the measured value within the quoted errors. In addition, the spots of glue to fix the foils together are not included in the model. This glue, which consists of hydrogen and carbon,

⁷³In appendix (A) one can find more information how the relative numbers of scattered thermal neutrons on the particular targets is deduced.

scatters neutrons pretty well, thus reducing the difference between the two targets.

Changing any parameter in the model does have an influence on $X(\frac{Pb}{Ni})$ on the 5-10% scale, but - due to the similar mass and cross sections of Pb and U - leaves the ratio $X(\frac{U}{Pb})$ nearly unaffected. In the energy regime above 3.5 MeV, the calculated value for $X(\frac{U}{Pb})$ is used to determine the background for the uranium target.

The rise in the ratio of the spectra below this energy, one can be explained by the contribution of gammas and electrons in the beam. These particles dominantly scatter off the lead target, as could already be shown in the discussion of the fast neutron beam measurements. Neither the gamma nor the electron spectrum is known for any of the targets, thus, there is no way to directly deduce the background for the uranium target from that one at the other two foils. Hence, one has to use an assumption to generate the background spectrum for uranium:

The fast measurements and the simulation show that the contribution of gammas and electrons to the background at the nickel target was much smaller than the one at the lead target. If one now assumes that one can neglect the influence of this type of events to the total Ni spectrum, the nickel measurement can be interpreted as clean measure of the neutron capture background. This means, the nickel spectrum would only be caused by the scattering of neutrons - even down to lower energies - and one would directly get the background of neutrons at the other two targets from that by using the determined ratios $X(\frac{Pb}{Ni})$ and $X(\frac{U}{Pb})$, respectively. The remaining background with the lead target is caused by gammas and electrons.

To visualise the impact of the error introduced by this assumption, fig. (4.11) plots the residuum to signal ratio in the energy range from 2 to 4.5 MeV. This ratio R is defined by:

$$R = \frac{N_{Pb} - X(\frac{Pb}{Ni}) \cdot N_{Ni}}{N_U - X(\frac{U}{Pb}) \cdot N_{Pb}}$$

where N_{target} ($target \in \{Ni, Pb\}$) stands for the spectra recorded in the thermal beam after subtracting the diffuse background. Hence, this ratio sets the residual background in comparison to the uranium spectrum where the neutron background has been subtracted. One can directly see from the plot that the residuum is of a negligible order of magnitude compared to the uranium spectrum and, thus, any error introduced by the analysis described is very small.

To translate the background from the Pb target to the one at the uranium target, the residuum has to be scaled by the relative cross section for gammas and electrons. As could be seen in the discussion of the fast measurements, this contribution has to be enhanced by a factor of more than 1 when transferring it from the Pb to the U data due to the strong Z dependence of the electromagnetic interaction cross sections. However, there is no possibility to distinguish between electron and gamma-induced background, hence, one does not know which scaling factor to use. According to the simulation of the gamma background, the gamma-induced part of the spectrum has to be enhanced by a factor of 1.3. The simulations with electrons show that at the uranium target there is 2.4 times the event rate than at the Pb target. As one does not know, whether the residuum is

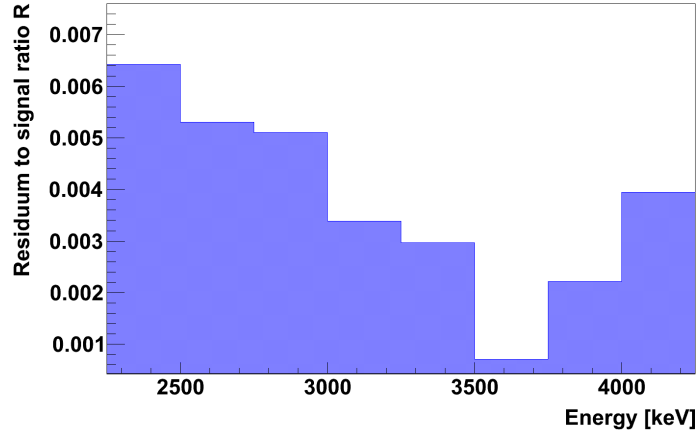


Figure 4.11: *The residuum to signal ratio in the thermal beam measurements. The residuum is defined as the remaining background on the Pb target, when subtracting the neutron capture contribution determined by the Ni measurement. The plot shows that the contribution of gamma and electron scattering in the thermal beam is on a level well below 1 % of the uranium fission signal. Therefore, every inaccuracy in the background modelling of this event class and in the scaling of this background to the uranium measurement scales with this small factor and is negligible in the final spectrum.*

consisting mainly of gamma radiation being converted at the target foils or of electrons being scattered off the foils, one has to average over both contributions.

One could choose to take the information gained from the fast neutron beam measurements and conclude that the electron contribution is only present below 3 MeV and assume the background to be gammas only above this threshold, but one has to take into account the different setup of collimators and shielding material in the thermal and fast beam. For example, in the fast beam there are lithium plates placed in the beam to get rid of any contamination of thermal neutrons. This shielding serves as additional material to convert gammas into electrons, but also shields electrons produced in the iron collimators in front of the lithium tiles. No conclusion for the ratio of electrons to gammas in the thermal beam can be drawn from that measurement.

Eventually, a scaling factor of 1.85 ± 0.55 was chosen, being the average of the scaling factors for electrons and gammas. As the contribution of this background is so small, no further investigation was performed. The error on this factor is chosen to be 0.55, conservatively covering the full range between the two individual factors. As mentioned, the error introduced by this to the final uranium spectrum is very small, as the residuum to be explained by electrons and gammas is minimal.

The final spectrum for the thermal neutron fission of the uranium target and the background considered can be seen in fig. (4.12). As already mentioned, the signal to background ratio in the thermal beam data is much better than in the fast beam. This directly

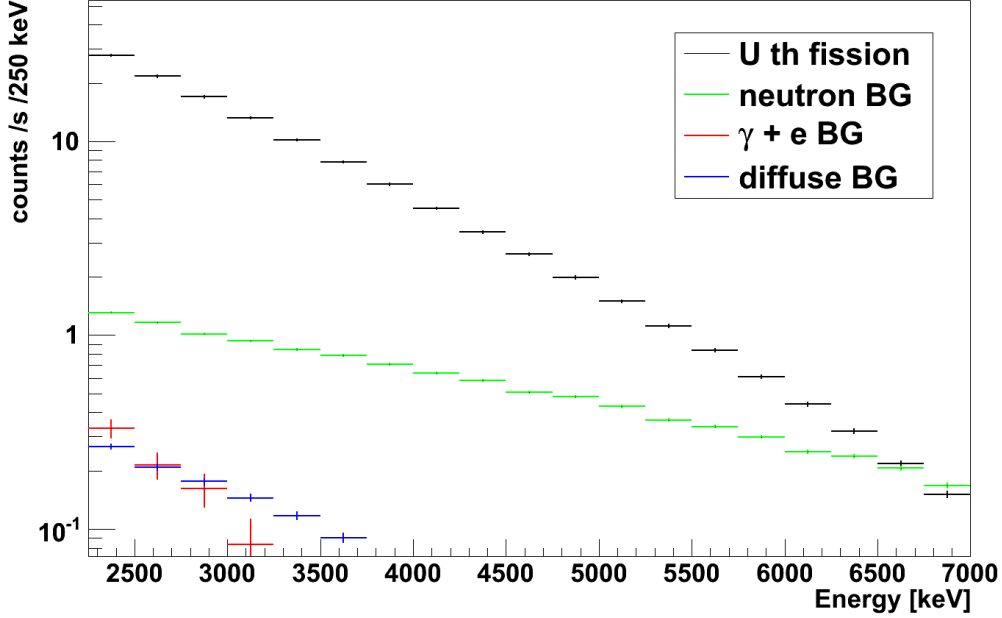


Figure 4.12: *The background and the fission spectrum of the uranium foil in the thermal neutron beam (logarithmic scale). The neutron induced background (green) is the dominating background, whereas the diffuse background (blue) and the gamma and electron contributions (red) are nearly negligible. One can further deduce a signal to background ratio of ≥ 1 up to about 6.5 MeV. This data is used in the following as the final thermal ^{235}U fission spectrum. The bars in x-direction illustrate the bin width of 250 keV.*

leads to smaller errors (as shown in fig. 4.13), as inaccuracies in the models used do not affect the final spectrum as much.

At this point, the beta spectra of the fission products of ^{235}U and ^{238}U are free of background induced by neutrons, gammas or electrons. The uranium spectrum obtained with the thermal neutron beam is the **background-free ^{235}U spectrum** and will be used for the normalisation to the BILL experiment in sec. (4.4). The uranium spectrum recorded in the fast neutron beam comprises ^{238}U fission and a small amount of fast fission on ^{235}U which still has to be removed to achieve the background-free β -spectrum of the fission products of ^{238}U .

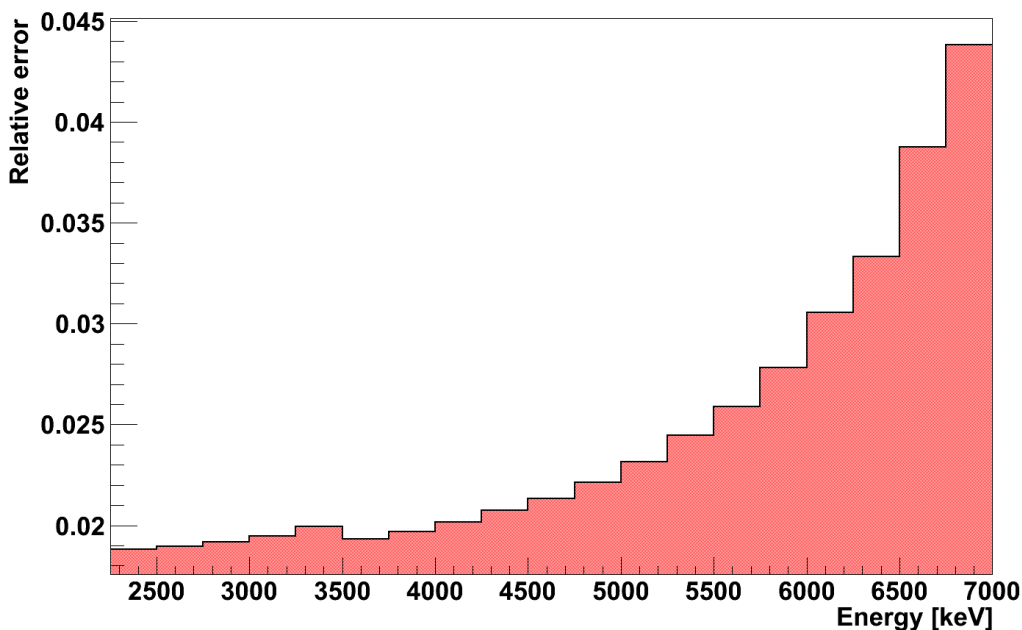


Figure 4.13: *The relative error of the beta spectrum of the fission products of ^{235}U after subtraction of the background. The errors are mainly due to statistics and are much smaller than in the case of the measurements with the fast neutron beam - see fig. (4.8).*

4.3 Subtraction of events due to fission of ^{235}U

The targets are composed of natural uranium and therefore consist to 0.7 % of ^{235}U and to 99.3 % of ^{238}U . Consequently, in the fast neutron beam not only fission of ^{238}U occurs, but also events from the ^{235}U fission have to be taken into account.

To determine the relative number of events originating from the two isotopes, one has to convolve the neutron spectrum, as determined by [Bre07] and given in section (2.1.1), with the fission cross sections. Although the natural abundance of ^{235}U is comparably small, the high fission cross section causes the ratio FR of fissioned nuclei to be

$$FR = \frac{\text{number of fissions of U235}}{\text{total number of fissions in target}} = 0.0344.$$

This means, 3.4 % of all fissions in the fast beam are due to ^{235}U and consequently a normalised spectrum from the fission of this isotope has to be subtracted.

However, knowing the relative amount of fissions does not directly allow to scale the spectra *above a given energy threshold*. As the beta spectra from the fission products of the two isotopes are not the same, they have different relative intensities in different energy regions. Hence, one has to measure either without any threshold - which is experimentally not possible - or rely on calculations of the spectra. Although it is the goal of this work

to measure the spectra without any bias from calculations, at this point one needs further input. In this context, one has to keep in mind that the use of this input does not affect the final spectrum of this measurement significantly. It applies only a higher order correction of the data measured here, as any error of the calculated spectra only affects the small amount of ^{235}U fissions in the fast beam and is thus suppressed by a factor of 0.034.

The analysis of the consulted calculations [Vog79, Vog81, Mue11] concludes that in the energy regime from 2.75 to 4.25 MeV the ratio of the integrated intensity of the beta spectra of ^{235}U to ^{238}U is 0.76. This means, for an equal number of fissions of ^{235}U and ^{238}U , the integral of the measured spectrum of ^{235}U in this energy regime would be only about $\frac{3}{4}$ of the one of ^{238}U . Thus, the spectrum of the thermal neutron measurement in the selected energy range is normalised to be $0.76 \cdot 0.034 = 2.6\%$ of the total spectrum in the fast beam. Afterwards, this normalised uranium spectrum from the thermal neutron beam measurement is subtracted from the total β -spectrum to clean the fast beam measurement from the ^{235}U content.

The normalisation factor of 0.76 is extracted from publications which assume different starting conditions than those present in the measurement. The next paragraph will show that none of these differences introduces errors big enough to affect the final value. It will also be shown, that it is valid to subtract the spectrum of the *thermal* ^{235}U measurement as background from the *fast* beam measurement, although - in general - the fission beta spectrum varies with the energy of the fission-inducing neutron.

Remarks on the normalisation of the ^{235}U content in fast neutron beam data

When comparing calculated fission beta spectra with a measurement, it is necessary to be aware of the potentially differing conditions or assumptions. For example, the **neutron spectrum** has a direct influence on the fission yields of the daughter nuclei and thus on the composition of the beta spectrum. In addition, the **time of irradiation** influences the spectrum, as the radioactive equilibrium of some isotopes may not be reached at times too short. As there is no calculation for the exact conditions present in the experiment performed herein, one has to estimate the impact of the differing starting conditions.

As reference spectra, two different calculations are reviewed:

- Vogel et al. [Vog79, Vog81] calculate the β - (and $\bar{\nu}$ -) spectra of different isotopes, including ^{235}U and ^{238}U . The spectra are given for the equilibrium state and for neutron beams with an energy of 25 meV, 0.5 MeV, and 14 MeV.
- Mueller et al. [Mue11] calculate the beta spectrum of - amongst others - ^{238}U . As this work is much more recent than the one of Vogel, more information of the isotopes contributing in the fission processes was available. In addition, the authors could use the ^{235}U data from [Sch85] to tune some of the parameters in their simulations. The fission rates of the isotopes were determined by a dedicated MCNP (Monte Carlo N-Particle) simulation and are determined for the conditions inside a nuclear reactor core. The two calculated irradiation times are 12 hours and 450 days.

The neutron spectrum All three data sets - the two calculations and the measurement described in the present thesis - use different incident neutron energies. [Vog81] provides results with different neutron energies, but they are always mono-energetic, not representing true conditions in a reactor core. [Mue11] simulates the fission yields considering the neutron spectrum inside a fuel element. And finally, this measurement directly uses the fast neutron spectrum from the fission of ^{235}U .

In addition to that, the procedure to correct for the ^{235}U contribution in the fast beam measurement is to subtract the normalised spectrum taken with the thermal beam. This assumes that the spectrum for ^{235}U in the thermal beam equals the one in the fast beam. To estimate the influence of these differing starting conditions and to legitimate the applied subtraction procedure, one can use the results of [Vog81]. From this paper, the difference between the calculated spectra for irradiation with thermal neutrons and with 0.5 MeV neutrons can be extracted. Fig. (4.14) shows the ratio of these two spectra to be very close to 1. Even at high energies the spectra differ from each other by less than 6%. Of course, in the experiment a fast neutron beam with a distinct spectrum is used and not a mono-energetic 0.5 MeV neutron beam, but this comparison can already show the smallness of the influence of the varying neutron energies on the spectrum.⁷⁴

The ratio between the beta spectra induced by neutrons with 0.5 and 14 MeV is also plotted in figure (4.14), giving an indication of the impact of higher neutron energies on the spectral shape of the final data. This shows an effect on a 20-40 percent level, but as the intensity of neutrons of 14 MeV in this experiment is approximately three orders of magnitude smaller than the one at 1 MeV, one does not have to correct for this.

In summary, the error introduced by assuming the ^{235}U spectrum to be the same in the thermal and the fast beam is only of the order of a few percent. As this correction only applies to the 3 percent of data in the fast beam that belongs to the fission of ^{235}U , the error is suppressed to be at the 10^{-3} level and can be neglected in the subsequent analysis.

The time of irradiation The fact that the paper, from which these statements are deduced, gives the spectra for radioactive equilibrium and not for the same time of irradiation as in the experiment, does not introduce a measurable error. In principle, the different duration of irradiation can directly affect the spectrum. In the experiment performed, the data taking was carried out within a limited time⁷⁵, while the data in [Vog81] was given for infinite measuring time. But as the first hours of data were discarded in the experiment, most of the short-lived isotopes have already reached radioactive equilibrium. These are responsible for the higher energy part of the spectrum and therefore one does not expect the spectrum to change much after half a day in the region above 2 MeV. The impact of this effect has already been discussed in sec. (3.5) and turned out to be small enough to neglect any error introduced by this.

⁷⁴The fast neutron beam used in this thesis (as discussed in sec. 2.1) dominantly consists of neutrons with energies up to 2 MeV.

⁷⁵The data of the first 11 hours was not used for the analysis; only the subsequent ~ 42 hours (16 h) were taken into account for the analysis of the fast (thermal) beam data.

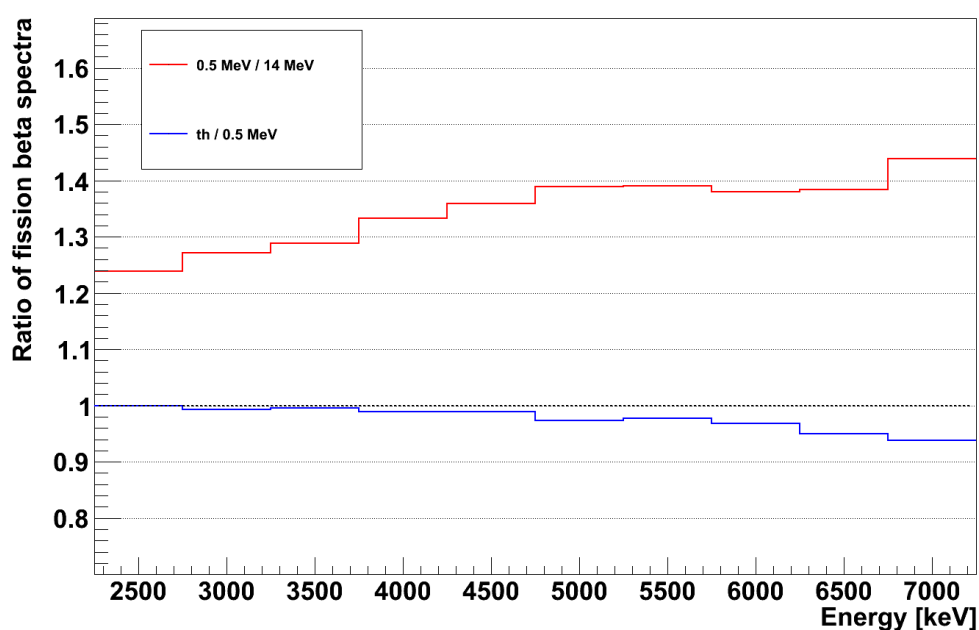


Figure 4.14: Ratios of the calculated fission spectra of ^{235}U obtained by an irradiation with neutrons of different energies (25 meV (th), 0.5 MeV and 14 MeV). One can see only small variations when changing the neutron energy from the thermal regime to 0.5 MeV (ratio 25 meV/0.5 MeV in blue). The spectrum changes more significantly when raising the incoming neutrons' energy to 14 MeV (ratio 0.5 MeV/14 MeV in red), but in the experiment these energies are suppressed by several orders of magnitude. Data taken from [Vog81].

4.3.1 The background-free beta spectrum of ^{238}U

At this point, a **background-free spectrum of ^{238}U** is obtained. Figure (4.15) presents the final ^{238}U spectrum - so far still convolved with the detector response and without absolute calibration performed - and illustrates the contributions of the discussed background sources. Even as the signal to background ratio is reaching 1 for energies of about 3.25 MeV, the statistical errors in this regime are still small, benefiting from a long measurement time and a sufficiently high count rate.

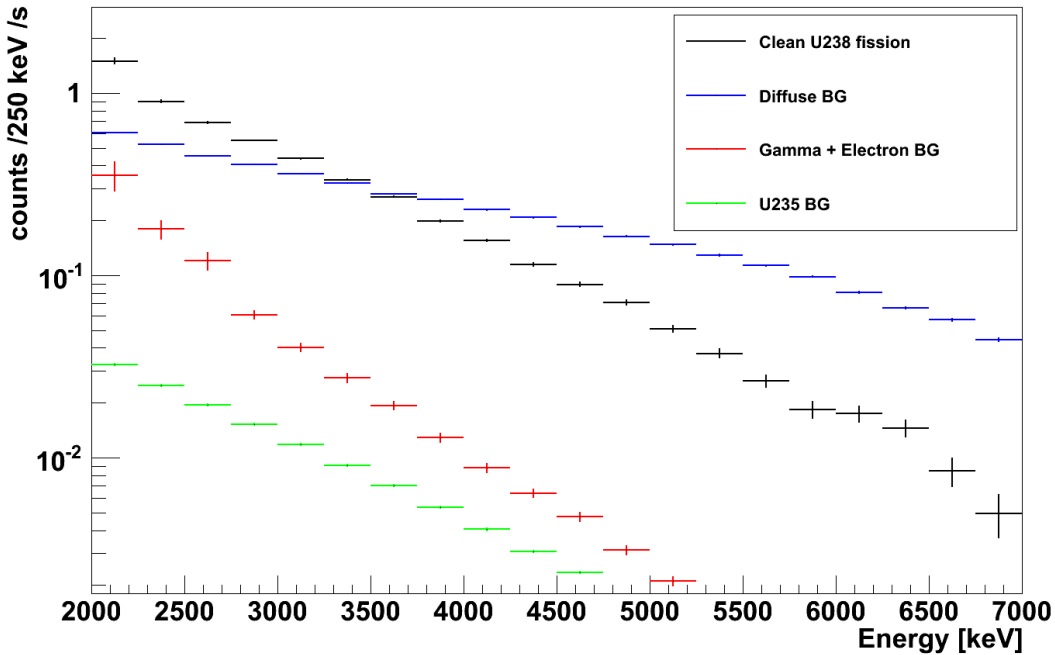


Figure 4.15: *Beta spectrum of the fission products of ^{238}U and the background considered in the analysis. At $\sim 3.5\text{ MeV}$ the signal reaches the level of the diffuse background (blue), which dominates the whole data set. Due to a long measuring time, the statistical error of this background is small. The gamma and electron background (red) is significantly contributing only up to $\sim 4\text{ MeV}$, whereas the small amount of ^{235}U fissions (green) plays a minor role at all energies. The spectrum is still convolved with the detector response function and has to be calibrated in absolute intensity. The extraction of the final spectrum will follow in sec. (4.4). The bars in x-direction illustrate the bin width of 250 keV.*

4.4 The normalisation: Comparison to the BILL spectrum

The background-free spectra of ^{235}U in the thermal beam and of ^{238}U in the fast beam are still convolved with the detector response function, as discussed in sec. (3.2). In addition, an energy-dependent normalisation may apply to the spectra due to the incompleteness of the simulation or inefficiencies in the electronics, the data acquisition, and the storing process.

This experiment is designed to compensate those effects by being calibrated via a comparison with an already known ^{235}U spectrum. For this purpose, data from the *BILL* spectrometer at the *Institut Laue-Langevin* in Grenoble was used [Sch81,Sch85]. This experiment measured the beta spectrum of the fission products of ^{235}U in a thermal neutron beam in the range from 2.0 to 9.5 MeV with an absolute precision of the rates of about 1.8% (1σ). This spectrum will be referred to as the *BILL spectrum*. Furthermore, the procedure explained in the following makes the knowledge of the fission rates in the target obsolete, greatly reducing systematic errors in the absolute normalisation, and even suppresses all errors made in the determination of the detector response function.

The BILL spectrum has to be convolved with the response function and compared to the obtained ^{235}U spectrum. This, on one hand, yields a normalisation function NF, which is defined as the bin-to-bin ratio of the spectrum determined in this work and the BILL spectrum - see equation (4.1). On the other hand, this converts the experiment-specific scale of *counts per second* into the useful scale of *betas per fission*. Afterwards, there remains only the scaling of the ^{238}U spectrum by the relative number of fissions between the two uranium targets, which will be done as a last step of the analysis chain in the subsequent sec. (4.5). While the absolute scale of NF is only relevant for this conversion of scales, the overall slope of the normalisation function describes the energy dependent efficiency correction.

This procedure can be characterized as:

$$NF = \frac{U235}{BILL \otimes resp} = \frac{U238}{U238_{true} \otimes resp} \quad (4.1)$$

with:

- NF: Bin-wise normalisation function;
- U235 and U238: Beta spectra of the fission products of the two isotopes measured in the present thesis;
- BILL: The beta spectrum of the fission products of ^{235}U measured by the BILL experiment;
- $U238_{true}$: The true β -spectrum as emitted by the fission daughters of ^{238}U ;
- resp: the response function of the detector, determined in sec. (3.2).

The normalisation function obtained is depicted in fig. (4.16). The plot gives two different normalisation functions, once for the case with and once without convolution of the BILL spectrum and response function. In general, it is necessary to take this response into account, but as will be shown later, the final ^{238}U spectrum does not change, if one neglects all influence of the response function.

While looking at the normalisation without response, one can see that the correction is largely energy dependent. When taking into account the response function, this variation diminishes to statistical variations, apart from deviations in the regime above ~ 6.5 MeV. This flatness is a prove for a good understanding of the detector and of the behaviour of the response function with energy. The rise towards higher energies may be a physical feature of the spectrum, but may also indicate a small remaining background not accounted for in the analysis and reaching up to high energies. If the potential background has a similar impact on both uranium spectra in the thermal and the fast beam, the influence of this is, due to the normalisation procedure, reduced considerably. However, the error of the final ^{238}U spectrum above 6.5 MeV is reaching 20 percent and it is assumed that any correction that would have to be applied but remains undiscovered is included in these error bars. The spectrum at 7 MeV is approximately two orders of magnitude less intense than at 3 MeV and such a background contribution would not affect the lower energy regime.

The obtained function can now be applied to the ^{238}U spectrum by solving equation (4.1) for the denominator on the right hand side, resulting in a spectrum free of any background, corrected for all influence of inefficiencies and normalised to the well-known BILL spectrum. The main drawback of this procedure is that the resulting spectrum $U238_{true} \otimes resp$ is still convolved with the detector response. A deconvolution of spectrum and response is fairly difficult and ambiguous. Because of that, a way to obtain the emitted beta spectrum would be to guess a spectrum, convolve it with the response function and compare it to this experiments data. After a set of repetitions one may find a spectrum sufficiently matching. This is laborious and, in addition, it may be of interest to be able to normalise the spectrum presented herein to another but the BILL spectrum. Hence, if anyone wanted to re-analyse or renormalise the spectra given herein, this would presume the knowledge of the full energy-dependent response function of the detector.

However, one can obtain a spectrum by assuming that the influence of the response function has no bin-to-bin correlation and is only a multiplicative object vanishing in the equation. Then, NF changes to:

$$\begin{aligned}
 NF' &= \frac{U235}{BILL \cdot resp} = \frac{U238}{U238_{true} \cdot resp} \\
 \Rightarrow NF'' &= \frac{U235}{BILL} = \frac{U238}{U238_{true}} \tag{4.2}
 \end{aligned}$$

with the same nomenclature as above. Combining the two equations (4.1) and (4.2) results in the simple relation:

$$U238_{true} \otimes resp = U238_{true} \cdot \frac{NF''}{NF} = U238_{true} \cdot \frac{BILL \otimes resp}{BILL} \tag{4.3}$$

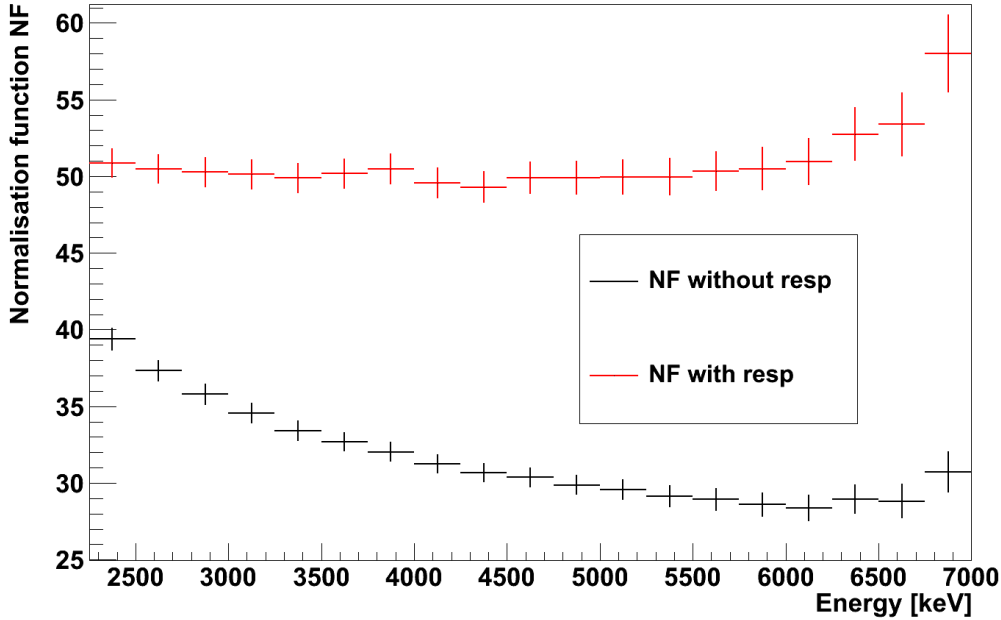


Figure 4.16: *Normalisation functions, defined as the bin-wise ratio of the ^{235}U spectrum measured in the present thesis and the BILL spectrum. The normalisation function (see also eq. 4.1) obtained by correctly taking the response function of the detector into account is given in red. This distribution is nearly flat, proving a good understanding of the detector response function. In addition, the function converts the scale of the spectrum - until now given in counts per second - into units of betas per fission. In black, the normalisation is calculated without convolving the BILL spectrum with the response function, see the text for a motivation of this procedure.*

It is remarkable that this procedure in the end yields the same ^{238}U spectrum as taking the response function correctly into account. This is based on the fact that a convolution of an exponential (the beta spectrum) with a Gaussian (the response function) is nearly the same as the original exponential. The proof of this statement will be given in sec. (5.2).

As a consequence, this thesis provides the reader with the ability to choose any other calibration spectrum (not only the BILL spectrum) and to redo all the following steps without the knowledge of the response function. For this purpose, section (5) provides the spectrum in tabular form.

Note on the error budget

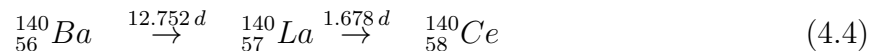
The statistical errors of the BILL measurement are negligible compared to the ones of this work's data set and do not play a role in the final error budget. Nevertheless, the error of the absolute normalisation, ranging from 1.7% at 1.3 MeV to 1.9% at 7.4 MeV has to be fully taken into account. This error directly translates into an additional uncertainty of the absolute rate of the final ^{238}U spectrum. When this spectrum is inserted in the prediction of a reactor antineutrino spectrum one has to be aware of this correlation between the measurement performed in the present thesis and the one of the BILL spectrum.

4.5 Absolute calibration of the β -spectrum

The last step towards the final β -spectrum of the fission products of ^{238}U is an absolute calibration of the spectrum. In the previous section, the beta spectrum of ^{235}U obtained by the thermal neutron beam irradiation was normalised to the BILL spectrum. The last missing parameter is the relative normalisation between the ^{235}U and the ^{238}U spectrum which is equivalent to the relative number of fissions of ^{238}U in the fast beam and ^{235}U in the thermal beam. This can directly be derived by performing gamma spectroscopy on the irradiated uranium foils. Both uranium targets were screened for gamma lines of the same fission products. From the peak area of these lines, the production rate of the isotopes in the beam and hence the fission rate can be determined, as will be described in the next subsection. For this purpose, the targets are transferred to the underground laboratory UGL of the Technische Universität München in Garching. In this lab, a germanium detector is set up that is in use for gamma spectroscopy and material screening for several neutrino and dark matter experiments. This detector has a relative efficiency of 150.5% and an energy resolution of 1.8 keV at 1.33 MeV and is able to provide background subtracted spectra of low activity samples. Its setup and performance is explained in detail in [Hof07] and will not be described here.

4.5.1 The determination of the fission rates

During the beam-time, neutron rich nuclei are produced by fission of uranium. To illustrate the analysis, the gammas from the subsequent decays ^{140}Ba and ^{140}La are discussed below:



In the following, Ba will be labelled as isotope m (mother) and Lanthanum as d (daughter). The decays and production during the beam-time can be expressed by the ordinary differential equations:

$$\begin{aligned}\dot{N}_m(t) &= p_m - \lambda_m N_m(t) \\ \dot{N}_d(t) &= p_d - \lambda_d N_d(t) + b_{m \rightarrow d} \lambda_m N_m(t)\end{aligned}\quad (4.5)$$

With $i \in \{\text{mother (m)}, \text{daughter (d)}\}$ it is:

- $N_i(t)$: Number of atoms of mother or daughter isotope at time t ;
- its time derivative $\dot{N}_i(t)$;
- p_i : Production rate of the isotope in the beam;
- λ_i : Decay constant of the unstable isotope;
- $b_{m \rightarrow d}$: branching ratio of the decay of the mother isotope into the given daughter isotope. As for the majority of nuclei in the chart, this is 1 for the case of Ba and La.

The production rate can be further described by:

$$p_i = Y_i \cdot FR \quad (4.6)$$

with Y being the fission yield⁷⁶ for the production of this isotope and FR being the fission rate in the target, which is the value to be determined⁷⁷. Barium is either directly produced by the fission or by the decay of neutron-rich isotopes with $A = 140$. As all of the isotopes prior to Ba in the decay chain have half-lives much smaller than Ba itself and also much smaller than the time that elapsed between the end of the irradiation and the gamma spectroscopy, the *cumulative fission yield* can be used for Y_m ; for La, Y_d represents the *individual yield*.

In the thermal beam only the fission yields of ²³⁵U have to be considered, whereas in the fast beam one has to combine the ²³⁵U and ²³⁸U fission yields. It was determined in sec. (4.3), that only around 3.4 percent of the total fissions were due to fission of ²³⁵U and the rest due to fission of ²³⁸U.

Solving the equations above directly leads to the number of nuclei at the end of the irradiation (labelled as t_0):

$$N_m(t_0) = \frac{p_m}{\lambda_m} (1 - e^{-\lambda_m t_0}) \quad (4.7)$$

$$N_d(t_0) = e^{-\lambda_d t_0} \left[\frac{p_d + p_m}{\lambda_d} (e^{\lambda_d t_0} - 1) - \frac{p_m}{\lambda_d - \lambda_m} (e^{(\lambda_d - \lambda_m) t_0} - 1) \right] \quad (4.8)$$

⁷⁶The fission yields were extracted from [Eng93] and are given in appendix (D.2).

⁷⁷As mentioned earlier, the intensity of the neutron beam does not change during the time of each measurement. Thus, also the fission rates are constant.

Without any feeding from fission ($p_i = 0$ after irradiation), the isotopes decay exponentially, resulting in differential equations similar to eqs. (4.5). The peak area PA for a particular γ line measured in the germanium detector is given by:

$$PA = \epsilon(E) \int_{t_{start}}^{t_{stop}} \lambda N(t) dt \quad (4.9)$$

with ϵ_E being the efficiency of detecting the full energy E of a photon emitted from the foil and t_{start} (t_{stop}) the start (stop) time of the measurement. ϵ includes not only the geometric coverage, but also the branching ratio of the decay and therefore the probability that a gamma quantum with the given energy is emitted in a decay⁷⁸. In addition, one has to include the occurrence of sum peaks causing leakage from the main peak: Several gammas can be emitted in a decay of an isotope, which is a process on time scales of nuclear physics (ps to ns, [Fir96a, Fir96b]). The germanium detector operates with shaping times in the lower μ s regime [Hof07] and cannot resolve the single photons. Hence, the deposited energy can be the sum of several gammas, which causes the main peak to shrink. This effect is determined by checking the term scheme and calculating the probability of several gammas to be emitted and detected at the same time. This is in the order of 10% and the data is corrected for this effect.

Eq. (4.9) can then be solved for the fission rate, resulting in an equation for the mother isotope Ba and for the daughter isotope La:

$$FR_m = \frac{\lambda_m \cdot PA}{\epsilon(E) Y_m (1 - e^{-\lambda_m t_0}) (e^{-\lambda_m t_{start}} - e^{-\lambda_m t_{stop}})} \quad (4.10)$$

$$FR_d = \frac{PA}{\epsilon(E) \lambda_d \left[\left(\frac{\lambda_m \bar{N}_m(0)}{\lambda_d(\lambda_d - \lambda_m)} - \frac{\bar{N}_d(0)}{\lambda_d} \right) (e^{-\lambda_d t_{stop}} - e^{-\lambda_d t_{start}}) - \frac{\bar{N}_m(0)}{\lambda_d - \lambda_m} (e^{-\lambda_m t_{stop}} - e^{-\lambda_m t_{start}}) \right]}$$

with:

$$\bar{N}_m(0) = \frac{Y_m}{\lambda_m} (1 - e^{-\lambda_m t_0})$$

$$\bar{N}_d(0) = e^{-\lambda_d t_0} \left[\frac{Y_d + Y_m}{\lambda_d} (e^{\lambda_d t_0} - 1) - \frac{Y_m}{\lambda_d - \lambda_m} (e^{(\lambda_d - \lambda_m)t_0} - 1) \right]$$

All of the parameters in this equations are known from literature and the peak areas are determined by measurement, hence it is possible to calculate the fission rates in the uranium foils during the beam-time. These germanium measurements were repeated five times to follow the decay of the isotopes, excluding that the selected peaks are spoiled by some other, unknown gamma line with a different decay constant.

⁷⁸The branching ratios were taken from [Fir96a].

4.5.2 γ - lines chosen for spectroscopy

Four lines from three different decays⁷⁹ are used, namely from the decay of ^{140}Ba , ^{140}La and ^{95}Zr . The isotopes ^{140}Ba and ^{95}Zr both combine an appropriate half-life ($\tau_{\frac{1}{2}}(\text{Ba}) = 13\text{ d}$, $\tau_{\frac{1}{2}}(\text{Zr}) = 64\text{ d}$) with relatively high fission yields of a few percent. Furthermore, these isotopes' decays are accompanied by the emission of gammas with high energy and with a sufficient branching ratio for this emission. This is important, as the fission of uranium leads to a variety of different isotopes with numerous different gamma lines acting as background for this measurement. Often, more than a single gamma is emitted in a decay, and therefore sum peaks of two or more gammas hitting the germanium simultaneously lead to the occurrence of additional lines in the spectrum. In general, the higher the energy of the investigated gamma, the less background one expects in the same energy regime. The chosen gamma lines of ^{140}Ba ($E_{\gamma}(\text{Ba}) = 537\text{ keV}$) and ^{95}Zr ($E_{\gamma}(\text{Zr}) = 757\text{ keV}$) are fairly high energetic and thus above most of the background. Unfortunately, a second and quite intense line of Zr at 724 keV, which could be used for redundancy, is spoiled by two other background lines and has to be rejected for the analysis. As mentioned above, ^{140}Ba decays into ^{140}La , the latter has a half-life of 1.7 d and emits - amongst others - two lines that can be used for the normalisation analysis. These two lines are at 487 keV and 1596 keV.

This selection of lines has several advantages. Firstly, as ^{140}La can be screened with two lines, it is very unlikely that there is an unrecognised background with a similar half-life⁸⁰, adding a constant value to both peaks. In addition, the Barium line can be compared to the ones from Lanthanum generating another redundancy. Secondly, the use of another isotope - ^{95}Zr - minimises unrecognised errors of possible inaccuracies in the fission yields.

4.5.3 Results of the germanium γ - spectroscopy

The results of the rate determinations are given in table (4.1). Therein, the fission rates are shown, calculated via equation (4.10) using input of the peak areas of the gamma lines as determined by the germanium spectroscopy. Each uranium target - the one irradiated with thermal neutrons, as well as the one from the fast neutron beam - have been screened five times. This, on one hand, reduces the statistical errors and, on the other hand, gives the possibility to detect potential background from other isotopes feeding the same line. Both targets were stored a few days after the irradiation to let a big part of the isotopes decay that would contribute to background. The last of the five measurements was performed approximately two weeks after the first one. As one can see from the values in the table, no sign for a systematic de- or increase of the rates can be found, proving that the chosen lines are background-free.

⁷⁹All atomic data used in this section is taken from [Fir96a, Fir96b].

⁸⁰As several measurements with the same foils were performed in a period of two weeks, background lines at the same energy but with another half-life would be identified by an unexpected time dependence.

The fission rates are given in $1/(s \cdot \epsilon)$. This comes from the fact that the combined efficiency of the germanium detector for the specific energy and the branching ratio of the gamma line in the radioactive decay cancel out in the final calculation of the normalisation factor⁸¹. This normalisation is defined as the number of fissions in the thermal beam divided by the number of fissions in the fast beam, hence, the efficiencies vanish. As a consequence, it is not useful to compare the fission rates from different gamma lines with each other. The only value finally to be the same, is the ratio of the fission rates in the thermal and the fast neutron beam. This value defines the normalisation constant by which the ^{238}U spectrum has to be scaled.

As the table shows, the normalisation constants determined from the different isotopes match nicely. Only the ^{95}Zr data indicates a slightly smaller normalisation (within the errors). However, due to the long lifetime of ^{95}Zr , the statistics of the peak was very low and furthermore there was some additional background in the vicinity of the peak, which could have led to some underestimation of the 757 keV peak. However, its relatively high error suppresses its influence in the weighted mean, which is dominated by the very clean La peaks.

The achieved normalisation of 44.4 ± 0.3 is a measure of the relative amounts of fissions during the beam-time. It contains both fissions of ^{235}U and of ^{238}U in the fast beam. The relative amount of fissions from ^{235}U is known to be 0.0344 of all fissions (see section 4.3). Thus, the final normalisation constant scaling the ^{238}U spectrum is $44.4 / (1 - 0.0344) = 45.98 \pm 0.3$. Together with the error of the μ peak normalisation (sec. 3.4.2) and the uncertainty on the absolute calibration of the BILL experiment, the error on the absolute scale of the final spectrum is $\sim 2.8\%$.

⁸¹The efficiencies are only important to determine the fraction of events building up sum peaks in the detector. As the peak areas are already corrected for this effect, no further dependence on the combined efficiency is existing.

Isotope	E_γ [keV]	thermal		Ratio th/f	fast	
		FR [$1/(s \cdot \epsilon)$]	Mean FR [$1/(s \cdot \epsilon)$]		Mean FR [$1/(s \cdot \epsilon)$]	FR [$1/(s \cdot \epsilon)$]
^{95}Zr	757	674.1 ± 7.3	679.0 ± 2.1	41.1 ± 2.9	16.5 ± 1.2	16.4 ± 1.5
		683.3 ± 3.6				17.4 ± 3.7
		664.5 ± 5.3				15.8 ± 3.6
		691.5 ± 5.0				15.9 ± 3.2
		675.6 ± 4.0				18.5 ± 5.3
^{140}Ba	537	368.9 ± 2.3	364.1 ± 0.7	44.9 ± 4.1	8.11 ± 0.74	8.0 ± 1.1
		366.6 ± 1.2				7.7 ± 1.9
		357.7 ± 2.0				8.3 ± 1.7
		365.4 ± 2.0				8.2 ± 1.8
		359.0 ± 1.7				9.0 ± 3.0
^{140}La	487	421.8 ± 2.5	423.3 ± 0.7	44.8 ± 0.4	9.45 ± 0.093	8.9 ± 0.4
		423.5 ± 1.1				9.3 ± 0.1
		421.1 ± 1.7				10.1 ± 0.2
		426.1 ± 1.7				9.3 ± 0.2
		423.2 ± 1.9				9.8 ± 0.3
^{140}La	1596	489.3 ± 2.1	482.3 ± 0.4	44.4 ± 0.3	10.9 ± 0.12	11.3 ± 0.3
		484.6 ± 1.0				10.9 ± 0.2
		479.6 ± 1.6				10.8 ± 0.3
		488.8 ± 1.7				10.8 ± 0.5
		480.6 ± 0.6				11.0 ± 0.3
Final normalisation factor:						
44.4 ± 0.3						

Table 4.1: Results of the γ - spectroscopy. Column 1 (C1) lists the decaying isotope. The energy of the gamma line analysed is shown in C2. C3 gives the value of the non-normalised fission rate FR in the uranium target in the thermal beam that is deduced from the peak area of the γ lines for every one of the five different measurements. The average of these is given in C4. The unit of FR being "1 per second and efficiency" is explained in the text. Analogously to the thermal neutron beam, the fission rate in the target irradiated in the fast beam is given in C6 and C7. The five different measurements are spread over two weeks.

For each gamma line, the ratio of C4 and C6 gives the normalisation factor depicted in C5 with its weighted mean beneath the column. The agreement between the four normalisation constants is a strong hint for the correctness of the method.

Chapter 5

The final ^{238}U β - and $\bar{\nu}$ - spectrum

After performing the analysis chain as explained in the last chapter, the final β -spectrum of the fission products of ^{238}U is obtained (fig. 5.1 and tab. 5.1).

The general technique in this analysis relies on the bin-wise normalisation of the measured ^{235}U spectrum to the BILL spectrum. This normalisation function was interpreted as an efficiency function and applied to the measured ^{238}U data. There might be groups preferring not to use the BILL but another spectrum, or in the future new measurements or corrections to the BILL spectrum might be performed. Thus, the spectrum is given in a form that every group is able to redo the normalisation and apply the conversion to the neutrino spectrum by themselves. To do so, the spectrum given simply has to be divided bin-wise by the BILL spectrum [Sch85] and multiplied by the preferred normalisation spectrum. The proof that this method is valid without the use of the response function is given in section (5.2).

5.1 Error budget

The analysis had to deal with several uncertainties and the significant ones were propagated to the final result. The errors not included are discussed and their minor influence on the data is proven within chapters (3 and 4). The main sources of errors can be grouped and handled in the following way:

- Statistical error: The by far dominating error stems from the subtraction of the diffuse background from the uranium data in the fast beam. The vicinity of the reactor core and the direct line-of-sight to the converter plates lead to a high amount of target-independent background. This directly results in a signal to background ratio of less than one, starting at around 3.5 MeV and thus explaining the quite high errors in the high energy regime (see sec. 4.2.1).
- Systematic errors: This source of errors comprises systematic errors that arise in the description of the electron background in the fast neutron beam or the electron and neutron background in the thermal beam (see. sec. 4.2.3). These errors are due to

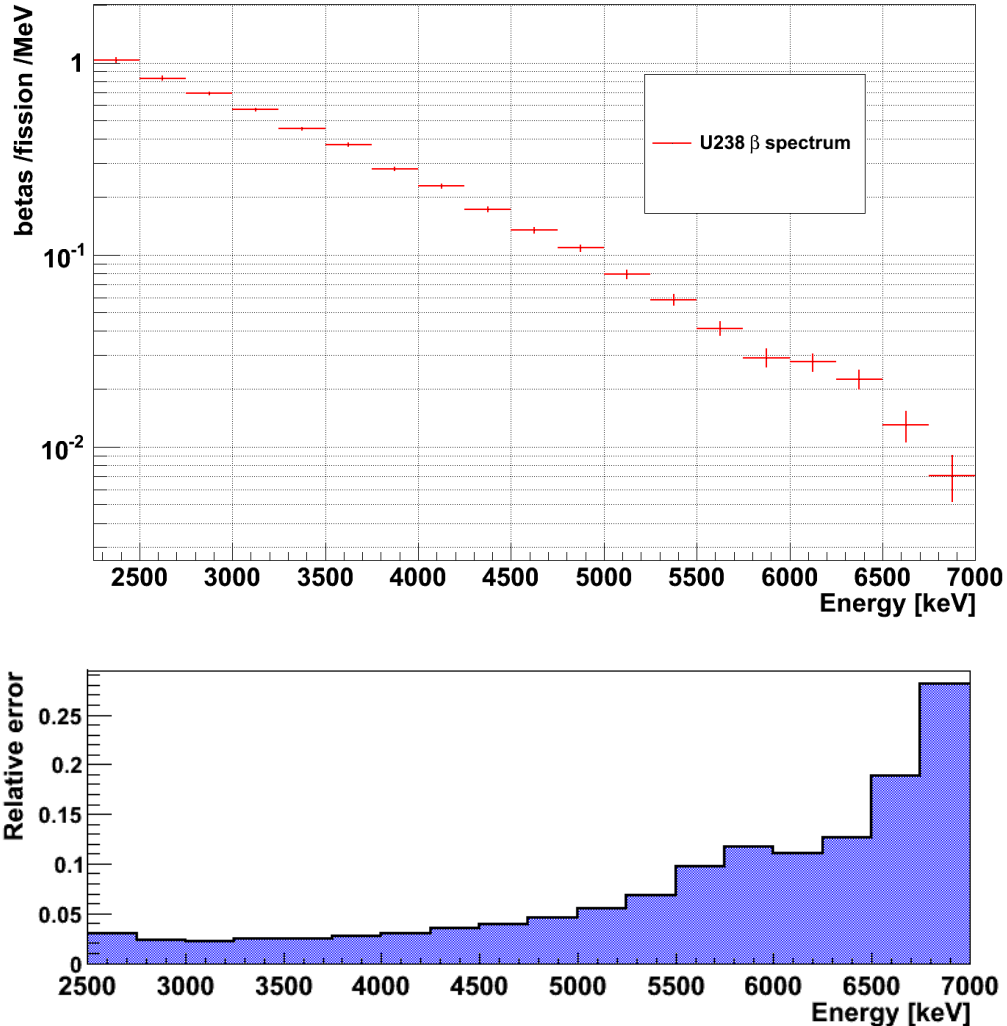


Figure 5.1: *Top: The final β -spectrum of the fission products of ^{238}U as measured in the present thesis. The data can be extracted from table (5.1). The bars in x -direction do not state any errors but illustrate the bin width of 250 keV. Bottom: The combined statistical and systematic error of the measured spectrum. Up to ≈ 5 MeV the error is beneath 5%. The error in the lower bins is slightly enhanced due to uncertainties in the background subtraction of electrons and gammas in the neutron beam. Above this energy, the error is dominated by the statistical error from the diffuse background subtraction (see. sec. 4.2). The illustrated error does not include the error on the absolute calibration of $\approx 2.8\%$ which is due to the dead-time determination by the muon peak analysis (sec. 3.4.2), the germanium spectroscopy (sec. 4.5) and the uncertainty of the absolute normalisation of the BILL experiment (sec. 4.4). This error on the normalisation may act as an energy-independent shift of the whole spectrum either to higher or lower intensities.*

Energy [keV]	N_β	$\frac{\text{betas}}{\text{fission}\cdot\text{MeV}}$	stat. err. [%]	norm. err. [%]	norm. err. BILL [%]
2250 - 2500	1.032		3.2	2.1	1.7
2500 - 2750	$8.302 \cdot 10^{-1}$		3.0	2.1	1.7
2750 - 3000	$6.922 \cdot 10^{-1}$		2.4	2.1	1.7
3000 - 3250	$5.698 \cdot 10^{-1}$		2.3	2.1	1.7
3250 - 3500	$4.533 \cdot 10^{-1}$		2.4	2.1	1.7
3500 - 3750	$3.740 \cdot 10^{-1}$		2.4	2.1	1.7
3750 - 4000	$2.807 \cdot 10^{-1}$		2.7	2.1	1.7
4000 - 4250	$2.279 \cdot 10^{-1}$		2.9	2.1	1.7
4250 - 4500	$1.725 \cdot 10^{-1}$		3.5	2.1	1.8
4500 - 4750	$1.343 \cdot 10^{-1}$		3.9	2.1	1.8
4750 - 5000	$1.084 \cdot 10^{-1}$		4.5	2.1	1.8
5000 - 5250	$7.891 \cdot 10^{-2}$		5.5	2.1	1.8
5250 - 5500	$5.831 \cdot 10^{-2}$		6.8	2.1	1.8
5500 - 5750	$4.137 \cdot 10^{-2}$		9.7	2.1	1.8
5750 - 6000	$2.909 \cdot 10^{-2}$		11.7	2.1	1.8
6000 - 6250	$2.765 \cdot 10^{-2}$		11.1	2.1	1.8
6250 - 6500	$2.248 \cdot 10^{-2}$		12.7	2.1	1.8
6500 - 6750	$1.296 \cdot 10^{-2}$		18.9	2.1	1.9
6750 - 7000	$7.078 \cdot 10^{-3}$		28.1	2.1	1.9

Table 5.1: *The final result of the measurement of the beta spectrum of the fission products of ^{238}U . The bin width is 250 keV. N_β is the beta spectrum given in units of betas per fission and MeV. The relative combined statistical and systematic error is given in column three, followed by the relative error due to uncertainties in the absolute scale normalisation. The last column shows the error on the absolute rate in the BILL measurement. To get the total uncertainty of the absolute normalisation of $\sim 2.8\%$ as quoted in the text, one has to quadratically add the errors in the two last columns. These are listed separately to be able to disentangle them when using another normalisation than the BILL spectrum. A detailed description of the error budget is given in the text within section (5.1).*

the lack of knowledge of internal parameters, e.g. the neutron beam profile or the involved cross sections of the particles. These errors were propagated quadratically, as the fits to determine these background were based on statistical methods and, furthermore, the single sources of inaccuracies are independent from each other.

- **Energy calibration:** The energy calibration (sec. 3.3) adds a systematic error to the scale of the energy axis, which can be translated into an error of the spectrum. This error is discussed in detail in the following section (5.1.1).
- **The three errors mentioned above are added quadratically and the resulting error is referred to as the combined statistical and systematic error of the beta spectrum.**
- **Absolute normalisation - Errors due to the ^{238}U experiment:** The error of the absolute normalisation induced by this measurement is dominated by the determination of the system dead-time via the muon peak analysis (sec. 3.4.2). The inaccuracy added by the gamma spectroscopy measurement only contributes a minor fraction. These errors add up to 2.1 % uncertainty of the total height of the spectrum.
- **Absolute normalisation - Errors induced by the BILL spectrum:** Apart from the mentioned error on the absolute normalisation, one additionally has to take into account the absolute rate error of the BILL measurement. As the absolute normalisation relies on the BILL spectrum, its errors have to be fully transported to the measurement of the present thesis. The systematic scaling error added is in the order of 1.8 %, varying with energy only in the 0.1 % range. As this error is independent from the absolute errors of the muon peak correction and the gamma spectroscopy, these have to be added in quadrature. This leads to a total uncertainty in the absolute normalisation of 2.8 %. In the tables giving the final β -spectra, the error of the BILL measurement is always quoted separately to distinguish it from the errors inherent to the present work's data and to be able to disentangle the error from the others when normalizing the spectrum with another than the BILL spectrum. As a result of the normalisation to the BILL spectrum, the spectra in this work have a correlation to the BILL spectrum. This is important to remember when including this spectra in a global reactor antineutrino analysis.

5.1.1 Impact of the inaccuracy of the energy calibration

In section (3.3) the energy calibration was determined to be:

$$E = (4.83 \pm 0.03) \cdot CN + (21.52 \pm 3.21),$$

with CN being the channel number and E the deposited energy of the electron. As during the analysis chain fits to the data and comparisons to predicted spectra were performed, the propagation of the error of the calibration to the final result is not trivial. The method of choice to translate the uncertainty of the energy calibration into an inaccuracy on the final spectrum is to repeat the whole analysis chain twice with different calibrations. For

this purpose, the calibration is altered to be at its upper and its lower 1σ boundary - once adding the quoted errors to the mean values and once subtracting them from the mean values. The two parameters in the linear calibration - the slope and the offset - are correlated negatively, but the error on the offset has minimal influence at the energy scale above the experimental threshold. It does not change the outcome of the estimation if both parameters are varied in the same direction. Thus, the change of the slope by $\pm 6.2\%$ dominates the result.

Every single step in the analysis is repeated with the alternative calibration and thus two alternative beta spectra are derived. The difference between the ones obtained in this way and the standard spectrum were taken as an estimate of the total error. As one can see in fig. (5.2), in the regime up to 5.5 MeV the spectra do not differ significantly. Above this energy, one gets deviations in the order of 4 percent. The deviations from an exponential behaviour of the beta spectrum - may they be due to statistics or due to a physical nature of the true beta spectrum - lead to higher uncertainties in this regime. Nevertheless, the inaccuracies induced by this are smaller than the ones already included. It was chosen to add this error quadratically to the ones already existing. This error is already included in table (5.1) in the combined statistical and systematic error in column 3.

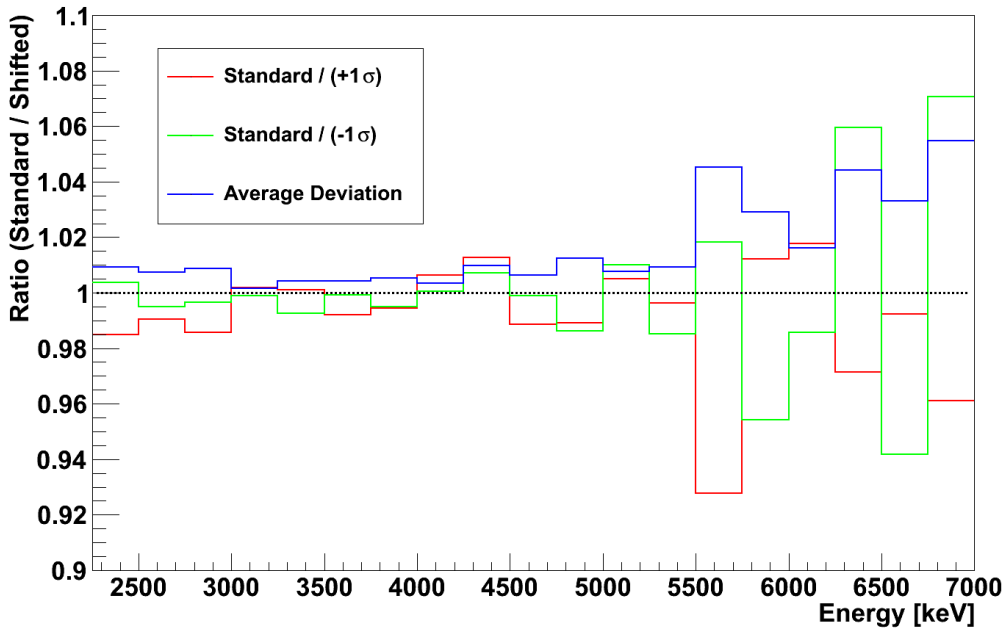


Figure 5.2: *The ratio of the standard beta spectrum as obtained in the data analysis and the spectrum derived with a shifted energy calibration. ($+1\sigma$) and (-1σ) denote the final beta spectra obtained, when changing the slope of the linear calibration by the quoted one sigma error up or down, respectively. The blue curve shows the average of the absolute deviations of both ratios. This average was used as additional error on the spectrum due to the inaccuracies in the energy calibration.*

5.2 The measured beta spectrum: Comparison to calculations

Various groups calculated the beta spectrum of the fission products of ^{235}U and ^{238}U . In this work, the final spectrum is compared to the predictions of [Met84, Mue11, Vog81]. These publications use a procedure to obtain the beta- and antineutrino spectrum called the *summation approach*. In this method, one builds the total β -spectrum of the fission products of an investigated isotope (uranium or plutonium) from the single beta spectra of the individual fission products and their daughters as is explained in section (1.3).

Fig. (5.3) shows the ratio⁸² of the spectrum from the present work to the spectrum from [Mue11]. The errors given illustrate the influence of the uncertainty of the measured spectrum only. No error from the calculation is taken into account here to clearly demonstrate the accuracy of the experimental method used. Also not taken into account is the overall error of 2.8% stemming from the normalisation with the muon peaks (sec. 3.4.2), the germanium spectroscopy (sec. 4.5) and the BILL comparison (sec. 4.4), which may lead to a small up- or down-shift of the whole spectrum. As discussed before, two different techniques were evaluated, both explained in sec. (4.4). In one analysis, the bin-to-bin influence of the detector-response function is totally neglected and thus this response cancels out when normalising the ^{238}U with the help of the ^{235}U spectrum. In this case, the ^{238}U β -spectrum obtained after the absolute calibration is the final beta spectrum. As a matter of principle, this spectrum is only an approximation to the true spectrum. The correct technique is to normalise the measured ^{238}U spectrum on the BILL ^{235}U spectrum convolved with the response function. This results in a final spectrum still convolved with the response. To compare a predicted spectrum with the one measured, in this case one has to convolve the calculation with the response function and compare the outcome of this with the data. Both of these methods are compared in figure (5.3) which illustrates the comparison of measurement and calculations.

The **comparison between measurement and calculation** reveals a slight spectral distortion. The spectrum obtained in this work is about 10% more intense than the prediction in the low-energy regime around 2.5 MeV, which decreases to a level of 1:1 at ~ 3.5 MeV. This behaviour is very similar to the one the group of [Mue11] observes when comparing their predicted ^{235}U spectrum with the BILL one. Alike, their simulation returns a spectrum that is less intense than the BILL spectrum at energies around 2.0 to 2.5 MeV, which constantly relaxes until reaching energies of around 4 MeV. The deviation between the simulation and the present measurement is slightly higher but shows the same trend. Between ~ 4.0 - 5.5 MeV, the shape of the predicted and measured ^{238}U spectrum are nearly the same, with the measurement being around 5% less intense. At energies higher than about 5.75 MeV, the statistical uncertainties start to exceed 10 percent, making it difficult

⁸²The calculations assume slightly different irradiation times and neutron spectra. As is discussed in sec. (4.3) these differences have only minor impact on the final spectrum and do not corrupt the comparability.

5.2. THE MEASURED BETA SPECTRUM: COMPARISON TO CALCULATIONS

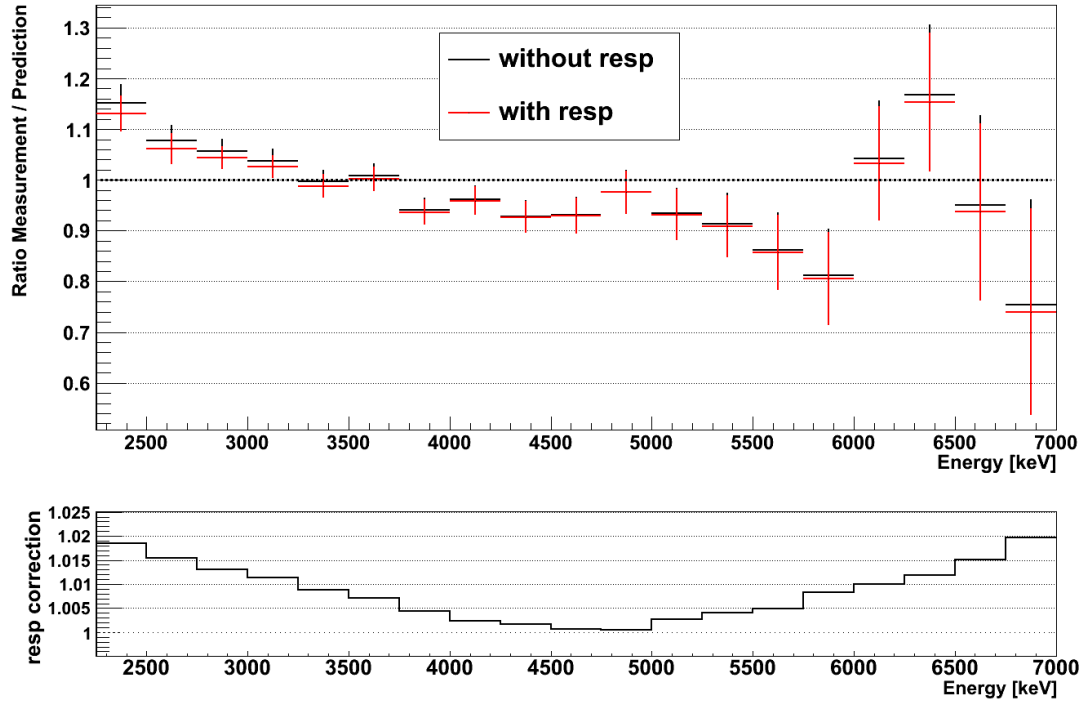


Figure 5.3: *Top*: The ratio between the beta spectrum of ^{238}U measured in the present thesis and the prediction from [Mue11]. In black, the approximated spectrum - generated by neglecting the bin-to-bin correlating effects of the response function - is used. In red, the result of the analytically correct technique is given. Both methods yield very similar results, leading to the conclusion that the use of the response function can be replaced by a bin-to-bin-independent, but still energy-dependent correction of less than 2%. This is also made clear in the lower plot, where the ratio of the two curves is illustrated, demonstrating the smallness of the deviation.

The prediction and the measurement, on the other hand, show a slight spectral distortion. The simulation underestimates the spectrum at lower energies and overestimates it in the range between 4 and 6 MeV.

to derive conclusive statements of the spectral behaviour. In sec. (5.4), a possible reason for the deviation between the predictions and the measured spectrum and the impact this has on the current reactor experiments are discussed on the basis of the final antineutrino spectrum.

The **influence of the response function** on the final data is minimal. The lower box in fig. (5.3) shows the ratio of the final result for the ^{238}U beta spectrum when neglecting all bin-to-bin correlations in the response function to the one with the correct response included. For the whole energy range, this ratio never exceeds 1.02. It is therefore possible to generate the final beta spectrum of ^{238}U by applying this minor correction factor to the spectrum achieved when neglecting the response function. Doing this, a clean and final beta spectrum of the fission products of ^{238}U is obtained. This proves that the response function is mainly a bin-to-bin uncorrelated multiplicative efficiency factor. The normalisation of the ^{238}U with the BILL spectrum can therefore be performed by the use of eq. (4.2) instead of being forced to apply the analytically correct calculation of eq. (4.1). In addition, this provides the possibility to normalise the ^{238}U spectrum with any other than the BILL spectrum, without the knowledge of the response function. Thus, any group that wants to normalise the spectrum to their own ^{235}U spectrum is provided with the possibility to do so. The small correction is already included in the given final β -spectrum in figure (5.1) and table (5.1).

Apart from [Mue11], the measured beta spectrum is compared to the ones predicted by two other groups. *Vogel et al.* [Vog81] and *Metzinger* [Met84] also predict spectra for the fission of ^{238}U . The ratio of the measured spectrum and their predictions is given in fig. (5.4).

One can directly see that in the energy regime around 3 MeV these two predictions are underestimating the spectrum significantly more than the one of Mueller et al. Furthermore, they show a different behaviour at higher energies, as the spectrum from Metzinger is decreasing with rising energy, whereas the simulation of Vogel et al. approaches the measurement at an energy of ≈ 4.5 MeV. This comparison shows the differences and uncertainties present in literature at the time being. Possible reasons for these deviations will be discussed in section (5.4) by means of the final antineutrino spectrum. The measurement performed within this thesis obtains the spectrum of the fission products of ^{238}U for the first time experimentally and thus will enhance the accuracy of the predictions of reactor spectra.

5.2. THE MEASURED BETA SPECTRUM: COMPARISON TO CALCULATIONS

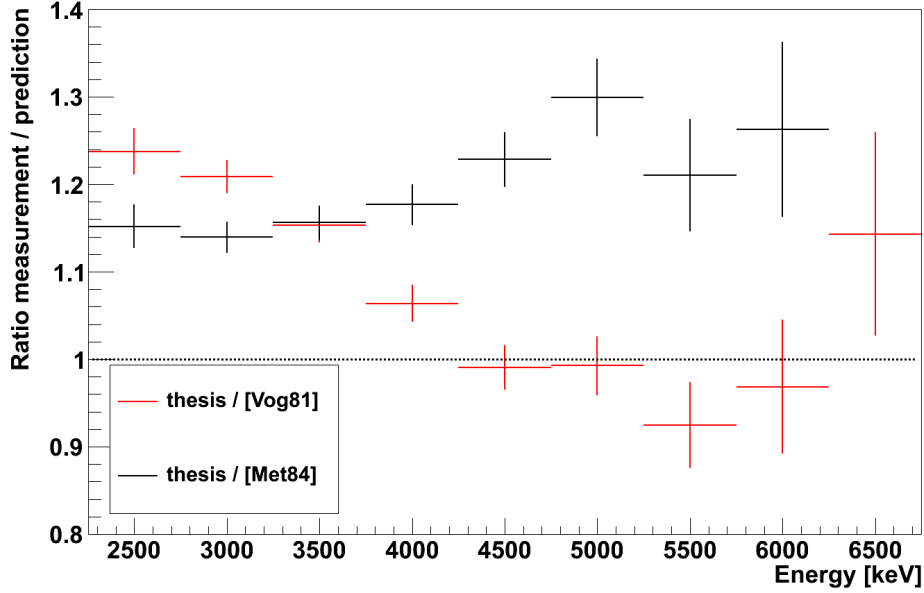


Figure 5.4: The ratio between the ^{238}U beta spectrum measured in the present thesis and the prediction from [Vog81] (red) and [Met84] (black). The deviations between measurement and calculation are comparably bigger than in fig. (5.3), where the deviation to the spectrum of [Mue11] are given. In the energy regime at around 3 MeV both groups underestimate the spectrum by roughly 15 to 20 percent. While the prediction of Vogel et al. then approaches the measurement for energies of ~ 4.5 MeV, the calculation of Metzinger turns out to underestimate the spectrum at higher energies even more.

5.3 Conversion into the antineutrino spectrum

The conversion of a measured β -spectrum - being the sum of several thousand single and partly unknown branches - into an $\bar{\nu}_e$ -spectrum is not possible analytically. The calculations following the *summation approach* benefit from the fact that on the single-branch level one can directly predict the antineutrino spectrum with nearly the same accuracy as the electron spectrum by summing up all involved antineutrino distributions [Mue11]. This is of course not possible for a conversion of the measured total β -spectrum of the fission products into the antineutrino spectrum. Two different procedures turned out to be appropriate for such a conversion:

The first one fits the experimental spectrum with a set of hypothetical β -spectra, which individually can be converted and summed up to the final neutrino spectra. This method was used for ^{235}U [Sch81,Sch85] and is, for example, discussed in [Vog07] and [Hub11]. For this purpose, the measured beta spectrum is divided into energy slices and a single beta spectrum is fitted to the highest energy bin. This spectrum is subtracted and the procedure is repeated until the full spectrum is described by individual beta spectra. There are some parameters and assumptions involved that may change the outcome of this procedure, as the number of hypothetical branches, the width of the energy slices or the average charge number Z of the theoretical decaying nuclei. It is stated in [Vog07, Hub11] that this method is accurate on the lower percent regime. However, for the present work the method of virtual branches is not applicable, as one of the main conditions to successfully use this conversion is an experimental spectrum that is statistically very well known up to the higher energies to allow the slicing into sufficiently fine bins [Hub11]. This is not the case for the spectrum measured here, as the background at the reactor site results in a relative error of more than 10 percent above 6.0 MeV, drastically rising towards higher energies. This conversion technique will therefore not be explained in more detail.

The second method of conversion is a more empirical one and is already described in [Vog81,Sch85]. It is carried out without the use of hypothetical branches or the knowledge of nuclear parameters and takes benefit from the fact that the spectra of electrons and antineutrinos have very similar shapes when restricting to kinetic energies higher than about 2.5 MeV. The only differences accounted for are due to their different mass and the electrical charge:

$$N_e(E_{tot} - E_{shift}) \cdot k(E) = N_{\bar{\nu}}(E_{\bar{\nu}}) \quad (5.1)$$

Herein, N_e and $N_{\bar{\nu}}$ are the spectra of electron and antineutrino, respectively. E_{tot} describes the total electron energy, including its mass, and $E_{\bar{\nu}}$ is the total antineutrino energy, which is equivalent to its kinetic energy. E_{shift} is an averaged energy shift accounting for the Coulomb attraction of the electron which is in the range of 0-100 keV. Finally, a correction term $k(E)$ remains that includes all unaccounted corrections. The k -factor has no direct physical equivalent and empirically describes the deviation from equality of N_{β} and $N_{\bar{\nu}}$. Of course, eq. (5.1) is only approximately valid for a single beta spectrum, but

when summing over a high number of single spectra one averages over all individual β - and $\bar{\nu}$ -spectra and the technique becomes more accurate.

The determination of $k(E)$ in the present work relies on the calculations performed via the *summation method*. As mentioned, it is a direct advantage of the summation method to be able to calculate the electron and antineutrino spectra with the same precision. Even if one assumes the fission β -spectra not to be predicted correctly, the converted antineutrino spectrum still corresponds to this beta spectrum predicted. It is said above that several groups have performed calculations with the summation method and thus the parameter $k(E)$ can be derived from every of these data sets. Figure (5.5) illustrates the factor $k(E)$ as it is extracted from the calculations and, additionally, is derived for the measured BILL spectra. This is obtained by simply solving equation (5.1) for $k(E)$ and substituting $E_{shift} = 50 \text{ keV}$.⁸³

$$k(E) = \frac{N_{\bar{\nu}}(E_{\bar{\nu}})}{N_e(E_{tot} - 50 \text{ keV})} \quad (5.2)$$

For each data set plotted in figure (5.5) different input spectra were used:

- Black: The electron spectrum is the one measured by the BILL collaboration [Sch85] for the fission products of ^{235}U . The authors applied the conversion procedure based on the summing of hypothetical beta branches, as briefly explained above. The obtained antineutrino spectrum is used to generate $k(E)$.
- Green: The BILL spectrum [Sch85] is used as basic β -spectrum, but this time the antineutrino spectrum is replaced by the one that was obtained by Mueller et al. in [Mue11]. This group's conversion method is a combination of the *summation method* and the hypothetical branch approach. This antineutrino spectrum is more intense than the one originally published by the BILL collaboration. One can directly see the rise of in average $\sim 3\%$ that lead to the *reactor antineutrino anomaly* [Men11], see also sec. (1.1.1).
- Red: Mueller et al. [Mue11] also predict the β - and $\bar{\nu}$ -spectra for ^{238}U . The factor k from these data is nearly equivalent to the one from ^{235}U . As this data is the most recent one for ^{238}U , a fit of a polynomial $f(E) = \sum_{i=0}^4 a_i x^i$ is performed (dashed red line) to the data points and in the following this function is used as $k(E)$ to convert the beta spectrum measured within the present work into the antineutrino one.
- Blue squares: For reasons of clarity, in the plot all predictions that are given in 500 keV binning are shown dotted. The blue data is extracted from the paper of Vogel et al. for the fission of ^{238}U [Vog81].
- Violet dots: Metzinger [Met84] also gives predictions for the ^{238}U $\bar{\nu}$ - and β -spectrum, depicted in violet.

⁸³The influence of a varying E_{shift} is minimal as will be discussed below.

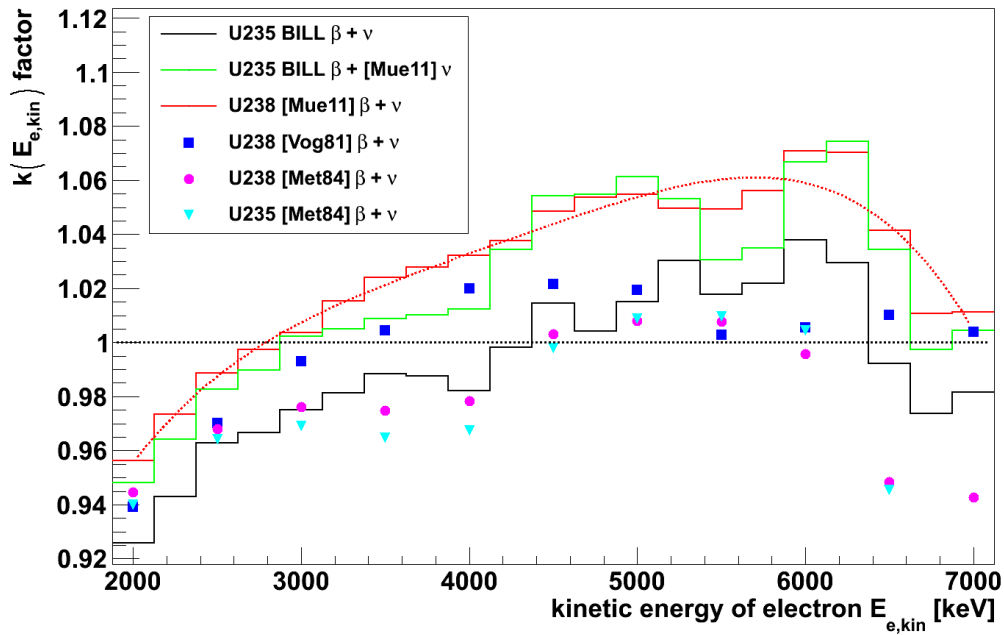


Figure 5.5: The factor $k(E)$ as a function of the kinetic energy of the emitted electron. $k(E)$ is defined by equation (5.1), describing the shape differences between electron - and antineutrino spectrum, as extracted from various publications. Herein, E_{shift} is set to 50 keV. The curves are generated by using different beta and antineutrino spectra as indicated in the legend and explained in the text in detail. One can see that the rough shape of the function is very similar for all different input spectra. k is close to 1, varying by about $\pm 5\%$. The dashed red line indicates a fit of $f(E) = \sum_{i=0}^4 a_i x^i$ to $k(E)$ obtained from the ^{238}U data of Mueller et al; this function is used for further analysis.

- Light-blue triangles: Analogously to the one before, Metzinger’s calculation for ^{235}U is depicted.

From this selection of data sets, one can conclude that the spectral shape of the correction function $k(E)$ is very similar for all predictions and the measured spectra. The differences are more in the absolute scaling, varying by approximately 2-4%, depending slightly on energy. For the further analysis, a fit to the data from Mueller et al. [Mue11] is used, as this is the most recent prediction of the ^{238}U beta and antineutrino spectrum⁸⁴. This choice obviously results in an $\bar{\nu}$ -spectrum that is $\approx 3\%$ more intense than the one that would be obtained by using solely the BILL data. [Hub11] also observes this shift when independently re-analysing the conversion procedure applied to the BILL data in the original publication [Sch85], supporting the use of the $k(E)$ factor chosen.

To account for the varying absolute scale of $k(E)$ in the predictions, a systematic error of 2% is added to the correction $k(E)$, representing the error of this conversion technique. The error is interpreted to be an error of absolute shift, and not a bin-uncorrelated one, reflecting the fact that the shapes of all predictions for $k(E)$ are similar. This error is summed quadratically to the already existing error of the absolute normalisation of the performed measurement, as these are statistically independent from each other, enlarging the uncertainty of absolute scale to 3.3%.

An additional statistical error of one percent is added to the data for the following reason: The antineutrino spectra given in the [Mue11] is binned in 250 keV bins centred around 2 MeV, 2.25 MeV and so on. However, building the ratio of the electron spectrum shifted by 561 keV and the neutrino spectrum requires one of both spectra to be described by a smooth function enabling an interpolation⁸⁵. This is accomplished by the exponential smoothing technique described in appendix (B). The interpolation is estimated to have an error of one percent on the bin entry which is that small, because the spectra can be approximately described by an exponential.

As the spectrum is obtained by shifting the beta spectrum by $(m_{e^-} + E_{shift})$, which is not a multiple of the bin width of 250 keV, the antineutrino spectrum now exists in an inconvenient binning. To present it in a way that enables a direct comparison to the predictions, the spectrum has to be re-binned. This is done by the method of exponential smoothing as explained in appendix (B), fitting simple exponentials to three bins. However, this technique can only be applied to spectra being innately smooth. Above an energy of ~ 6 MeV this is not the case any more as one can also derive from the illustration of the beta spectrum in fig. (5.1). The exponential smoothing method is inaccurate and a linear

⁸⁴The reader may tend to choose another correction than the one suggested. As the correction k is a factor to be applied bin-to-bin, the spectrum can be easily changed to whatever correction is appreciated.

⁸⁵To clarify this with an example: To get the value of k for the bin in the electron spectrum with an energy from 3000 - 3250 keV, this bin has to be compared with the antineutrino spectrum integrated from 3561 - 3811 keV, which corresponds to the described shift of $(m_e + 50 \text{ keV})$. Of course, the antineutrino spectrum is not given in such a binning, therefore, it has to be interpolated and re-binned.

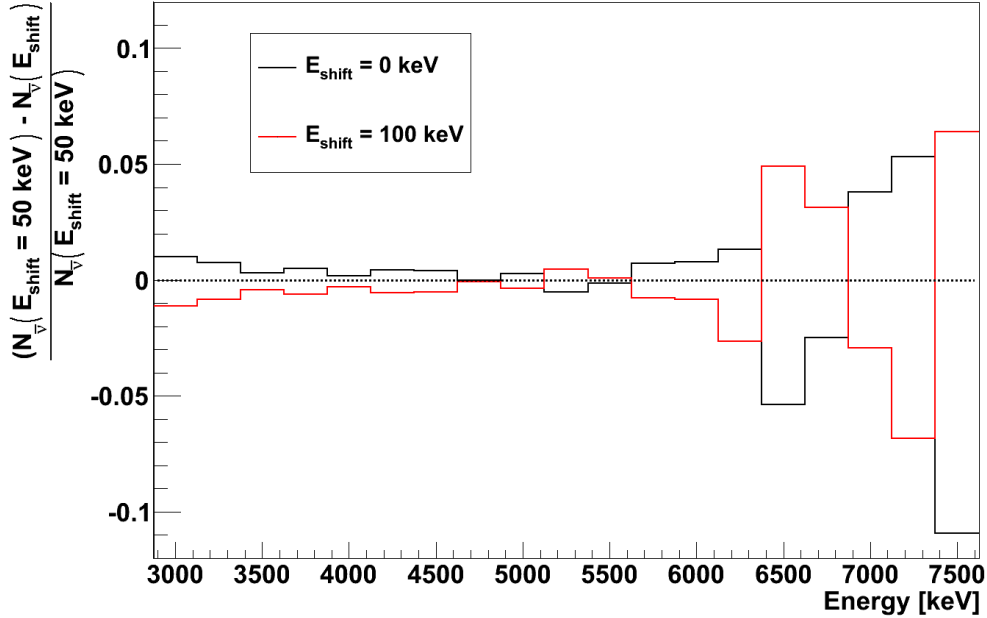


Figure 5.6: The standard conversion procedure was performed by assuming an average E_{shift} due to the Coulomb attraction of 50 keV. Two extreme values - $E_{shift} = 0$ keV and $E_{shift} = 100$ keV - were also computed. The plot shows the relative deviation of these two cases from the standard neutrino spectrum. The absolute difference does not vary much in the range below 6.5 MeV and increases to $\pm 5\%$ above this. To account for this in the analysis, the average value of the two absolute deviations was calculated bin-wise and half of this was added to the total error of the final antineutrino spectrum.

interpolation was performed for the region above 6 MeV. In appendix (B.2) the whole re-binning procedure is explained in more detail together with the estimation of its errors.

The analysis above uses a value of 50 keV for E_{shift} . This was chosen as an average value for the Coulomb attraction of the emitted electron in the vicinity of the nucleus [Vog81]. To investigate the influence on the final spectrum, the analysis is repeated with $E_{shift} = 0$ keV and $E_{shift} = 100$ keV. This changes the absolute value of $k(E)$, but as the β -spectrum is shifted by ± 50 keV compared to the standard analysis, this effect should ideally cancel out. Figure (5.6) depicts the influence of varying E_{shift} . As one can see, the low-energetic part of the spectrum is hardly affected by this, however, in the high-energetic part, where the spectrum cannot be accurately described by an exponential, the influence is of the order of 5%. To include the uncertainty due to E_{shift} , the average of the absolute deviation for both tested alternatives was taken (bin-wise) and half of this value was added quadratically to the total error of the spectrum. This adds less than one percent to the error up to 6 MeV and contributes to few percent above this.

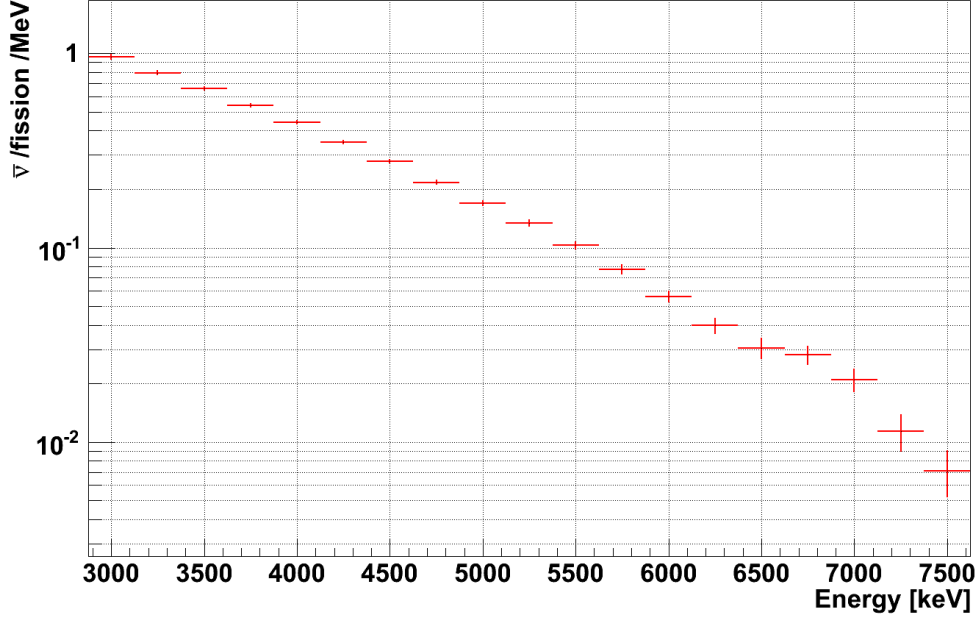


Figure 5.7: *The final antineutrino spectrum of the fission products of ^{238}U as obtained in this thesis. The errors plotted do not include the error on the absolute normalisation of about 3.3 percent. The depicted bars in x-direction only illustrate the bin width of 250 keV, but do not indicate any error.*

Finally, the $\bar{\nu}$ -spectrum of the fission products of ^{238}U is depicted in figure (5.7) and tab. (5.2). This includes all uncertainties discussed in the analysis of the beta spectrum and all systematic corrections and estimated errors of the conversion procedure. The binning is identical to the one common in literature allowing a direct comparison to predictions and the use in the analysis of reactor antineutrino experiments.

Energy [keV]	$N_{\bar{\nu}}$	$\frac{\bar{\nu}}{\text{fission}\cdot\text{MeV}}$	error [%]	norm. error [%]
3000	$9.586 \cdot 10^{-1}$		3.5	3.3
3250	$7.952 \cdot 10^{-1}$		3.1	3.3
3500	$6.603 \cdot 10^{-1}$		2.6	3.3
3750	$5.406 \cdot 10^{-1}$		2.6	3.3
4000	$4.433 \cdot 10^{-1}$		2.6	3.3
4250	$3.498 \cdot 10^{-1}$		2.8	3.3
4500	$2.787 \cdot 10^{-1}$		2.9	3.3
4750	$2.171 \cdot 10^{-1}$		3.3	3.3
5000	$1.700 \cdot 10^{-1}$		3.7	3.4
5250	$1.341 \cdot 10^{-1}$		4.1	3.4
5500	$1.032 \cdot 10^{-1}$		5.0	3.4
5750	$7.737 \cdot 10^{-2}$		5.9	3.4
6000	$5.618 \cdot 10^{-2}$		7.6	3.4
6250	$3.973 \cdot 10^{-2}$		10.6	3.4
6500	$3.048 \cdot 10^{-2}$		12.6	3.4
6750	$2.805 \cdot 10^{-2}$		11.7	3.4
7000	$2.093 \cdot 10^{-2}$		14.1	3.4
7250	$1.139 \cdot 10^{-2}$		21.9	3.4
7500	$7.132 \cdot 10^{-3}$		30.0	3.4

Table 5.2: *The $\bar{\nu}$ -spectrum of the fission products of ^{238}U . The energies given represent the center of the 250 keV wide bins. The error quoted in the third column is the combined inaccuracy of all error sources, apart from the global absolute normalisation uncertainty which is quoted in the last column.*

5.4 Discussion of the results

The $\bar{\nu}_e$ -spectrum obtained has been corrected for all experimental background discussed and represents the pure electron antineutrino spectrum of the fission products of ^{238}U . The spectrum is derived from the β -spectrum recorded using a fast neutron beam emitted by fissioning of ^{235}U (see sec. 2.1.1) and within a time window of ~ 42 hours, beginning approximately 11 hours after the start of the irradiation. Only small deviations from the spectrum at radioactive equilibrium are expected (sec. 3.5).

5.4.1 The $\bar{\nu}$ -spectrum: Comparison of experiment and prediction

In sec. (5.2) the β -spectrum recorded has been compared to predictions of the *summation approach* and the differences seen between measurement and calculation directly transfer to the antineutrino spectrum. The ratio of the antineutrino spectrum of ^{238}U measured in the present thesis to two predictions is given in fig. (5.8).

The errors plotted are solely due to the statistical and systematic uncertainties of the measurement - no errors of the predictions are included. The shaded area represents the error of the absolute normalisation. Similarly as for the β -spectra, the measurement yields a higher antineutrino rate than the prediction by the *summation approach* at energies $\lesssim 4$ MeV. It is remarkable that the predictions exceed the measurement at energies higher than ~ 4 MeV, although the *summation approach* misses part of the short-lived isotopes⁸⁶. The uncertainties the spectra constructed by the *summation method* suffer from are described in [Hub11] and [Mue11]. Only one contribution to the uncertainty will be discussed in more detail in the following:

As mentioned, the *summation method* relies on measurements of individual beta spectra of the fission daughters of the fuel isotopes. These spectra have often been deduced from measurements of the gamma lines emitted in the beta decay with the help of γ -spectrometers with a high energy resolution but a low detection efficiency. It is discussed in [Har77] that those measurements may miss or underestimate the weight of higher-excited nuclear levels, hence, underestimating the intensity of lower β -endpoints. This directly translates into the predictions of the $\bar{\nu}_e$ -spectrum, in which the high-energetic part is enhanced. This spectral distortion is called *pandemonium effect*.

There exist measurements of beta spectra with techniques not affected by the pandemonium effect, see Greenwood et al. [Gre92] and Tengblad et al. [Ten89]. More recently, in 2010, Algora et al. [Alg10] contributed to this field by the determination of the beta spectra of seven additional isotopes with the total-absorption spectrometry (TAS) technique. The spectra of five of the seven isotopes could be confirmed to be affected by the pandemonium effect and its impact on the total $\bar{\nu}_e$ -spectra of the main fuel isotopes is investigated

⁸⁶The authors of [Mue11] quote the error due to the missing contribution to be approximately 10 percent at 2 MeV rising to more than 20% above 7 MeV.

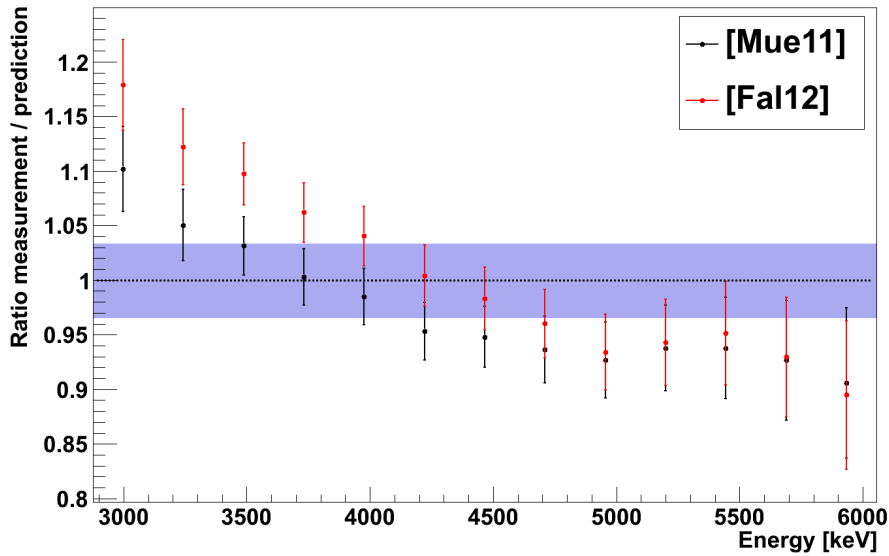


Figure 5.8: The ratios of the antineutrino spectrum obtained in the present thesis to two predictions. [Mue11] is the same publication for which a comparison was discussed using the beta spectra in sec. (5.2). [Fal12] uses a slightly different data set and some spectra of isotopes identified to suffer from the pandemonium effect are replaced by new data. This spectrum was provided by [FalPC], one of the authors of [Fal12]. The influence of the pandemonium effect on the spectrum is further discussed in the text. The error bars represent only the combined statistical and systematic errors introduced by the measurement - to illustrate the accuracy of the experiment performed, the error of the predictions is neglected. The shaded area illustrates the additional error of $\sim 3.3\%$ obtained for the absolute normalisation.

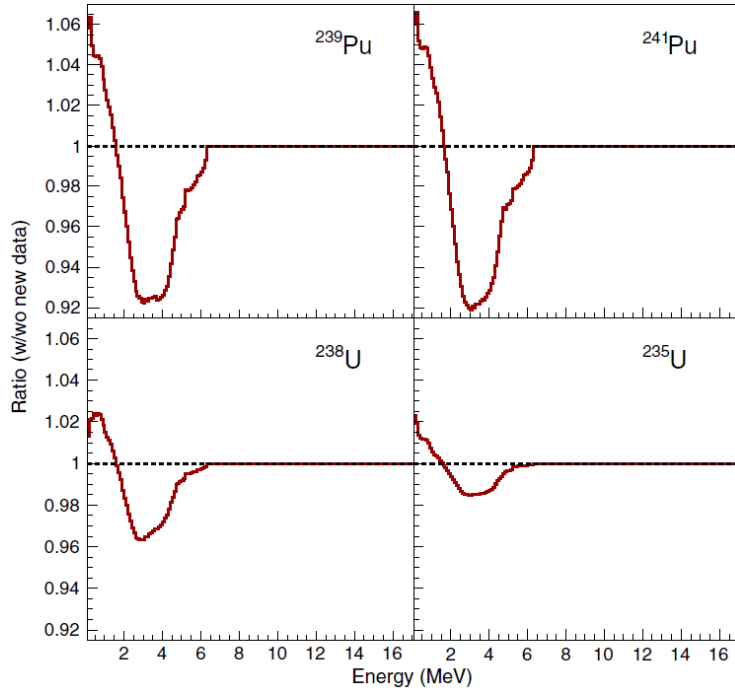


Figure 5.9: *The predicted $\bar{\nu}$ -spectra of the fission products of the four main fuel isotopes including the new TAS data [Alg10] divided by the same spectra but without new TAS data included. Although only five nuclei were identified to suffer from the pandemonium effect and were replaced in the data set, the spectra have changed significantly. One can directly see that the overestimation of high-energetic beta-branches in the old data set is attenuated in favour of the low-energy regime. Plot reprinted with submission from [Fal12].*

in [Fal12]. Figure (5.9) illustrates the remarkable impact these five isotopes have on the total spectra by giving the ratio of the spectra without correction to the corrected ones. As the overestimation of high-energetic beta-branches is attenuated in the new data set, a redistribution of high-energy events to lower energies can be seen. This is of the order of several percent.

The authors of [Fal12] provided us with the new predictions for the ^{238}U antineutrino spectrum expected after 12 h of irradiation. The ratio of the spectrum obtained in the present thesis to the one mentioned is given in fig. (5.8) together with a prediction of [Mue11] not including the new data from [Alg10]. Although it is corrected for the five pandemonium nuclei, the data of [Fal12] differs from the measurement in the lower energy regime more than that of [Mue11]. It is important to mention that up to now isotopes with relatively low Q-values have been re-investigated. Thus, the overestimation of the beta-branches producing electrons with energies of approximately 2 - 5 MeV is reduced and the events are assigned to energies below the experimental threshold of the setup in the present thesis. There are measurements ongoing [FalPC] re-evaluating beta decays of additional potential pandemonium isotopes with higher Q-values. This will probably reduce

the high-energetic content in the *summation approach* above ~ 4 MeV and enlarge the flux predicted for energies up to 4 MeV. As a consequence, this may reabsorb the spectral effect introduced by the correction and further adapt the predictions to the measurement. It is hard to estimate how big the effect of the remaining pandemonium nuclei is in the predictions with the *summation method* - but as is shown in fig. (5.9) the replacement of only five isotopes can cause effects of several percent.

5.4.2 Impact of the results on reactor $\bar{\nu}$ experiments

The discussion of figs. (5.8) and (5.9) strongly emphasizes the importance of the measurements performed within the present thesis. The predictions quote errors of more than 10 % at an energy of 3 MeV and more than 15 % at 6 MeV [Mue11], only partly including further unknown errors due to the potential existence of additional pandemonium nuclei⁸⁷. With the setup described in the present thesis, an error of 3.5 % (stat. + sys.) \pm 3.3 % (norm.) at 3 MeV and 7.6 % (stat. + sys.) \pm 3.4 % (norm.) at 6 MeV is reached, enhancing the precision of the knowledge of the antineutrino spectrum.

The impact of the slight changes on the spectral shape (see fig. 5.8) can be illustrated by multiplying the spectrum with the cross section of the inverse beta decay (IBD). The integral of this product is directly proportional to the event rate in a liquid-scintillator detector like Double Chooz and is identical to the mean antineutrino cross section per fission as defined in sec. (1.1.2) in eq. (1.1) on page 4 and shown in a reduced form in eq. (5.3). Figure (5.10) compares the energy dependence of the product for the ^{238}U spectrum measured with two predictions by the *summation method* [Mue11] and [Fal12, FalPC]. One can directly see the improvement reached in the present thesis due to the reduction of the error of the spectrum.

Furthermore, it is of interest to calculate the reduced mean antineutrino cross section per fission, $\sigma_{f, \text{reduced}}^{\text{meas}}$, from the experimental data:

$$\begin{aligned} \sigma_{f, \text{reduced}}^{\text{meas}}(^{238}\text{U}) &= \int_{2.875 \text{ MeV}}^{7.625 \text{ MeV}} S_{U238, \text{meas}}(E) \cdot \sigma_{IBD}(E) dE \\ &= 8.51 \cdot 10^{-43} \\ &\pm 9.07 \cdot 10^{-45} (\text{stat.} + \text{sys.}) \pm 2.80 \cdot 10^{-44} (\text{norm.}) \frac{\text{cm}^2}{\text{fission}} \end{aligned} \quad (5.3)$$

with $S_{U238, \text{meas}}(E)$ being the measured antineutrino spectrum per fission of ^{238}U and $\sigma_{IBD}(E)$ the cross section for the inverse beta decay. The first error includes all energy-dependent experimental errors as described before and the second error (norm.) represents the global energy-independent error due to the uncertainties in the absolute normalisation. For a correct interpretation of this value, one has to take into account that the integral is not evaluated from 0 MeV to infinity but only covers the energy range of the experiment

⁸⁷Also, [Hub11] argues that the error in the predictions assigned to weak-magnetism corrections may be assumed to be too low.

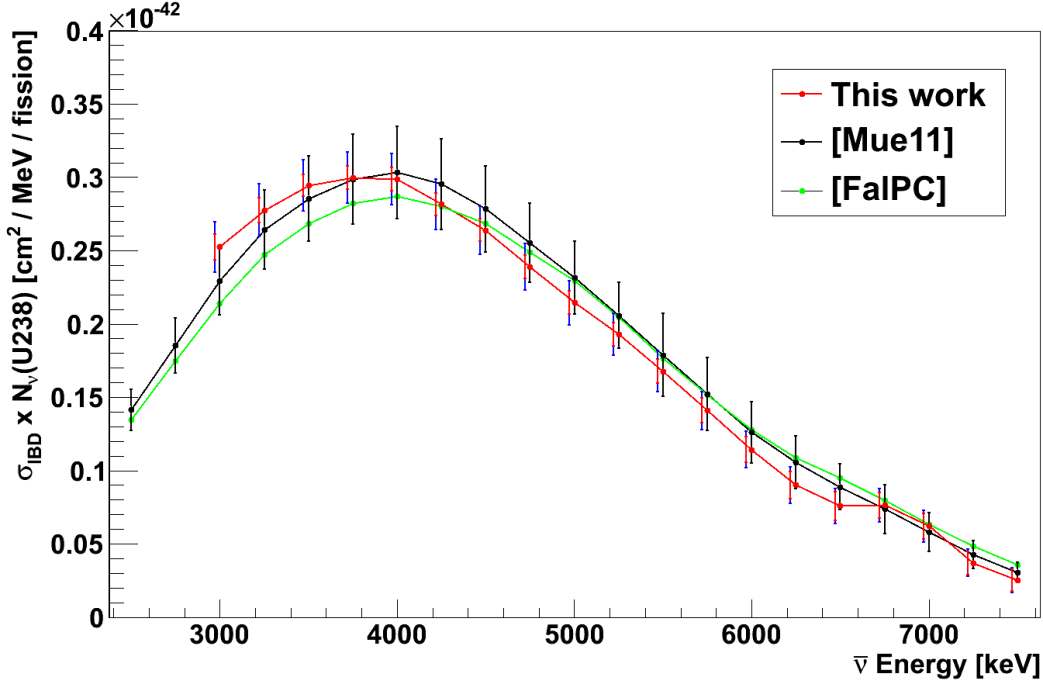


Figure 5.10: Energy dependence of the product of the antineutrino spectrum $N_\nu(U238)$ of ^{238}U and the cross section σ_{IBD} of the inverse beta decay. The integral of the product is the mean antineutrino cross section per fission and, thus, directly proportional to the event rate in a detector. The black data points are calculated from the ^{238}U data given by the summation approach in [Mue11] and the green data represents the new pandemonium-corrected data from [Fal12, FalPC]. The red data points are generated with the measured data from the present thesis. The different data sets have the same binning and the error bars of the red data points are shifted to slightly lower energies only for reasons of visualisation. These error bars of the measured data represent the total error of the experiment, including the contribution due to the combined statistical and systematic error in red and the energy-independent error of the absolute normalisation, added linearly, in blue. The lines are not a fit to the data, but connect the data points to guide the eye. Also due to visualisation issues, the error bars of the green data are not shown; these are of the same order as the black ones. As a direct consequence of the spectral differences between the $\bar{\nu}$ -spectra of prediction and measurement, one can see that the maximum of the product for the measured spectrum is ~ 250 keV lower than the ones for the predictions. The integral of the products is very similar, see also the text.

performed (2.875-7.625 MeV)⁸⁸. This is indicated by the label '*reduced*'. The mean cross section per fission obtained by integrating over this limited range is, obviously, smaller than the common one. However, it is possible to compare this value to the predicted mean cross section per fission $\sigma_f^{pred}(^{238}\text{U})$. In [Men11], $\sigma_f^{pred}(^{238}\text{U})$ is calculated to be $10.10 \cdot 10^{-43} \frac{\text{cm}^2}{\text{fission}} \pm 8.15\%$. The authors of the publication mentioned provide the ^{238}U antineutrino spectrum $S_{U238,pred}(E)$ in [Mue11], enabling us to also calculate the reduced cross section for the limited range and determining the ratio R of the average cross section calculated from measurement and prediction:⁸⁹

$$\begin{aligned} R_{reduced} &= \frac{\int_{2.875 \text{ MeV}}^{7.625 \text{ MeV}} S_{U238,meas}(E) \cdot \sigma_{IBD}(E) dE}{\int_{2.875 \text{ MeV}}^{7.625 \text{ MeV}} S_{U238,pred}(E) \cdot \sigma_{IBD}(E) dE} \\ &= \frac{8.51 \cdot 10^{-43}}{8.76 \cdot 10^{-43}} = 0.97 \pm 0.08 \pm 0.03 \text{ (norm.)} \end{aligned} \quad (5.4)$$

The error of ± 0.08 is calculated by using the relative error for the predicted mean cross section of 8% and the error (stat. + sys.) of the measurement in the present thesis. This error would be only ± 0.01 if one neglects the error of the predictions, only taking into account the uncertainties of the measurement. The experimental error from the normalisation (norm.) is 0.03. For this limited range, measurement and prediction lie well within the errors quoted. An analogous comparison to the new predictions from [FalPC, Fal12] yield a ratio R of 1.00 with an error identical to the one above.

Up to now, the discussion considers only the ^{238}U content, which contributes - as mentioned earlier - roughly 10% to the total antineutrino spectrum. Thus, differences between prediction and measurement are suppressed by a factor of 10 when translating it to the data analysis of, e.g., Double Chooz, which takes into account the full antineutrino spectrum including the contribution of the other three isotopes. A potential impact of the measurement on the Double Chooz data is under investigation at the moment. Any change in the expected event rate has only a small influence on the final value of ϑ_{13} as the anchoring on the Bugey 4 spectrum, as discussed in sec. (1.1.2), absorbs part of the changes to be applied to the predictions. Nevertheless, one can also see a spectral distortion in the energy range around the peak in the event rate (see fig. 5.10) that may affect the outcome of the final global fit of the spectral analysis in the Double Chooz data. The peak is reached approximately one bin (250 keV) lower in the measurement than in the predictions. The first rough estimations made in discussions with the Double Chooz reactor - group point at

⁸⁸As one can see in fig. (5.10), the experiment largely covers a range contributing most to the average cross section.

⁸⁹The antineutrino spectrum has a threshold of 3 MeV. One may follow the trend that the measured spectrum exceeds the predictions at low energy bins and may assume this to occur also for bins lower than this. In fact, if one assumes that the measured spectrum exceeds the predicted one in the bin below the threshold by the same ratio as it does in the lowest bin above threshold, the inclusion of this bin in the analysis enhances the given ratio $R_{reduced}$ of the event rates by only 1%.

possible changes of the value of ϑ_{13} in the regime of few percent and the reduction of the error bars will have an influence on the precision of the final value. To make a statement more precise, the spectrum has to be included in the analysis under consideration of the correlations with the BILL spectra. This work is currently in progress. Furthermore, in the Double Chooz analysis, the mass-squared difference Δm_{31}^2 (and hence the frequency of the oscillation) is currently fixed and only the amplitude of the oscillation is a free parameter. Knowing the antineutrino spectrum emitted from the core, it is also possible to leave Δm_{31}^2 as a free parameter in the spectral fit. The slight shift of the maximum of the peak in fig. (5.10) will have an influence on the value of the mass-squared difference. In addition, the reactor antineutrino spectrum serves as necessary input for a reactor rate modulation analysis, which is a background-independent rate-only analysis of the Double Chooz data [DCPre].

Concerning the reactor antineutrino anomaly, which may be caused by the existence of sterile neutrinos, an influence of the ^{238}U $\bar{\nu}_e$ -spectrum measured in the present thesis on the current status is expected to be of less than one percent [LhuPC]. The deviation from the prediction is small and hardly affects the predicted count rate seen in the former experiments. Furthermore, some of the experiments included in the analysis of the anomaly are supplied by reactors highly enriched in ^{235}U , suppressing the influence of this spectrum even more. Nevertheless, it is an important step to prove that the contribution of ^{238}U has the predicted influence on the total spectrum and does not take part in an unexpected way. A further analysis including the spectrum measured in the present thesis in the actual calculations is on its way [LhuPC].

Furthermore, the experimental determination of the antineutrino spectrum of ^{238}U will improve the accuracy of geoneutrino experiments. The reduction of the error bars allows more precise spectral fits of the data, in which reactor neutrinos are a severe source of background.

Finally, also experiments dedicated to reactor monitoring, and thus the field of non-proliferation of nuclear weapons, benefit from the measurement of the ^{238}U spectrum. The precise knowledge of the $\bar{\nu}_e$ -spectrum enhances the capability to recognise changes in the composition of a fuel assembly.

Chapter 6

Summary and Conclusions

Accurate predictions of the total antineutrino spectrum emitted by a reactor core are crucial for the analysis of reactor neutrino experiments. Currently, these experiments are concerned with the determination of neutrino parameters, the search for sterile neutrinos and the development of small and cheap neutrino detectors for purposes of non-proliferation of nuclear weapons. It is also planned to determine the neutrino mass hierarchy with reactor neutrinos, e.g., as considered by the JUNO collaboration. In addition, antineutrinos from reactors act as background for the search for geoneutrinos and the diffuse supernova neutrino background.

The antineutrino spectrum emitted by a reactor core is generated by the beta decays of the fission products of the four main fuel isotopes, ^{235}U , ^{238}U , ^{239}Pu , and ^{241}Pu . There exist two complementary approaches to predict the total $\bar{\nu}_e$ -spectrum emitted by a reactor. The so-called *summation approach* calculates the amount of each radioactive isotope produced and builds the total spectrum by adding the thousands of branch-level antineutrino spectra of these fission products. This method is claimed to be accurate on the 10-20 percent level. In the second method, one directly measures the total beta spectrum of each of the main fuel isotopes, subsequently converts these β -spectra into the corresponding antineutrino spectra and adds these four contributions to the total spectrum. The difficulty in this approach is the conversion of the beta spectrum into the $\bar{\nu}_e$ -spectrum without the knowledge of the constituting individual branch-level spectra. Nevertheless, this method is much more precise than the summation approach. Of course, both methods need the knowledge of the individual fission rates of the fuel isotopes at any time, a task not further discussed in the present thesis.

Up to now, the antineutrino spectra of three of the fuel isotopes, namely ^{235}U , ^{239}Pu , and ^{241}Pu , have already been determined experimentally by the BILL experiment at the ILL in Grenoble in the 1980's. This was done by the irradiation of target foils with thermal neutrons. ^{238}U , an even-even nucleus, can only be fissioned with fast neutrons of energies above $\sim 1\text{ MeV}$, but those neutron beams have not been available at nuclear reactors so far.

The present thesis completes the experimental approaches by measuring the antineutrino spectrum of the fission products of ^{238}U . An experiment was performed at the neutron

source FRMII in Garching. This neutron source provides one beam place, where both a fast and a thermal neutron beam are available without the need to change the experimental setup. The detector chosen consisted of a spectroscopic module, made of a plastic scintillator and a photomultiplier, and a multi-wire chamber (MWC). These two detectors were operated in coincidence, which allowed to reduce the gamma background emitted from the target or the calibration sources by more than 99.5 %.

For calibration purposes, a ^{207}Bi source and two target foils of polyvinylidene chloride (PVDC) and natural In were used. The ^{207}Bi source emitted mono-energetic electrons from internal conversion with an energy of ~ 1 MeV. The two calibration foils were each irradiated by thermal neutrons, producing ^{38}Cl and ^{116}In , which emit beta spectra with an endpoint of 3.3 MeV and 4.9 MeV, respectively. The calibration turned out to be linear over the whole energy range and an error of less than one percent could be reached.

The response function of the setup was determined by simulation and could be cross checked with the help of the spectrum obtained in the ^{207}Bi measurement. The resolution of the system was determined to be $8\% \cdot \frac{1}{\sqrt{E[\text{MeV}]}}$ (FWHM). Furthermore, the whole setup was shown to work with high stability in time.

The general idea of the experiment is based on a normalisation to the BILL spectrum of ^{235}U mentioned above. As the experimental site at FRMII allows to change the energy of the neutron beam, the beta spectrum of the fission products could be determined for ^{238}U as well as for ^{235}U ; this was accomplished by irradiating natural uranium targets with fast neutrons and thermal neutrons, respectively. However, before the comparison to and normalisation to the BILL spectrum could be performed, several background contributions had to be subtracted from the raw data. In the fast neutron beam, the main contribution in the measurement of the uranium target was identified to be due to *diffuse background*. This event class is fed by gammas, electrons and neutrons scattered in the vicinity of the detector and generating a target-independent rate of coincident events. This contribution could be measured very precisely. But as the signal-to-background ratio is 1 at ~ 3.25 MeV and is further decreasing to higher energies, it finally restricts the sensitivity of the experiment to electron energies up to 7 MeV. Further target-dependent background due to gammas and electrons present in the beam could be determined by the use of dummy targets made of Pb and Ni. This background and the contribution of fissions of ^{235}U ($\sim 3\%$ of the total fission rate in the fast beam) were also subtracted to achieve a background-free ^{238}U beta spectrum. The lower threshold of the experiment was caused by the influence of neutron captures on the plastic scintillator detector itself. As no accurate calculation of the event rate and the spectrum induced by these captures can be given, the lower experimental threshold for the beta spectrum is set to 2.5 MeV.

The background situation in the thermal neutron measurement was very different. As the converter plate of the reactor - that produces the fast neutrons - was removed from the line of sight of the beam line, the diffuse background was largely reduced. The main background to the thermal measurement was caused by neutrons scattered off the target foil and being captured on the material in the vicinity of the detector, thus producing gammas

and electrons. Additional background due to electrons and gammas present in the beam was subtracted. The signal-to-background ratio in the thermal beam was better than the one in the measurement with the fast neutron beam, reaching a value of ~ 5 at 3.25 MeV and a value of ~ 1 at 6.5 MeV.

The β -spectrum of the fission products of ^{235}U obtained was compared to the BILL spectrum. It finally turned out that the normalisation function - defined as the ratio of the spectra measured in the present thesis and the BILL spectrum - was nearly energy-independent, which points at a good understanding of the response function of the detector described in the present thesis. This normalisation function also acted as an absolute calibration to convert the experiment-unique scale of $\frac{\text{betas}}{\text{MeV}\cdot\text{s}}$ to the general scale of $\frac{\text{betas}}{\text{MeV}\cdot\text{fission}}$. The normalisation function received was applied to the ^{238}U beta spectrum. This terminated most of the systematic errors that would be introduced by an inaccurate knowledge of the neutron beam intensity, the beam profile, the participating cross sections and, therefore, of the total fission rate in the target foils. By the comparison to the BILL spectrum, the spectrum of ^{235}U was normalised in absolute height to the very accurate BILL experiment. To apply an absolute calibration of the ^{238}U -spectrum, the relative number of fissions between the thermal and the fast neutron beam measurement had to be determined. This was achieved by performing γ -spectroscopy on the irradiated targets. A germanium spectrometer was used to determine the intensity of the gamma lines of ^{95}Zr , ^{140}Ba and ^{140}La - isotopes that are produced with relatively high yield in the fission process of ^{235}U and ^{238}U . From the peak area of the gamma lines emitted in the decay of the respective radioactive isotopes, the uranium fission rate in the thermal beam could be identified to have been a factor of 44 larger than the one in the fast neutron beam.

Another result of the comparison to the BILL spectrum is very important to mention: In principle, the spectrum obtained by the measurement described within the present thesis has to be de-convolved from the response function to obtain the true beta spectrum of the fission products of ^{238}U . This is an ambiguous task and would have introduced further errors. However, it could be shown that the normalisation to the BILL spectrum cancels the impact of the detector response function on the data. As a consequence, the reader may chose to normalise the spectrum given in the present thesis to any other but the BILL spectrum by simply dividing the final spectrum by the BILL spectrum (bin-wise) and then multiplying it by the calibration spectrum preferred without necessity to know the response function of the setup used in the present thesis.

As a last step in the analysis chain, the electron spectrum obtained was converted into an antineutrino spectrum. Due to the high statistical errors at the high-energy end of the spectrum, the conversion procedure formerly applied to the BILL spectra was not feasible. Instead, another empirical conversion procedure was chosen. Averaged over many decays, the electron and the antineutrino spectra are very similar. The dominant differences between the β -spectrum and the $\bar{\nu}_e$ -spectrum can be corrected for by a shift of the electron

spectrum to higher energies by approximately 560 keV. This shift largely accounts for the fact that part of the energy provided in the beta decay is absorbed in the mass of the electron. Furthermore, it includes an effective correction of the Coulomb-attraction of the charged electron. The remaining differences between the electron and the antineutrino spectra are energy-dependent and of the order of 5 %. These remaining corrections could be extracted from the already known measurements of the BILL spectrum and from the predictions of the spectra by the summation method.

As final result, the antineutrino spectrum of the fission products of ^{238}U is given in 250 keV bins in a range from 2.875 MeV to 7.625 MeV in table (5.2) on page 118. The combined statistical and systematic error is 3.5 % at 3 MeV, 7.6 % at 6 MeV and $\gtrsim 14\%$ at energies $\gtrsim 7$ MeV (all errors, also in the following, are given at 68 % confidence level). In addition to the errors quoted, a nearly energy-independent error of 3.3-3.4 % has to be added due to uncertainties in the absolute calibration. This uncertainty due to the absolute calibration is partly composed of errors inherent in the experiment: the uncertainty of the γ -spectroscopy and a dead-time correction with the help of a muon-induced peak in the data at 13 MeV. Aside from these, it includes an error due to the conversion method of 2 % and an uncertainty of 1.7-1.9 % due to the absolute calibration error of the BILL measurement. These two contributions have to be considered when including the spectrum measured in the present thesis in global fits of the current reactor antineutrino experiments, as correlations to the BILL spectrum and the predictions occur.

A comparison of the antineutrino spectrum obtained in the present thesis and the predictions by the summation approach (see fig. 5.8 on page 120) results in the conclusion that a slight energy-dependent correction has to be applied to the spectrum used in the reactor experiments up to now. At an energy of ~ 3 MeV, the predictions underestimate the antineutrino spectrum by ~ 10 -15%. This tension between measurement and prediction relaxes with rising energy and around 4 MeV the spectra obtained by calculation and experiment are very similar. Above ~ 4 MeV the predictions tend to over-estimate the spectrum by a bit less than 10%. This spectral distortion may finally lead to a slight change of the value of ϑ_{13} obtained in the Double Chooz experiment, for example.

One reason for the difference of experiment and prediction is introduced by the pandemonium effect, which adds a systematic uncertainty to the predictions. This effect leads to a systematic overestimation of high-energetic beta-branches in the measurements of some fission daughters and causes a spectral distortion in the predictions. There are new measurements ongoing with the goal to further identify and correct for isotopes suffering from the pandemonium effect.

However, the average antineutrino cross section per fission, σ_f , which is directly proportional to the absolute detected neutrino rate in a reactor antineutrino experiment, is determined to be identical to the predicted one in the energy range considered. The value for $\sigma_{f, \text{reduced}}$ obtained in the present thesis is $8.51 \cdot 10^{-43} \pm 9.07 \cdot 10^{-45}$ (stat. + sys.) $\pm 2.80 \cdot 10^{-44}$ (norm.) $\frac{\text{cm}^2}{\text{fission}}$; the label 'reduced' indicates that the average antineutrino

cross section per fission is not derived by integrating the total antineutrino spectrum, but only the part inside the experimental energy boundaries. The ratio of the value obtained in the measurement to the ones from the summation approach is 0.97 and 1.00, depending on the prediction chosen, with an error in the 10% regime dominated by the error of the predictions.

It is noteworthy that the antineutrino spectrum of the fission products of ^{238}U is not differing from the predictions enough to explain the reactor $\bar{\nu}$ anomaly. Other explanations for the lack of antineutrinos seen by the reactor experiments performed so far have to be found. The significance of the reactor anomaly is currently subject of discussion in the literature and it has to be clarified whether the anomaly is created by faulty predictions of the expected antineutrino rates or by real physical processes, e.g. the existence of sterile neutrinos with a mass in the eV regime. It is an important input to the discussion, that the spectrum of ^{238}U contributes in the predicted way.

Furthermore, this first experimental determination of the antineutrino spectrum of the fission products of ^{238}U enhances the accuracy and prediction of all current and future reactor-based antineutrino experiments by improving the predictions for the total antineutrino spectrum emitted by a reactor core. It supports experiments concerned with the determination of the neutrino parameters as well as the non-proliferation of nuclear weapons by monitoring of reactor assemblies with neutrinos and helps to improve neutrino experiments investigating geoneutrinos and the diffuse supernova neutrino flux, where antineutrinos from reactors act as significant background to the signal.

In conclusion, the results of the experiment performed in the present thesis allow to calculate the $\bar{\nu}_e$ -spectrum emitted by nuclear reactors without the necessity to use predictions for the antineutrino spectrum of the fission products of the fuel isotopes.

Appendix A

Neutron scattering

Neutrons are not scattered by the same amount off the three target foils. This originates from inherent differences in the scattering cross section and the amount of nuclei in the targets. As the absolute neutron flux in the beam is not known, one can only estimate the relative amount of scattered neutrons compared between the particular targets. One can define the total target-specific scattering cross section X of a target by:

$$X_{Target} = \sum_i N_i \int_E \sigma_i(E) \Phi(E) dE \quad (\text{A.1})$$

with $i \in \{\text{Ni, Pb, U}\}$, σ being the total neutron scattering cross section for the various isotopes, N being the number of atoms of this isotope in the beam and Φ being the spectral neutron flux. The integral represents the mean neutron scattering cross section, averaged over the particular energy spectrum.

In the thermal beam, the spectrum reduces to mono-energetic neutrons and equation (A.1) can be simplified:

$$X_{Target} = \sum_i N_i \sigma_{i,th}. \quad (\text{A.2})$$

For the calculation of X in the thermal beam, the following cross sections have been used:

- σ_{Ni} : 18.5 barn - total bound neutron scattering cross section for natural Ni⁹⁰
- σ_{Pb} : 11.12 barn - total bound neutron scattering cross section for natural Pb
- σ_U : 8.908 barn - total bound neutron scattering cross section for natural U

For the fast beam, the integral has to be evaluated bin-wise. For each bin of the fast neutron spectrum⁹¹ the average value of the neutron scattering cross section⁹² is calculated

⁹⁰The total bound thermal neutron scattering cross sections are taken from [Sea92].

⁹¹The neutron spectrum is described in section (2.1.1).

⁹²This includes both elastic and inelastic processes. The data for this is taken from the *Pointwise ENDF-VII at 300 K*. database [END12]

and multiplied with the neutron flux in this bin. The integral in eq. (A.1) reduces to a sum over all bins to calculate the mean scattering cross section.

The exact determination of target atoms N in the beam is limited by the knowledge on the beam profile. The beam is collimated to a width of about 3 cm, but due to an unknown opening angle, the size of the beam may have widened at the target position. Hence, the foil in the center of the targets is always fully irradiated, while the beam only covers part of the surrounding nickel foils (the backing foils of 10 μm thickness in which the active targets are wrapped). As this amount of nickel in the beam is not known precisely and the cross section for scattering on nickel varies from the ones of uranium and lead, the calculation of the relative number of scattered neutrons leads to systematic uncertainties. In addition, this estimation assumes a homogeneous neutron flux density over the beam cross section.

The number of target atoms for each isotope is determined via:

$$N = \frac{V \cdot \rho}{M} \quad (\text{A.3})$$

With ρ and M being the mass density and the atomic mass of the isotope, respectively, and V being the volume of material in the beam. As mentioned, this volume contributes the biggest error to the final value of the total target-specific cross section. The error quoted in the result below is given for an uncertainty of 25% of the beam width at the target position, which is a conservative estimation. The exact value of this analytical calculation of the cross section (as well as its error) is not used in the data analysis of the uranium spectra, as it can be extracted directly from the thermal neutron beam measurements; but the similarity of the theoretical value and the one measured affirms the interpretation of the additional background in the thermal beam to be caused by neutrons (sec. 4.2.3). In addition, this can show that scattering of neutrons is not a significant source of background in the fast neutron beam data (sec. 4.2.1).

Eventually, one can calculate the relative number of scattered neutrons in the thermal beam to be:

$$\begin{aligned} X \left(\frac{Pb}{Ni} \right)_{th} &\equiv \left(\frac{X_{Pb}}{X_{Ni}} \right)_{th} = 0.57 \pm 0.06 \\ X \left(\frac{U}{Pb} \right)_{th} &\equiv \left(\frac{X_U}{X_{Pb}} \right)_{th} = 0.96 \pm 0.01 \end{aligned}$$

Even with a quite high error in the relative amount of scattered neutrons on the lead compared to the Ni target, the ratio of U and Pb is estimated with a rather small error, due to the similar neutron scattering cross section of uranium and lead.

In the fast beam the values are:

$$X \left(\frac{Pb}{Ni} \right)_f \equiv \left(\frac{X_{Pb}}{X_{Ni}} \right)_f = 0.74 \pm 0.03$$
$$X \left(\frac{U}{Pb} \right)_f \equiv \left(\frac{X_U}{X_{Pb}} \right)_f = 1.04 \pm 0.01$$

The error in the fast beam is smaller than in the thermal beam. The origin for this is the difference in the scattering cross sections for thermal and fast neutrons on nickel. As explained, the error is dominated by the uncertainty in the beam width, which effectively influences the number of nickel atoms in the beam in the two foils surrounding the targets. The cross section for thermal neutrons scattered off nickel is higher than the one for the other isotopes, but for fast neutrons this is the other way around. Thus, in the fast beam a higher amount of neutrons scatter off the central target foil and the additional amount of nickel plays a minor role. However, also for the fast beam the values are not used in the analysis, but are predicted only to qualitatively estimate the relative magnitude of the scattering processes.

Appendix B

Exponential smoothing

B.1 The method of exponential smoothing

At some point, the spectra given in literature and the spectra obtained in this work have to be compared with each other but are presented in different binning. In most cases, the width of the binning is the same, namely 250 keV, but the center of the bin is shifted. The histograms in this work are generated in a way that the energy of 0 keV is the left border of the first bin. Subsequently, each bin is centered around $125 \text{ keV} + (i - 1) \cdot 250 \text{ keV}$, with i being the number of the bin. The convention in some papers - including the BILL paper [Sch85] - is to center the bins around $(i - 1) \cdot 250 \text{ keV}$ without shifting it by 125 keV. Furthermore, the conversion method from the electron spectrum into an antineutrino spectrum requires a shift of 561 keV. After this, the resulting histogram has to be re-binned into a convenient binning. This leads to the need of a re-binning procedure when comparing the two kinds of histograms.

An accurate way of performing the re-binning for the fission beta spectra is *exponential smoothing*. This method yields very small errors, as the beta spectra of the fission products themselves can be approximated by exponentials to a large extent. To obtain the bin content of the transformed histogram, for each of the new bins one fits a simple exponential e^{-aE} to the four surrounding bins of the original histogram. The gained function can now be integrated to get the bin entry of the new spectrum (see fig. B.1). This is repeated for every single bin in the new histogram, except for the first and the last bin of the new histogram. Here one has to take the fit function of the second and the last-but-one bin, respectively, and generate the re-binned entry from these, which does not affect the goodness very much.

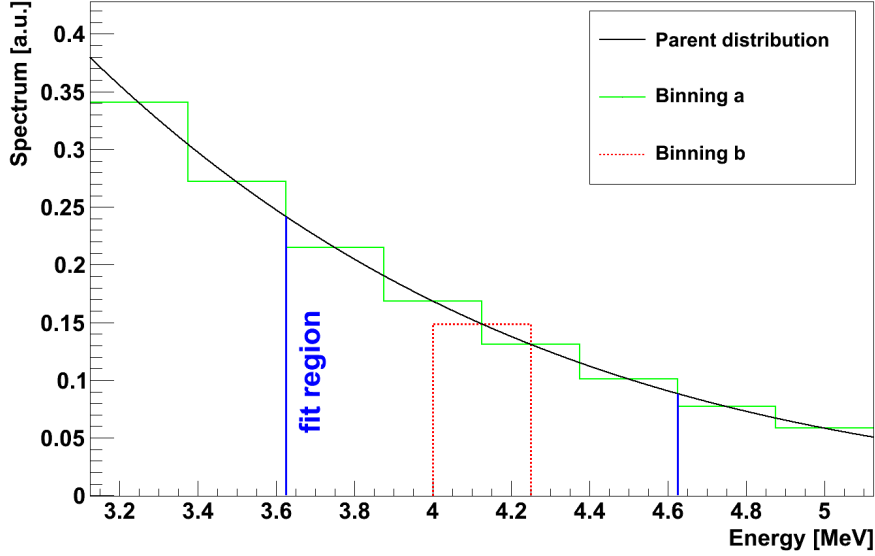


Figure B.1: To calculate the bin content of the transformed histogram, the four surrounding bins of the original histogram (green) are fitted by an exponential. The bin entry of the new, re-binned histogram (red) is the integral of this fit function over the bin width.

Applying this procedure, e.g., to the BILL spectrum results in an energy independent underestimation by 5%, which is corrected for and is far below the experimental errors.

The error is determined in the following way: A test parent function $f(E) = \exp(g(E))$, with $g(E)$ being a polynomial of third order is fitted to the full BILL spectrum. This function now serves as parent to create two histograms H1 and H2 with different binning. H1 is then converted into the binning of H2 to create histogram H1'. The resulting converted histogram H1' is then compared to H2 and

The way to estimate the error of the re-binning method is used for every histogram that has to be re-binned: An appropriate parent function is generated to mimic the characteristics of the histogram which has to be re-binned. From this parent function, two different histograms H1 (with the old binning) and H2 (with the new binning) are created. These now perfectly match the spectrum one would measure if assuming the parent function to be the true spectrum. Subsequently, H1 is re-binned into the binning of H2, creating histogram H1'. The resulting converted histogram H1' is then compared to H2 and the bin-wise deviations between these is interpreted as error of the re-binning method for each bin individually. See also fig (B.2) for clarification of this technique.

For the BILL spectrum, a parent function $f(E) = \exp(g(E))$, with $g(E)$ being a polynomial of third order is fitted to the full spectrum. It turns out that, over the whole energy range, the error is in the range of $5 \cdot 10^{-3}$.

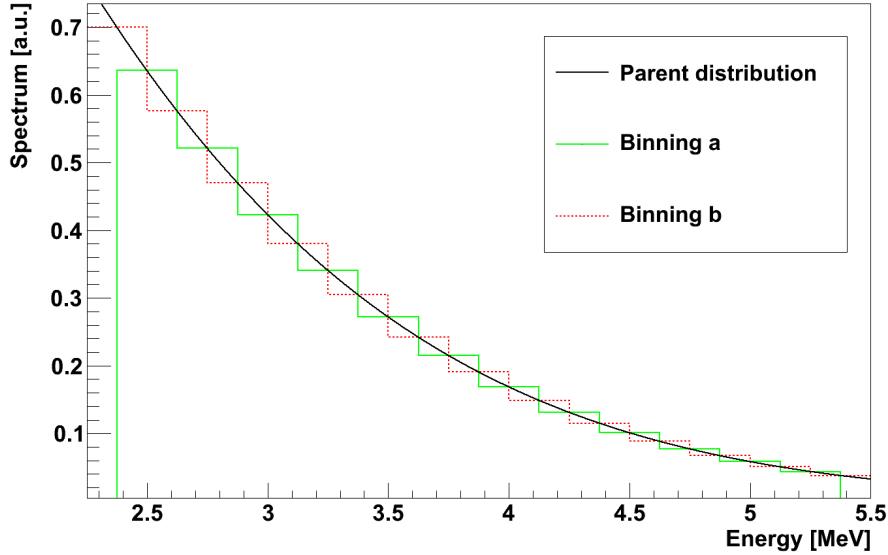


Figure B.2: *The assumed parent distribution is given as continuous function (black). From this, one can obtain histograms in any binning by integrating the parent function over the bins chosen. Shown are the two binnings that are used in literature (green) and in the present work (red). To estimate the error of a re-binning procedure, one re-bins one histogram to the binning of the other and compares the output with the true spectrum directly derived from the parent function.*

B.2 Test of the re-binning method on the final data

The method of exponential smoothing can only be applied to spectra that innately are sufficiently smooth, i.e. functions that can be described by an exponential function with an exponent of grade much smaller than the number of bins of the histogram. This is the case for all β - and $\bar{\nu}$ -spectra predicted for the fission fragments of the isotopes investigated. However, the spectrum measured in this thesis differs from an exponential at energies above 6 MeV, because of which the procedure cannot be applied in this energy range.

In the exponential smoothing method performed to re-bin the final antineutrino spectrum, three bins of the original histogram are fitted by an exponential. One can directly test the accuracy of the fitting procedure by comparing the integral of the fit over one of these bins with the original bin content. Hence, the test is a measure how well the original data is reproduced by the fit. Figure (B.3) shows the ratio of the antineutrino data (see also sec. 5.3) and the fit for each bin. In the region up to energies of ~ 6 MeV, the fit is able to reproduce the data with an accuracy of mostly better than 3%, but above ~ 6 MeV, as expected, the fit differs a lot from the data. This is a direct result of the

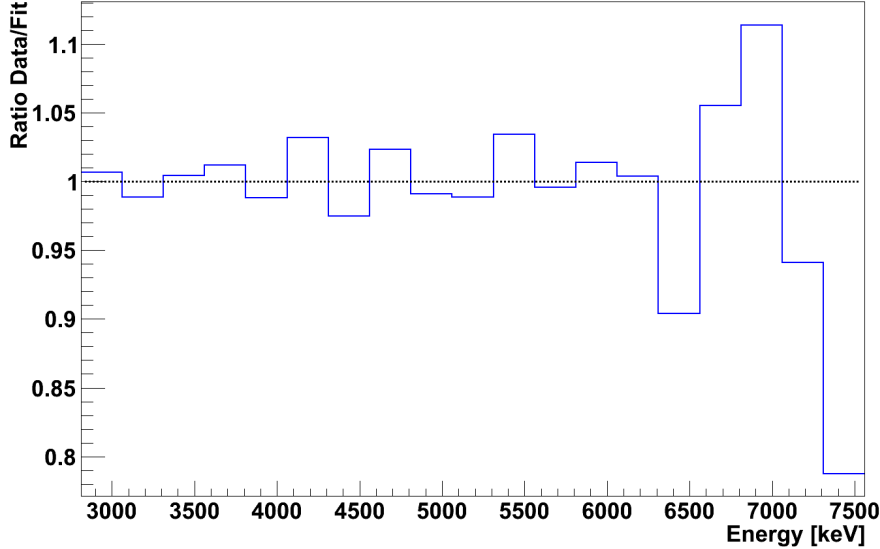


Figure B.3: *Test of the error of the re-binning technique of exponential smoothing. The plot shows the ratio of the original data and the integral of the fit-function over the corresponding bin. Below 6 MeV, the error is not exceeding $\sim 3\%$, however, at higher energies the spectrum is not sufficiently smooth to apply an exponential fit to good accuracy. Hence, the re-binning procedure is altered to a linear interpolation, given in fig. B.4).*

non-exponential-like behaviour of the measured data in this regime.

To lower the error induced by the re-binning method for energies above 6 MeV, a linear interpolation between two neighbouring points is performed to calculate the bin content of the shifted bin. This technique is able to lower the error to below 5 percent above 6 MeV. This is evaluated by fitting a polynomial of order six to the antineutrino spectrum. The obtained fit function does not reproduce the spectrum at several points, but it is only generated to produce a parent function imitating the slope of the antineutrino spectrum. From this parent function a histogram is generated, which then is re-binned by a simple linear interpolation. From the comparison of the re-binned spectrum with the original parent fit-function, one directly gets an estimate of the errors made with this method of interpolation.

Figures (B.4) illustrates the method performed and shows the deviation of the re-binned histogram from the true values obtained by integration of the parent function. One directly observes that the errors of this technique can be minimised to values beneath 5% in contrast to the 10-20% obtained by the method of exponential smoothing (fig. B.3). As the function is mostly left-bended, this interpolation leads to this slight overestimation. Although the parent function used for this test differs from the real spectrum, the slope of the function is very similar and thus the deviations obtained can be interpreted to be approximately the same for the re-binning procedure applied.

B.2. TEST OF THE RE-BINNING METHOD ON THE FINAL DATA

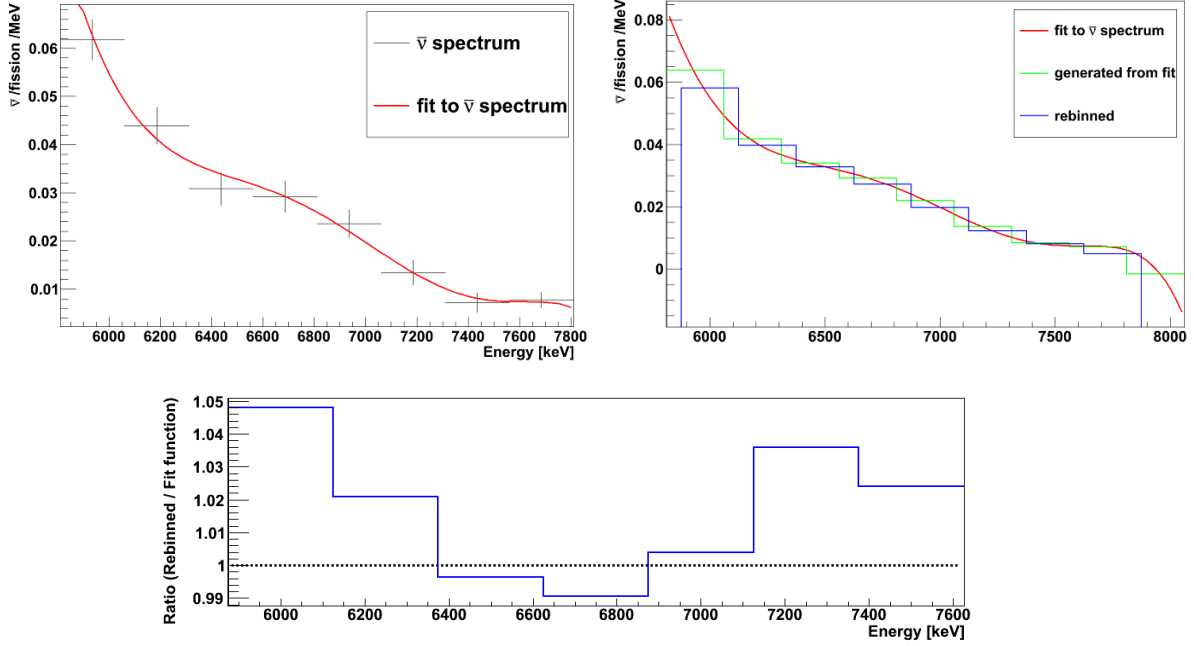


Figure B.4: *The technique to test the inaccuracy of the linear interpolation. A polynomial of order 6 is fitted to the antineutrino spectrum (top left) to generate a smooth parent function imitating the characteristics of the real data. Top Right: This function is used to generate a histogram (green), which subsequently is re-binned via a linear interpolation into another one with now different binning (blue). Bottom: The re-binned spectrum then is compared bin-wise to the integral of the parent function over the bin tested. The ratio of the re-binned histogram and the fit-function shows only small variations which is a major improvement in contrast to the exponential smoothing in the regime above 6 MeV, see fig. (B.3).*

Hence, the re-binned antineutrino spectrum is corrected for this. The error one introduces by this is estimated to be one third of the correction itself. This was determined by varying the parameters of the parent function within the errors quoted by the fit, locally changing the slope at different positions and re-doing the test. As the error of the correction is small compared to the already existing one at these high energies, it has nearly no effect on the final error bars.

In the final presentation of the $\bar{\nu}_e$ -spectrum in figure (5.7) and tab. (5.2) on page 117f., the errors of this re-binning are already included.

Appendix C

Tests of the electronics

To test the linearity, the behaviour at high count rates, and the dead-time determination, the whole electronics chain including the photomultiplier was tested. In the following, the most relevant tests are discussed.

C.1 Test of linearity

The energy calibration in section (3.3) is based on three calibration points at about 1 MeV, 3 MeV and 5 MeV. A linear fit to these data points shows the linearity of the whole electronics chain, including the photomultiplier. As a test of the energy calibration at higher energies, one can have a look on the position of the muon peak explained in section (3.4). This peak is populated by muons crossing the scintillator and can be found at the expected energy of 13 MeV. The correct position of this peak is a hint for the linearity above 5 MeV and already shows that possibly occurring quadratic terms in the calibration function are small. This was also tested prior to the beam time:

Two LEDs⁹³ with a wavelength near the peak of the scintillator emission were installed in the cross piece of the experiment. A diffuse reflector at the target position was illuminated by the LEDs. For this test, the multi-wire chamber was removed from the setup and thus the photons could enter the scintillator unhindered. The photomultiplier then detected the light and the signal was processed through the electronic chain.

Both LEDs were triggered at the same time but by different pulser modules. LED + was kept at a constant luminosity corresponding to about 2 percent of the ADC range, switching it off and on but never changing the voltage supplied.

At first, LED I was set to a luminosity corresponding to a low ADC channel and LED + was off. Then LED + was additionally turned on, increasing the signal - and thus the ADC channel fed - by a certain amount X . Then LED + was turned off again and LED I was manually increased in light output to the former sum-channel of both LEDs. Now,

⁹³In the following the LEDs will be labelled as LED I and LED +.

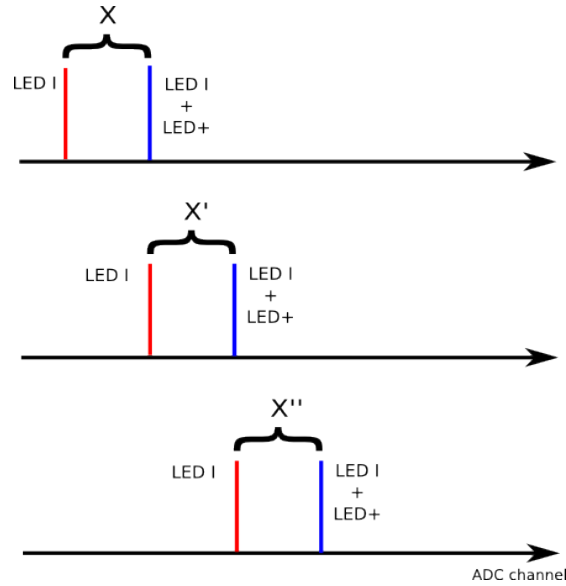


Figure C.1: *LED I* is set to a luminosity corresponding to a random low ADC channel (red line, upper plot). When switching on *LED +*, the additional light increases the signal height by a certain amount X (blue line). Afterwards, *LED +* is switched off, the value X is saved and *LED I* is increased in luminosity to approximately the sum value of both LEDs (red line, second plot). Again, *LED +* is turned on and one determines the value X' . This is repeated until the whole range of the ADC is tested. As all X^i have an identical value, the electronic chain, including the PM, is proven to be linear up to high luminosities.

LED + was turned on again and the signal increase X' was recorded⁹⁴. This procedure was repeated until all the active area of the ADC was covered, always recording X when adding *LED +* to the light of *LED I*. Figure (C.1) illustrates this method. It turned out, that the value for X was always the same, independent from the luminosity of *LED I*. This means, no matter how high the light signal from *LED I* (representing the energy deposition of a particle in the scintillator) was, the additional light added always the same signal height to it. This directly proves the linearity of all of the electronics at once.

C.2 Test of the automatic dead-time correction

The data acquisition system determines and saves the dead-time together with the spectral data. As the measurements with the fast and the thermal neutron beam have different count rates⁹⁵, the dead-times and thus the normalisation of the spectra varies. For the absolute normalisation of the ^{238}U spectra, it is of importance to know the relative

⁹⁴It is of no importance to exactly tune the luminosity of *LED I* to the sum of both LEDs. This is only done to test the linearity in every regime. For a quick solution one could also have tested the value X once for low intensity of *LED I* and compare it to a value at the upper end of the ADC range.

⁹⁵See table (D.1) in appendix (D) for a comparison of the count rates in the different measurements.

C.2. TEST OF THE AUTOMATIC DEAD-TIME CORRECTION

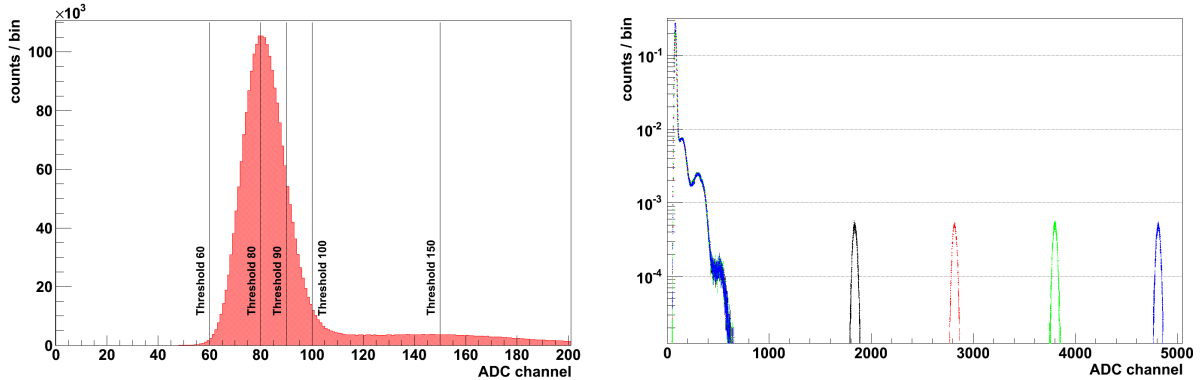


Figure C.2: *Left:* The Bi source was placed near the detector, resulting in a high count rate of about 10 kHz. By changing the threshold of the main amplifier of the PM-chain (vertical lines), it was possible to adjust the count rate passed to the electronics in a range from ≈ 100 Hz to 10 kHz. *Right:* For each of these thresholds several spectra were recorded with different heights of a pulser signal. In the plot shown, the threshold was chosen to be very low, resulting in a high count rate. Even with a high count rate, there is no energy dependence of the efficiency as is demonstrated by the equal areas of the pulser peaks.

amount of fissions in the two beams (as determined in sec. 4.5) and the efficiency of the system in the individual measurements. The latter is directly connected to the dead-time of the electronics and can be simply measured in situ by investigating the area of the muon peak as explained in (3.4.2). However, in principle it could be possible that the loss of intensity in the muon peak is not an energy independent dead-time effect, but some kind of saturation effect, influencing only the high-energetic part of the spectrum at high count rates. Although these effects are quite unlikely, it has to be shown that:

- ... the automatic dead-time correction of the ADC-MPA system is not correct. Otherwise, the loss in the muon peak would have been corrected for in the live time normalisation.
- ... the system loses effectivity at higher count rates, but this happens with the same magnitude for all energies.

For this purpose, a laboratory measurement was performed. The ^{207}Bi source was placed near the detector, generating a high count rate of about 10 kHz in the photomultiplier. In the following measurements, the input threshold of the main amplifier was varied, passing an adjustable count rate to the subsequent electronic devices. In addition, a pulser signal with a rate of 50 Hz was fed to the ADC to determine the true dead-time of the system. This signal height of the pulser was varied, to scan the full ADC range and see if there is energy-dependent loss of efficiency. Figure (C.2) illustrates the test performed.

In every measurement at one particular count rate, the pulser peaks had all the same area. Hence, the efficiency of the electronics is not energy-dependent and the dead-time can be interpreted as a global efficiency loss. However, it turned out that the peaks at higher

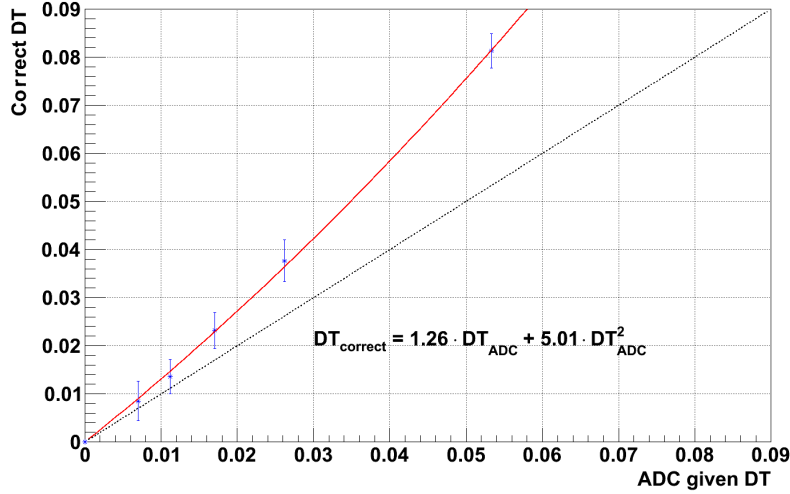


Figure C.3: *The true dead-time of the system, defined by comparing the area of the pulser peak with the known real frequency, as a function of the dead-time automatically determined by the data acquisition system. One can clearly see a deviation from the ideal straight line indicated.*

count rates lost intensity relative to low count rate measurements, even when correcting for the dead-time quoted by the ADC.

It is obvious from figure (C.3) that the true dead-time deviates from the one determined by the DAQ. This has two contributions: Firstly, the DAQ can only calculate the dead-time from the incoming signal. If the dead-time is produced by a device prior to the ADC, the DAQ cannot recognise this as dead-time. And secondly, the data acquisition quotes the dead-time generated by the ADC and the signal transport to the PC inaccurately. Further tests showed that the truth is the combination of these two points, but as the muon peak provides the possibility to renormalise the spectra correctly, these cross checks are not of interest here.

Of course, the test explained above does not include the PM and its pre-amplifier. It could only be shown that the electronics has no energy-dependent efficiency, but the PM may saturate in some way. To test the functionality of the photomultiplier, a similar test was performed, replacing the pulser signal, which was fed into the electronics after the main amplifier, by a pulsed LED. For this test, the source was placed at different distances from the PM, generating different count rates. Analogously to the test of the electronics, for every count rate different intensities of the LED were measured, scanning the whole dynamic range of the system. As in the prior test, it could be shown that a loss in efficiency occurred, which was independent of the pulse height of the LED and only a function of the count rate. Hence, also the PM is not a possible source of a spectral distortion.

C.2. TEST OF THE AUTOMATIC DEAD-TIME CORRECTION

From these tests, it can be concluded that the loss in intensity of the muon peak in the thermal uranium measurement is due to an energy-independent efficiency loss and does not lead to spectral distortions. Thus, this peak is a measure of the dead-time and the efficiency of the setup, including the electronic dead-time effects and possible inefficiencies of the MWC at higher count rates.

Appendix D

Tables

D.1 The main measurements

The irradiation time of the most important measurements are given in table (D.1). One spectrum may consist of several shorter files⁹⁶, but only the sum of all uranium measurements and the background data are given and handled as one long measurement.

Target	Beam	Time [s]	R(co) [1/s]	R(w/o co) PM [1/s]	R(w/o co) MWC [1/s]
U	th	56920	430	5000	1500
U	fast	151613	50	1300	190
Pb	th	177566	35	1760	110
Pb	fast	188093	15	1200	55
Ni	th	3558	70	2634	120
Ni	fast	84301	16	-	-
w/o	th	2973	10	475	15
w/o	fast	29767	10	1160	30

Table D.1: *The main measurements used in the analysis. The table indicates the spectrum of the neutron beam, the time of irradiation and the count rate $R(\text{co})$ for the coincidence mode. The last two columns give the count rate R without coincidence and therefore distinguish between the rates in the PM and the MWC. For uranium only the time for the used data set, i.e. without the first 11 hours, is given.*

⁹⁶The measurements were stopped and directly continued only for purposes of data handling and storing, during the irradiation of a target, no changes were applied to the detector, the electronics setup or any other parameters.

D.2 Fission yields

Isotope	Y(^{235}U , th) [%]	Y(^{235}U , f) [%]	Y(^{238}U , f) [%]
^{95}Zr	6.5	6.43	5.14
^{140}Ba	6.21	5.98	5.82
^{140}La	0.0052	0.0002	0.00002

Table D.2: *The fission yields of the isotopes used for the determination of the fission rate in the uranium foils during irradiation. For Zr and Ba these are the cumulative yields and for La this is the individual yield. Values taken from [Eng93].*

List of Figures

1.1	The reactor anomaly	4
1.2	Reactor fuel evolution and fission yield distribution	10
2.1	Sketch of the experimental site at FRM II	17
2.2	The multi-leaf collimator at SR10	17
2.3	Neutron guidance in SR10	18
2.4	The fast neutron spectrum	19
2.5	Gamma spectrum present in the fast neutron beam	21
2.6	The experimental setup; front view	22
2.7	The experimental setup; side view	23
2.8	The plastic scintillator	24
2.9	The spectroscopic module	25
2.10	The boards of the multi-wire chamber	26
2.11	The electric field configuration inside the multi-wire chamber	27
2.12	The detector module	28
2.13	Photograph of the experimental setup	29
2.14	The target mounting device	30
2.15	Electronics and DAQ	33
3.1	Exemplary Coincidence matrix	41
3.2	The detector response functions	44
3.3	Energy deposition in the target foils	45
3.4	Influence of backscattering and bremsstrahlung on the deposited energy	47
3.5	Comparison of ^{207}Bi data and simulation	48
3.6	Peak determination in the ^{207}Bi calibration	51
3.7	^{207}Bi pre-calibration with the peak at 1.7 MeV	53
3.8	Influence of the Gaussian broadening on Kurie plots	54
3.9	Final energy calibration	56
3.10	Stability of the ^{207}Bi peak position	60
3.11	Dead-time determination by analysis of the muon peaks	61
3.12	Off-equilibrium effects in the ^{235}U data	64
4.1	Sketch of the analysis chain	69

LIST OF FIGURES

4.2	Impact of decay-correlated background on the β -spectrum I	71
4.3	Impact of decay-correlated background on the β -spectrum II	72
4.4	Measured spectra in the fast neutron beam without coincidence	74
4.5	Measured spectra in the fast neutron beam in coincidence	75
4.6	Residual low-energy background in Pb and Ni measurements: Comparison to simulation	77
4.7	Results of the χ^2 fit to the gamma-induced background in the fast neutron beam	79
4.8	Relative error of the β -spectrum of ^{238}U after subtracting the beam induced background (fast neutron beam)	81
4.9	Measured spectra in the thermal neutron beam in coincidence	84
4.10	Thermal neutron scattering off Pb and Ni	85
4.11	Influence of gamma and electron scattering on the thermal uranium measurement	87
4.12	Measured β -spectrum of the fission products of ^{235}U (thermal fission)	88
4.13	Relative error of the beta spectrum of ^{235}U	89
4.14	Ratio of ^{235}U beta spectra induced by neutrons with different energies	92
4.15	The measured β -spectrum of ^{238}U and its backgrounds	93
4.16	The normalisation function obtained by the comparison to the BILL data	96
5.1	The final beta spectrum of the fission products of ^{238}U	104
5.2	The impact of the inaccuracy of the energy calibration	107
5.3	Comparison of prediction and measurement of the beta spectrum of ^{238}U I	109
5.4	Comparison of prediction and measurement of the beta spectrum of ^{238}U II	111
5.5	Conversion procedure: The correction factor $k(E)$	114
5.6	The influence of E_{shift} on the conversion	116
5.7	The final $\bar{\nu}_e$ -spectrum of the fission products of ^{238}U	117
5.8	$\bar{\nu}$ -spectrum of ^{238}U : Comparison of measurement and predictions	120
5.9	Impact of five pandemonium nuclei on the fission spectra	121
5.10	Product of the antineutrino spectrum of ^{238}U and the IBD cross section	123
B.1	Visualisation of the re-binning procedure: Exponential smoothing	138
B.2	Generation of histograms from parent function	139
B.3	The inaccuracy of the exponential smoothing on the final data	140
B.4	Testing the accuracy of the re-binning by means of linear interpolation	141
C.1	Testing the linearity of the electronics	144
C.2	Test of energy-dependence of the efficiency	145
C.3	Test of the dead-time determination of the ADCs	146

List of Tables

1.1	Characteristics of antineutrinos emitted in thermal fission of ^{235}U and ^{239}Pu	7
2.1	Electronic devices and DAQ	35
3.1	Results of the Kurie calibration by means of In and Cl	55
3.2	Test of the final energy calibration	57
3.3	Ratio of the muon rates in the main measurements	63
3.4	Calculation of off-equilibrium effects	65
4.1	Absolute calibration: Results of γ -spectroscopy	102
5.1	The final β -spectrum of the fission products of ^{238}U	105
5.2	The final $\bar{\nu}_e$ -spectrum of the fission products of ^{238}U	118
D.1	The main measurements	149
D.2	Fission yields	150

LIST OF TABLES

Bibliography

- [Aar13] M. G. AARTSEN ET AL.: "Measurement of the Atmospheric ν_e flux in IceCube", Phys. Rev. Lett. 110, 151105 (2013).
- [Abe12a] Y. ABE ET AL.: "Indication of Reactor $\bar{\nu}_e$ Disappearance in the Double Chooz Experiment", Phys. Rev. Lett. 108, 131801 (2012).
- [Abe12b] Y. ABE ET AL.: "Reactor $\bar{\nu}_e$ disappearance in the Double Chooz experiment", Phys. Rev. D 108, 052008 (2012).
- [Ada11] P. ADAMSON ET AL.: "An improved measurement of muon antineutrino disappearance in MINOS", Phys. Rev. Lett. 108, 191801 (2012).
- [Ago03] S. AGOSTINELLI ET AL.: "GEANT4 - a simulation toolkit", Nucl. Instr. Meth. A 506, no. 3, pp. 250-303 (2003).
- [Agu01] A. AGUILAR ET AL.: "Evidence for neutrino oscillations from the observation of $\bar{\nu}_e$ in a $\bar{\nu}_\mu$ beam", Phys. Rev. D 64, 112007 (2001).
- [Ahn12] J. K. AHN ET AL.: "Observation of Reactor Antineutrino Disappearance in the RENO Experiment", Phys. Rev. Lett. 108, 191802 (2012).
- [Akh11] E. K. AKHMEDOV: "Neutrino oscillations: Theory and phenomenology", Nucl. Phys. Proc. Suppl. 221, pp. 19-25 (2011).
- [Alg10] A. ALGORA ET AL.: "Reactor Decay Heat in ^{239}Pu : Solving the Discrepancy in the 4-3000-s Cooling Period", Phys. Rev. Lett. 105, 202501 (2010).
- [An12] F. P. AN ET AL.: "Observation of Electron-Antineutrino Disappearance at Daya Bay", Phys. Rev. Lett. 108, 171803 (2012).
- [An13] F. P. AN ET AL.: "Improved measurement of electron antineutrino disappearance at Daya Bay", Chin. Phys. C 37, no. 1, 011001 (2013).
- [Anj10] J. C. ANJOS ET AL.: "Monitoring Nuclear Reactors with Antineutrino Detectors: the ANGRA Project", AIP Conf. Proc. 1222, pp. 427-430 (2009).

BIBLIOGRAPHY

- [Ans95] P. ANSELMANN ET AL.: "*GALLEX solar neutrino observations: Complete results for GALLEX II*", Phys. Lett. B 357, pp. 237-247 (1995), Erratum-ibid. B 361, pp. 235-236 (1996).
- [App03] M. APPOLONIO ET AL.: "*Search for neutrino oscillations on a long base-line at the CHOOZ nuclear power station*", Eur. Phys. J. C 27, pp. 331-374 (2003).
- [Ara05] T. ARAKI ET AL.: "*Experimental investigation of geologically produced antineutrinos with KamLAND*", Nature 436, pp. 499-503 (2005).
- [Arc13] M. ARCHIDIACONO ET AL.: "*Sterile Neutrinos: Cosmology vs Short-BaseLine Experiments*", arXiv:1302.6720v2 [astro-ph.Co] (2013).
- [Bea10] J. F. BEACOM: "*The Diffuse Supernova Neutrino Background*", Ann. Rev. Nuc. Part. Sci. 60, pp. 439-462 (2010).
- [Bed13] A. G. BEDA ET AL.: "*Gemma experiment: The results of neutrino magnetic moment search*", Phys. Part. Nucl. Lett. 10, pp. 139-143 (2013).
- [Bel12] G. BELLINI ET AL.: "*Cosmic-muon flux and annual modulation in Borexino at 3800 m water-equivalent depth*", JCAP 05, 015 (2012).
- [Bel13] G. BELLINI ET AL.: "*Measurement of geo-neutrinos from 1353 days of Borexino*", Phys. Lett. B 722, pp. 295-300 (2013).
- [Bem02] C. BEMPORAD ET AL.: "*Reactor-based neutrino oscillation experiments*", Rev. Mod. Phys. 74, pp. 297-328 (2002).
- [Ber13] J. BERINGER ET AL.: "*Review of Particle Physics*", Phys. Rev. D 86, 010001 (2012) and 2013 partial update for the 2014 edition (URL: <http://pdg.lbl.gov>).
- [Bev03] P. R. BEVINGTON AND D. K. ROBINSON: "*Data Reduction and Error Analysis for the Physical Sciences*", Third Edition, McGraw-Hill Higher Education, New York (2003).
- [Bir64] J. G. BIRKS: "*The Theory and Practice of Scintillation Counting*", Pergamon Press, London (1964).
- [Bre07] H. BREITKREUTZ: "*Spektrale Charakterisierung des Therapiestrahls am FRM II*", Diploma thesis, Technische Universität München (2007).
- [BrePC] H. BREITKREUTZ - author of [Bre07], Forschungs-Neutronenquelle Heinz Maier-Leibnitz (FRM II), Technische Universität München, personal communication.
- [Bru97] R. BRUN AND F. RADEMAKERS: "*ROOT - An object oriented data analysis framework*", Nucl. Inst. and Meth. in Phys. Res. A 389, pp. 81-86 (1997). See also <http://root.cern.ch/>.

- [Bur12] R. BURKHARDT: "*Abschätzung der Abschirmwirkung des Garchinger Untergrundlabors (UGL) durch die Messung des Myonen-Flusses inner- und außerhalb des UGLs*", Bachelor thesis, Technische Universität München (2012).
- [Car59] R. E. CARTER ET AL.: "*Free Antineutrino Absorption Cross Section. II. Expected Cross Section from Measurements of Fission Fragment Electron Spectrum*" Phys. Rev. 113, pp. 280-286 (1959).
- [Chr79] L. G. CHRISTOPHOROU ET AL.: "*Fast gas mixtures for gas-filled particle detectors*", Nucl. Inst. Meth. 163, pp. 141-149 (1979).
- [Cow53] C. L. COWAN JR. AND F. REINES: "*Detection of the free neutrino*", Phys. Rev. 92, pp. 830-831 (1953).
- [DataA] Data sheet: *Canberra HV Power Supply Model 3102 D*, available at www.canberra.com/products/radiochemistry_lab/pdf/Model-3102D-SS-NSP0003.pdf, CANBERRA Industries Inc. (June 2013).
- [DataB] Data sheet: *Ortec Scintillation Preamplifier 113*, available at old.ortec-online.com/electronics/preamp/113.pdf, AMETEK Inc. (June 2013).
- [DataC] Data sheet: *Ortec Amplifier 575A*, available at old.ortec-online.com/electronics/amp/575a.htm, AMETEK Inc. (June 2013).
- [DataD] Data sheet: *Ortec Linear Gate and Stretcher 542*, available at www.ortec-online.com/download/542.pdf, AMETEK Inc. (June 2013).
- [DataE] Data sheet: *Canberra Analog to Digital Converter 8701*, available at www.canberra.com/products/radiochemistry_lab/pdf/Model-8701-SS-CSP0068.pdf, CANBERRA Industries Inc. (June 2013).
- [DataF] Data sheet: *Canberra HV Power Supply Model 3106 D*, available at www.canberra.com/products/radiochemistry_lab/pdf/Model-3106D-SS-CSP0067.pdf, CANBERRA Industries Inc. (June 2013).
- [DataG] Data sheet: *Canberra Model 2006 Proportional Counter Preamplifier Power Supply Model 3106 D*, available at www.canberra.ru/html/products/detectors/preamplifiers/2006.pdf, CANBERRA Industries Inc. (June 2013).
- [DataH] Data sheet: *Ortec Spectroscopic Amplifier 672*, available at www.ortec-online.com/download/672.pdf, AMETEK Inc. (June 2013).
- [DataJ] Data sheet: *Ortec Timing Single Channel Analyzer 551*, available at www.ortec-online.com/download/551.pdf, AMETEK Inc. (June 2013).

BIBLIOGRAPHY

- [DataK] Data sheet: *FAST ComTec Multiparameter Multichannel Analyzer System MPA-3*, available at <http://www.fastcomtec.com/products/multiparameter-multichannel-analyzers/mpa-3.html>, FAST ComTec (June 2013).
- [Dav68] R. DAVIS ET AL.: "*Search for neutrinos from the sun*", Phys. Rev. Lett. 20, pp. 1205-1209 (1968).
- [DCPre] DOUBLE CHOOZ COLLABORATION: Publication in preparation. Working title: "*Background-independent oscillation analysis in Double Chooz*", first draft (Aug. 2013).
- [Den10] M. DENIZ ET AL.: "*Measurement of $\bar{\nu}_e$ -electron scattering cross section with a CsI(Tl) scintillating crystal array at the Kuo-Sheng nuclear power reactor*", Phys. Rev. D 81, 072001 (2010).
- [Dec94] Y. DECLAIS ET AL.: "*Study of reactor antineutrino interaction with proton at BUGEY nuclear power plant*", Phys. Lett. B 338, pp. 383-389 (1994).
- [Ele03] ELECTRON TUBES LIMITED: "*Understanding Photomultipliers*", Product brochure by Electron Tubes Enterprises, available at <http://www.et-enterprises.com/> (2003).
- [Eme82] D. EMENDÖRFER AND K. H. HÖCKER: "*Theorie der Kernreaktoren, Band 1: Der stationäre Reaktor*", Bibliographisches Institut Mannheim/Wien/Zürich, 2. Aufl. (1982).
- [END12] Website of NUCLEAR DATA CENTER OF THE KOREA ATOMIC ENERGY RESEARCH INSTITUTE, Pointwise ENDF-VII at 300 K, <http://atom.kaeri.re.kr/> (Sept. 2012).
- [Eng93] T. R. ENGLAND ET AL.: "*Evaluation and Compilation of Fission Product Yields*", Los Alamos National Laboratory, LA-UR-94-3106; ENDF-349 (1993); compiled by <http://ie.lbl.gov/fission.html> (Jan. 2013).
- [Fal07] M. FALLOT ET AL.: "*Towards reactor neutrino applied physics*", International Conference on Nuclear Data for Science and Technology, DOI: 10.1051/ndata:07758, available at <http://dx.doi.org/10.1051/ndata:07758> (2007).
- [Fal12] M. FALLOT ET AL.: "*New antineutrino energy spectra predictions from the summation of beta decay branches of the fission products*", Phys. Rev. Lett. 109, 202504 (2012).
- [Fal50] D. L. FALKOFF AND G. E. UHLENBECK: "*On the Beta-Gamma-Angular Correlation*", Phys. Rev. 76, Nr. 2 (1950).

- [FalPC] M. FALLOT, SUBATECH (Univ. de Nantes - CNRS/in2p3 - EMN), author of [Fal12], personal communication.
- [Fan52] U. FANO: "*Tables for the analysis of β - spectra*", M.S. National Bureau of Standards, Applied Mathematics Series Nr. 13, Washington (1952).
- [Fir96a] R. B. FIRESTONE: "*Table of Isotopes*", Eighth Edition, Volume I, John Wiley & Sons, INC. (1996).
- [Fir96b] R. B. FIRESTONE: "*Table of Isotopes*", Eighth Edition, Volume II, John Wiley & Sons, INC. (1996).
- [Fog12] G. L. FOGLI ET AL.: "*Global analysis of neutrino masses, mixings and phases: entering the era of leptonic CP violation searches*", Phys. Rev. D 86, 013012 (2012).
- [For12] D. V. FORERO ET AL.: "*Global status of neutrino oscillation parameters after Neutrino-2012*", Phys. Rev. D 86, 073012 (2012).
- [Fur10] H. FURUTA ET AL.: "*Development of Advanced Monitoring System with Reactor Neutrino Detection Technique for Verification of Reactor Operation*", IAEA-CN-184/63 (2010).
- [Gae02] R. GÄHLER AND M. STEFFENS: "*The New Neutron Source FRM-II*", Technische Universität München, Forschungs-Neutronenquelle Heinz Maier-Leibnitz (FRM II) (2002).
- [Gan11] A. GANDO ET AL.: "*Partial radiogenic heat model for Earth revealed by geoneutrino measurements*", Nat. Geosc. 4, pp. 647-651 (2011).
- [Gan13] A. GANDO ET AL.: "*Reactor On-Off Antineutrino Measurement with KamLAND*", arXiv:1303.4667v2 [hep-ex] (2013).
- [Gar05] *Garfield 8.01*, responsible person at CERN: Rob Veenhof, <http://garfield.web.cern.ch/garfield/>, Reference W5050, Updated Version (2005).
- [GEA13] Homepage of the GEANT4 collaboration, <http://geant4.cern.ch/> (2013).
- [Goe00] V. GÖBNER AND G. VON HASSEL (EDITORS): "*Neutrons for industry and medicine*", Technische Universität München, Forschungs-Neutronenquelle Heinz Maier-Leibnitz (FRM II), (2000).
- [Gre92] R. C. GREENWOOD ET AL.: "*Total absorption gamma-ray spectrometer for measurement of beta-decay intensity distributions for fission product radionuclides*", Nucl. Inst. Meth. A 314, pp. 514-540 (1992).

BIBLIOGRAPHY

- [Gro92] M. GROSS ET AL.: "*Determination of high Q_β -values by beta-gamma-coincidence measurements with a plastic scintillator telescope*", Nucl. Inst. and Meth. in Phys. Res. A 3, pp. 512-519 (1992).
- [Gru05] F. GRÜNAUER: "*Design, optimization, and implementation of the new neutron radiography facility at FRM-II*", PhD thesis, Technische Universität München (2005).
- [Haa08] N. H. HAAG: "*Bestimmung des Antineutrinospektrums der Spaltprodukte von ^{238}U* ", Diploma thesis, Technische Universität München (2008).
- [Hah89] A. A. HAHN ET AL.: "*Anti-neutrino Spectra from ^{241}Pu and ^{239}Pu Thermal Neutron Fission Products*", Phys. Lett. B 218, pp. 365-368 (1989).
- [Ham07] HAMAMATSU PHOTONIS K. K.: "*Photomultiplier Tubes, Basics and Applications*", Third edition, available as pdf on www.hamamatsu.com (2007).
- [Har77] J. C. HARDY ET AL.: "*The essential decay of pandemonium: A demonstration of errors in complex beta-decay schemes*", Phys. Lett. B 71, pp. 307-310 (1977).
- [Has01] G. VON HASSEL AND W. WASCHKOWSKI (EDITORS): "*Experimental facilities at FRM-II*", Technische Universität München, Forschungs-Neutronenquelle Heinz Maier-Leibnitz (FRM II), (2001).
- [Hof07] M. HOFMANN: "*Low-background gamma spectroscopy for the neutrino oscillation experiment DOUBLE CHOOZ*", Diploma thesis, Technische Universität München (2007).
- [Hos06] J. HOSAKA ET AL.: "*Three flavor neutrino oscillation analysis of atmospheric neutrinos in Super-Kamiokande*", Phys. Rev. D 74, 032002 (2006).
- [Hub11] P. HUBER: "*Determination of antineutrino spectra from nuclear reactors*", Phys. Rev. C 84, 024617 (2011), Errata: Phys. Rev. C 85, 029901(E) (2012).
- [Ian12] A. IANNI ET AL.: "*Artificial neutrino source experiment in Borexino*", J. Phys. Conf. Ser. 375, 042066 (2012).
- [Jon12] C. L. JONES: "*Reactor Simulation for Antineutrino Experiments using DRAGON and MURE*", Phys. Rev. D 86, 012001 (2012).
- [JunPC] M. JUNGWIRTH, Forschungs-Neutronenquelle Heinz Maier-Leibnitz (FRM II), Technische Universität München, personal communication.
- [Kal82] J. KALEF-EZRA ET AL.: "*Electron backscattering from low Z thick absorbers*", Nucl. Inst. and Meth. 195, pp. 587-595 (1982).
- [Kli68] J. VAN KLINKEN ET AL.: "*Beta- and gamma-ray measurements on the decay of ^{38}Cl* ", Nucl. Phys. A 112, pp. 372-384 (1968).

-
- [Kli94] Y. V. KLIMOV ET AL.: "*Neutrino method remote measurement of reactor power and power output*", Atomic Energy 76, no. 2 (1994).
- [Kop03] V. I. KOPEIKIN ET AL.: "*Reactor as a Source of Antineutrinos: Thermal Fission Energy*", Phys. Atom. Nucl. 67, pp. 1892-1899 (2004).
- [Kur12] Y. KURODA ET AL.: "*A mobile antineutrino detector with plastic scintillators*", arXiv: 1206.6566v1[physics.ins-det] (2012).
- [Law98] D. LAWRENCE ET AL.: "*The Palo Verde neutrino oscillation experiment*", Nucl. Phys. Proc. Suppl. 66, pp. 396-399 (1998).
- [LhuPC] D. LHULLIER, author of [Mue11] and member of the Double Chooz reactor group, CEA Saclay, personal communication.
- [Li13] Y. - F. LI ET AL.: "*Unambiguous Determination of the Neutrino Mass Hierarchy Using Reactor Neutrinos*", arXiv:1303.6733v1 [hep-ex] (2013).
- [Led78] C. M. LEDERER ET AL.: "*Table of isotopes*", John Wiley & sons, 7th edition (1978).
- [Leo94] W. R. LEO: "*Techniques for Nuclear and Particle Physics Experiments*", Second Revised Edition, Springer Verlag, Berlin (1994).
- [Mai58] F. C. MAIENSCHIN ET AL.: "*Gamma Rays Associated With Fission*", Second United Nations International Conference on the Peaceful Uses of Atomic Energy, A/Conf.15/P/670 (1958).
- [Mar94] G. MARLEAU ET AL.: "*DRAGON: A Collision Probability Transport Code for Cell and Supercell Calculations*", Report IGE-157, Institut de génie nucléaire, École Polytechnique de Montréal, Montréal, Québec (1994).
- [MeiPC] J. MEIER, Forschungs-Neutronenquelle Heinz Maier-Leibnitz (FRM II), Technische Universität München, personal communication (2009).
- [Men11] G. MENTION ET AL.: "*The Reactor Antineutrino Anomaly*", Phys. Rev. D 83, 073006 (2011).
- [Men13] G. MENTION: "*The reactor antineutrino anomaly*", J. Phys. Conf. Ser. 408, 012025 (2013).
- [Met84] J. METZINGER: "*Zum Einfluß der Betastärkefunktion auf Reaktor- und Neutrinophysik*", PhD thesis, Ruprecht - Karls - Universität Heidelberg (1984).
- [Mir13] A. MIRIZZI ET AL.: "*The strongest bounds on active-sterile neutrino mixing after Planck data*", arXiv:1303.5368v2 [astro-ph.CO] (2013).

BIBLIOGRAPHY

- [MoePC] R. MÖLLENBERG, participating author of [Wur12], personal communication; PhD thesis in preparation, Technische Universität München.
- [Mue11] TH. A. MUELLER ET AL.: "*Improved predictions of reactor antineutrino spectra*", Phys. Rev. C 83, 054615 (2011).
- [MUR12] *MURE, MCNP Utility for Reactor Evolution, User Guide - Version 1.9*, Handbook available at <http://lpsc.in2p3.fr/MURE/pdf/UserGuide.pdf> (2012).
- [Pal13] M. PALLAVICINI ET AL.: "*Recent results and future development of Borexino*", Nucl. Phys. Proc. Suppl. 235-236, pp. 55-60 (2013).
- [PDG04] S. EIDELMANN ET AL.: "*Review of Particle Physics*", Phys. Lett. B 592, 1 (2004).
- [Pho06] Data sheet for the photomultiplier XP3540 from *photonis*, available at <http://my.et-enterprises.com/pdf/XP3540.pdf> (2006).
- [Por10] A. PORTA: "*Reactor neutrino detection for non proliferation with the Nucifer experiment*", J. Phys. Conf. Ser. 203, 012092 (2010).
- [Pre07] W. H. PRESS ET AL.: "*Numerical Recipes, The Art of Scientific Computing*", Third Edition, Cambridge University Press (2007).
- [Roe10] A. RÖHRMOSER: "*Core model of new German neutron source FRM II*", Nuclear Engineering and Design 240, pp. 1417-1432 (2010).
- [RoePC] A. RÖHRMOSER - author of [Roe10], Forschungs-Neutronenquelle Heinz Maier-Leibnitz (FRM II), Technische Universität München, personal communication.
- [Sau77] F. SAULI: "*Principles of operation of multiwire proportional and drift chambers*", CERN, Service d'Information scientifique, Genf (1977).
- [Sai01] SAINT-GOBAIN CRYSTALS: "*Scintillation Products - Organic scintillators*", Saint-Gobain Crystals & Detectors, available at <http://www.detectors.saint-gobain.com/> (2001).
- [Sai08a] SAINT-GOBAIN CRYSTALS: "*BC-400, BC-404, BC-408, BC-412, BC-416 Premium Plastic Scintillator, Product Data Sheet*", Data sheet available at www.detectors.saint-gobain.com (2008).
- [Sai08b] SAINT-GOBAIN CRYSTALS: "*BC-620 Reflector Paint for Plastic Scintillators, Product Data Sheet*", Data sheet available at www.detectors.saint-gobain.com (2008).
- [Sch95] P. SCHMÜSER: "*Feynman-Graphen und Eichtheorien für Experimentalphysiker*" Second Edition, Springer-Verlag (1995).

- [Sch81] K. SCHRECKENBACH ET AL.: "*Absolute Measurement of the Beta Spectrum from ^{235}U Fission as a Basis for Reactor Antineutrino Experiments*", Phys. Lett. 99 B, pp. 251 - 256 (1981).
- [Sch85] K. SCHRECKENBACH ET AL.: "*Determination of the Antineutrino Spectrum from ^{235}U Thermal Neutron Fission Products up to 9.5 MeV*", Phys. Lett. 160 B, pp. 325 - 330 (1985).
- [Sch97] N. SCHMITZ: "*Neutrino Physik*", Teubner Studienbücher, Stuttgart (1997).
- [Sea92] V. F. SEARS: "*Neutron scattering lengths and cross sections*", Neutron News 3, pp. 26 - 37 (1992).
- [Sha98] A. SHARMA: "*Properties of some gas mixtures used in tracking detectors*", GSI-Darmstadt, SLAC-J-ICFA-16-3 (1998).
- [Sra12] O. ŠRÁMEK ET AL.: "*Geoneutrinos*", Adv.High Energy Phys. Vol. 2012, 235686 (2012).
- [Str03] A. STRUMIA AND F. VISSANI: "*Precise quasielastic neutrino/nucleon cross-section*", Phys. Lett. B 564, pp. 42 - 54 (2003).
- [Sug06] H. SUGIYAMA ET AL.: "*Systematic limits on $\sin^2(2\Theta_{13})$ in neutrino oscillation experiments with multi-reactors*", Phys. Rev. D 73, 053008 (2006).
- [Tab71] T. TABATA ET AL.: "*An empirical equation for the backscattering coefficient of electrons*", Nucl. Inst. and Meth. 94, pp. 509 - 513 (1971).
- [Ten89] O. TENGBLAD ET AL.: "*Integral $\bar{\nu}$ -spectra derived from experimental β -spectra of individual fission products*", Nucl. Phys. A 503, pp. 136 - 160 (1989).
- [Tho10] F. A. THORNE: "*Spectral Analysis of Neutrino and Background Events in the solar Neutrino Experiments BOREXINO and LENA*", Diploma thesis, Technische Universität München (2010).
- [Tol12] N. TOLICH ET AL.: "*Final results from SNO*", J. Phys. Conf. Ser. 375, 042049 (2012).
- [Tso69] N. TSOULFANIDIS ET AL.: "*The use of an analytical response function for unfolding beta spectra*", Nucl. Inst. and Meth. 73, pp. 98 - 102 (1969).
- [Tso71] N. TSOULFANIDIS ET AL.: "*Measurements of time-dependent energy spectra of beta-rays from uranium-235 fission fragments*", Nucl. Sci. Eng. 43, pp. 42 - 53 (1971).
- [Vog79] P. VOGEL ET AL.: "*Reactor antineutrino spectra and their application to antineutrino-induced reactions*", Phys. Ref. C 19, pp. 2259 - 2266 (1979).

BIBLIOGRAPHY

- [Vog81] P. VOGEL ET AL.: "*Reactor antineutrino spectra and their application to antineutrino-induced reactions. II*", Phys. Ref. C 24, pp. 1543-1553 (1981).
- [Vog07] P. VOGEL: "*Conversion of electron spectrum associated with fission into the antineutrino spectrum*", Phys. Ref. C 76, 025504 (2007).
- [WagPC] F. - M. WAGNER - responsible person for the medical application facility at FRM II, Forschungs-Neutronenquelle Heinz Maier-Leibnitz (FRM II), Technische Universität München, personal communication.
- [Wie11] M. E. WIESER AND T. B. COPLEN: "*Atomic weights of the elements 2009 (IUPAC Technical Report)*", Pure Appl. Chem. 83, pp. 359-396 (2011).
- [Wol10] J. WOLF ET AL.: "*The KATRIN Neutrino Mass Experiment*", Nucl. Inst. Meth. A 623, pp. 442-444 (2010).
- [Wur12] M. WURM ET AL.: "*The next-generation liquid-scintillator neutrino observatory LENA*", Astropart. Phys. 35, pp. 685-732 (2012).
- [Yam92] T. YAMASHITA ET AL.: "*Measurement of electron drift velocities and positive ion mobilities for gases containing CF₄ II*", Nucl. Inst. Meth. in Phys. Res. A 317, 213 (1992).
- [Zha13] C. ZHANG ET AL.: "*Reactor Antineutrino Anomaly with known θ_{13}* ", Phys. Rev. D 87, 073018 (2013).

Acknowledgment

Es ist nicht möglich, ein solches Experiment ohne die Hilfe und den Rat von Kollegen und Freunden zum erfolgreichen Abschluss zu bringen. So fühle ich mich all denjenigen zu Dank verpflichtet, die mich im Laufe dieser Arbeit unterstützt haben, sei es bei der direkten Durchführung des Experiments, durch wertvolle Diskussionen über die Datenanalyse aber auch abseits der Physik.

Mein erster Gedanke gilt Klaus Schreckenbach, der die Idee zu diesem Experiment hatte und mich bei allen Phasen der Arbeit mit seinem Wissen, konstruktiver Kritik und tatkräftiger Unterstützung im Labor begleitet hat. Auch wenn er die Resultate und Abgabe dieser Arbeit noch gesehen hat, so durfte er die Veröffentlichung leider nicht mehr miterleben. Vielen Dank für die unschätzbare und freundliche Hilfe.

Herzlicher Dank gebührt Lothar Oberauer, Stefan Schönert und Franz von Feilitzsch, deren Art den Lehrstuhl zu leiten eine äußerst sympathische Atmosphäre unter all uns Mitarbeitern geschaffen hat. Spezieller Dank an meine Betreuer Lothar Oberauer und Tobias Lachenmaier für die intensiven Diskussionen, in denen ich ungemein von deren Erfahrungsschatz profitieren durfte. Walter Potzel möchte ich danken für die vielen wertvollen Ratschläge und Anmerkungen, die ich in unzähligen und zeitaufwändigen Gesprächen erhalten habe.

Vielen Dank an alle Mitarbeiter des E15, nicht nur für die physikalische Unterstützung, sondern auch für die schöne Zeit am Lehrstuhl und die Freundschaften, die daraus entstanden sind. Namentlich möchte ich mich zudem bei Martin Hofmann bedanken, dessen universelle Hilfestellungen beim Experiment und in der Analyse eine entscheidende Rolle gespielt haben. Achim Gütlein, Andreas Zöller und Randolph Möllenberg haben viel Zeit investiert, mir die Analyse mit Hilfe der Geant4 Simulation zu ermöglichen. Außerdem bedanke ich mich bei Veronika Chobanova, die mich während ihrer Zeit am Lehrstuhl sehr bei der Bestimmung der Detektor-Parameter unterstützt hat. Danke an Patrick Pfahler, der mich nicht nur bei den schmucken Zeichnungen geholfen hat, sondern mit dem ich auch in Frankreich viele ebenso produktive und lehrreiche wie unterhaltsame Wochen verbringen konnte. Danke auch an Timo Lewke, vor allem dafür, dass ich ihn so oft ablenken durfte, wenn mir der Kopf nicht nach der Physik stand.

Vielen Dank ebenfalls an Jean-Côme Lanfranchi, zum einen für meine sorgenfreie Zeit auf der Cluster-Stelle, aber besonders auch für die netten Ausflüge nach Frankreich und die immer präesente Melodie der "Seven Days" auf dem Gang.

Unserer guten Seele, Maria Bremberger, ein großes Dankeschön für die selbstverständliche Art, mit der sie uns Doktoranden immer den Kopf frei hielt, indem sie unseren Verwaltungskram erledigte, bevor wir überhaupt von dessen Existenz wussten. Das Sekretariat war für mich zudem immer eine Anlaufstelle, wenn ich mal eine Aufheiterung gebraucht habe!

Special thanks also to David Lhuillier and Muriel Fallot and their groups in Saclay and Nantes, respectively. I enjoyed the fruitful and excessive discussions concerning the predictions and appreciated the valuable input you provided to finish the analysis. Merci beaucoup!

Thanks also to the other collaborators of Double Chooz and its reactor group - I enjoyed being part of this international network! Thank you for all the discussion about my work and for the time we spent together at the meetings and the Château!

Meine Kollegen an der Neutronenquelle FRMII haben einen großen Beitrag zum Experiment geleistet. Jens Klenke, Thomas Bücherl und - im Besonderen - Franz M. Wagner haben ihre Zeit investiert, das Experiment vorzubereiten und zu unterstützen. Des Weiteren danke ich Harald Breitzkreutz, Christian Hesse, Johann Meier, Anton Röhrmoser, Susanne Wolff, Karl Zeitelhack, dem ANTARES-Team und den Mitarbeitern des Strahlenschutzes für all die vielseitige Hilfe, die mir zuteil wurde.

Der größte Dank jedoch gilt meiner Familie! Die bedingungslose Unterstützung, die ihr mir seit jeher schenkt, hat mir nicht nur bei dieser Arbeit den nötigen Rückhalt gegeben. Und du, Vanessa, bist seit so langer Zeit an und auf meiner Seite. Ich danke dir für den liebevollen Zuspruch, der mich bei allem begleitet.

*In dankbarer Erinnerung an
Arno und Eva John*